

UNIVERSITY OF NAPLES “FEDERICO II”

DOCTORATE SCHOOL OF STRUCTURES FOR
ENGINEERING AND ARCHITECTURE



RAPID DRAWDOWN ON EARTH DAM STABILITY
AFTER A STRONG EARTHQUAKE

Federica Rotili

A Dissertation Submitted in Partial Fulfilment of the Requirements for
the Degree of PHILOSOPHIAE DOCTOR in
STRUCTURAL, GEOTECHNICAL AND SEISMIC ENGINEERING
XXIX Cycle

TUTOR

Prof. Stefania Sica

Prof. Luca Pagano

COORDINATOR

Prof. Luciano Rosati

UNIVERSITY OF NAPLES “FEDERICO II”

DOCTORATE SCHOOL OF STRUCTURAL ENGINEERING AND ARCHITECTURE

Date: April 2017

Author: Federica Rotili
Title: Rapid drawdown on earth dam stability after a strong earthquake
Department: Department of Structures for Engineering and Architecture
Degree: Philosophiae Doctor

Permission is herewith granted to University to circulate and to have copied for non-commercial purposes, at its discretion, the above title upon the request of individuals or institutions.

Signature of Author

THE AUTHOR RESERVES OTHER PUBLICATION RIGHTS, AND NEITHER THE THESIS NOR EXTENSIVE EXTRACTS FROM IT MAY BE PRINTED OR OTHERWISE REPRODUCED WITHOUT THE AUTHOR'S WRITTEN PERMISSION.

THE AUTHOR ATTESTS THAT PERMISSION HAS BEEN OBTAINED FOR THE USE OF ANY COPYRIGHTED MATERIAL APPEARING IN THIS THESIS (OTHER THAN BRIEF EXCERPTS REQUIRING ONLY PROPER ACKNOWLEDGEMENT IN SCHOLARLY WRITING) AND THAT ALL SUCH USE IS CLEARLY ACKNOWLEDGED.

To my father

3.2.	SOIL CONSTITUTIVE LAW	97
3.2.1.	SIMPLIFIED MODELS	98
3.2.1.1.	HYSTERETIC MODEL.....	98
3.2.1.2.	DYNAMIC PORE PRESSURE GENERATION: FINN AND BYRNE MODELS (1991)	99
3.3.	BOUNDARY CONDITIONS (B.C.)	101
3.3.1.	B.C. FOR THE DAM STATIC ANALYSIS	101
3.3.2.	B.C. FOR THE DAM DYNAMIC ANALYSIS	102
3.3.3.	APPLICATION OF THE DYNAMIC INPUT	104
3.4.	SLOPE STABILITY ANALYSIS IN A CONTINUUM APPROACH	107
4.	THE CASE STUDY	113
4.1.	CAMPOLATTARO DAM.....	113
4.2.	SOIL MATERIALS	115
4.2.1.	SHELLS.....	115
4.2.2.	DRAINS.....	116
4.2.3.	CORE.....	116
4.2.4.	FOUNDATION.....	120
4.2.5.	MAIN PARAMETERS FOR THE DIFFERENT DAM ZONES	123
4.3.	NUMERICAL MODELLING.....	123
4.3.1.	GEOMETRY	123
4.3.2.	INTERACTION BETWEEN THE PHASES	126
4.3.3.	CONSTITUTIVE MODELS.....	127
4.3.4.	STATIC STAGES: CONSTRUCTION, FIRST RESERVOIR FILLING AND OPERATION	131
4.3.5.	DYNAMIC STAGE.....	135
4.3.6.	DRAWDOWN STAGE	145
5.	RESULTS	149
5.1.	STATIC ANALYSES	150
5.2.	SEISMIC ANALYSES.....	153
5.3.	DRAWDOWN ANALYSES.....	170
6.	FINAL REMARKS.....	193
	APPENDIX: UNSATURATED SOIL MECHANICS.....	199
A.1.	INTRODUCTION.....	199

A.2. SOIL SUCTION.....	201
A.3. SOIL WATER CHARACTERISTIC CURVE	207
A.4. PERMEABILITY FOR UNSATURATED SOILS.....	212
A.5. SHEAR STRENGTH OF UNSATURATED SOILS.....	214
References	221

Abstract

The research activity carried out during the PhD period focused on the numerical modelling of earth dams. In particular, dam response to a drawdown of the reservoir after a strong earthquake was investigated, accounting for different operating conditions. The interest on such a topic comes from the fact that in Italy and worldwide there are many large dams, most of which are earth dams, placed very close to active faults and hence subjected to high seismic hazard. In such conditions, the structure may be asked to face the earthquake first and the emergency rapid drawdown later. Individually, each stage may be critical from the viewpoint of dam stability; if the two stages occur simultaneously or consecutively the effects on the embankment may be very dangerous.

Worth mentioning are the strong earthquakes occurred in central Italy (L'Aquila, 2009; Amatrice and Norcia, 2016) in the last decade, against which the authorities in charge of the dam safety acted completely unprepared to face the emergency, due to the lack of pre-arranged predictive/interpretative tools. Especially, after the latest events of Amatrice and Norcia (2016), the possible negative effect of a drawdown carried out after a strong earthquake had arisen greater interest than in the past. The seismic activity near the Campotosto Lake (central Italy), with its three dams (Sella Pedicate, Rio Fucino and Poggio Cancelli), caused huge apprehension in the local authorities and population, worried about dam safety after a so long and severe seismic sequence (2016-2017). Dam managers, on the other hand, were wondering whether lowering or not the reservoir.

The investigated research theme is quite new in the geotechnical field. In the past, the single dam stages were examined separately. In this work, the drawdown simulation has been performed after a dynamic stage and no previous studies have been found to date on such an issue.

The first chapter of this thesis illustrates a brief introduction of the problem and its complexity.

The second chapter reports a detailed state-of-the-art on existing methods for modelling the static (including the reservoir drawdown) and seismic response of earth dams. The overview on the analysis methods, with their

pro and cons, allowed the selection of the most suitable approach to model both the static and the seismic response of the dam. With reference to the latter issue, the Performance Based Design approach was applied in order to define the dam performance objectives with identification of different limit states. In the performed computation, the seismic stage is a fundamental one because it provides the initial stress state for the following drawdown analysis.

In the third chapter, the mathematical formulation necessary to solve the selected boundary value problem will be presented. Some constitutive models suitable to represent soil behaviour under cyclic loading will be briefly described, together with the boundary conditions required in each simulation stage.

In the fourth chapter, the case study selected to perform the advanced dynamic analyses and the rapid drawdown simulation will be explained in detail. The selected case history is the Campolattaro dam, a zoned earth dam, built between the 1980s and the 1990s, in a high seismicity area. A detailed geotechnical characterization of the dam soils was achieved thanks to a new investigation carried out during the PhD period. The numerous data available allowed the calibration of the adopted constitutive models, especially under cyclic loading. Then the different steps followed to simulate the construction, earthquake and drawdown stages will be illustrated.

In the fifth chapter analysis results will be provided trying to highlight the different factors affecting the dam response during the drawdown (initial stress state, stress change due to seismic stage; drawdown rate, R ; drawdown ratio, L/H).

From the performed analyses it emerged that dam stability, ascertained in terms of global factor of safety (FOS), is higher if the drawdown is carried out without accounting for the earthquake. Conversely, the occurrence of an earthquake (whichever its severity) could reduce the safety of the upstream shell during the drawdown, especially at the beginning of the lowering operations, i.e. $L/H < 0.3$. Moreover, the dam response during a drawdown is obviously affected also by the drawdown rate. The faster the drawdown, the smaller is the FOS and less important become the effects of the initial conditions on the slope stability.

Acknowledgements

I would like to express my sincere thanks to my tutor Prof. Stefania Sica who believed in my ability, giving me the opportunity to study a very challenging geotechnical topic, who guided me through this work with precious suggestions, motivations and support, and most of all behaved as an elder sister.

I am grateful to my tutor Prof. Luca Pagano whose suggestions helped me to overcome dead spots.

I would like also to thank Prof. Roberto Vassallo and Prof. Enzo Massimiliano Fontanella for their precious advices and their work during the review of my Ph.D. dissertation.

I want to thank all my colleagues for sharing with me the good and bad moments that I had during the last three years. Special thanks to Alessandra, Michele, Angelo, Roberto, Angelo I., Maria Grazia, Mariapia and Stefania.

Finally, I am grateful to my family, especially my mother, and boyfriend, for their constant support and encouragement.

1. Introduction

According to the Italian Dam Service (may 2014), the heritage of Italian large dams includes 538 structures of various typologies (e.g. gravity dams, arch dams, arch-gravity dams, etc.), materials (e.g. earth, concrete, masonry) and age. Among these, 165 are earth dams.



Figure 1-1. Italian dams (Italian Dam Service, 2016).

Many earth dams built in the twentieth century were designed underestimating the seismic hazard of the site. In recent years, new studies on the seismic hazard of the country have been carried out and many dams today are located in areas of higher seismicity compared to the past. Thus arises the need to evaluate or, in some cases, to re-evaluate the seismic safety of these dams, which do not fit the safety criteria required by current seismic regulations. Unfortunately, for existing dams such assessment is

not simple because it raises a number of problems related to the absence of an “ad hoc” methodology to carry out the seismic assessment and the uncertainties linked to the actual state of the dam.

In addition to the risk associated to dams in seismic areas, the drawdown of the reservoir may also be a critical stage for the stability of dams in operation. The lowering of water level has two effects: reduction of the stabilizing effect exerted by the external hydrostatic pressure (unloading effect on the upstream shell) and modification of the internal pore water pressure.

In these days the aforementioned issue has become particularly crucial since the long sequence of the latest earthquakes in Central Italy (Amatrice and Norcia, 2016) is causing huge concern in the local administrators and dam managers. For safety reasons, these latter ones may be pushed to lower the reservoir of the dams placed in the epicentral zones. Figure 1-2 shows the seismic activity near the Campotosto Lake (Central Italy), where three dams (Sella Pedicate, Rio Fucino and Poggio Cancelli), built in the early twentieth century, form the reservoir.

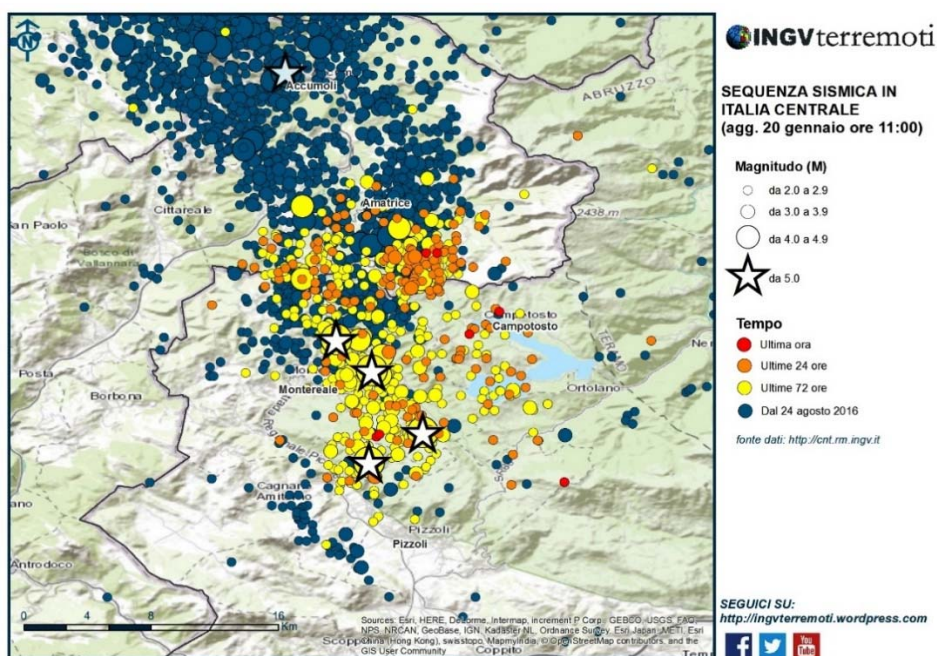


Figure 1-2. Seismic activity in Central Italy around the Campotosto Lake from August 24th 2016 to January 20th 2017 (INGV, 2017).

1.1 AIM OF THE WORK

The evaluation of the effects of a rapid drawdown on dam stability after a strong earthquake is the scope of this study.

The lack of literature studies, technical regulations or guidelines on this issue led to investigate the key factors that may influence the problem to find the proper procedures to perform a safe drawdown of the reservoir for dams hit by strong earthquakes.

For this purpose, a deep literature review on dam stability due to a drawdown has been carried out. On the basis of the classical limit equilibrium approaches, the phenomenon is known to depend on strength characteristics of the soil, slope geometry and drawdown ratio.

The development of numerical approaches, instead, allowed to perform transient seepage and coupled analyses, so other variables, such as soil permeability and stiffness and drawdown rate, have been added to the former ones.

However, since earth dam response depends on past loading conditions, the study of the problem required that the several stages of the dam lifetime (construction, first filling, operation, seismic stage, drawdown) should be reconstructed in the simulation.

Afterwards, a case study of an existing zoned dam has been modelled, evaluating its seismic response before performing the drawdown analyses. The dynamic stage has been computed considering as input a series of accelerograms that fulfil the seismic hazard of the dam site, according to the current national regulations (D.M. 14/01/2008, M.I.T. 26/06/2014).

In most of literature studies on slope drawdown, the soil is considered as a two-phase medium, i.e. above and below the phreatic surface it is assumed dry or completely saturated, respectively. Actually, during a rapid drawdown, this assumption is very rough, especially if the earth dam is made of fine and compacted soils, characterized by very low permeability. So, in the drawdown simulation, the mechanics of unsaturated soils was also introduced.

2. State-of-the-art on earth dam static and dynamic modelling

Assessment of earth dam safety is a very challenging issue for geotechnical engineers, especially when existing earth dams are concerned since their response depends on several loading conditions that can occur.

In very recent years the seismic response of existing dams has arisen a very large interest due to the increased awareness of the risk connected to these structures in high seismicity zones and to the fact that most of these structures were not specifically designed to resist against earthquakes. Due to the long sequence of the last earthquakes occurred in central Italy (L'Aquila, 2009; Amatrice and Norcia, 2016) also the drawdown effect after a strong earthquake is arising greater interest than in the past.

This chapter illustrates a state-of-the-art on the static and seismic modelling of earth dams.

Firstly, the effects induced by a rapid drawdown on submerged slopes are recalled.

Secondly, the existing methods used for the evaluation of the seismic response of earth dams are described. Each method has its own pros and hence has its own limitations. It is therefore essential to be aware of the limitations of these methods.

Subsequently, the Performance Based Seismic Design (PBSD) criteria are introduced in order to assess the earth dam performance under static and seismic loading. The high risk associated to dams due to relevant social, economic and environmental consequences of a failure requires dam performance to be known in each stage of the dam life.

2.1. RAPID DRAWDOWN

The stability of a slope depends on its geometry, soil properties and the forces acting internally and externally (Berilgen, 2007). The pore water pressure and external water load (reservoir) are examples of such internal and external forces that may have consequences both from hydrostatic and

hydrodynamic perspectives on the slope stability. Whether a slope is partially or totally submerged, the internal and external forces that affect the slope can change as the water level changes. As a result of the water level change, both seepage-induced pore pressures due to transient flow and stress-induced pore pressure changes, Δu , develop inside the slope. Pore pressure changes dissipate over time and consolidation takes place. The rate of dissipation of Δu and decrease in seepage-induced pore pressures depend on the drawdown rate and the hydraulic conductivity and compressibility characteristics of the slope materials.

In highly permeable soils, stress-induced Δu mostly dissipate during drawdown. In soils with low permeability, seepage-induced and stress-induced pore pressure changes are not likely to dissipate at the same rate with the external water level changes; consequently, totally or partially undrained soil behaviour will be observed (Figure 2-1).

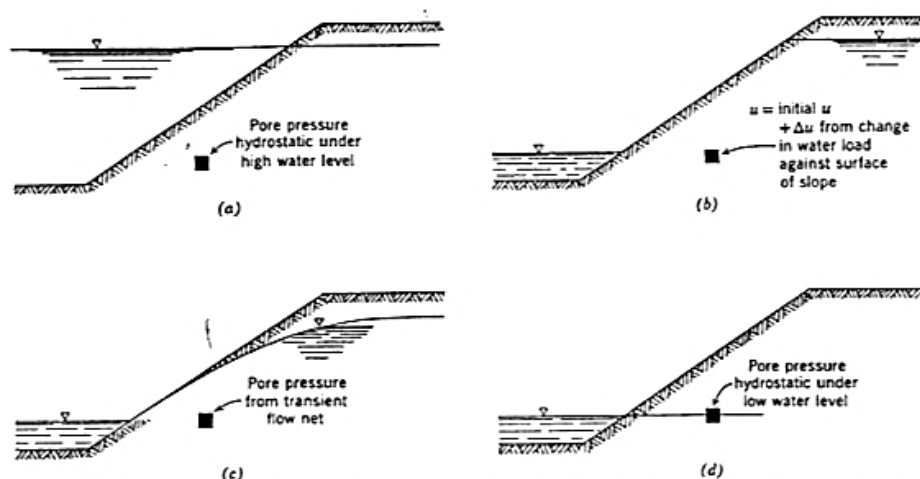


Figure 2-1. Response of slope to rapid drawdown. (a) Initial equilibrium condition. (b) After drawdown but before consolidation adjustment. (c) After consolidation adjustment. (d) Final equilibrium condition (Lambe and Whitman, 1969).

If the change in external water level happens without allowing the drainage of the slope soils, it is called sudden or Rapid DrawDown (RDD). Due to the rapid drawdown there will be a worsening of the slope stability conditions, which may lead to slope failures. In the past, many similar failures have been observed in natural and constructed slopes. It is important to study and understand the stability of the slopes near reservoirs, rivers, lakes and seas where RDD occurs in order to secure the safety of

people and critical infrastructure in the surrounding areas. Advanced solutions of this challenging problem will result in safe and economic treatment of areas that are under RDD related risks.

To define the safety factor of the submerged slope, either the classical slope stability analysis based on limit equilibrium (generally using method of slices) or numerical solutions (finite element methods, finite difference methods, etc.) are widely used.

Traditionally, in slope stability analysis, undrained parameters (total stress analysis) are used for the short-term stability analysis, and drained parameters (effective stress analysis) are used for the long-term stability analysis. In the geotechnical literature, procedures for RDD stability analysis are extensively reported for both conditions, as will be illustrated in detail in the following sections. Pore water pressures are needed for the effective stress analysis, where the effects of seepage-induced pore pressures are determined by the help of numerical techniques such as the finite element or finite difference methods, which, in turn, are used in the limit equilibrium analysis. However, total stress methods are utilized more frequently, mainly due to the difficulty in determining the pore pressures required in the effective stress methods. In recent years, it has become more common to use the numerical methods, especially the finite element method for the stability analysis of slopes. The finite element method can be used for the stress, seepage, and stability analysis of slopes, taking into account nonlinear material behaviour, complex boundary and loading conditions. It has also become possible to perform coupled analysis of stress-induced pore pressure generation and dissipation over time.

In the sixties Morgenstern (1963) listed slope failures all over the world (France, USA, Australia, India) caused by a rapid drawdown (Table 2-1).

Based on these failures, Morgenstern offered a simple way to assess the stability of the upstream slope of dams by stability charts. The latter ones facilitate the computation of the factor of safety during rapid drawdown. As the reservoir level is lowered, the factor of safety decreases if it is assumed that no dissipation of pore pressure occurs during the drawdown. Pore pressures due to the drawdown may be estimated using the pore-pressure coefficient defined by Skempton (1954), \bar{B} , depending on changes in total stress caused by the drawdown.

Name	Height: (ft)	Upstream slope	Soil properties	Notes and references
Cercey	37.7	2.4:1	$c' = 2.6$ per sq. in. $\phi' = 26^\circ$	Drained shear box tests carried out many years after failure, Mayer (1936)
Wassy	54.0	1.5:1	$c' = 2.8$ per sq. in. $\phi' = 23^\circ$	do.
Grosbois	57.0	1.9:1	$c' = 3.6$ per sq. in. $\phi' = 25.7^\circ$	do.
Charmes	55.7	1.9:1	$c' = 4.1$ per sq. in. $\phi' = 26.6^\circ$	do.
Bear Gulch	63.0	3:1	—	Sherard (1953)
Belle Fourche ..	122.0	2:1	$c = 7.9$ per sq. in. $\phi = 9.7^\circ$	Undrained direct shear tests after failure, Sherard (1953)
Brush Hollow ..	73.0	3:1	$c_u = 13.5-28.4$ per sq. in.	Unconfined compression tests after failure, Sherard (1953)
Mount Pisgah ..	76.0	1.5:1	—	Sherard (1953)
Utica	70.0	2:1	—	Reinius (1948)
Eildon	90.0	1.35:1	—	Schatz and Boesten (1936)
Aiai-ike	42.5	1:1-2:1	$c' = 1.5$ per sq. in. $\phi' = 18^\circ$	Consolidated undrained triaxial tests, Akai (1958)
Fruitgrower's ..	36.0	3:1	—	Sherard (1953)
Forsyth	65.0	2:1	—	Sherard (1953)
Standley Lake ..	113.0	2:1	—	Sherard (1953)
Willingdon	55.0	2:1	—	Rao (1961)
Palakmati	46.0	2:1-3:1	—	Rao (1961)

Table 2-1. Some drawdown failure of earth dams (Morgenstern, 1963).

The pore pressure coefficient \bar{B} is defined as:

$$\bar{B} = \frac{\Delta u}{\Delta \sigma_1} = B \left[1 - (1 - A) \left(1 - \frac{\Delta \sigma_3}{\Delta \sigma_1} \right) \right] \quad (2.1)$$

where Δu is the change in pore water pressure and $\Delta \sigma_1$ is the major principal stress change. In eq. (2.1) is reported also the relationship between \bar{B} and the pore-pressure coefficients A and B given by Skempton (1954).

Thus, the change in pore water pressure during drawdown can be expressed as:

$$\Delta u = \bar{B} \Delta \sigma_1 \quad (2.2)$$

The smaller the value of \bar{B} , the smaller the changes in pore water pressure during the drawdown. Because these changes are expected to represent decreases in pressure, the smaller the decrease in pressure during drawdown, the higher will be the final values of pore water pressure.

Higher values of pressure correspond directly to lower factors of safety. Thus, the factor of safety will decrease as \bar{B} becomes smaller, all other factors remaining the same. Bishop (1952, 1954) and Morgenstern (1963) suggested a value of \bar{B} equal to unity which represents a lower-bound and, thus, conservative value. Consequently, and based on equation (2.2), the change in pore water pressure becomes equal to the major principal stress change, $\Delta\sigma_1$, ($\bar{B} = 1.0$ in Eq. (2.2)). This assumption can be explained considering that, during the drawdown, the minor principal stress decreases more than the major principal stress and the incremental change in principal stress ratio is greater than one. With B approximately equal to one, and A less than one, \bar{B} must be greater than one, which is usually the case if the shear stresses are sufficiently large to endanger the stability of the dam during drawdown. Therefore the suggested value is reasonable.

For geometrical sections of the slope and soil parameters commonly encountered in the earth dam field, the stability calculations were carried out by Morgenstern (1963) with the help of a computer in order to obtain the stability charts.

The author considered four slope inclinations in terms of the cotangent of their inclination to the horizontal β (2 : 1, 3 : 1, 4 : 1 and 5 : 1), three values of friction angle, ϕ' , (20°, 30° and 40°) and three values of cohesion, expressed by the dimensionless ratio $c'/\gamma H$ (equal to 0.0125, 0.025 and 0.05). These values represent most of the range encountered in drawdown problems.

For all combinations in the range of shear strength parameters chosen, the minimum factor of safety for each slope has been determined for values of the drawdown ratio L/H of 0, 1/4, 1/2 and 1 (Figure 2-2).

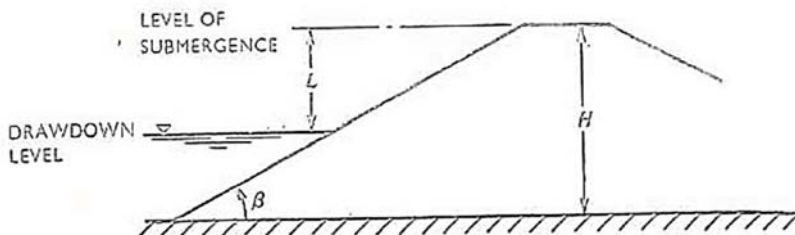


Figure 2-2. Drawdown ratio L/H (Morgenstern, 1963).

The stability charts showing the variation of the factor of safety with the drawdown ratio are given in Figure 2-3.

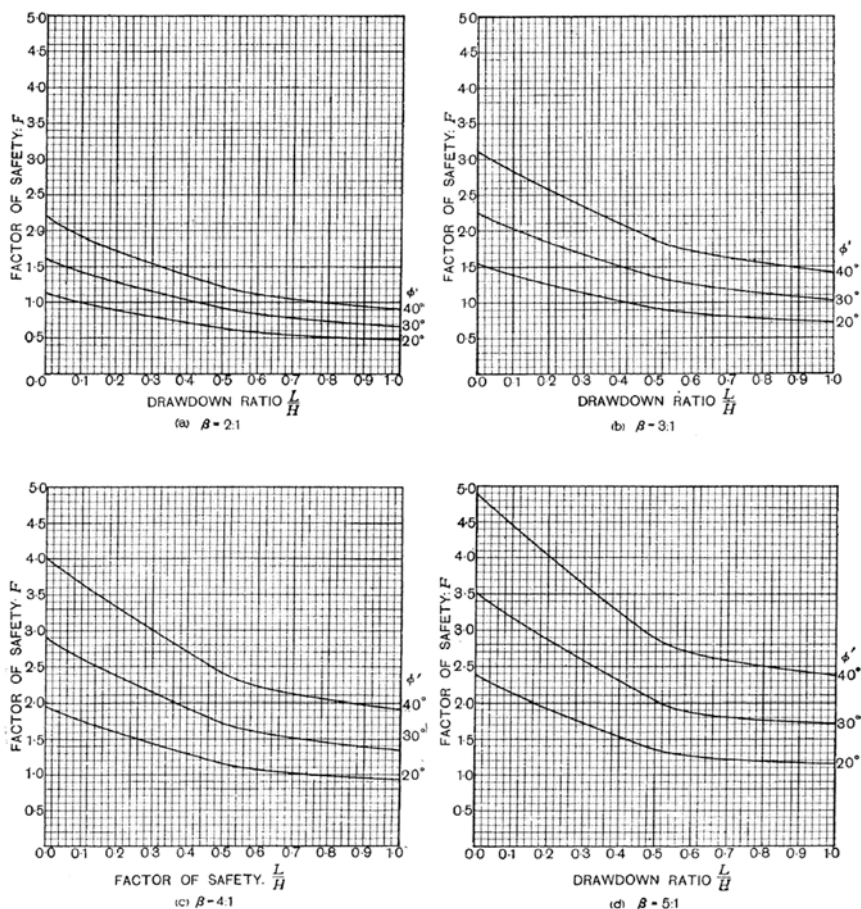


Figure 2-3. Drawdown stability chart for $\frac{c'}{\gamma H} = 0.0125$ (Morgenstern, 1963).

For the case of complete drawdown, the minimum factor of safety is given directly by the charts but in the case of partial drawdown the author recommends an iterative evaluation to find the minimum factor of safety, varying the position of the critical slip circle, whose depth is not known a priori.

Morgenstern (1963), for the construction of the charts, has assumed that no dissipation occurs during drawdown; Newlin and Rossier (1967), instead, focused on the dependence of the stability of the upstream slope of an earth dam on the magnitude of excess pore water pressure developed upon a possible failure surface. The magnitude of this excess pore water pressure varies with changes in reservoir level, consolidation of the soil mass, and changes in void ratio on the failure surface due to shear strain. Variations in water pressure due to changes in the reservoir level have a pronounced effect and are frequently approximated by making gross assumptions concerning the relative position of the reservoir level and of the saturation line.

The authors applied the approximate approach to the nonsteady state problem of drainage developed by Casagrande (1952) for airport pavements and for drawdown of dams, extending the theory to cover the case of partial drawdown. As a result, they obtained a dimensionless equation relating the time factor $(T = k \cdot H \cdot t / C \cdot n \cdot L^2)$ to the drainage ratio U (the ratio of the drained area, i.e. the area above the new reservoir level as level 2 in Figure 2-4, to total area) for various drawdown ratios P (Figure 2-4), which for $P=1$ leads to the same equation obtained by Casagrande for complete (100%) drawdown. The above mentioned equation is:

$$T = \left(\frac{P}{1-P} \right) \ln \frac{1 - \left(\frac{P}{2-P} \right) U}{1-U} \quad (2.3)$$

Solutions for Eq.(2.3) are graphically presented in Figure 2-5 where U is plotted versus T for various values of P from 0.1 to 1.0, and C is a correction factor (the computed C values by drawdown tests ranged from 0.3 to 0.7).

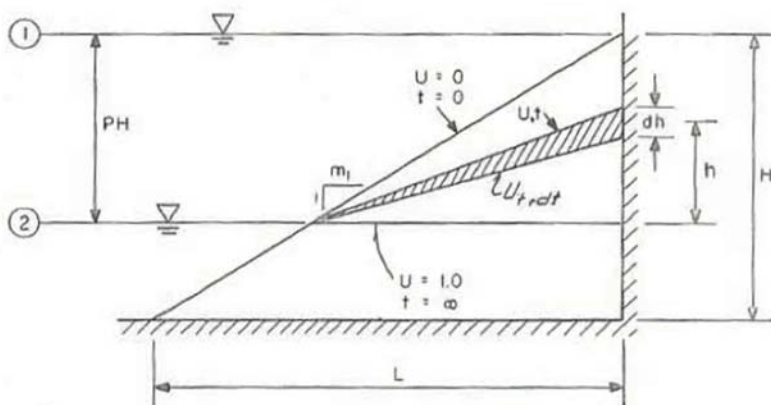


Figure 2-4. Assumed progress of drainage (Newlin and Rossier, 1967)

The authors, then, carried out drawdown laboratory tests involving a homogeneous and isotropic slope with known boundary conditions. They focused on comparing the instantaneous lowering of the reservoir level with the time required for recession of the saturation line. So, using test results and assuming that the hyperbola has the characteristics required to fit the shape of the saturation lines obtained at various times during drawdown, the authors were able to determine the drained area of the slope and the drainage ratio U .

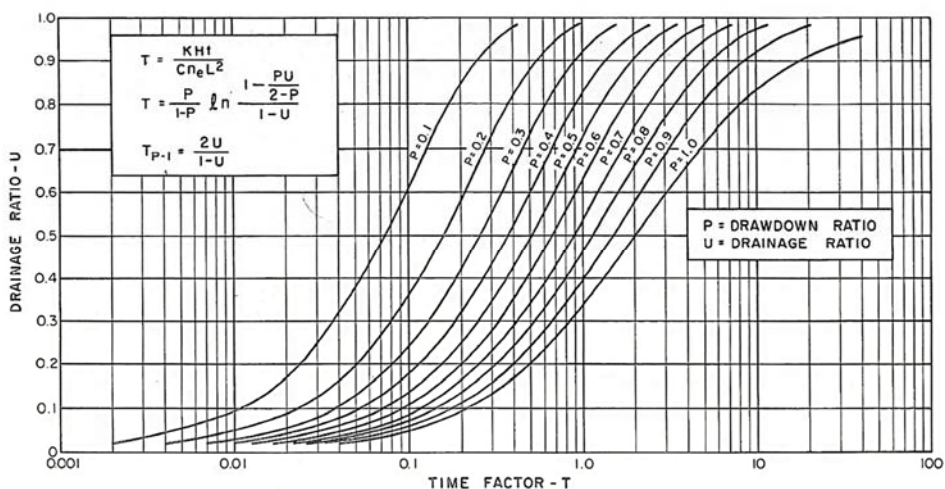


Figure 2-5. Relationship between drainage ratio, drawdown ratio and time factor (Newlin and Rossier, 1967).

Since the relationship between U and T is established as shown in Figure 2-5 and the relationship between U and h/H is established as shown in Figure 2-7, it is possible to relate T to h/H . The result of combining the two figures is presented graphically in Figure 2-8.

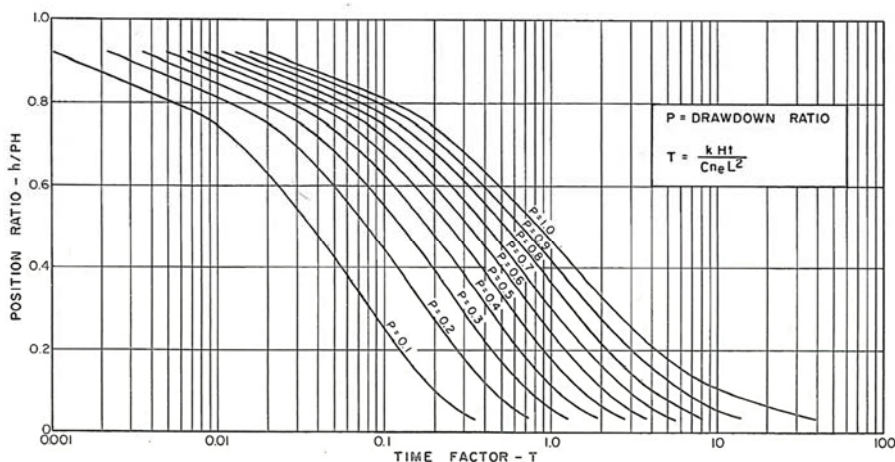


Figure 2-8. Relationship between position ratio and time factor (Newlin and Rossier, 1967).

So, the solution of a drawdown problem is reduced to the determination of the time factor T , to find the position ratio h/H through the use of Figure 2-8, and to plot the saturation line. If the drainage ratio U is desired, it may be obtained directly from Figure 2-5.

The development of numerical approaches and their application to the field of soil mechanics provide a new method for estimating the stability of slopes under different submergence conditions, flanking the traditional approach based on stability charts, developed by Morgenstern. The chart approach is limited by geometry, material property and the limit state assumed by the author together with analysis method and failure mechanism. These limits can be overcome by applying the numerical strategies (FEM, FDM) widely adopted nowadays.

Lane and Griffiths (2000) used the finite-element method to identify critical cases of partial submergence and rapid drawdown for partially submerged slopes. The aim of the study is to go beyond the limits of traditional methods which cannot cover the full range of possible critical cases or adequately represent inhomogeneous slopes and complex loading conditions. Thus, the finite-element method can perform a wider range of

analysis than can be handled by traditional methods. Utilizing the finite-element method, potentially critical conditions of rapid drawdown from partial submergence have been identified and new charts developed.

By the finite-element approach, rapid drawdown is modelled when the piezometric surface is specified as per the original water level, but the face loads are based on the drawdown reservoir level, which in this case is below that of the piezometric values. This approach overcomes the Morgenstern's hypothesis of no dissipation during drawdown. Another advantage is the automatic identification of the most critical failure mechanisms, irrespectively of the drawdown ratio.

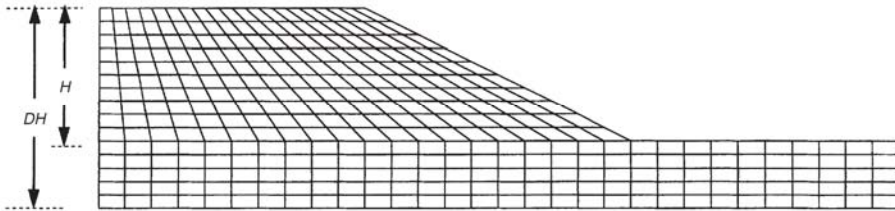


Figure 2-9. Geometrical fem model (Lane and Griffith, 2001).

Comparisons between the Morgenstern and the finite-element predictions are shown in Figure 2-10.

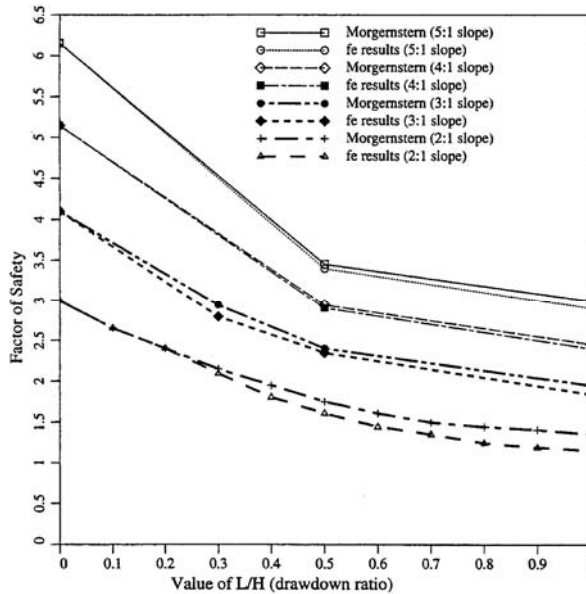


Figure 2-10. Comparison of Morgenstern and Finite-Element analysis results for rapid drawdown conditions for 2:1 Slope: $\phi' = 40^\circ$; $c'/\gamma H = 0.05$; $D = 1.0$ (Lane and Griffiths, 2000).

Desai (1977) also analysed the slope stability problem under drawdown, considering different rates and using a numerical approach to locate the internal free surface, later followed by a limit-state analysis for the global factor of safety (FOS) estimation. A range of drawdown rates relative to soil permeability were considered. Desai (1977) results can be considered as representative of a semirapid drawdown in that they are faster than for equalization to be complete, but they are slower than for rapid drawdown. Desai estimated that the difference in the FOS between his analysis and for rapid drawdown would be a reduction of the order of 2–8%. Figure 2-11 shows a comparison of the results of Desai (semirapid drawdown) and for those of Morgenstern and the finite-element solution (both for rapid drawdown). It emerges that the impact of the rapid condition is greater than Desai prediction - up to 40% in some cases.

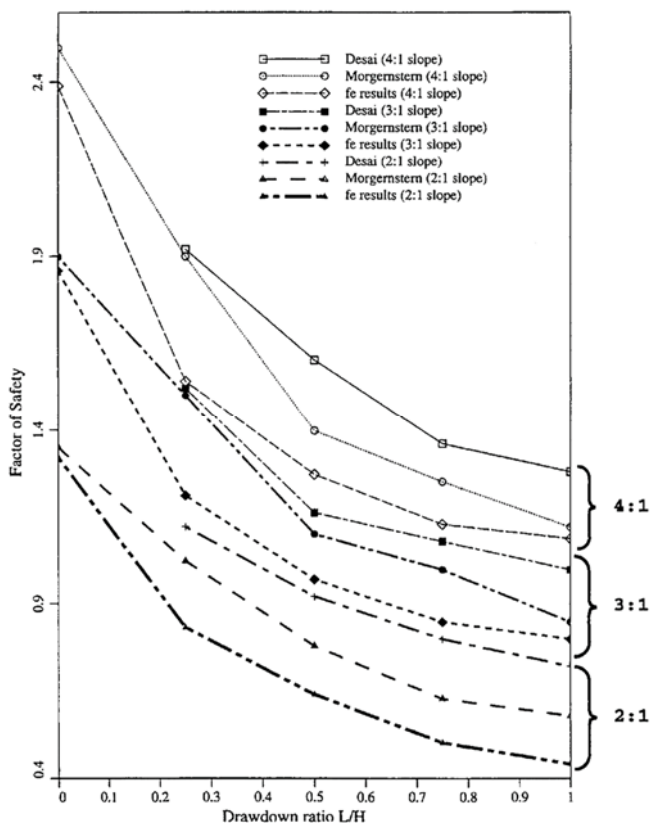


Figure 2-11. Comparison of Desai, Morgenstern, and Finite-Element analysis results for rapid drawdown conditions for 2:1 Slope: $\phi' = 25^\circ$; $c'/\gamma H = 0.0125$; $D = 1.0$ (Lane and Griffiths, 2000).

A comprehensive discussion on stability methods in the case of a sudden drawdown was undertaken by Wright and Duncan (1987), who classified the methods into two groups: in the first group, pore-water pressure is evaluated first, and the strength of the soil is considered to be independent of the drawdown process; in the second group, the influence of consolidation stress on shear strength is considered. The charts of Morgenstern (1963) and the newer calculations by Lane and Griffiths (2000) and by Viratjandr and Michalowski (2006) fall within the first group. In the latter study, the authors use the kinematic approach of limit analysis. To make the calculations manageable and presentation of the results possible for a wide range of parameters, they introduce the same simplifying (conservative) assumption accounted by Morgenstern. Prior to drawdown, the hydraulic potential is uniform throughout the saturated mass (Figure 2-12a), and a fictitious (instantaneous) draining process is considered during which the equipotentials remain vertical within a portion of the slope (Figure 2-12b), whereas the potential remains constant (but different) on both sides of that portion. Such an assumption leads to an overestimation of the hydraulic gradients, and it is acceptable for practical calculations.

The authors (Viratjandr and Michalowski, 2006) considered both the toe failures (Figure 2-12c) and under-the-toe mechanisms of collapse (characteristic of shallow slopes). When a zoned earth dam with central core is considered, another assumption is made about the failure surface, which is supposed enclosed entirely within the shell material (i.e. it does not intersect the core of the earth dam). Four sets of stability charts are presented as results of the performed analyses, for different conditions of rapid and slow drawdown process.

An example is presented in Figure 2-14 where H is the slope height; and L_1 and L_2 are the water levels in the reservoir and in the slope (measured from the crest level, Figure 2-13), respectively.

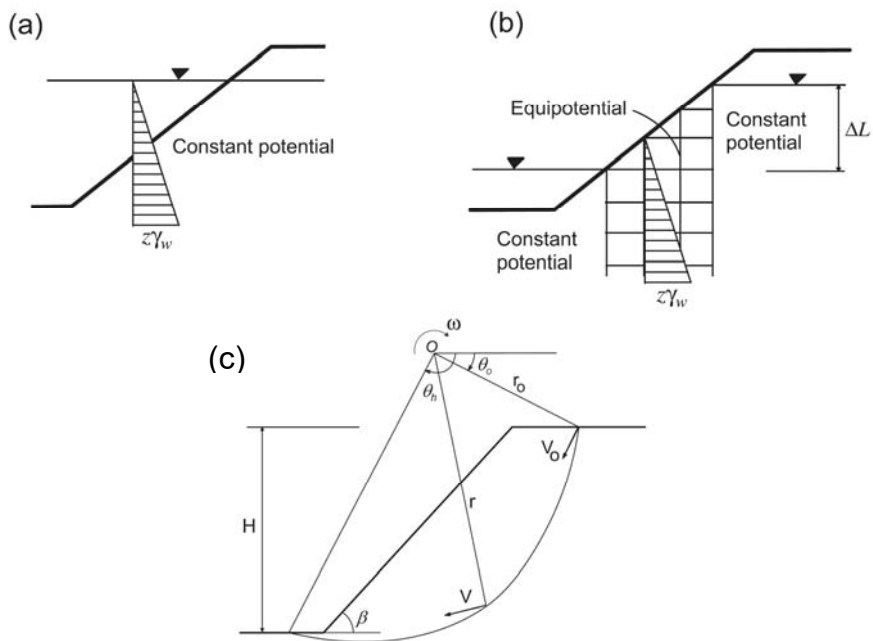


Figure 2-12. Idealized hydraulic conditions: (a) before drawdown; (b) equipotentials during a fictitious (instantaneous) drawdown process; (c) toe failure mechanism (Viratjandr and Michalowski, 2006).

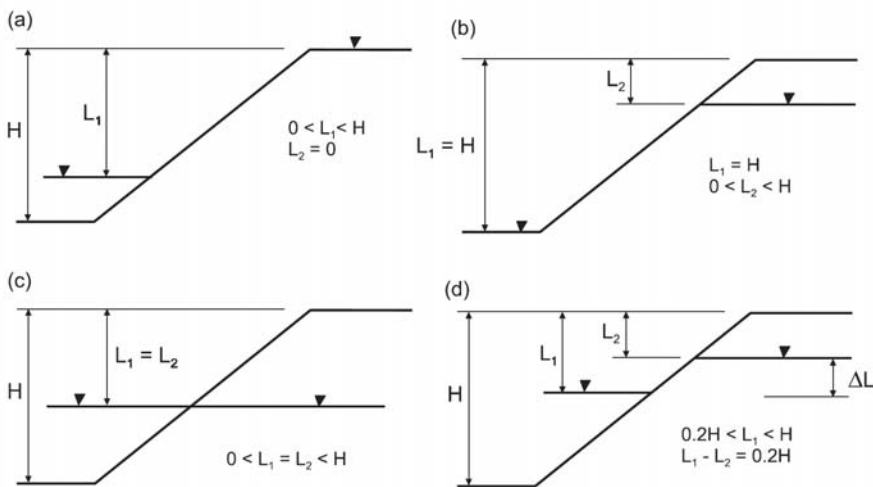


Figure 2-13. Drawdown regimes assumed by Viratjandr and Michalowski (2006).

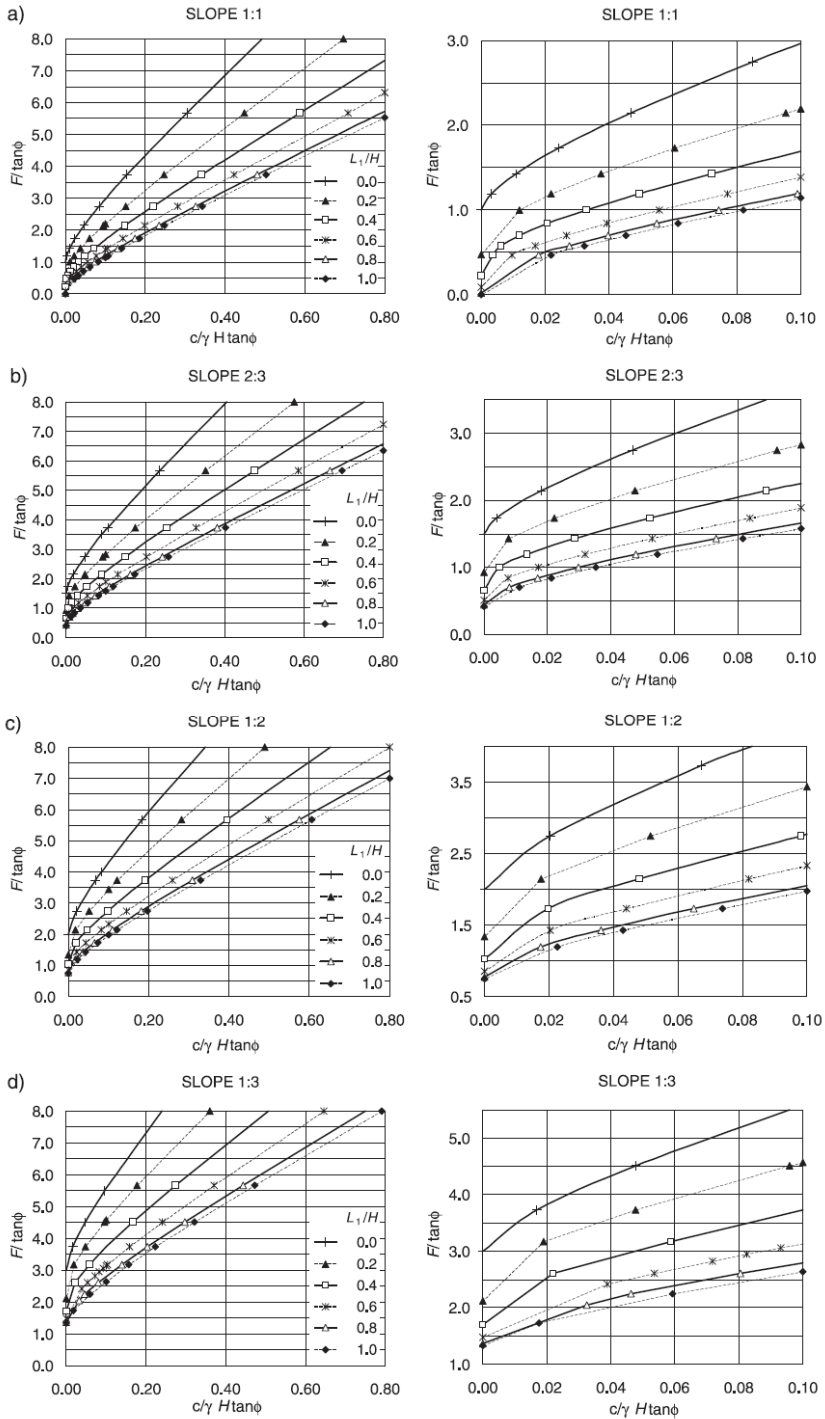


Figure 2-14. Rapid drawdown charts, $L_2=0$ (Viratjandr and Michalowski, 2006).

The changes in safety factor associated with different draining regimes are presented in Figure 2-15 for a slope with inclination 1:2, $c'/\gamma H = 0.05$, and $\phi' = 40^\circ$. The rapid drawdown is indicated by the curve marked with open diamonds and are close to Morgenstern (1963) results for the rapid drawdown. Morgenstern results are not shown in Figure 2-15 to avoid cluttering the graph.

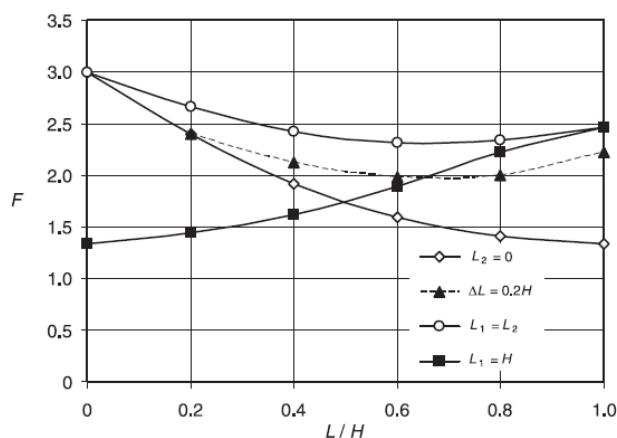


Figure 2-15. Variation in safety factor caused by various drawdown processes for slope 1:2, $c'/\gamma H = 0.05$, and $\phi = 40^\circ$ (Viratjandr and Michalowski, 2006).

The slow drawdown process is shown by the curve marked with open circles. This is the safest process for emptying the reservoir. A faster process, with a constant difference in water levels ($L_1 - L_2 = 0.2H$, solid triangles) is characterized by slightly lower safety factors, but it is far safer than the rapid drawdown process. If the water is drawn rapidly from the reservoir (open diamonds), the subsequent change in the phreatic surface in the slope leads to an increase in the safety factor, as indicated by the curve marked with solid squares.

For two drawdown processes, marked in Figure 2-15 with open circles and solid triangles, the safety factor reached its minimum at about $L/H \approx 0.65$ and 0.70 , respectively. This is an interesting phenomenon indicating that the extreme states of full submergence and the state after full drawdown may be safe states, whereas the slope becomes most vulnerable to collapse somewhere before the reservoir is fully drained.

The appearance of this critical pool level was pointed out by Lane and Griffiths (2000), and they offered an explanation of this phenomenon as a

result of two competing effects, namely the change in the load of the slope (due to buoyancy) and the change in the frictional resistance of the soil, both caused by the water level change.

Comparison between the safety factor during a rapid drawdown calculated by Lane and Griffiths (2000) and by Viratjandr and Michalowski (2006) is presented in Figure 2-16 for a slope with an inclination of 1:2 and $c'/\gamma H = 0.05$, and for two values of ϕ' , namely 20° and 40° . The results for $\phi' = 20^\circ$ coincide very closely, whereas the safety factor for $\phi' = 40^\circ$ reaches a maximum difference of about 14% at the end of the process. Although this difference is not unreasonable, Viratjandr and Michalowski (2006) point to the difference in the soil model used in both methods as an explanation for this deviation. The limit analysis is based on the perfect plasticity model with the yielding described by the Mohr–Coulomb criterion and the deformation governed by the normality rule (associativity). The calculation of Lane and Griffiths (2000), on the other hand, included the soil model with the non-associative flow rule (incompressible material). Since non-associativity leads to reduced limit loads on a structure, it would expect the non-associative model to provide lower safety factors.

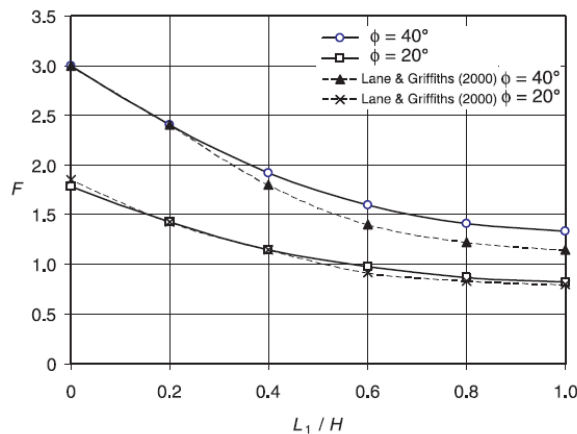


Figure 2-16. Comparison of the rapid-drawdown results ($L_2 = 0$, $c'/\gamma H = 0.05$) with the finite element calculations (Viratjandr and Michalowski, 2006).

The studies presented so far have focused on the calculation of the factor of safety considering different drawdown ratios. Berilgen (2007) and later Alonso and Pinyol (2009, 2016) point out that the drawdown rates affect the stability of the slope; drawdown rates of 0.1 m/day are common, of 0.5

m/day are quite significant, 1 meter/day and higher rates are rather exceptional.

Berilgen (2007) investigates slope stability during drawdown considering different soil permeabilities, drawdown rates and drawdown ratios, accounting for nonlinear material behaviour. Slow, fully rapid and transient drawdown (Figure 2-17), corresponding to different rates of drawdown to the hydraulic conductivity of the slope materials, are investigated.

Analysis	Material behavior	Transient seepage	Deformation	Consolidation	Stability
Coupled analysis	Undrained	✓	✓	✓	✓
Fully slow drawdown	Drained	NA	✓	NA	✓
Fully rapid drawdown	Undrained	NA	✓	NA	✓

NA, not applicable.

Table 2-2. Analyses types for slope stability during drawdown (Berilgen 2007).

For this purpose, coupled transient seepage and deformation analysis (including consolidation) using the FEM approach, together with slope stability analysis, are performed. In deformation analysis, saturated two-phase and nonlinear elasto-plastic behaviour of the soil are taken into account. For slope stability analysis and computation of the global safety factor (FOS), the strength reduction method is used.

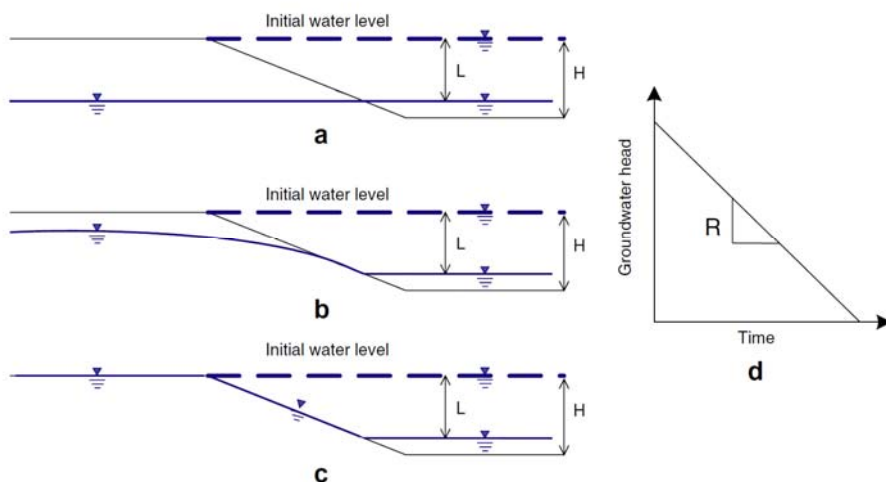


Figure 2-17. Phreatic level after drawdown: (a) fully slow drawdown (drained); (b) transient drawdown; (c) fully rapid drawdown; and (d) drawdown rate (Berilgen 2007).

In these analyses, 3:1 slopes with two different heights, H (7 m and 14 m), two different drawdown rates, R (1 m/day and 0.1 m/day), two isotropic

hydraulic conductivity values ($k = 10^{-4}$ and $k = 10^{-6}$ cm/s) and various drawdown ratios were considered ($L/H = 0.2, 0.4, 0.6, 0.8, 1.0$).

According to the analysis results, for soils of low hydraulic conductivity ($k = 10^{-6}$ cm/s) and high drawdown rate ($R = 1$ m/day), the slope behaviour approaches to that of fully rapid drawdown condition, and the phreatic surface remained nearly at the slope surface. In this situation, a fully rapid drawdown assumption may be made and seepage and consolidation analysis may be omitted.

For the same soil of low permeability, at a drawdown rate 10 times slower ($R = 0.1$ m/day) the FOS vs. L/H curve is still close to the fully rapid drawdown curve (Figure 2-18). It can be concluded that even for a 0.1 m daily drawdown rate, still very little drainage takes place in soils of low permeability.

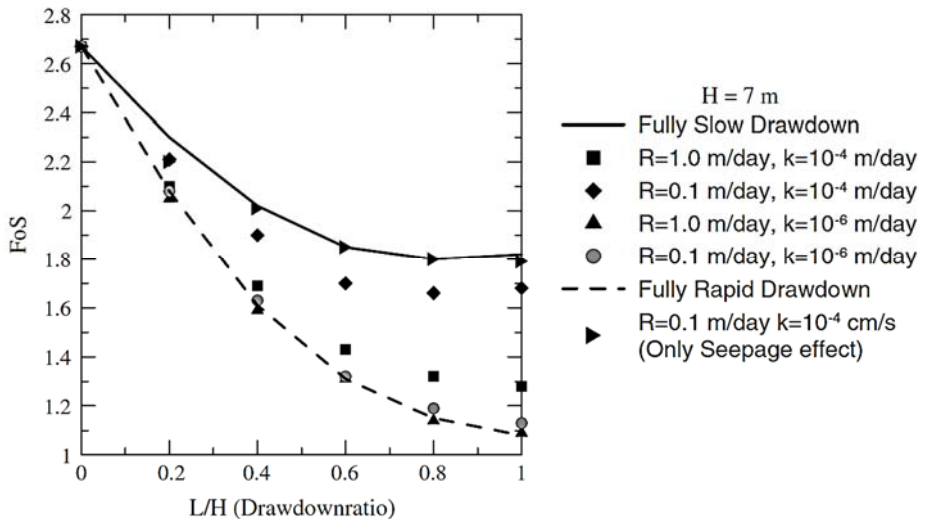


Figure 2-18. Variation of FOS with drawdown ratio for $H = 7$ m slope (Berilgen 2007).

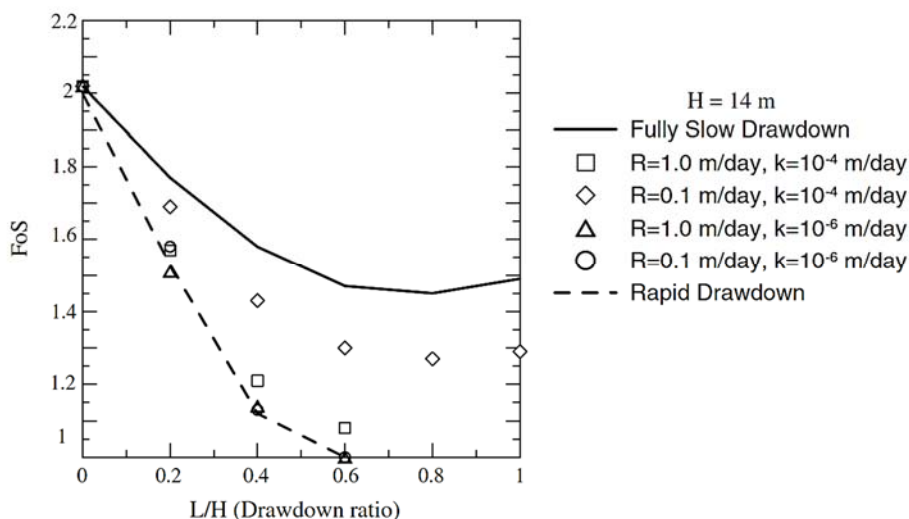


Figure 2-19. Variation of FOS with drawdown ratio for $H = 7$ m slope (Berilgen 2007).

In the case of relatively higher soil hydraulic conductivity ($k = 10^{-4}$ cm/s) and a rather slow drawdown rate ($R = 0.1$ m/day), even though there is partial drainage during the drawdown, the computed FOS values are still lower than those for the case of fully slow drawdown and higher than fully rapid drawdown, the difference being higher for $H = 14$ m (Figure 2-19). Such cases justify performing advanced coupled analyses, as they cannot be approximated by the limiting cases.

For a high drawdown rate such as $R = 1$ m/day, even for soils of moderate permeability ($k = 10^{-4}$ cm/s), the slope behaviour approaches towards the fully undrained behaviour, indicating that even for the slopes formed of rather high hydraulic conductivity soils (as the dam shells), during high rates of drawdown, not much drainage is possible and as far as the stability is concerned the behaviour may be considered to be similar to that of fully rapid drawdown condition.

Comparing the stability of two slopes of the same soil but different heights Berilgen (2007) observes that for the slope with $H = 7$ m the FOS is 2.67, and for the slope with $H = 14$ m the FOS is 2.02 for complete submergence, i.e., $L/H = 0$. This is due to the difference in strength/stress ratios ($c'/\gamma H$). Hence, even though for a slope with $H = 7$ m, 100% drawdown (equal to the slope height, i.e., $L/H = 1$) can be achieved without failure, for a slope of $H = 14$ m when drawdown level reaches about 60% ($L/H = 0.60$), the

slope may fail (i.e., $FOS = 1$) unless the hydraulic conductivity is high and drawdown rates are very slow. These results demonstrate the critical importance of drainage conditions on slope stability during drawdown, especially for slopes which do not possess a high degree of safety prior to drawdown.

Alonso et al. (2009, 2016) focused on different approaches available for calculating pore water pressure distributions during and after the drawdown of a dam considering the soil as a three-phase medium (in the studies presented earlier the soil was assumed as a two-phase medium). They pointed out that pore water pressures in an initially submerged slope, later subjected to drawdown, depend on several factors, both soil parameters and “external” conditions: soil permeability (saturated and unsaturated), soil water retention properties, mechanical soil constitutive behaviour, rate of water level lowering and boundary conditions.

All the analyses presented by the authors were carried with the code Code_Bright, which is based on the finite element method for analysis of thermo-hydro-mechanical problems. The code deals with the deformable porous media as a mixture of three phases (solid, liquid, and gas). Solid corresponds to soil skeleton, and liquid and gas correspond to water and dry air filling the pores, respectively. In this study, two models were used to simulate soil response. A linear elastic model was selected as a simple model to analyse the effect of the mechanical response on the pore water pressure evolution in slopes subjected to a drawdown. A more complex elastoplastic constitutive soil model was used to analyse the Glen Shira Dam. The Barcelona basic model (BBM, Alonso et al., 1990) was selected as a proper constitutive model for simulating soil response in complete or partial saturation. It is a critical state model defined in terms of the net stress (the total stress in excess of the air pressure) and suction (the difference between the pore water pressure and air pressure), which can simulate the dependence of the stiffness and strength on suction and collapse (the soil deformation at a constant stress due to the reduction in suction). Further details on unsaturated soils will be provided in Appendix A.

The retention curve has been defined by means of a Van Genuchten (1980) model. In the model, the parameters P_0 and λ control the air entry value and the shape of the retention curve, respectively. The maximum and minimum degrees of saturation, S_{rmax} and S_{rmin} , were assumed to be respectively 1

and 0. The relative permeability (k_{rel}) varied with the degree of saturation (S_r), following a cubic law ($k_{rel} = k_{sat} \cdot S_r^3$, with a constant saturated permeability for each soil considered).

The first example presented by Alonso et al. (2009, 2016) is a slope, initially fully submerged, then emptied with a realistic drawdown rate of 0.5 m/g. The authors show how the hypothesized stiffness of the soil and the analysis approach affect the evolution of pore water pressures calculated after the instantaneous drawdown. Considering the point P_B (Figure 2-20), in the case of a rigid soil, no immediate effect of the drawdown occurs, as expected. In the coupled analysis, the instantaneous pore water pressure drops in relation to the compressibility of the soil skeleton.

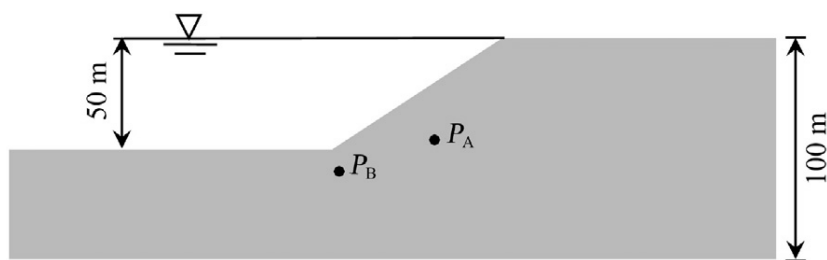


Figure 2-20. Geometry of the slope (Alonso et al., 2016).

The stiffer the soil is, the lower the stress-induced change in the pore water pressure will be (Figure 2-21). Immediately after the drawdown, a dissipation process begins. The rate of pore water pressure dissipation is controlled not only by the initial conditions after the drawdown, but also by the permeability and stiffness of the soil. In an uncoupled analysis, the calculated dissipation rates are higher, because of the implicit assumption of an infinitely rigid soil. Eventually, all cases result in the same long term solution. The coupled analysis leads systematically to lower pore water pressures than the uncoupled (pure flow) analysis during the initial stage of dissipation. This is due to the effect of the initial state after the drawdown, controlled by the change in stress. However, since pore water pressures dissipate faster for a stiffer soil, this situation changes after some time, and pore water pressures recorded may also achieve the same value at some particular time (pore pressure patterns in Figure 2-21 may cross), depending on the position of the point in the slope.

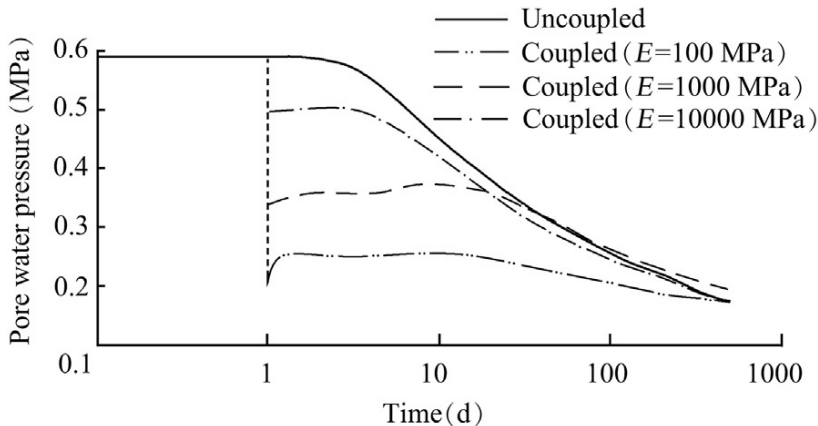


Figure 2-21. Pore water pressure evolution after instantaneous drawdown at point P_B (Alonso et al., 2016).

The pure flow analysis is a conservative approach in terms of slope safety against failure. Anyway, it is important to note that the unrealistic uncoupled analysis leads to a lower pore pressure prediction in the long term. This is a result of the implicit assumption of infinite skeleton stiffness in the uncoupled calculation, leading to higher dissipation rates than the coupled analysis depending on the water retention curve and the relative permeability law adopted in calculations.

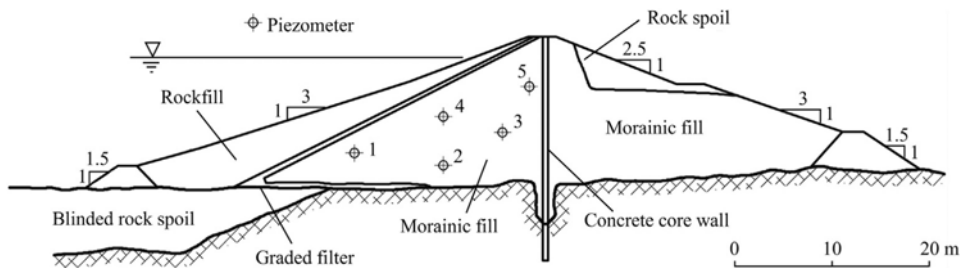


Figure 2-22. Maximum cross-section of Glen Shira Dam (Alonso et al., 2016).

In the Glen Shira Dam case study, the dam was expected to experience fast drawdown rates because the reservoir level change followed a pumping storage scheme. Several calculations under saturation and unsaturation conditions were performed with the following hypotheses:

- a pure flow analysis, in which the soils were considered rigid (Case 1);

- an instantaneous drawdown at the maximum intensity, followed by pore water pressure dissipation, with the soils simulated as elastic materials (Case 2);
- a coupled analysis, in which the soils were considered elastic (Case 3);
- a coupled analysis, in which the soils were considered elastoplastic according to the BBM model (Case 4).

In order to measure the pore water pressure distribution inside the upstream shell for comparison with the computed distributions, five piezometers were placed as shown in Figure 2-22.

This case study shows that the classical analysis methods cannot catch the recorded behaviour. The method of instantaneous drawdown (Case 2) or undrained analysis is conservative, but very unrealistic. At the opposite extreme, the pure flow analysis (Case 1) leads to a systematic and unsafe underestimation of pore water pressures during the drawdown. Coupled analysis captures the actual measurements well. In the case of the Glen Shira Dam, plastic strain during the drawdown was probably null, and the simpler elastic approach provided a good approximation of recorded pore water pressures (Figure 2-23).

The literature studies have highlighted the importance of the analysis assumptions made in the evaluation of the slopes stability due to RDD. Coupled transient seepage and deformation analysis performed by continuous approaches provide a better fit with slope response.

With the exception of Alonso et al. (2009, 2016), most of the literature studies investigated the RDD effects on earth slopes assuming completely dry or saturated the soil above and below the phreatic surface, respectively. In the analysis performed in this thesis a 2-phase approach was adopted until the start of the drawdown stage. By then, a 3-phase approach was selected.

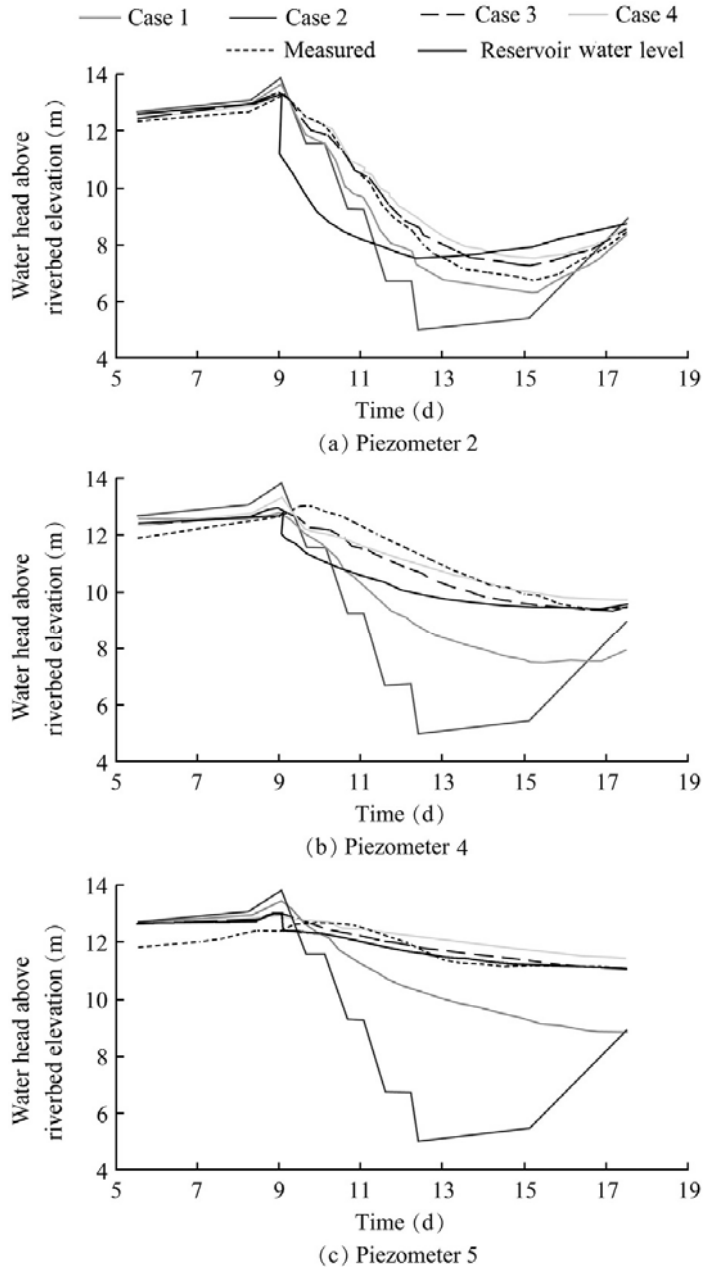


Figure 2-23. Comparison of measured pore water pressures obtained from different piezometers and calculated results in different cases (Alonso et al., 2016).

2.2. SEISMIC RESPONSE

The increased concern developed in recent years on the seismic risk associated to dams and the enhancement of the seismic hazard studies have highlighted the need to evaluate or to re-evaluate the seismic safety of many existing dams, which do not meet the safety criteria required by the current seismic regulations. Many earth dams built in the early twentieth century were indeed designed adopting a rough assessment of the seismicity of the site, which often is underestimated compared to the actual knowledge. To the frequent underestimation of the site seismicity shall be also added the low awareness designers had in the past with regard to earthquake vulnerability of earth dams. The latter ones were preferred to other constructive typologies where the seismic hazard at the dam site was considered high, without accompanying that choice with an appropriate mechanical characterization of the construction materials and/or by an adequate construction technique.

For existing dams such assessment is not simple because it raises a number of problems related to the absence of an “ad hoc” methodology for the seismic assessment and the uncertainties linked to the actual state of the dam. Sometimes it is difficult to find both the original projects, with details on the geotechnical investigation carried out on soils, and the “state of fact of the dam” at the end of construction, which may be different compared to the original project.

Today a number of analysis methods exist, which can be used for the evaluation of the seismic response of earth dams. These methods fall into several categories according to the main objectives of the analysis, such as the assessment of:

- dam stability, or
- permanent displacements of the dam body, or
- overall dynamic response of the dam.

According to the analysis objectives, a complete framework of the available procedures is provided in Table 2-3 (Sica, 2003).

<i>Class</i>	<i>Main Features</i>		<i>Input data</i>	<i>Output data</i>
<u>Pseudostatic approaches</u>	Global stability analysis assuming the soil as a rigid-plastic material		Dam geometry (2-D) Soil strength parameters Site seismic category	Safety factor with respect to global instability mechanisms
<u>Simplified dynamic approaches</u>	Newmark method	Input motion given by an accelerogram	Dam geometry Soil strength parameters Input accelerogram	Permanent displacement related to assumed sliding mechanism
	Newmark-derived method	Input motion given by an accelerogram	Dam geometry Soil strength parameters Peak ground acceleration Peak ground velocity	
	Shear Beam approach	Uniform shear strain across the dam	Dam geometry Constitutive law (linear elastic) Input accelerogram	Acceleration Time history of shear stresses and strain across the dam
<u>Dynamic approaches</u>	Soil assumed as a continuum and deformable medium	1-phase approach	Dam geometry (2-D or 3-D) Constitutive law (1-phase material) Input accelerogram	Acceleration Permanent displacements (if advanced constitutive law are implemented)
		2-phase approach and excess pore water pressure model	Geometry (2-D or 3-D) Constitutive law (1-phase material) Relationship between total stresses and excess pore water pressures Input accelerogram	Acceleration Excess pore water pressures Indirect estimation of permanent displacements
		Coupled advanced approach	Geometry (2-D and 3-D) Advanced soil Constitutive law Soil permeability, Sr_0 Input accelerogram	Acceleration Permanent displacements Excess pore water pressures Post seismic effects

Table 2-3. Available approaches to study the dynamic behaviour of earth dams (Sica S., 2003).

With regard to the approaches which can be used for the seismic assessment of earth dams, the Italian technical legislation (DM 14.01.2008, §7.11.4) allows to assess the behaviour of embankments under seismic conditions by the same methods used for natural slopes (§7.11.3.5.2), that is:

- pseudo-static analyses;
- simplified dynamic analyses to assess deformations;
- dynamic analyses.

2.2.1 ANALYSIS METHODS

The approaches developed to analyse the seismic behaviour of geotechnical systems can be classified on several bases:

- geometry assigned to the soil-structure system (1-D, 2-D, 3-D);
- constitutive model describing the material stress-strain response (i.e. linear elastic, non linear elastic, elastoplastic with or without hardening);
- modelling of the interaction phenomena among different phases (soil, water and air);
- seismic loads description (i.e. peak ground acceleration, response spectrum, acceleration time history).

In the following paragraphs, the three main classes of methods will be analysed.

2.2.1.1. Pseudo-static method

In the early stages of geotechnical earthquake engineering, the standard seismic method for earth dams (Terzaghi, 1950) was based on the simplified assumption that dams were absolutely rigid bodies fixed on their foundation and, thus, experiencing a uniform acceleration equal to the base ground acceleration.

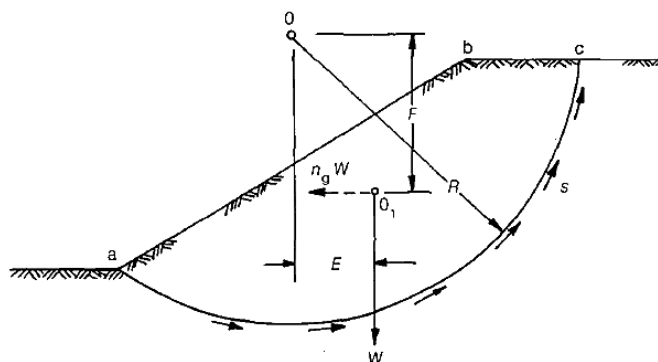


Figure 2-24. Pseudo static approach: forces acting on a rigid wedge sliding on a plan surface (Terzaghi, 1950).

In the pseudo-static approach the earthquake is modelled as a horizontal and vertical static force, applied in the centre of gravity of a potential

sliding mass (Figure 2-24). The pseudo-static force is given by the product of the weight W of the unstable mass by a dimensionless coefficient k_h (or k_v), defined seismic coefficient.

Once introduced the equivalent static forces through the following relations:

$$F_h = \frac{a_h \cdot W}{g} = k_h \cdot W \quad (2.4)$$

$$F_v = \frac{a_v \cdot W}{g} = k_v \cdot W \quad (2.5)$$

the seismic analysis consists in a slope stability assessment by limit equilibrium methods (Bishop, 1955; Janbu, 1957; Morgenstern & Price, 1965 etc.).

The basic idea of this method is that equilibrium calculations are carried out in a similar way as for the static problem, but with the addition of the inertial loads (F_h and F_v) caused by the earthquake.

One potential drawback of this procedure is that the inertial forces do not act permanently and in one direction but rather fluctuate rapidly in both magnitude and direction; thus, even if the factor of safety drops momentarily below unity, the slope would not necessarily experience an instability but might merely undergo some permanent deformations (displacements).

Earth embankments rarely behave as rigid bodies. In order to take into account the amplification of the seismic motion from the base to the dam crest, Ambraseys (1960) analysed the response of dams with different geometries assuming a viscoelastic behaviour of soil. As a result of such analysis, correlations between the dam height and the seismic coefficient were provided (Figure 2-25).

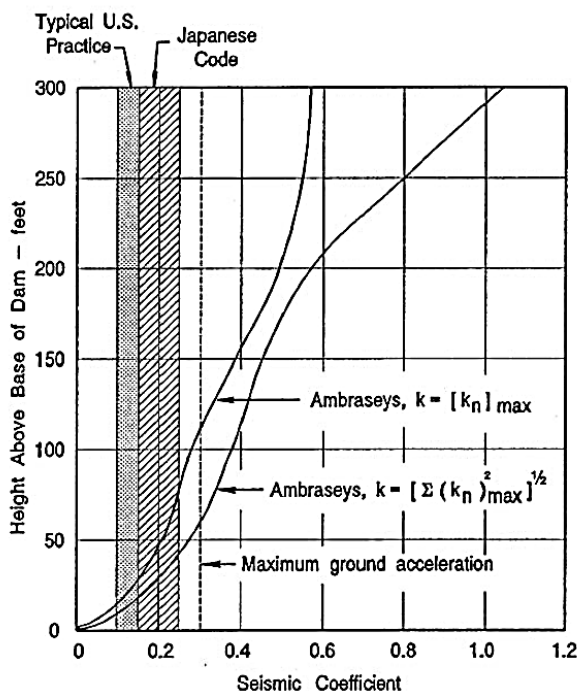


Figure 2-25. Variation of the seismic coefficient k with dam's height (Ambraseys N., 1960).

Seed and Martin (1966) suggested a new method to predict seismic forces and their variation with time. They investigated the viscoelastic response of a dam idealized as an infinitely long triangular cross-section with uniform and homogenous material properties under El Centro earthquake accelerations. Assuming triangular wedge-shaped sliding masses, an average seismic coefficient, k_{av} was defined for the trial wedge as:

$$k_{av} = \frac{1}{W} \cdot \sum m(y) \cdot \ddot{u}_a(y) \quad (2.6)$$

where W is the weight of the sliding mass, m is the mass of an incremental slice of the sliding mass, \ddot{u}_a is the absolute acceleration of the slice at the instant under consideration and y is the distance to the incremental slice from the top of the dam, as shown in Figure 2-26.

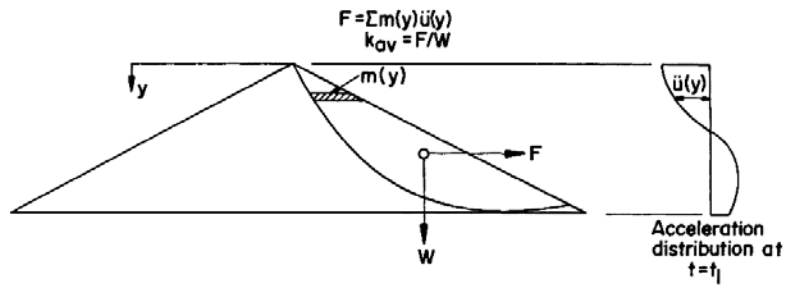


Figure 2-26. Concept of average seismic coefficient (Seed & Martin, 1966).

One of the main limits of the pseudo-static method consists of considering the failure along a well-defined sliding surface as the only type of damage that an earth structure could suffer during an earthquake. Although this assumption could be reasonable in the case of retaining walls, in the case of earth dams the failure could be due to other mechanisms as freeboard loss and liquefaction or fracture of dam elements (core or filter) that assure water tightness. Furthermore, despite several attempts to improve the method, many other factors affecting the global stability of the dam are neglected, like the frequency content of the earthquake, the inhomogeneity of the dam soil, the asynchronous seismic input.

Literature papers report many case histories of earth dams failed either partially or totally during earthquakes, even if the pseudo-static approach had given a positive result about safety. Lower San Fernando Dam (Seed, 1979) and Hebgen Dam (Steinbrugge and Cloud, 1962) are two classic examples.

Recently, the studies presented by Bozzoni et al. (2015) and Derosa et al. (2015) illustrate the application of a procedure developed for the assessment of the seismic response of embankment dams by means of simplified approaches. The aim of both studies is to perform extensive parametric pseudo-static and simplified dynamic analyses (§2.2.1.2) by increasing the seismic input at selected dams. The results of these analyses are stored in a GIS platform and subsequently used to evaluate the seismic response of these dams to a hypothetical earthquake scenario. A numerical interpolation procedure was developed in the webGIS platform by Eucentre. This allows an expeditious estimation of the seismic response of earth dams in the aftermath of an earthquake.

2.2.1.2. Simplified dynamic analysis

The simplified dynamic approach, first introduced by Newmark (1965), was developed to evaluate permanent displacements under cyclic loading.

According to this method, the potential sliding mass behaves like a rigid block and the shear resistance is assumed constant. When the inertial force induced by the earthquake reaches values such that destabilizing forces (static and dynamic) exceed soil resistance, the block starts sliding. The first displacements occur when the induced acceleration exceeds the so-called “critical acceleration a_y ”, i.e. the threshold acceleration that causes the block to slide. The yield acceleration can be readily determined using conventional limit equilibrium methods ($a_y = k_y g$, where “ k_y ” is the critical seismic coefficient).

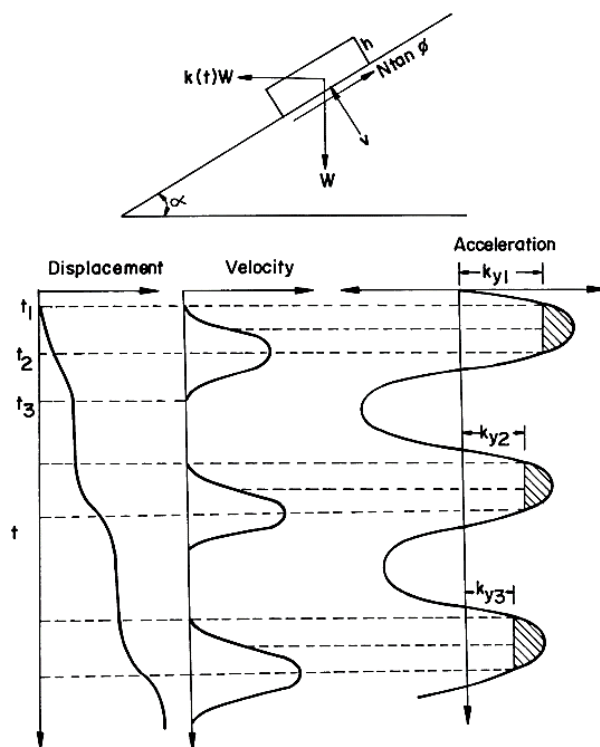


Figure 2-27. Integration of effective acceleration time-history to determine velocities and displacements (Newmark, 1965).

Irreversible displacements are calculated by double integration of the acceleration, when it exceeds the critical one. The sum of partial displacements provides the cumulative displacement of the sliding mass.

One of the major drawbacks of the Newmark approach is that, due to the rigid mass assumption, the acceleration induced by the seismic motion is the same in every point of the dam. Actually, dams are flexible bodies, hence seismic motion induces different inertial forces in any point of the dam, depending on the features of the seismic input (duration, amplitude, frequency content) and material stiffness and damping. In these conditions, the rigid block assumption leads to an overestimation of the irreversible displacements induced by seismic motion.

To overcome the main drawbacks of the method, numerous Newmark-derived methods were developed (i.e. Makdisi and Seed (1978) for embankments and earth dams; Yegian et al. (1991) for embankments; Franklin and Chang (1977) for dikes; Richards and Elms (1979) for gravity walls; Towahata and Islam (1987) for sheet pile walls; Steedman (1998) for gravity and sheet pile walls).

For example, Makdisi and Seed (1978) suggested calculating an average acceleration along the potential slippage surface with the procedure proposed by Chopra (1966) by finite element method, with the aim to take into account the spatial and temporal variability of the seismic acceleration into the dam body. Typical variation of effective peak acceleration on a sliding mass as obtained from the dynamic response of embankments, k_{\max} , with the depth of the dam is depicted, in Figure 2-28, divided by the maximum crest acceleration, \ddot{u}_{\max} .

Despite the improvements from different authors, such simplified methods are useful only for a preliminary assessment of the dam safety and in cases with limited nonlinear behaviour of soil (weak earthquake motions) due to the simplified behaviour attributed to soil. In addition, these methods provide only the horizontal displacements of the trial-sliding wedge, without any information about the loss of the freeboard and the overall performance of the dam and facilities.

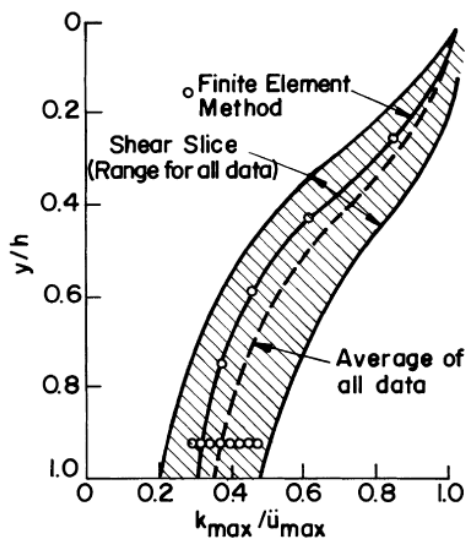


Figure 2-28. Variation of “maximum acceleration ratio” with depth of sliding mass (Makdisi and Seed, 1978).

2.2.1.3. Dynamic analyses

Advanced methods of analysis model the dam response considering both:

- the real behaviour of soil under cyclic and dynamic loading;
- the transient nature of the earthquake.

One of the first attempts to consider the transient nature of earthquakes is represented by the *Shear beam (SB)* (or shear wedge) approach (Figure 2-29). As stated by Gazetas (1987), the origins of this method have been attributed to Mononobe et al. (1936), who first introduced the 1D shear beam model for earth dams in the 1930s.

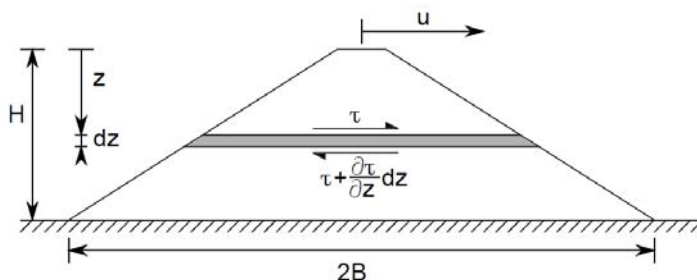


Figure 2-29. Shear beam approach for 2-D seismic analysis of dams. After Gazetas (1987).

Hatanaka (1952, 1955) showed that during an earthquake shear deformations are predominant compared to bending ones and performed 2D shear beam analyses in rectangular canyons. Ambraseys (1960) extended the shear beam model to account for a truncated wedge shape, rectangular canyon and underlying elastic layer. Since then, a number of researchers extended and used this method in various cases (Gazetas, 1987).

The SB model, in its original form, was based on the following major simplifying assumptions:

- a. only horizontal displacements and simple shearing deformations take place;
- b. displacements, shear stresses and strains are uniformly distributed along horizontal planes across the dam;
- c. the dam consists of a homogeneous material which behaves as a linear viscoelastic solid and is described by constant shear modulus, damping ratio, and mass density;
- d. the dam is either infinitely long or built in a rectangular canyon and is subjected to a synchronous rigid base lateral motion.

The approach was then verified and extended to cover a variety of conditions in order to account for the inhomogeneity of dam soil and the 3D effects for dams built in narrow canyons. Different closed form relations have been defined in order to calculate fundamental periods, modal displacements and amplification functions (Table 2-4, Gazetas, 1987).

This method, still simplified, does not take into account the complex nonlinear behaviour of the soil, including the necessary assumptions (a) and (b) for shear model, which in some cases may be too restrictive.

As mentioned before, the shear beam method can provide closed-form solutions for dynamic analysis of earth dams. However, the associated closed-form solutions assume linear elastic or visco-elastic material behaviour and therefore they pose restrictions on the applications of the method. If material nonlinearity is considered, then the SB equations cannot be solved analytically, and therefore numerical techniques have to be employed.

Steady-state midrest base transfer function		Steady-state midrest base transfer function					
$A/F = [i(z=0) - i_g] / i_g$		$A/F = [i(z=0) - i_g] / i_g$					
Inhomogeneous shear beam	Fundamental period $T_1 \bar{C}/H$	Ratio of natural periods T_1/T_2	n th Natural circular frequency $\omega_n H/\bar{C}$	n th Modal displacement $U_n(x=0, z)$	n th Mode participation factor F_n	I. "Rigid-rock" amplification	II. "Elastic-rock" amplification
$G = G_0 \zeta^m$ $0 \leq m \leq 1$	$\frac{1.6\pi}{(4+m)(2-m)\beta}$	$\frac{\beta_2}{\beta_1}$	$\frac{\beta_n}{8} (4+m)(2-m)$	$\zeta^{-m/2} J_q \left[\beta_n \zeta^{1-m/2} \right]$	$\frac{2}{\beta_n} \frac{1}{J_{q+1}(\beta_n)}$	$\frac{(a_0/2)^q}{\Gamma(q+1)} J_q(a_0)$	$\frac{(a_0/2)^q}{\Gamma(q+1)} J_q(a_0) \alpha J_{q-1}(a_0)$
$G = G_0 \zeta^{2/3}$	2.57	2	$\frac{7}{9} n\pi$	$\zeta^{-2/3} \sin \left[n\pi \left(1 - \zeta^{2/3} \right) \right]$	$\frac{2}{n\pi}$	$\frac{a_0}{\sin a_0}$	$\frac{a_0}{\sin a_0 + i\alpha} \left(\frac{\sin a_0}{a_0} - \cos a_0 \right)$

where:

- \bar{C} = average shear wave velocity in the dam
- $\alpha_0 = \omega_n H/\bar{C}$; $\zeta = z/H$; $J(r)$ denotes the gamma function; $q = m/(2-m)$
- α = rigidity contrast ratio = $\rho C / \rho_s C_s$; where r refers to the properties of the supporting base; $i = \sqrt{-1}$
- $\beta_n = \beta_n(m)$ is the n th root of the period of the dam, $T_n = \frac{4\pi}{\beta_n(2-m)} C_b$ (Dakoulas et al., 1985), tabulated below for the first five modes ($n = 1 - 5$) and five values of the parameters m : (0, 1/2, 4/7, 2/3 and 1)

m	β_n mode n				
	1	2	3	4	5
0	2.405	5.520	8.654	11.792	14.931
1/2	2.903	6.033	9.171	12.310	15.451
4/7	2.999	6.133	9.273	12.413	15.554
2/3	3.142	6.283	9.525	12.566	15.708
1	3.832	7.106	10.174	13.324	16.471

Table 2-4. Some analytical expressions for inhomogeneous shear-beam models (Gazetas, 1987).

Elgamal et al. (1985, 1987) carried out several dynamic analyses applying the SB method. In 1985 one-dimensional elasto-plastic analysis of earth dams was implemented considering a dam as one-dimensional (1D), inhomogeneous (in terms of stiffness) hysteretic shear beam, subjected to horizontal base excitation. This method was applied on the case of Santa Felicia earth dam predicting accelerations, stresses and strains at several points of the dam. The hysteretic stress-strain behaviour was modelled using elasto-plastic constitutive equations based on multi-surface kinematic plasticity (Prevost, 1977). The smooth backbone curve was approximated by linear segments along which the tangent modulus was constant. Therefore, the degree of accuracy of the solution was dependent on the number of linear segments adopted. Each segment corresponded to a yield surface in the three-dimensional stress space, thus defining a set of nested surfaces. The proposed non-linear approach was not compared to field data, but it was compared to results of finite element (FE) analysis of the same dam. The authors commented that SB approach may represent a practical and inexpensive (in terms of time and computational demand) analysis tool alternative to the more elaborate FE analysis.

In 1987, the same authors extended the previously-mentioned approach to consider also the longitudinal dimension of the dam, and therefore was able to account for the effect of the lateral canyon constraint on the seismic response of earth dams. The case study was again the Santa Felicia dam (Elgamal et al., 1987) and the applied approach showed that taking into account the longitudinal dimension of the dam provides different results in terms of seismic-induced effects. Therefore, the study highlighted the importance of modelling the canyon effect for narrower dams (crest length over height ratio, $L/H \approx 4.7$ for Santa Felicia dam).

The shear beam method was also extended to the three-dimensional (3D) analysis of dams. Abdel-Ghaffar and Koh (1982) developed another method to analyse 3D isotropic linear elastic dams whose elastic moduli varied spatially (inhomogeneous) and which were founded on rigid canyons. The computed modes and natural frequencies of vibration were compared to measured results from full-scale tests and earthquake response records with reasonable agreement. However, the authors did not compare any results from 3D and 2D analyses to identify their differences and highlight the importance of performing a full 3D seismic analysis. Moreover, nonlinear elasto-plastic material behaviour was introduced by

Abdel-Ghaffar and Elgamal (1987b) who considered the hysteretic response of a 3D inhomogeneous uniform earth dam. The dam was assumed to sit on a trapezoidal rigid canyon and vibrate in all three directions, upstream-downstream, vertical and longitudinal. This method was also applied on Santa Felicia dam (Abdel-Ghaffar and Elgamal, 1987a) and was compared to finite element solutions with acceptable accuracy, emphasising its applicability in analysing a large structure at a reasonable computational cost.

The method of Abdel-Ghaffar and Elgamal (1987b) was extended by Elgamal (1992) to include dam-alluvial foundation interaction and a more general canyon geometry configuration.

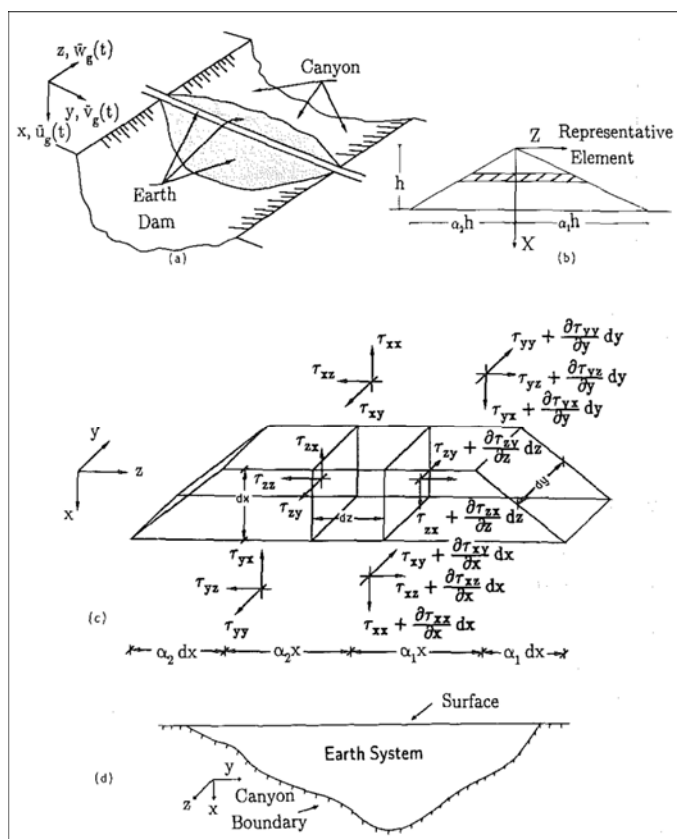


Figure 2-30. Geometry of the system considered by Elgamal (1992): (a) physical problem, (b) UD cross-section, (c) shear stresses acting on a soil element and (d) geometric configuration of computational model.

Although the shear beam approach takes into account the dynamic response of a dam, it still carries its own limitations. More advanced numerical methods evolved which are able to handle more complicated boundary value problems.

Such methods are the Finite Element (FE), Finite Difference (FD) and Boundary Element (BE) approaches, which are able to overcome the mentioned restrictions and are the most widely used nowadays.

The FE method treats a continuum as an assemblage of discrete elements defined by nodal points at their boundaries. The dynamic FE method solves the equation of motion (Equation (2.7)) for dynamic equilibrium with time. Solutions of the primary unknown quantities (such as displacements and pore pressures) are provided at these nodes and their value at any other point in the whole domain can be obtained by using interpolation functions (Potts and Zdravković, 1999).

$$[M]\{\ddot{u}\} + [C]\{\dot{u}\} + [K]\{u\} = \{P(t)\} \quad (2.7)$$

where $[M]$, $[C]$ and $[K]$ are the mass, damping and stiffness matrices respectively with entries referring to the nodal points, whereas $\{\ddot{u}\}$, $\{\dot{u}\}$, $\{u\}$ and $\{P(t)\}$ are the acceleration, velocity, displacement and external loading vectors, respectively. The stiffness matrix, $[K]$ contains information about the constitutive behaviour of the materials (Potts and Zdravković, 1999).

Dynamic finite element analysis involves both spatial discretisation of the problem into small regions (the finite elements) and temporal discretisation according to the applied loading history. Then, appropriate boundary conditions are applied and advanced constitutive models may be assigned to different regions and for different time periods. The acceleration time history is applied at a part of the FE mesh (normally at the soil-bedrock interface, depending on the stiffness of the two materials and the impedance contrast).

The finite difference method (FD) is perhaps the oldest numerical technique used for the solution of sets of differential equations, given initial values and/or boundary values (see, for example, Desai and Christian 1977). In the finite difference method, the derivatives in the set of governing equations are replaced directly by an algebraic expression

written in terms of the field variables (e.g., stress or displacement) at discrete points in space; these variables are undefined within the elements.

The finite element method in contrast has a central requirement that the field quantities (stress, displacement) vary throughout each element in a prescribed way, using specific functions controlled by parameters. The formulation involves the adjustment of these parameters to minimize error or energy terms.

Both methods produce a set of algebraic equations to solve. Even though these equations are derived in quite different ways, it is easy to show (in specific cases) that the resulting equations are identical for the two methods. It is pointless, then, to argue about the relative merits of finite elements or finite differences in the engineering field.

The advantage of these methods compared to the previous ones is the ability to:

- i. Handle complicated geometries
- ii. Simulate sophisticated material behaviour
- iii. Account for soil skeleton and pore fluid interaction
- iv. Simulate reservoir hydrodynamic pressures (modelling the reservoir water)
- v. Model the site more accurately (by advanced boundary conditions) and include any nearby structures, such as spillway, drainage galleries etc.
- vi. Simulate the previous (static) loading history (such as layered construction, water impoundment, consolidation etc.)

2.2.2 MORE RECENT APPLICATIONS

The previous paragraphs focused on the dynamic methods and their development over the years. Here are presented some studies and results presented in the last decade on seismic response of earth dams performed using FE or FD methods.

In the following paragraphs some of these studies are explained in detail. According to these studies, the seismic response of an earth dam is strongly affected by several factors, such as the past loading history, the

characteristics of the seismic input (magnitude, duration and frequency content), the mechanical properties of soils and the analysis approach.

2.2.2.1 FEM: Sica et al., 2008

Sica et al. (2008) dealt with the influence of past loading history on the seismic response of earth dams by interpreting the static and dynamic behaviour of a real case-history: the El Infiernillo Dam. Settlements, pore water pressures and accelerations measured during different stages of the dam lifetime have been interpreted by using a coupled dynamic approach derived from the u - p formulation of the Biot consolidation theory (where u is the skeleton displacement and p the pore pressure). Such formulation, combined to the Hujieux model as constitutive law, has been solved numerically by the finite element method and implemented in the GEFDYN code (Aubry et al., 1985 and 1996).

Two monitored cross sections of the El Infiernillo Dam have been analysed (Figure 2-31). The former has been used to model the static stages up to the first impounding in order to reproduce the observed static behaviour and to calibrate the model parameters. The latter helped to simulate all stages of the dam life in order to compare predicted and observed seismic induced effects.

The adopted finite element meshes are shown in Figure 2-32. Linear shape functions were therefore used for displacements and, for coupled elements, linear shape functions for pore water pressures have been adopted as well.

After validation of the selected mathematical-numerical model by computing the dam response to the seismic events of 19/09/85 and 30/05/90, in terms of accelerations and crest settlements (Figure 2-33 and Figure 2-34), a parametric study was performed to evaluate the influence of pre-seismic loading histories on dynamic analysis results.

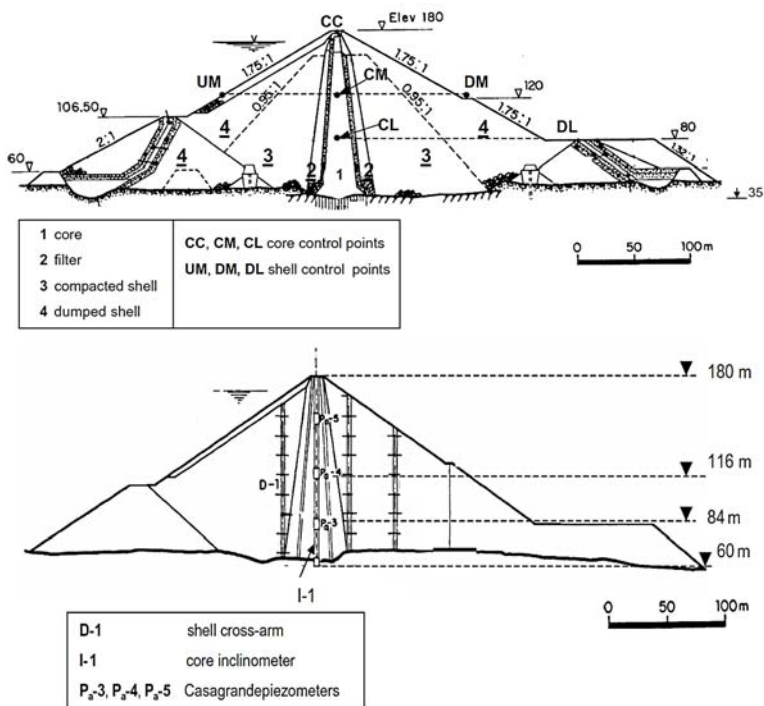


Figure 2-31. El Infiernillo dam: monitored cross section A and B (Sica et al., 2008).

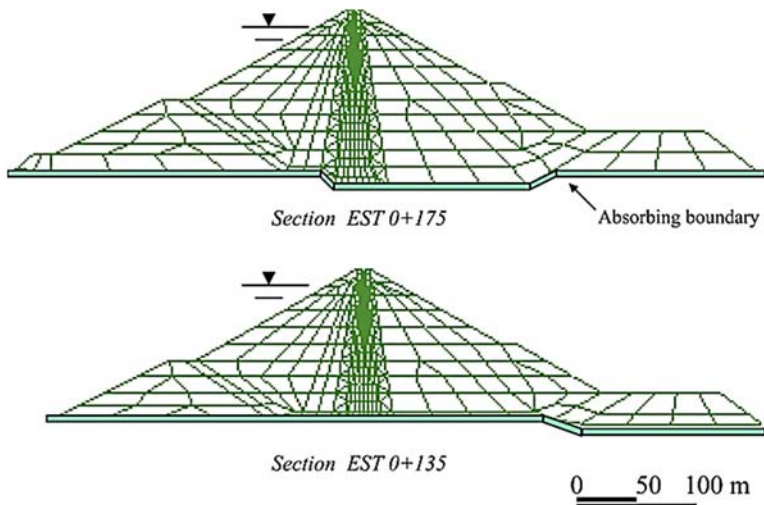


Figure 2-32. El Infiernillo dam: finite element meshes adopted (Sica et al., 2008).

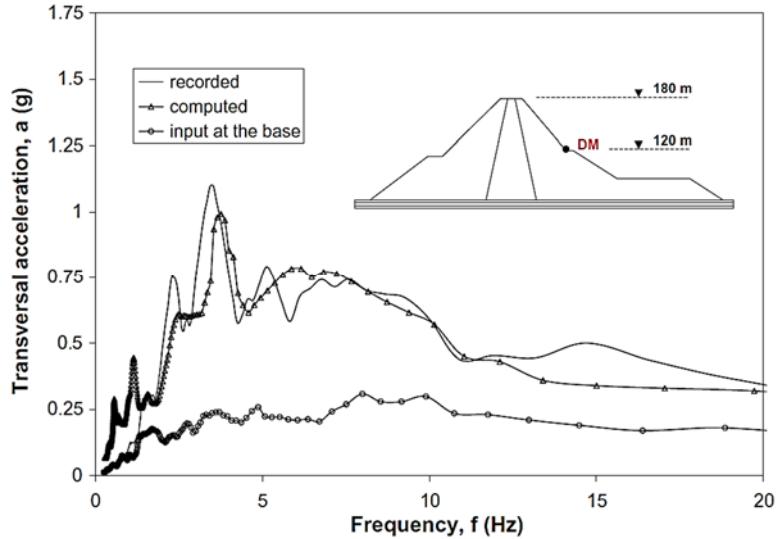


Figure 2-33. Response spectra of the recorded and computed acceleration at the location DM for the 1985 earthquake (Sica et al., 2008).

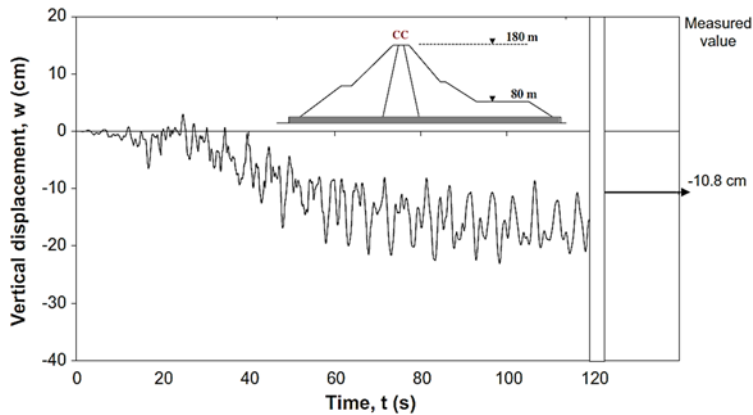


Figure 2-34. Vertical displacement computed during the 1985 earthquake at the dam crest. The measured permanent settlement was indicated with a black arrow (Sica et al., 2008).

Different past “static” and “seismic” loading histories were simulated (Figure 2-35) and dam performance evaluated in terms of seismic-induced freeboard loss.

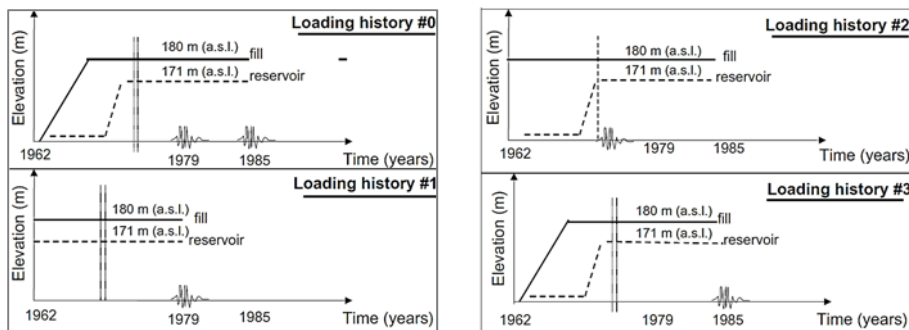


Figure 2-35. Pre-seismic loading histories simulated in the parametric study (Sica et al., 2008).

For the particular case-history and with the constitutive parameters assigned to the dam soils, it was found that past “seismic” loading histories (Figure 2-36), especially the ones which included strong motion events, may be very important in correctly predicting the freeboard loss caused by subsequent seismic events (Figure 2-37). The study clearly brings up dam soil hardening effects due to past seismic history. This aspect should be taken into account when a back-analysis of the dam observed behaviour is planned (especially in the case of existing dams, to characterize the behaviour of coarse grained materials), and the seismic performance of the structure should be assessed in light of modern performance-based design/verify philosophies.

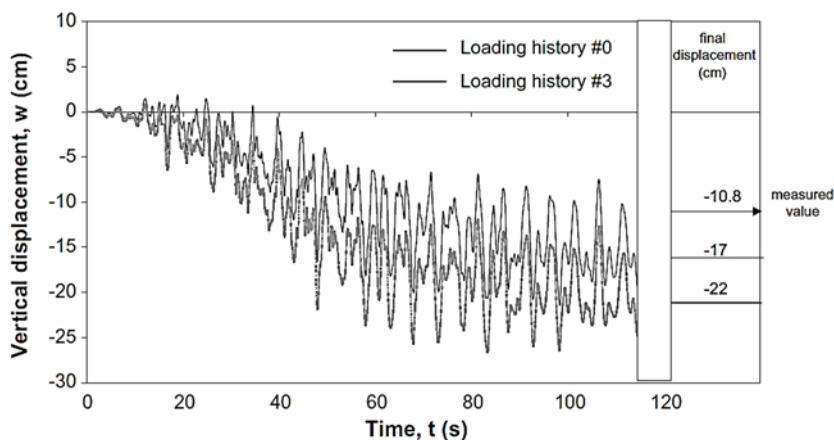


Figure 2-36. Vertical settlement at the dam crest induced by the 1985 earthquake for loading histories #3 and #0 (Sica et al., 2008).

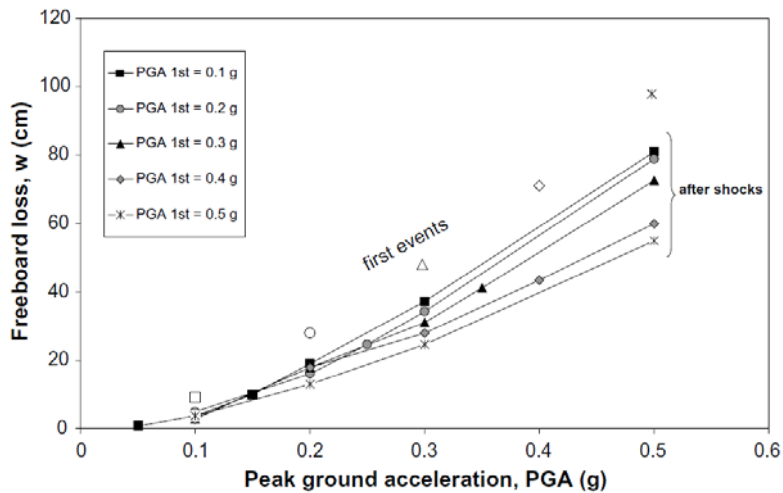


Figure 2-37. Dam freeboard loss induced by first events (open symbols) and aftershocks (continuous lines) characterized by different peak ground accelerations at the dam base (Sica *et al.*, 2008).

2.2.2.2 FEM: Elia *et al.*, 2011

In 2011, Elia *et al.* performed the seismic analyses of two existing earth dams in Italy using a fully coupled effective stress nonlinear approach implemented in a finite-element (FE) code. Both dams are located in the south of Italy, one is homogeneous and one is zoned; the first embankment is in Puglia along the Marana Capacciotti stream, approximately 13.5 km southwest of the city of Cerignola (Foggia, Italy). The second is the San Pietro dam, located in Campania along the Osento stream, between the towns of Aquilonia (Avellino, Italy) and Monteverde (Avellino, Italy).

The program used in this work is DIANA-SWANDYNE II (Dynamic Interaction and Nonlinear Analysis-SWANsea DYNAMIC program Version II), a two-dimensional (plane strain and axisymmetric) non-commercial FE code that implements the Biot (1941) coupled dynamic equations by using the u-p simplification; that is, assuming the fluid acceleration relative to the solid skeleton is negligible. The code can be used for static, consolidation, and dynamic analyses. The mechanical behaviour of the involved clayey and granular soils is described through advanced elastoplastic constitutive models, calibrated on laboratory and in situ test results. Before the application of the seismic motions, appropriate FE static analyses were

performed in both cases to define the initial stress state and the internal variables of the material models.

The numerical analyses of the Marana Capacciotti dam were performed by using the mesh shown in Figure 2-38. To minimize the lateral boundary effects during the dynamic analyses, the overall length of the foundation was chosen to be three times the base of the dam.

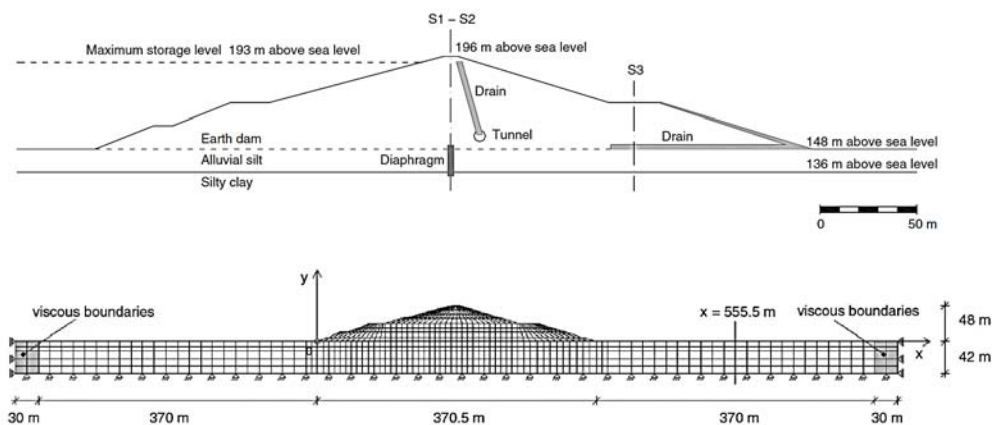


Figure 2-38. Cross section of the Marana Capacciotti dam and FE mesh adopted (Elia et al., 2011).

For the evaluation of the dynamic response of the Marana Capacciotti dam, the results of a seismic hazard study carried out by the Italian National Institute of Geophysics and Volcanology (INGV) on the entire Italian territory were used (INGV 2004). From the INGV interactive maps of seismic hazard (INGV 2007), a peak ground acceleration of 0.275 g was obtained at the dam site for a return period of 1000 years and 0.194 g for a return period of 475 years. Three acceleration time histories were selected from a database of earthquake records (Ambraseys et al. 2000) and linearly scaled to the mentioned maximum acceleration values. The peak ground accelerations predicted by the seismic hazard study are referred to input motions recorded at the ground rock surface; that is, at the “outcropping” rock. In the dynamic analyses of the dam, the scaled records were filtered by the authors to a maximum frequency of 10 Hz, transferred to the “inside” bedrock formation through a standard deconvolution analysis, and applied at the base of the FE discretization of the system (as suggested by Kwok et al., 2007).

With reference to NOCERA (Umbria-Marche earthquake, 1997) seismic input (Table 2-5), the comparison of the input motion applied at the bedrock and the acceleration time histories computed along the dam axis at the crest of the embankment and at the dam base in terms of Fourier spectra is showed in Figure 2-39. The results indicate that an amplification of the seismic signal occurs between the bedrock and the crest.

Input	T_R (years)	a_{\max} outcrop (g)	a_{\max} bedrock (g)	f_{\max} (Hz)	Dominant frequency (Hz)	Record length (s)
LOMA_1	1,000	0.275	0.177	10	1.39	40.0
LOMA_2	475	0.194	0.128	10	1.39	40.0
TOLMEZZO	1,000	0.275	0.214	10	1.49	35.0
NOCERA	1,000	0.275	0.148	10	2.63	40.0

Table 2-5. Characteristics of the Input Motions Used in the Dynamic Analyses of the Marana Capacciotti Dam (Elia et al., 2011).

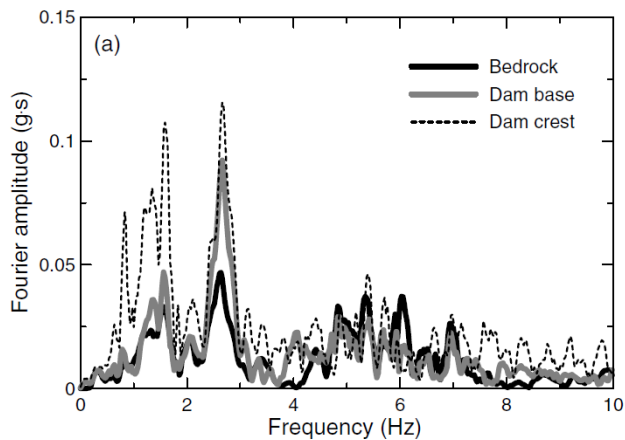


Figure 2-39. Comparison of the Fourier spectra computed (a) along the Marana Capacciotti dam axis (Elia et al., 2011).

The advanced constitutive assumption adopted in the FE analysis allows the realistic simulation of the nonlinear and irreversible response of the soils subjected to the dynamic action, leading to a final permanent horizontal displacement of the crest equal to 0.35 m and a crest settlement of 0.54 m, essentially due to plastic strain accumulation throughout the shaking. The overall behaviour of the dam in displacement reveals a greater deformation pattern of the downstream slope with respect to the upstream one, but does not give a precise indication of the occurrence of a failure mechanism inside the embankment and its foundation layer (Figure 2-40). Because the seismic action applied at the bedrock is very severe ($T_R = 1000$

years), the results can be considered indicative of a satisfactory dynamic performance of the dam in this extreme condition.

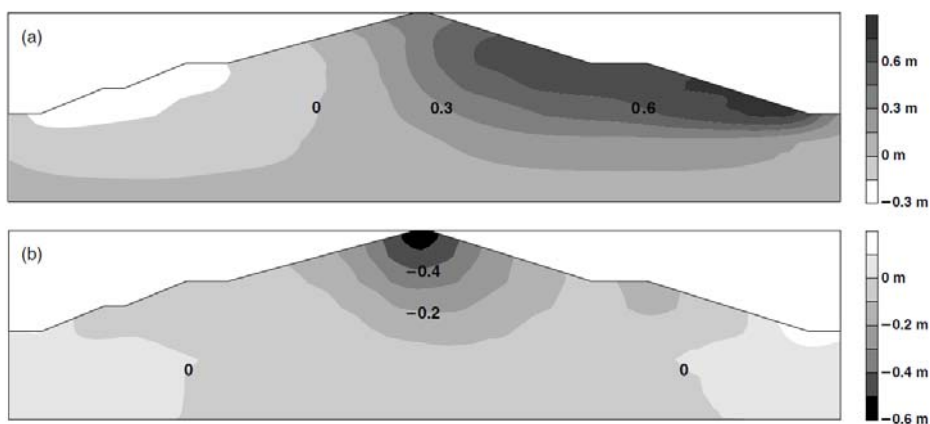


Figure 2-40. Contour lines at the end of the shaking (Marana Capacciotti dam): (a) horizontal, (b) vertical displacements (Elia et al., 2011).

Since the FE code DIANA-SWANDYNE II is based on an effective stress formulation, it allows the user to monitor the pore pressure regime at every single node of the mesh during the simulations. Although it was not directly imposed by the user, the system behaves in undrained conditions during and after the shaking; the material permeabilities are too low to allow the dissipation in only 60 s of the excess pore water pressures cumulated during the first 40 s. At the end of the dynamic simulation, the satisfaction of the equilibrium condition for both the solid and the fluid phases was imposed (i.e., a long-term, fully drained condition was also considered). This leads to further settlement of the downstream slope of approximately 0.025 m (Figure 2-41).

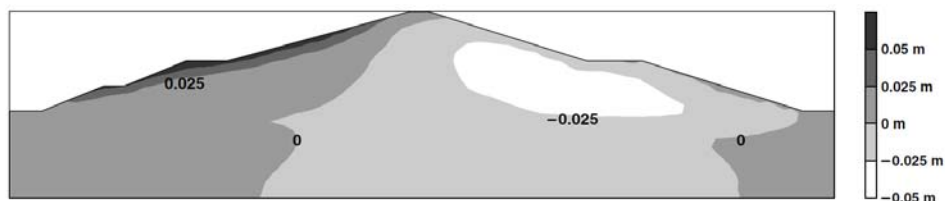


Figure 2-41. Contour lines of additional settlements caused by consolidation (Marana Capacciotti dam) (Elia et al., 2011).

The same procedure employed for the stability analysis of the Marana Capacciotti dam was adopted to study the dynamic response of the San Pietro dam (Figure 2-42).

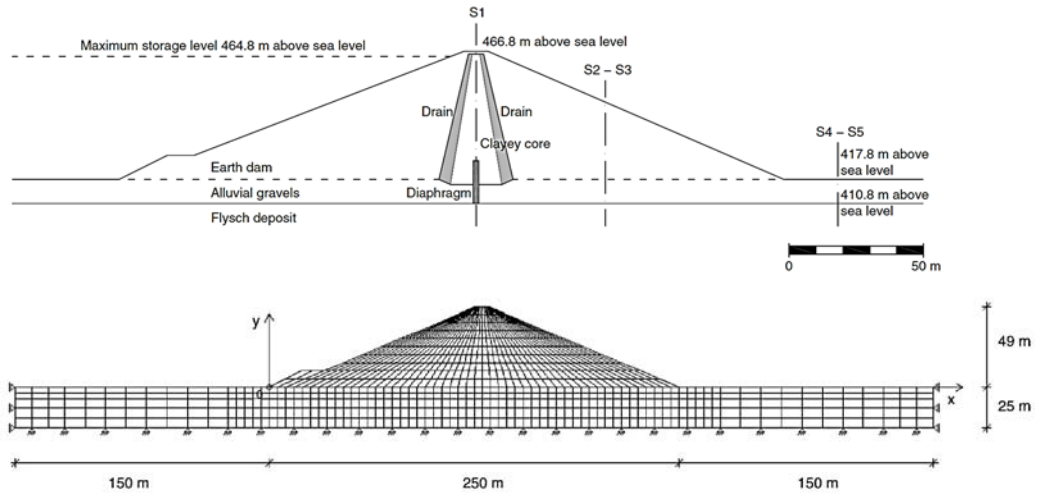


Figure 2-42. Cross section of the San Pietro dam and FE mesh adopted (Elia et al., 2011).

The dynamic behavior of the San Pietro dam was studied by applying two different input motions directly at the base of the embankment; that is, neglecting the wave propagation in the dam foundation layer caused by the high stiffness of both the injected alluvial gravels and the overconsolidated flysch deposit. The first seismic motion is represented by the east-west horizontal component of the accelerogram registered at Bisaccia (Avellino, Italy) during the Irpinia earthquake of November 1980, whereas the second is an artificially generated earthquake (Calabresi et al. 2004). For the dam site, the CNR-GNDT (Galadini et al. 2000) seismic hazard study predicts a peak ground acceleration of 0.35 g for a return period of 475 years. Therefore, the maximum acceleration of the real input motion and the elastic response spectrum from which the artificial earthquake was generated have been scaled to this reference value (Table 2-6).

Input	T_R (years)	a_{\max} bedrock (g)	v_{\max} (m/s)	T_D (s)	I_A (m/s)	f_{\max} (Hz)	Dominant frequency (Hz)	Record length (s)
Real	475	0.35	0.65	69.6	4.4	10	0.51	72.7
Artificial	475	0.41	0.38	26.4	4.1	10	4.34	30.0

Table 2-6. Characteristics of the Input Motions Used in the Dynamic Analyses of the San Pietro Dam (Elia et al., 2011).

The results of the fully coupled dynamic simulations are summarized in Figure 2-43 in terms of profiles with non-dimensional depth $z=H$ of the ratio $a_{max}=a_{base}$ of the maximum acceleration recorded along the dam axis to the base input value.

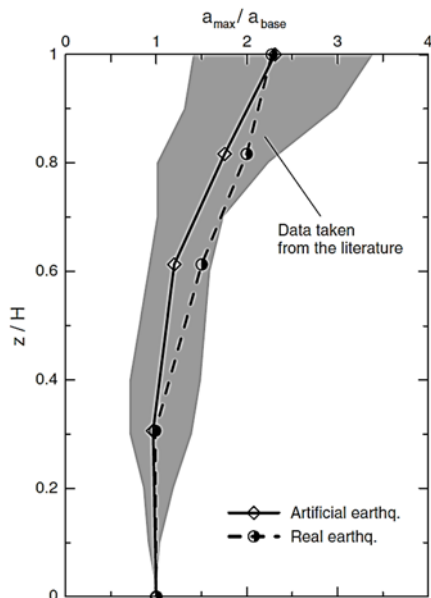


Figure 2-43. Profiles of $a_{max}=a_{base}$ computed at the end of the FE dynamic analyses of the San Pietro dam and comparison with literature results (Elia et al., 2011).

In both the analyses, the profiles are characterized by a significant amplification of the seismic signal at the crest of the dam. In the case of the real input motion, the peak acceleration at crest is equal to 0.93 g, whereas by applying the artificial earthquake the corresponding maximum acceleration is equal to 0.81 g, with a magnification factor of approximately 2.3 times the peak base amplitude in both cases.

The maximum crest settlement relative to the dam base induced by the earthquake (equal to 0.68 m) is equivalent to the 15% of the service freeboard (4.5 m) and to the 34% of the freeboard at the maximum impounding level of the reservoir (2.0 m). Similar results were obtained in final permanent horizontal and vertical displacements when the artificial input motion is applied at the base. In this case, the crest horizontal displacement is equal to 0.35 m, whereas the maximum crest settlement is equal to 0.77 m, equivalent to the 17% of the service freeboard and to the

38.5% of the freeboard at the highest impounding level. More generally, the dam behaviour is stable during and after the dynamic input motions, and no failure mechanism inside the embankment can be recognized in both the FE simulations.

To perform a direct comparison between the dynamic behaviour of the two embankments, the San Pietro dam was subjected to the same NOCERA input motion used for the study of the Marana Capacciotti dam.

The results of this comparison presented in terms of Fourier spectra obtained at the crest of the two embankments showed that:

- 1) in both cases, the signal is amplified at approximately 2.6 Hz, close to the dominant frequency of the input motion (2.63 Hz);
- 2) the Marana Capacciotti dam amplifies the frequencies more in the range 0.85 to 1.56 Hz, which are close to its fundamental period of vibration [equal to 1.21 Hz, as shown by Elia et al. (2011)], than those in the range 4.5 to 5.5 Hz;
- 3) in the San Pietro dam analysis, some amplification occurs at 1.53 Hz, but a larger amplification can be observed for the frequencies between 4.85 and 6.95 Hz.

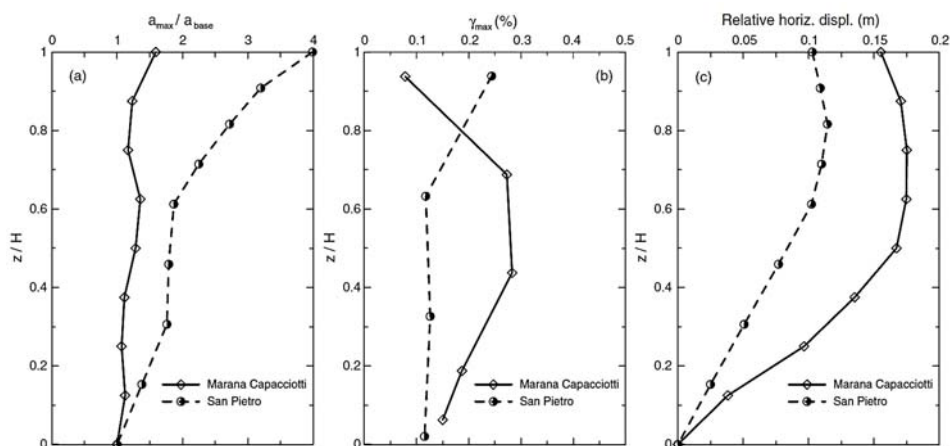


Figure 2-44. Comparison of the Marana Capacciotti and the San Pietro dam analyses in terms of (a) profiles of $a_{max}=a_{base}$ along the dam axes, (b) profiles of maximum shear strain with depth, (c) profiles of maximum horizontal displacement relative to the dam base with depth (Elia et al., 2011).

Moreover, a greater overall amplification effect is highlighted in the case of the San Pietro dam, because the NOCERA earthquake is shaking the

system close to its first natural period (2.59 Hz). This effect can be observed in the profiles of $a_{\max}=a_{\text{base}}$ obtained along the two dam axes are compared (Figure 2-44a). A larger amplification of the input signal occurs in the top part of the San Pietro dam, with an acceleration magnification factor at its crest of approximately 4.0 more than the peak bedrock amplitude. The result is essentially correlated to a lower shear-strain level induced by the seismic action in the San Pietro embankment, as indicated by Figure 2-44b, in which the profiles of maximum shear strain recorded along the two dam axes are reported against normalized depth. The lower shear strain amplitude induced by the earthquake is accompanied by higher material stiffness and lower hysteretic damping during the shaking, thus enhancing the transmission of the high frequencies of the seismic signal and increasing the amplification of the peak acceleration at the surface. Nevertheless, the seismic-induced displacements obtained from the San Pietro analysis are significantly smaller than those induced by the same earthquake on the Marana Capacciotti dam, as shown in Figure 2-44c, in terms of profiles of maximum horizontal displacement relative to the dam base recorded at the end of the simulations along the dam axes.

2.2.2.3 FEM: Pelecanos et al., 2015

Pelecanos et al. (2015) applied the finite element method for investigating the seismic response of the La Villita dam, which experienced six major seismic events during the period between 1975 and 1985 (Table 2-7). Although it did not fail, it sustained some deformations. The earthquake motions were recorded by three accelerometers which were installed on the dam soon after the end of construction.

No	Date	M_s	Epic. dist.: km	Max. rock accel.: g	Max. berm accel.: g	Max. crest accel.: g	Rock predom. period: s	Berm predom. period: s	Crest predom. period: s
EQ1	11/10/1975	4.5	52	0.07	0.09	0.36	0.2	0.18	0.32
EQ2	15/11/1975	5.9	10	0.04	0.08	0.21	0.18	0.34	0.77
EQ3	14/03/1979	7.6	121	0.02	0.14	0.40	0.16	0.32	0.28
EQ4	25/10/1981	7.3	31	0.09	0.24	0.43	—	0.29	0.27
EQ5	19/11/1985	8.1	58	0.12	—	0.76	0.57	—	0.75
EQ6	21/11/1985	7.5	61	0.04	—	0.21	0.37	—	0.65

Table 2-7. Summary of earthquake events on La Villita dam (Pelecanos et al., 2015).

Because of the available ground motion data, a number of researchers have previously investigated this dam. Based on the previous findings, the premise of the Pelecanos et al. study is that the observed acceleration record

is the result of the combination of (a) the dynamic behaviour of the dam structure and (b) the high acceleration peaks due to a localised failure close to the monitoring instrument.

The study also differs from previous ones due to the finite element code used and the constitutive model. The authors employed the Imperial College finite-element program (ICFEP) (Potts & Zdravković, 1999, 2001). Two-dimensional plane-strain static and dynamic coupled-consolidation analyses are carried out in order to model the history of the dam prior to the earthquake events and its subsequent seismic response. The constitutive model used is a cyclic non-linear model (CNL), which adopts a logarithmic function to describe the backbone curve (Puzrin and Burland, 2000; Taborda et al., 2010; Taborda, 2011) coupled with a Mohr–Coulomb failure criterion. The logarithmic relation dictates the degradation of shear stiffness, G , and the increase of damping, ξ , with cyclic shear strain, γ (see Appendix in Pelecanos et al., 2015). The results presented in this work showed a similar response at the crest between the recorded and calculated response at the berm (Figure 2-45).

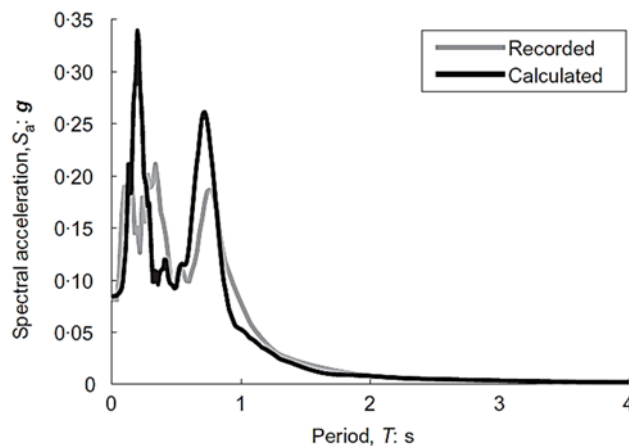


Figure 2-45. Comparison of calculated results and recorded data at the berm of the dam for EQ2 with the new updated material parameters in terms of response spectra (Pelecanos et al., 2015).

Comparing the response spectra at the dam crest for the EQ5 recording (Figure 2-46), calculated by Pelecanos et al. (2015) and by Elgamal (1992) it is evident that the predicted response of the newest work is in better agreement with the recorded signal with the respect of the prediction calculated by Elgamal (1992).

The high acceleration values at high frequencies in the response spectrum of the recorded motion are believed to originate from asymmetric high peak values of acceleration observed in the recorded acceleration time history at the crest of the dam for EQ5. The authors believed that those high values of recorded acceleration and displacements could be due to the possible pre-existence of a discontinuity in the embankment. They supposed that perhaps some minor localised failure at the position close to the monitoring instrument may have happened before, which could have created a local discontinuity. This could have been originated possibly from a previous seismic event or even from some construction processes. In order to reach a better agreement between the recorded and the calculated response (Figure 2-46) the authors filtered the high frequencies from the recorded accelerations at the dam crest.

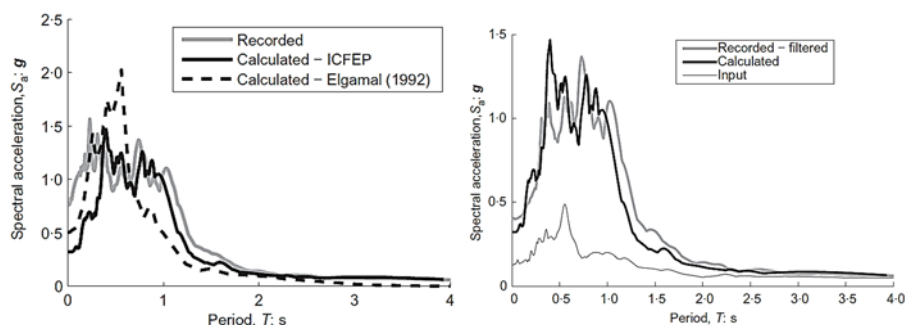


Figure 2-46. Comparison of calculated results and recorded data at the crest of the dam for EQ5 with the new updated material parameters in terms of response spectra (Pelecanos et al., 2015).

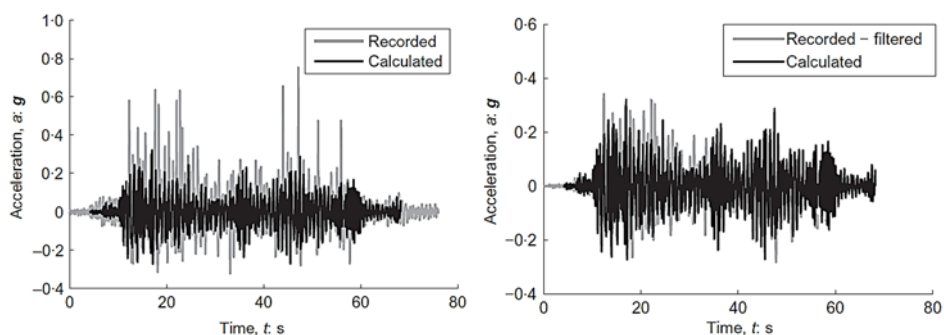


Figure 2-47. Comparison of calculated results and recorded data at the crest of the dam for EQ5 with the new updated material parameters in terms of accelerograms (Pelecanos et al., 2015).

The frequency for the filtering was obtained from a parametric study and was taken as the magnitude at which the high values of peak acceleration

(due to the localised slip failure) vanish, making the record symmetric and consequently representative of the overall dynamic behaviour of the dam structure. The filtering operation, anyway, does not filter out the predominant frequency of the input motion which is around 1.8 Hz (i.e. period of 0.57 s). It is shown that the peak values of recorded accelerations vanish along with the observed asymmetry in the record, leading to a better agreement between the calculated and recorded acceleration–time histories. Therefore, after filtering, the recorded residual seismic displacements disappear and the calculated and recorded displacement–time histories agree very well.

2.2.2.4 FDM Studies

Most of the research works for assessing the seismic response of earth dams are performed with different FEM codes, as reported in previous sections. For the finite difference method, instead, the code FLAC (ITASCA) is the most widely used both for two-dimensional and for three-dimensional analysis.

Costanzo et al. (2011) illustrate the procedure followed for the seismic safety assessment of the dam on Melito River in the territory of Gimigliano (CZ) in Calabria, through different approaches. After a careful seismological study to determine the input motions to be used in the advanced dynamic analysis (according to current national regulations, DM 14.01.2008), and mechanical characterization of the constitutive materials of the dam–foundation system, they have performed:

- Simplified dynamic analyses;
- Advanced dynamic analyses by FLAC2D.

The Sarma method allowed the calculation of the critical accelerations and the respective critical sliding surfaces; four different possible triggering phenomena were identified (Figure 2-48).

These zones correspond to sliding mechanisms of circular surfaces along the downstream (SV1, bottom, and SV2, top) and upstream shell (SM3, top, and SM4, bottom); the latest (SM3 and SM4) have been calculated with empty reservoir, a more cautionary condition due to the absence of the weight of the water, which induces a stabilizing effect. In fact, the SM5

surface, that is the critical one for the upper part of the detected maximum water level conditions, is deeper and characterized by a critical acceleration twice as the value calculated when the reservoir is empty.

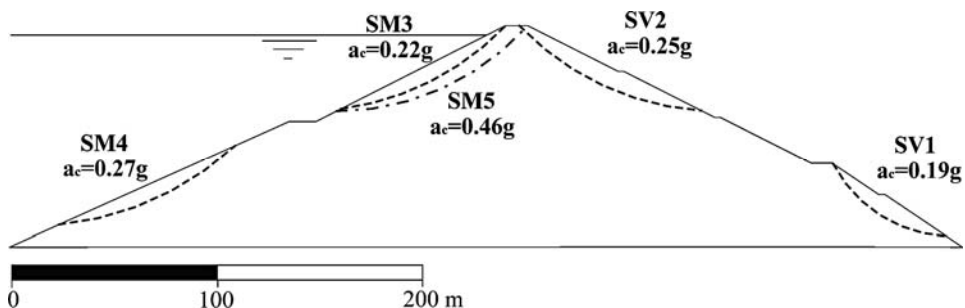


Figure 2-48. Critical surfaces and accelerations in different embankment zones (Costanzo et al., 2011).

A first simplified prediction of permanent displacements induced by seismic load was obtained by applying various empirical correlations available in literature (Table 2-8). These allow a preliminary assessment of earthquake-induced permanent displacements based on the ratio η of the critical acceleration of the potentially unstable mass and the maximum, a_{smax} , expected at the reference site ($\eta = a_c / a_{smax}$). For the Melito dam these displacements were evaluated using the relationship by Ambraseys and Menu (1988), Rampello et al. (2006), Ausilio et al. (2007) (Table 2-8).

Fonte	Accelerogrammi	Affioramento	Espressione	
AMBRASEYS & MENU, 1988	48 registrazioni di eventi superficiali <i>near field</i> con $M_s = 6.4 + 7.7$		$\log u = 0.90 + \log[(1 - \eta)^{2.53} (\eta)^{-1.09}] + 0.3\epsilon$ mediana: = 0 90° percentile: = 1.282	
RAMPELLO et al., 2006	Registrazioni italiane con $M_L = 4 + 6.6$ (database SISMA)	roccia	90° percentile:	$\log u = 2.11 - 3.26\eta$
			media:	$\log u = 1.32 - 3.26\eta$
AUSILIO et al., 2007a	Registrazioni italiane con $M_L = 4 + 6.6$ (database SISMA)	roccia - terreno	<i>upper bound</i> :	$\log u = 2.768 - 3.637\eta$
			90° percentile:	$\log u = 2.367 - 4.078\eta$
			mediana:	$\log u = 1.669 - 4.039\eta$

Table 2-8. Literature correlations between displacement and acceleration ratio adopted in the analyses (Costanzo et al., 2011).

The results obtained applying the empirical relationships were then compared with simplified dynamic analysis: Newmark (1965), dynamic “uncoupled” analysis (Tropeano et al., 2009), “coupled” analysis (stick-slip, Ausilio et al., 2008).

The maximum displacement evaluated by the latter procedures are comparable with the maximum value estimated through the empirical relationships considered above (Figure 2-49).

Then, the study was completed by performing two-dimensional advanced dynamic analyses with a finite difference code (FLAC2D). The dynamic analysis of the dam focused on two limit states, damage and collapse, using the selected accelerometers coming from the seismic hazard study. The geometric model was made by quadrangular elements whose height has been established by Kuhlemeyer and Lysmer (1973):

$$h_{\max} < \frac{V_s}{k \cdot f_{\max}} \quad (k = 10; f_{\max} = 10\text{Hz}) \quad (2.8)$$

as a function of the shear waves velocity of soils and the maximum frequency of interest of the selected accelerometers.

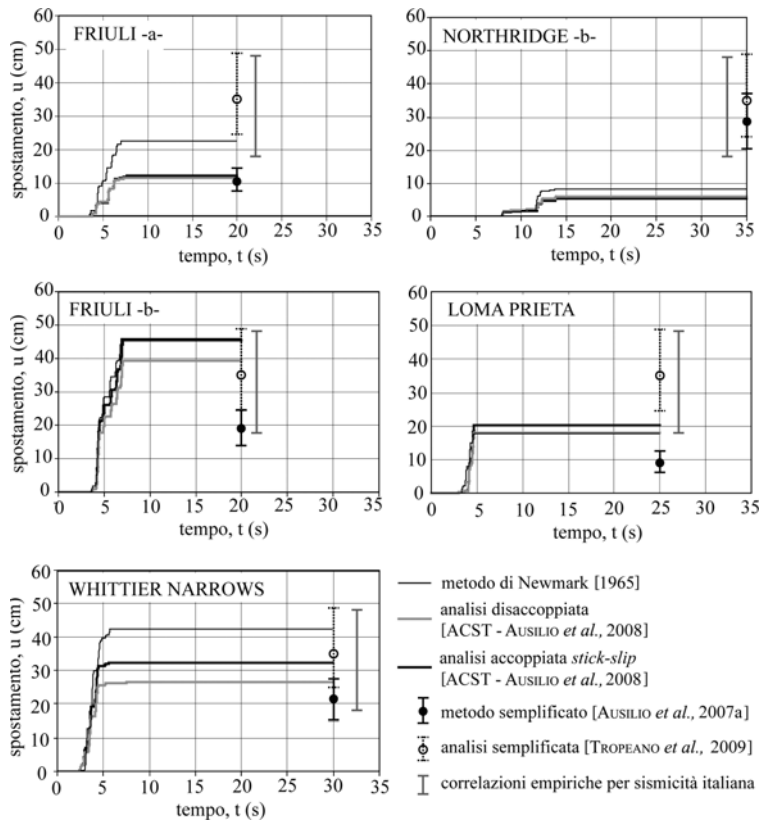


Figure 2-49. Displacements predicted by simplified uncoupled and one-dimensional dynamic analyses (Costanzo et al., 2011).

Along the lateral boundaries of the model special absorbent elements were introduced (free-field boundaries), which, in addition to avoiding the waves reflection like viscous dampers introduced by Lysmer and Kuhlemeyer (1969), forced the nodes of the lateral boundaries to reproduce the free-field motion, obtained from the 1D seismic site response analysis.

A Mohr-Coulomb constitutive law was assigned to the dam body soils in the static stage and a non-linear $G-\gamma$ behaviour in the dynamic stage. The foundation soils was assigned, instead, a linear elastic law.

The analysis results performed both with maximum water level and empty reservoir have shown that the dam body tends to attenuate the amplitude of the seismic signal from the foundation soil during the collapse limit state analyses, contrary to what happens for DLS analyses (Figure 2-50). This behaviour is attributed to the increase of dissipated energy due to higher level of deformation mobilized by the earthquake occurs in the SLC, which in this case is of the order of 0.3%, corresponding to a reduction factor of the shear modulus equal to 0.1.

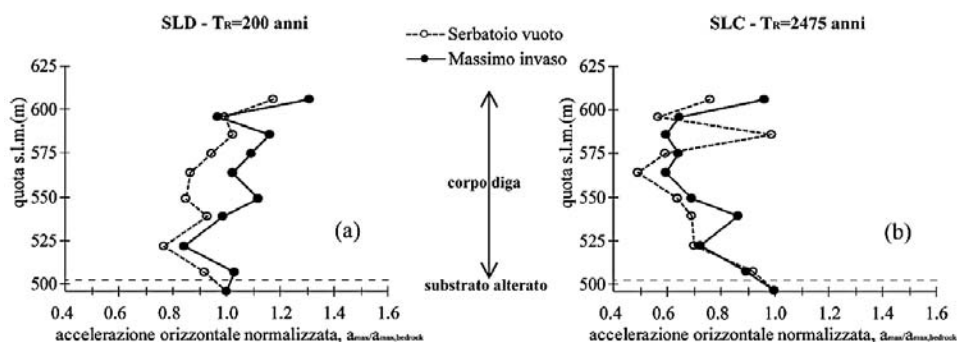


Figure 2-50. Peak acceleration profiles at the dam axis, computer for the Northridge input motion at the serviceability (a) and collapse (b) limit states (Costanzo et al., 2011).

Figure 2-51 compares the displacement contours relative to the more severe earthquakes (Northridge-b and Friuli-b), which induce more significant horizontal displacements respectively on the downstream (53 cm on the crest, 110 cm on the bottom) and upstream slope (40 cm on the crest, 44 cm at the bottom).

Superimposing the displacements distributions to the critical sliding surfaces identified by pseudo-static analysis, the authors determined the average displacement, weighed by the thickness, along the vertical center

of gravity of potentially unstable masses. The average values obtained are comparable to those obtained with simplified methods, which are usually related to a rigid body or to a sliding surface.

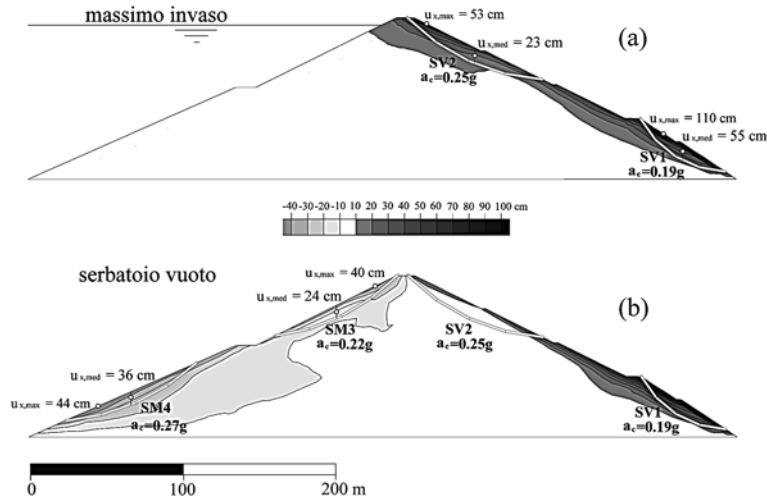


Figure 2-51. Critical surfaces versus horizontal displacements contours with peak and mean values computed for the most critical design earthquakes relevant to maximum impounding (Northridge-b, plot a) and empty reservoir (Friuli-b, plot b) (Costanzo et al., 2011).

Uncoupled methods and simplified dynamic analysis allowed to estimate maximum displacement values systematically lower than those obtained from the empirical correlation of Ambraseys and Menu, but comparable with those provided with relationships based on Italian seismicity (Tropeano et al., 2009). Two-dimensional analyses provided predictions more conservative of all other methods, with horizontal displacements on surface of 110 cm at the bottom and 55 cm at the crest. Average values calculated along the center of gravity of the vertical the sliding surfaces are about half of more superficial sliding surfaces, resulting in the order of 60 cm at the bottom and 32 cm on the crest, comparable with those estimated with the other methods.

Aliberti et al. (2016) performed a similar study on the on the seismic performance of the San Pietro dam (a zoned earth dam located in Southern Italy), through pseudo-static, simplified-displacement and dynamic 2D finite difference analyses.

Values of the expected permanent displacements were evaluated through several empirical relationships using input motions (Table 2-9) selected

from an Italian and a worldwide database according to the prescription of the Italian technical code.

N. Earthquake	Station – record (date)	M_w (-)	a_{max} (g)	F_s (-)	R^2 (-)	D_{ms} (-)	T_m (s)	I_A (m/s)	P_D ($10^{-4}g \cdot s^2$)
<i>CLS</i> ($a_{max} = 0.414 g$): $6.0 \leq M_w \leq 7.0$, $1 km \leq d_m \leq 25 km$									
#1 Loma Prieta	Gilroy Array # 1 – 000 (18/10/1989)	6.9	0.411	1.008	0.817	0.072	0.290	1.07	5.63
#2 Loma Prieta	Gilroy Array # 1 – 090 (18/10/1989)	6.9	0.473	0.875	0.843	0.148	0.387	1.29	11.09
#3 Parkfield -02 CA	Parkfield – Turkey Flat # 1 – 270 (28/09/2004)	6.0	0.245	1.688	0.908	0.106	0.366	0.49	3.40
#4 Parkfield -02 CA	Parkfield – Turkey Flat # 1 – 360 (28/09/2004)	6.0	0.196	2.111	0.900	0.095	0.449	0.84	10.96
#5 Northridge	Wonderland Ave – 185 (17/01/1994)	6.7	0.172	2.406	0.941	0.087	0.448	1.16	13.28
<i>LLS</i> ($a_{max} = 0.304 g$): $6.0 \leq M_w \leq 7.0$, $1 km \leq d_m \leq 25 km$									
#3 Parkfield -02 CA	Parkfield – Turkey Flat # 1 – 270 (28/09/2004)	6.0	0.245	1.239	0.913	0.106	0.366	0.26	1.83
#4 Parkfield -02 CA	Parkfield – Turkey Flat # 1 – 360 (28/09/2004)	6.0	0.196	1.550	0.888	0.099	0.449	0.45	5.91
#5 Northridge	Wonderland Ave – 185 (17/01/1994)	6.7	0.172	1.766	0.935	0.087	0.448	0.63	7.16
#6 Iwate, Japan	IWT010 – NS (13/06/2008)	6.9	0.226	1.348	0.929	0.065	0.517	2.38	16.01
#7 Tottori Japan	SMNH10 – EW (06/10/2000)	6.6	0.231	1.318	0.809	0.140	0.500	0.84	14.82

Table 2-9. Result of the accelerogram selection for the CLS (a,b) and the LLS (c,d) and main parameters of the scaled accelerograms (Aliberti et al., 2016).

Specifically, the relationships provided by Crespellani et al. (1998), Rampello and Callisto (2008), Saygili and Rathje (2008), Madiari (2009) and by Biondi et al. (2011), with reference to a rigid block analysis, were considered together with the relationships proposed by Ausilio et al. (2007) and by Rathje and Antonakos (2011), starting from a decoupled rigid block analysis, and by Bray and Travasarou (2008) through a coupled stick-slip analysis. These relationships correlate the expected permanent displacement u_o of a sliding block to the horizontal component of the yield acceleration ($a_c = k_{h,c} \cdot g$) and to some suitable seismic parameters describing the energy and the frequency content of the input motion. A shape factor S is then introduced to account for the actual plastic mechanism, leading to the horizontal (u_x) and vertical (u_y) components of the permanent displacement $u = S \cdot u_o$ of the soil mass. The horizontal component $k_{h,c}$ of the yield acceleration coefficient was evaluated through pseudo-static analyses. Comparable values of $k_{h,c}$ were detected in the case of horizontal acceleration directed downstream ($k_{h,c} = 0.175$) or upstream ($k_{h,c} = 0.176$) assuming, in both cases, a vertical seismic coefficient directed upwards ($k_v = -0.5k_h$).

Peak values of the horizontal and vertical permanent displacement were obtained at the Collapse Limit State (CLS) using accelerogram #2 and are equal to about $u_x = 45$ cm and $u_y = 18$ cm.

Some of the results of the dynamic analyses are shown in Figure 2-52 in terms of contours of vertical and horizontal components of permanent displacement evaluated using the records #5 and #6, which resulted the most severe input motions for the CLS (Collapse Limit State) and the LLS (Life-save Limit State), respectively.

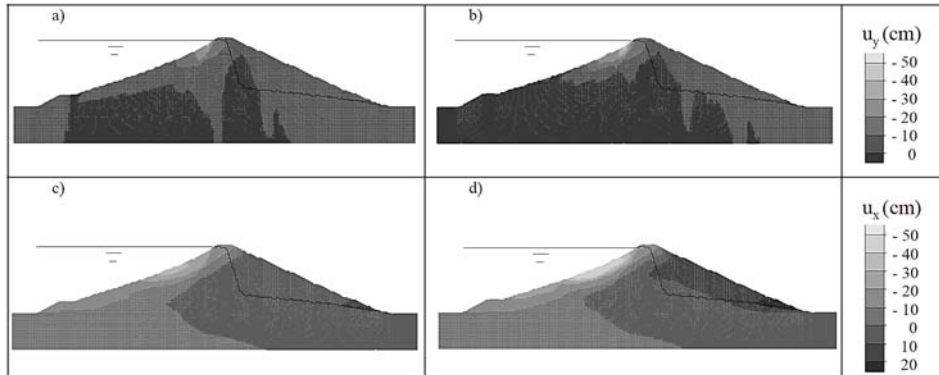


Figure 2-52. Contours of vertical (a,b) and horizontal (c,d) components of permanent displacements computed for the CLS and the LLS (Aliberti et al., 2016).

Permanent displacements are concentrated in the shallowest areas of the dam section and, generally, the larger displacements occur in the upstream shell of the dam, without intersecting the core. The maximum value of permanent displacements was obtained for the LLS in the analyses carried out using input motion #6, probably due to its large energy content (Table 2-9). The largest value of the vertical permanent displacement at the crest of the dam is about 16 cm which is much smaller than the service freeboard.

Albano et al. (2015) carried out a study on the assessment of the seismic performance of a bituminous faced rockfill dam, focusing on the Menta dam case study. A large number of bidimensional calculations were performed on representative sections of the dam (A-A' in Figure 2-53), with few selected analyses performed on a full three dimensional model. In both cases the calculations have been conducted with finite difference codes (respectively FLAC2D and FLAC3D) implementing models (Figure 2-54a and b) which extend to about 80 m below the dam's base and 100 m sideways to include a meaningful part of the rocky foundation, the embankment's body and the bituminous lining.

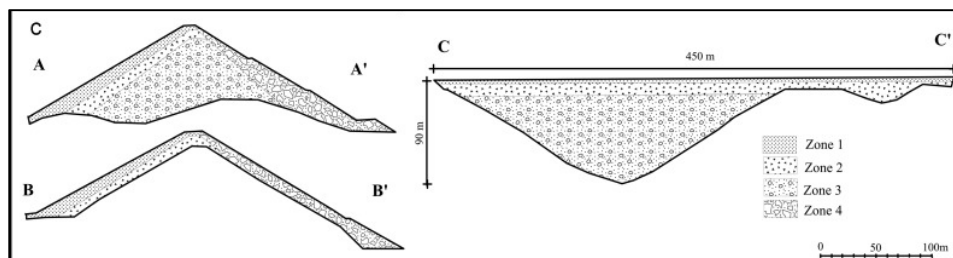


Figure 2-53. Sections of the Menta dam (Albano et al., 2015).

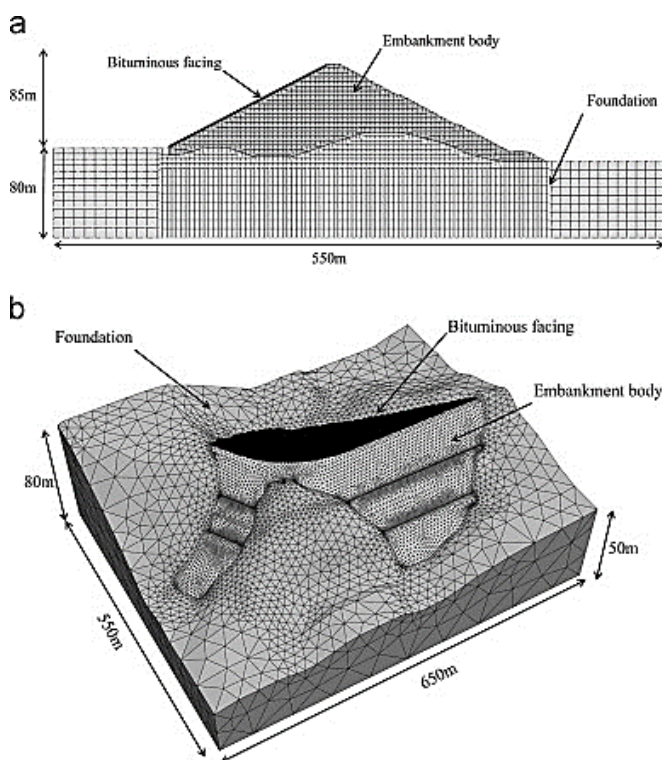


Figure 2-54. Geometrical models built for the two (a) and three (b) dimensional analyses (Albano et al., 2015).

A validation of the choices regarding the geometrical and mechanical simulation of the rockfill embankment has been made using a series of dynamic tests performed on four different smaller scale models representative of different dam's sections. Such a goal has been pursued implementing for each test a model with the same characteristics adopted for modelling the real dam (constitutive model, assignment of water pressures and calculation procedure). The dynamic tests were conducted on a vibrating table installed in the centrifuge of the Laboratories of the

California Institute of Technology at Pasadena, assigning an acceleration of 100 g (correspondent to a scaling factor $N=100$) to models five hundred times smaller than in the reality. Therefore, considering this reduction factor and the amplification given by the centrifuge, the dam studied in the centrifuge tests is five times smaller than the real one. An artificial seismic input, representative of the spectrum assumed at the time for the Menta dam, was given at the base of each model and three acceleration time histories were measured by accelerometers placed at different levels in the embankment.

The seismic input assigned to the 2D and 3D models consists of horizontal accelerations parallel to the trace of the section studied in the 2D analysis, i.e. orthogonal to the crest of the main part of the dam in the 3D analyses, being this situation the most critical for the performance of the dam.

The acceleration time histories assigned at the base of the model have been taken from a continuously updated database where earthquakes occurring worldwide are collected [PEER and ITACA].

Selection from this database has been accomplished based on the similarity between the spectrum of the considered event and the one representative of the investigated site. The reference elastic spectra representative of the seismic hazard at the dam's site, computed for a rigid outcrop, have been initially determined from a study performed by Meletti and Montaldo (2007), subsequently adopted by the Italian Code (2008). In particular, the spectra obtained for the two limit states (Damage Limit State, DLS, and Collapse Limit State, CLS, with return periods T_R of respectively 200 years and 3900 years) have Peak Ground Accelerations (PGA) equal to 0.179g and 0.496g, respectively (Figure 2-55).

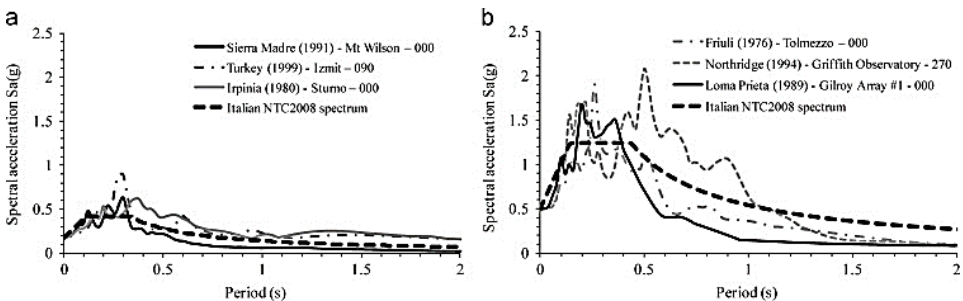


Figure 2-55. Spectral shapes of the selected accelerograms versus those specified by the National Technical Code for serviceability (a) and collapse (b) limit states (Albano et al., 2015)

A total number of 24 calculations has been so far performed with the two-dimensional model assuming full and empty reservoirs and considering minimum and maximum temperature, the latter relevant for the properties of the bituminous lining. Among these calculations, the most troublesome cases have been then re-analyzed with the 3D model, in order to account for the real geometry of the dam. In particular, 3D simulations have been performed only for full reservoir, being this latter the most critical situation, and for the lowest temperatures as this condition produces the major stresses in the lining.

The performed numerical study has shown that the seismic response of the dam is dictated by the concurrence of several factors and that critical conditions can be hardly identified just considering a single one. For instance, the amplification of seismic signals at the embankment crest and the deformation of the embankment are significantly influenced by resonance effects, which depend not only on the intensity and duration of earthquakes but also on the dynamic characteristics of the foundation-embankment system. A significant role is also played by the water in the reservoir, whose presence causes an increase of the rockfill stiffness and a reduction of irreversible phenomena such as permanent settlements.

Most of the deformation occurs on the upper part of the embankment while the lower part, due to its higher stiffness, remains substantially stable. The spectral amplifications produced by a DLS (Koçaely) and a CLS earthquake (Northridge) can be seen in Figure 2-56b and c. From the comparison between the two figures, a higher amplification of the seismic signals produced for the DLS than for CLS condition can be noted, which is a clear effect of the increase of damping with strains.

The most meaningful effects (residual settlements, settlement ratios and integrity of the lining) predicted from 2D analyses have been summarized in Table 2-10 for all the performed calculations. The integrity of the lining has been checked by computing the failure using the function proposed by Desai and by looking at the pattern of maximum tensile deformation obtained in the DLS analysis.

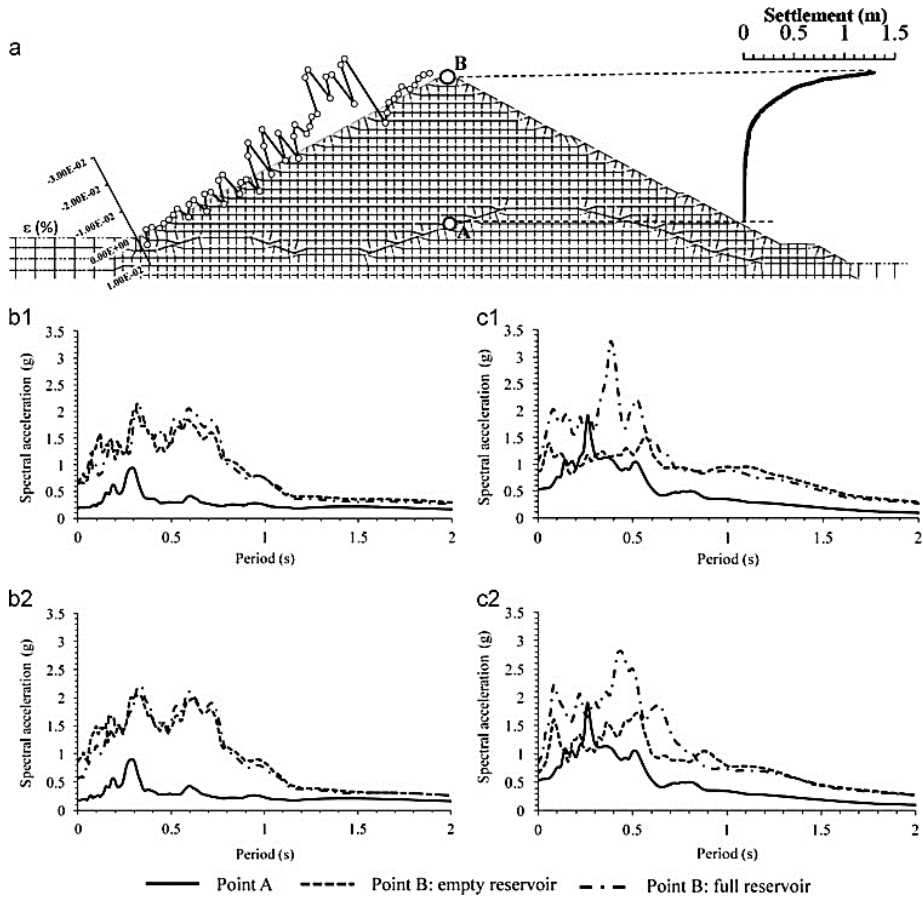


Figure 2-56. Example of two dimensional calculation: (a) cross section with indication of reference points; (b) spectral accelerations for DLS analyses (Koçaeli earthquake) (b1: $T_{min}=1\text{ }^{\circ}\text{C}$; b2: $T_{max}=26\text{ }^{\circ}\text{C}$); (c) spectral accelerations for CLS analyses (Northridge earthquake) (c1: $T_{min}=1\text{ }^{\circ}\text{C}$; c2: $T_{max}=26\text{ }^{\circ}\text{C}$) (Albano et al., 2015).

Limit state		CLS			DLS			
Seismic event		Northridge 1994	Loma Prieta 1989	Friuli 1976	Irpinia 01 1980	Koçaeli - 1999	Sierra Madre 1991	
Empty reservoir	T_{min} (1 °C)	Residual displacement (cm)	271	66.1	114	21.4	22.8	4.7
		Settlement ratio (%)	3.2	0.78	1.34	0.25	0.27	0.06
		Lining cracking (Y/N)	Y	Y	Y	N (0.08 ^a)	N (0.038 ^a)	N (0.022 ^a)
T_{max} (26 °C)		Residual displacement (cm)	326	57.2	112	14.4	11	4.9
		Settlement ratio (%)	3.83	0.67	1.32	0.17	0.13	0.06
		Lining cracking (Y/N)	Y	N	N	N (0.133 ^a)	N (0.042 ^a)	N (0.043 ^a)
Full reservoir	T_{min} (1 °C)	Residual displacement (cm)	139	30.1	52.9	19.3	19.8	3.5
		Settlement ratio (%)	1.63	0.35	0.62	0.22	0.23	0.04
		Lining cracking (Y/N)	Y	Y	Y	N (0.071 ^a)	N (0.063 ^a)	N (0.04 ^a)
T_{max} (26 °C)		Residual displacement (cm)	141	26.1	73.7	12.3	11.5	6.3
		Settlement ratio (%)	1.65	0.31	0.87	0.14	0.13	0.07
		Lining cracking (Y/N)	N	N	N	N (0.074 ^a)	N (0.101 ^a)	N (0.073 ^a)

^a Maximum tensile strain of the lining expressed as percentage.

Table 2-10. Main results of the two-dimensional calculation (Albano et al., 2015).

In comparison with the two-dimensional plane strain conditions, the three dimensional simulations better capture the mechanisms governing the propagation of seismic waves and the deformation of the whole foundation-embankment-lining system. A first interesting effect visible from the performed 3D calculation concerns the modification (filtering and amplification) of the waves traveling through the system, which is induced by the combination among mutual geometrical arrangement of the different portions of the dam, mechanical properties of the materials, and frequency content of the applied motion. Such a coupling can be seen from the comparison between the spectra at the basement and the top of the embankment (Figure 2-57).

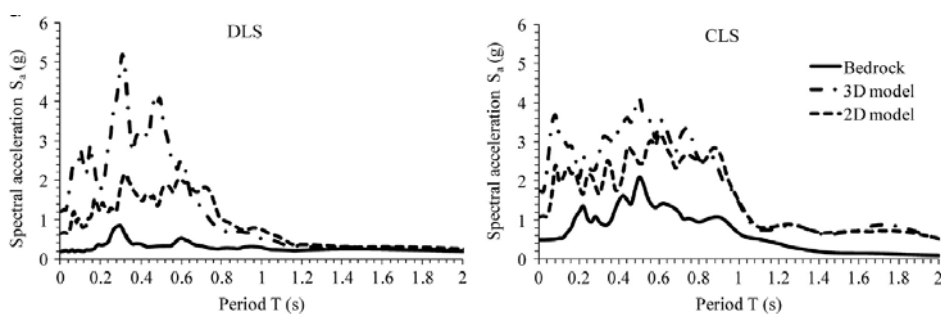


Figure 2-57. Spectral accelerations at the reference sections (Albano et al., 2015).

The time histories of the horizontal (positive when directed downstream) and vertical (positive when directed downward) displacements components for a point located at the crest of the dam (white triangle in Figure 2-58) indicate that deformation takes place increasingly during the seismic events but suddenly stops after earthquakes have ceased. This result is particularly important as it indicates that the embankment body is substantially stable and that an uncontrolled sliding of the slope is unlikely. In addition, the computed residual vertical displacements (equal to 0.1 and 0.76 m for DLS and CLS, respectively) are in both cases significantly lower than the available freeboard.

It is finally not trivial to notice that the residual vertical and horizontal displacements computed with 3D analyses are generally lower than those computed with the 2D model (reported in the same plots for reference). Such a result, certainly induced by the presence of the rigid rocky abutments, implies that simplified bi-dimensional analyses are substantially conservative.

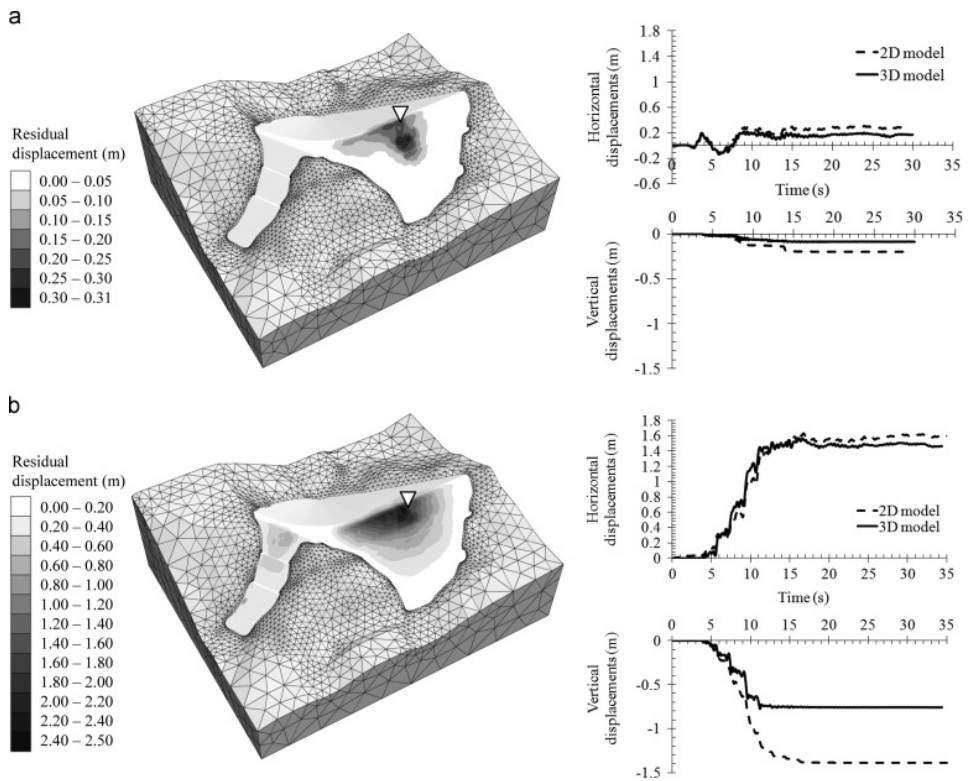


Figure 2-58. Pattern of residual displacements and time history of horizontal and vertical displacements for a point on the dam's crest (white triangle) for DLS (a) and CLS (b) (Albano et al., 2015).

2.3. PERFORMANCE BASED SEISMIC DESIGN (PSBD) FOR DAMS

In the last years, the geotechnical design criteria moved from a simple force-strength approach to a multi-level probabilistic performance criteria called Performance Based Seismic Design (PSBD).

The most important design objective is the safety against collapse, but at the same time, performance in terms of functionality and economy have assumed a central role in the design criteria.

The PSBD is a design criteria whose goal is the achievement of specified performance targets when the structure is subjected to a defined seismic input. The specified performance target could be a level of displacement, level of stress, maximum acceleration, mobilized strength.

The use of PBSD is definitely less widespread in geotechnical engineering than in structural engineering. Anyway, since the sixties the geotechnical community has been used to apply analytical methods for predicting permanent displacements in earth structures under seismic loading, which is basically a performance criterion as opposed to the classical concept of limit equilibrium. Even if from the last decade of the XX century geotechnical engineers from different countries have promoted the development of PBSD methods (Plank, 2000), the application of this philosophy to earth and rockfill dams has been pursued only in limited cases. Among various factors to be considered, significant uncertainties exist in the definition of the performance targets, since these structures include different components (foundation, embankment, waterproofing and drainage systems, pipelines and operating machines), so tightly interconnected that evaluating the consequences of a damage on a single part is impossible without considering the whole system. Furthermore, it is widely acknowledged that prediction of the seismic response of earth structures, even with the most modern numerical tools, is not easy due to a number of factors, among which three dimensional geometries (Prevost, Abdel-Ghaffar, & Lacy, 1985), nonlinear irreversible stress-strain response of the soil materials (Sica et al., 2008), interaction between different materials, e.g. core-shell interaction in zoned dams, or embankment body-bituminous facing for rockfill dams (Costanzo et al., 2011; Albano, 2013). Some examples of predictions on dams inspired to the principles of PBSD can be found in the literature (Sica & Pagano, 2009; Tani, Tsukuni, & Shiomi, 2009; Elia et al., 2011; Albano, 2013; Pelecanos et al., 2015).

PBSD criteria can be applied to both new and existing dams (i.e. designed with conventional methods) with the main goal to predict their performance under static and seismic loading because of the high risk associated to relevant social, economic and environmental consequences of failure.

Applying the PBSD approach to an existing earth dam means the reconstruction of the whole building process (excavation, foundation reinforcement and/or waterproofing, origin and placement of materials) and soil behaviour by collecting the available experimental investigations or performing new ones.

The procedure proposed for the application of PBSD on existing earth dams could be defined into the following four steps (Albano, 2013):

- definition of performance objectives (depending on the importance of the dam);
- selection of the input accelerograms;
- setting up the numerical model of the dam (geometry, boundary conditions, selection and calibration of constitutive model);
- evaluation of dam response.

2.3.1 DEFINITION OF PERFORMANCE OBJECTIVES

The definition of adequate performance objectives consists in a clear statement of limit conditions to be avoided with prescribed levels of probability (or return periods). Generally this objective can be achieved only after a cost benefit analysis depending on the type and importance of the new structure, the consequences of damage and repair costs. Selection of performance objectives for existing dams is not straightforward but depends on the type of structure to be studied. International codes and, more recently, Italian codes (M.LL.PP., 2008; M.I.T., 2014) have introduced PBSD concepts for the design of new structures. With regard to existing earth and masonry dams, specific guidelines have been proposed (C.S.LL.PP., 2009; M.I.T., 2014), which give a clearer definition of the performance objectives with identification of different limit states. In particular, a correspondence is established between the limit states defined in the Eurocode 8 (EC8) and the limit conditions not to be attained by the dam. Furthermore, each of these conditions is related to a tolerated probability of failure P_{V_R} that, according to the expected life of the dam, gives the return periods to be assigned in the analysis (Table 2-11) according to the following relation:

$$T_R = -\frac{V_R}{\ln(1 - P_{V_R})} \quad (2.9)$$

where V_R is the reference period defined by Italian regulations as the product between the expected life of the dam, V_N , and the usage coefficient, C_U (§2.4 M.LL.PP., 2008)

For every limit state, a corresponding limit condition is defined, such limit condition must not be attained in order to satisfy the corresponding limit state.

The Operative Limit State (OLS) and Damage Limit State (DLS) are defined serviceability limit states and, for these limit states, the dam must retain all the functionalities. The Life-save Limit State (LLS) and Collapse Limit State (CLS) are ultimate limit states against which the dam may suffer damages but it is still able to retain water (no collapse) and to control the reservoir level.

LIMIT STATE		P_{VR}
Serviceability limit state	OLS – Operational Limit State	81%
	DLS – Damage Limit State	63%
Ultimate limit state	LLS – Life Safety Limit State	10%
	CLS – Collapse Limit State	5%

Table 2-11. Limit states definition and corresponding probability of failure (P_{VR}).

Generally, the safety assessment of reservoirs shall be carried out with refer to the following conditions:

1. normal operation (facilities suffer limited damages but the reservoir level can be controlled);
2. repairable damage, no uncontrolled release of water (slopes suffer local instabilities but the stability of the embankment is ensured; facilities are damaged without uncontrolled release of water);
3. irreparable damage, no uncontrolled release of water (like in point 2);
4. damage that causes the uncontrolled release of water, or otherwise risk of loss of human lives (cracks or excessive deformations of embankment and/or foundation cause uncontrolled seepage and/or overtopping; damage of facilities affects the capability to control the reservoir level);
5. collapse of the structure (global instability or liquefaction of embankment and/or foundation).

The OLS is defined by exiting condition 1.

The DLS is defined by the transition from state 2 to state 3.

The LLS is defined by the achievement of condition 4.

The CLS is defined by the achievement of condition 5.

According to the Italian codes (M.LL.PP., 2008; C.S.LL.PP., 2009; M.I.T., 2014), it is possible to avoid verification of the operational limit state (OLS) only for non-strategic dams.

2.3.2 DEFINITION OF THE SEISMIC HAZARD

The use of recorded accelerograms is allowed for dynamic analysis of geotechnical systems, provided that their choice is representative of the seismicity of the area and adequately justified on the basis of seismogenic sources, magnitude and distance from the source. The above factors determine the maximum horizontal acceleration expected at the site.

Several studies have been published proposing methods for identifying earthquake scenarios that can be derived through seismic hazard analysis (SHA), which is linked to the estimation of some key measures of strong ground motion expected to occur in a pre-defined time interval at a given site (Gupta, 2002). There are two basic methodologies for SHA, namely the deterministic and probabilistic approaches.

In the deterministic seismic hazard analysis approach (DSHA), strong-motion parameters are estimated for the maximum credible earthquake, which is assumed to occur at the closest possible distance from the site of interest (the magnitude and distance combination are fundamental in record selection). In this approach the seismotectonic setting of the surrounding area and all available data on past earthquakes of this region should be known (Krinitzsky, 1995; Romeo et al., 2000).

DSHA involves the assumption of a particular seismic scenario upon which a ground motion hazard evaluation is based.

When applied to structures for which failure could have catastrophic consequences, such as large dams, DSHA provides a straightforward framework for evaluation of the worst-case ground motions. However, it

provides no information on the likelihood of occurrence of the earthquake (Kramer, 1996).

On the other hand, if probabilistic seismic hazard analysis (PSHA) is employed to estimate earthquake loads, definition of the design earthquake scenario is no longer straightforward. More specifically, PSHA carries out an integration over the total expected seismicity during a given exposure period to provide an estimate of strong-motion parameters with a specified confidence level (Cornell, 1968; Algrmissen et al., 1982; Reiter, 1990; Anderson et al., 1978; Krinitzky, 1998). By performing PSHA in order to generate hazard curves, i.e., plots of spectral acceleration for various return periods, a site-specific uniform hazard response spectrum can be calculated (Malhotra, 2006) that is used for establishing spectral matching with a preselected family of records.

In short, the results of a SHA are needed by engineers to face the problem of selecting and scaling recorded accelerograms (Evangelos et al., 2011).

2.3.3 DEFINITION OF THE SEISMIC INPUT PARAMETERS

The selection of a series of real accelerograms, to be applied in the dynamic analysis of existing dams, is typically made as follows:

- Estimation of PGAs for selected return periods at the reference site;
- Disaggregation of seismic hazard for the reference site;
- Selection of a series of accelerograms (spectrum compatibility criterion).

For the selection of adequate seismic input, it is important to define a return period associated to the selected limit state. The return period is connected to the reference period (V_R) (Table 2-12 and Table 2-13).

In order to evaluate the reference period, the geotechnical engineer must assign to the dam a category, V_N , (Smaller dams: if the dam height < 15 m and the reservoir volume < 1000000 m³; Large dams: if the dam height > 15 m or the reservoir volume > 1000000 m³) and a function, C_U , (strategic, relevant or normal).

According to Italian regulation, an existing dam is an “embankment that has, at the date of the safety assessment and / or intervention project, the structure completely realized” and its nominal life V_N can be assumed equal to 50 years.

Dams	V_N (years)	C_U	V_R (years)
Strategic	≥ 50	2.0	100
Relevant		1.5	75
Normal		1.0	50

Table 2-12. Table H1, Nominal life V_N , coefficient C_U and reference period V_R for the classifications of dams (MIT 2014).

Dams	OLS	DLS	LLS	CLS
	$P_{V_R}(\%) = 81$	$P_{V_R}(\%) = 63$	$P_{V_R}(\%) = 10$	$P_{V_R}(\%) = 5$
Strategic	60	100	950	1946
Relevant	45	75	710	1460
Normal	30	50	475	975

Table 2-13. Return periods for every limit state and for classification of dams (MIT 2014).

2.3.3.1 Estimation of PGAs for selected return periods

For the determination of PGA for a site, recently a seismic hazard map of Italy has been created with the ESSE1 project (Meletti, 2007). By applying a probabilistic hazard analysis, the entire Italian territory has been discretized with a regular grid of 0.05° and, for every grid point, various shaking parameters have been estimated and some thematic maps have been created. These maps report two shaking parameters: a_g , the maximum acceleration value on flat rock soil (PGA) (Meletti and Montaldo, 2007); and $S_e(T)$, the elastic response spectrum, expressed in terms of accelerations, as a function of the period T (Montaldo and Meletti, 2007). The a_g maps have been defined for different exceedance probabilities in 50 years (Figure 2-59); the $S_e(T)$ maps have been defined for the same exceedance probabilities but also for different periods.

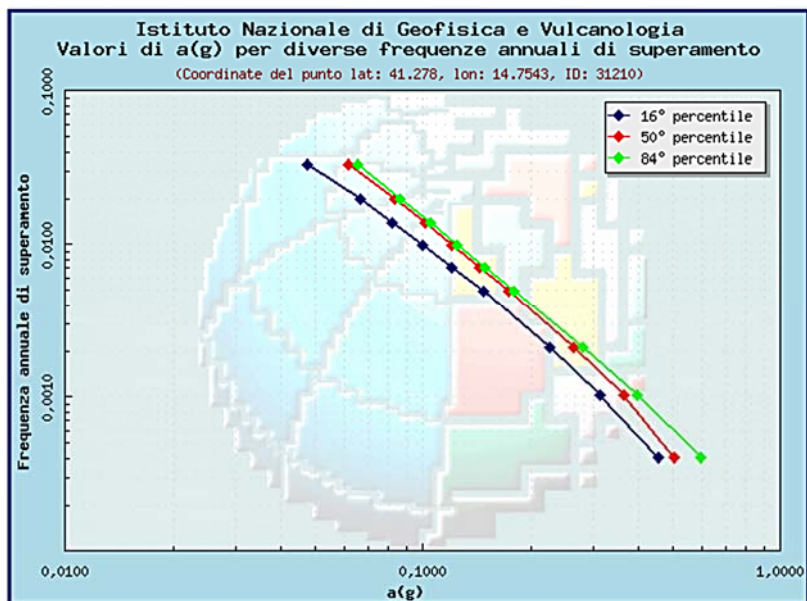


Figure 2-59. a_g values for different overcoming annual frequencies.

2.3.3.2 Disaggregation

Since earthquake magnitude (M) and distance (R) (in km) of the rupture zone from the site of interest are the most common parameters related to a seismic event, it is evident that the simplest selection procedure involves identifying these characteristic (M , R) pairs.

Seismic hazard disaggregation (McGuire, 1995; Bazzurro and Cornell, 1999) provides insights into the earthquake scenarios driving the hazard at a given ground motion level. The work proposed by Spallarossa and Barani (2007) presents the disaggregation at each grid point of the Italian probabilistic seismic hazard map, which was defined by Gruppo di Lavoro MPS (2004). The work is focused on hazard values corresponding to the 50th percentile of the hazard distribution obtained by using a specific logic tree (Gruppo di Lavoro MPS, 2004). The Italian seismic hazard map, indeed, was not developed in terms of the mean hazard values but in terms of the median hazard. Thus, the disaggregation is performed using the inputs along the logic tree path that provided hazard values closest to the reference 50th percentile hazard. Peak ground horizontal acceleration (PGA) values (for rock conditions) corresponding to different mean return

periods are disaggregated by magnitude and distance (M, R). The maps presented by the authors is helpful for selecting ground motion records for design and/or dynamic analyses (i.e. numerical ground response analyses).

The data and maps available are referred to an exceeding probability of 50 years, or rather have been evaluated with reference to $V_R = 50$ years. This category includes ordinary structures ($V_N \geq 50$ years) belonging to the user Class II ($C_U = 1$).

The use of the available data is possible for any class of structure and its reference life, using the exceeding annual frequency λ (1/years), which is the reverse of the return period, and then referring it to the exceeding probability in 50 years (Figure 2-60).

Deliverable D2, <http://esse1.mi.ingv.it/d2.html>

Accesso ai dati e alle mappe relative

Probabilità di eccedenza in 50 anni	Corrispondente periodo di ritorno	Corrispondente frequenza annuale di superamento	Mappa (cliccare per vedere l'ingrandimento)	Dati (cliccare per scaricare il file zippato)
81%	30	0.0332		 (file zip - 631 kb)
63%	50	0.0199		 (file zip - 642 kb)
50%	72	0.0139		 (file zip - 651 kb)
39%	101	0.0099		 (file zip - 657 kb)
30%	140	0.0071		 (file zip - 650 kb)
22%	201	0.0050		 (file zip - 666 kb)
10%	475	0.0021		MPS04 zonesismiche.mi.ingv.it
5%	975	0.0010		 (file zip - 682 kb)
2%	2475	0.0004		 (file zip - 686 kb)

Figure 2-60. Access point for data and maps according to the study of Meletti and Montaldo (2007) (<http://esse1.mi.ingv.it/d2.html>).

2.3.4 SELECTION OF ACCELEROGRAMS

According to Italian technical standards (DM 14.01.2008) "*limit states, both ultimate and serviceability, can be verified by use of accelerograms, or artificial or simulated or natural. Each accelerogram describes a component, horizontal or vertical, of the seismic action; the set of three components (two horizontal, mutually perpendicular and one vertical) constitutes a group of accelerograms.*"

Artificial accelerograms are generated with dynamic random methods implemented in different computer codes such as SIMQKE (Gasparini and Vanmarcke, 1976) or BELFAGOR (Mucciarelli et al., 2004). The algorithms allow to control maximum amplitude, frequency content and duration, in such a way as to be fully consistent with the target values ('target') of a_g and $S_a(T)$. The DM 14.01.2008 requires that the compatibility requisite with the response spectrum (for a standard structural damping $\xi = 5\%$) is satisfied with a maximum deviation (in fault) of 10%. Despite random methods produces records compatible with the code prescriptions, some studies demonstrate that the number of cycles or the signal energy could be far from values of a real record, producing an incorrect response of nonlinear systems (Carballo and Cornell, 2000). So the use of artificial accelerograms is not allowed in dynamic analyses of geotechnical systems.

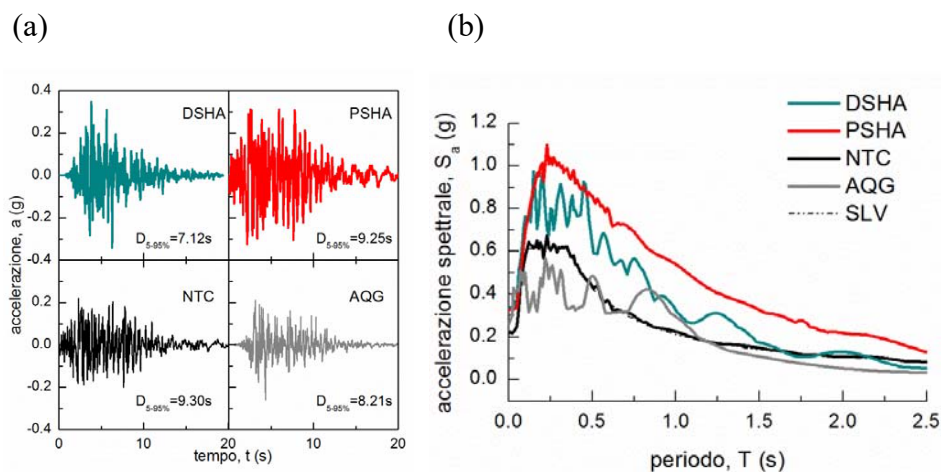


Figure 2-61. Artificial accelerograms generated by several approaches used for the site seismic response analyse in the L'Aquila valley (a); acceleration response spectra compared with the LLS target spectrum (b) (Silvestri and d'Onofrio, 2014).

Simulated accelerograms (or 'synthetic') typically originate from modeling aimed at DSHA analysis over very wide areas, simulating the seismogenic

mechanism and seismic waves propagation from very large depth up to the surface; they contain a priori the compatibility requirements for the reference seismic event. Reconstruction of large-scale models that integrate source mechanisms and propagation, however, requires involving of seismic-tectonic and geological expertise, and the use of experimental resources such as deep geophysical surveys, and computational expertise as parallel computing systems. So these instruments appear excessive for the design of a single ordinary structure, while they are justifiable for the design of major infrastructure, as well as for microzonation studies (Silvestri et al., 2014).

In contrast to artificial accelerograms, synthetic ones can simulate better natural accelerograms, as shown in Figure 2-62, in which two signals used to simulate the seismic response to S. Giuliano di Puglia are compared ($M_w = 5.7$).

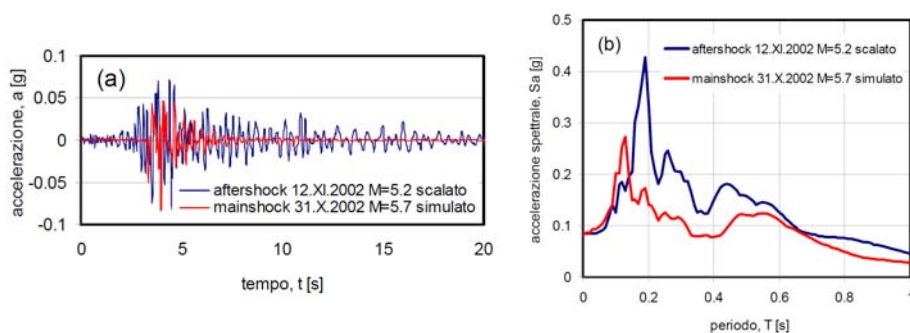


Figure 2-62. Accelerograms (a) and acceleration response spectra (b) of a synthetic signal and an aftershock scaled to the same maximum amplitude, used for the simulation of the mainshock of earthquake of Molise (Silvestri and d'Onofrio, 2014; modified Puglia R., 2008).

Registered accelerograms contain the natural characteristics of seismic phenomena and are the only one allowed to run dynamic analysis; if they are carefully selected they should be consistent with the seismic hazard assessment. That because they could reproduce the:

- seismogenic characteristics of the source (magnitude and fault mechanism);
- propagation characteristics (distance, acceleration amplitude and frequency content).

Compared to the past, there is a growing availability of on-line catalogs that provide free access to a large amount of recordings. (PEER, 2010) (ITACA, 2010), but one potential drawback of this method is that it is difficult to find compatible records especially for very strong motions. This approach nowadays is widely adopted in the literature regarding earth dams and is the best choice for a dynamic analysis. In order to select the appropriate set of natural accelerograms, a spectrum compatibility criterion must be used based on following indexes (Bommer and Acevedo, 2004):

- An amplitude scale factor

$$F_S = \frac{a_{\max,n}}{a_{\max,r}} \quad (2.10)$$

where $a_{\max,n}$ is the PGA provided from the seismic hazard map and $a_{\max,r}$ is the peak acceleration value of the selected time history;

- A spectral shape factor, that represents the compatibility of the frequency content by using the measure of the deviation between the spectral shapes in a fixed range period

$$D_{rms} = \frac{1}{n} \sqrt{\sum_{i=1}^n \left(\frac{S_a(T_i)}{a_g} - \frac{S_{ar}(T_i)}{a_r} \right)^2} \quad (2.11)$$

that is the standard deviation between “spectral shapes” defined for n periods T_i . In the equation n is the number of period set which the spectral shape is specified, $S_a(T_i)$ is the spectral acceleration of the record at period T_i , $S_{ar}(T_i)$ is the target spectral acceleration at the same period value, while a_g and a_r are the peak ground acceleration of the record and the zero-period anchor point of the target spectrum, respectively. A small value of D_{rms} indicates closer matching between the shapes of the record and target spectra. In general, the value of D_{rms} depends on the size of the earthquake record data bank and the number of records required. It is also dependent on the period range of interest that must be specified for spectral matching, with a shorter range being preferable to a longer one.

According to Bommer and Acevedo (2004), the upper and lower limits of the scale factor should be equal to 0.25 and 4, and preferably F_s must be contained in the range 0.5-2.

Katsanos et al. (2011) highlighted that the D_{rms} is dependent on the period range of interest specified for spectral matching, with a shorter range being preferable to a longer one. For instance, Bommer et al. (2003) noticed that when spectral matching was sought in the range of moderate to long periods (0.4–0.8s), the values of D_{rms} required for returning 30 accelerograms were of the order of 0.15. In contrast, when matching was done for shorter periods (0.1–0.3s), D_{rms} was as low as 0.06, which implies spectral compatibility was easier to be achieved.

In some cases, it is impossible or unsatisfactory to suit all the requirements for compatibility with automated procedures, manual selections may be preferred. In this case, it is necessary to resort gradually to searches on parameterized database, for example, first by imposing the satisfaction of the most immediate requirements (e.g. fault mechanism, magnitude, distance from the source) and later carrying out a further 'screening' based on F_s and D_{rms} or similar parameters.

To select a series of accelerograms different tools are available (for example, REXEL by Iervolino et al., 2009).

When a series of recorded accelerograms is selected using the spectrum-compatibility criteria, setting a proper period range, where the average spectrum has to be compatible with the reference one, is very important.

So, the natural period of an earth dam, which depends on the embankment geometry and on the stiffness of the construction materials, has to be evaluated. The following relations can be used:

1. the first, proposed by Prato and Delmastro (1987), applies to triangular and homogeneous sections:

$$T_1 = \frac{2.6 \cdot H}{V_s} \quad (2.12)$$

where H is the dam height;

2. the second, proposed by Dakoulas and Gazetas (1985), returns the period T_n of the n -th mode in the form

$$T_n = \frac{16 \cdot \pi}{(4 + m) \cdot (2 - m) \cdot \beta_n} \frac{H}{V_{S,m}} \quad (2.13)$$

where m is the exponent of the power relation $G(z) = G_H (z/H)^m$ which expresses the stiffness variation with depth, $V_{S,m}$ is the average speed of shear waves in the dam body, β_n is a factor defined once fixed m and n .

The relation proposed by Prato and Delmasto (1987) could provide a quick estimation of the natural period of a homogeneous earth dam, allowing the identification of the proper period range which minimizes D_{rms} . This was confirmed by Costanzo et al. (2011) who applied eq. (2.12) to evaluate the natural period of the rockfill dam (§2.2.2.4). The formula returned a period of 0.55 s; the value is in good accordance with the first fundamental period evaluated with eq. (2.13), 0.56 s.

For a zoned dam, however, the materials that constitute the dam body have different stiffnesses and therefore it is not easy to identify the value of V_S to insert in equation (2.12). As will be shown in chapter 4, considering an average shear velocity for the 2D cross section of a zoned dam allows a fairly accurate assessment of the fundamental period. This procedure will be detailed in Chapter 4 with reference to the selected case-history (Campolattaro Dam).

3. Boundary value problem

Coupled numerical analyses are carried out with the aim to satisfy the whole set of equations encompassing *equilibrium, compatibility, soil-fluid interaction* (soil-water for a 2-phase medium, soil-water-air for a 3-phase medium) and *constitutive models* of the different materials included in the analysis domain.

Appropriate initial conditions and boundary conditions have to be defined to solve the field equation set.

In this Chapter, the mathematical formulation adopted for the solution of the specific boundary value problem of the static and dynamic equilibrium of a dam is presented.

3.1 COUPLED FORMULATION

Let the particles of the medium move with velocity $[v]$. In an infinitesimal time dt , the medium experiences an infinitesimal strain determined by the translations $v_i \cdot dt$. The corresponding components of the strain-rate tensor, ξ , may be written as:

$$\xi_{ij} = \frac{1}{2}(v_{i,j} + v_{j,i}) \quad (3.1)$$

where partial derivatives are taken with respect to components of the current position vector $[x]$.

The equations of motion (3.15), together with the definitions (3.1) of the rates of strain, constitute five equations in seven unknowns (3 + 3 components of the stress and strain rate tensors and 1 velocity). Three additional relations are provided by the constitutive equations that define the behaviour of the particular material at hand. Soil behaviour is usually expressed in the form:

$$[\overset{\sim}{\sigma}]_{ij} = H_{ij}(\sigma_{ij}, \xi_{ij}, \kappa) \quad (3.2)$$

in which $[\overset{\sim}{\sigma}]_{ij}$ is the co-rotational stress-rate tensor, $[H]$ is a function of stress (σ_{ij}), strain-rate (ξ_{ij}) and history of loading (κ). The co-rotational stress rate is equal to the material derivative of the stress as it would appear

to an observer attached to the material point and rotating with it at an angular velocity equal to the instantaneous angular velocity $[\omega]$ of the material. Its components are defined as:

$$[\tilde{\sigma}]_{ij} = \frac{d\sigma_{ij}}{dt} - \omega_{ik}\sigma_{kj} + \sigma_{ik}\omega_{kj} \quad (3.3)$$

in which $d[\sigma]/dt$ is the material time derivative of $[\sigma]$, and $[\omega]$ is the rate of rotation tensor.

When the medium is a three-phase soil, $[\tilde{\sigma}_{ij}]$ is an effective tensor defined as the sum of the total stress and the total pore pressure:

$$[\tilde{\sigma}]_{ij} = \sigma_{ij} + \bar{P}\delta_{ij} \quad (3.4)$$

with $\bar{P} = S_w P_w + S_g P_g$.

The differential equations describing the fluid-mechanical response of a porous multi-phase material are summarized below.

3.1.1. DARCY'S LAW

The fluid transport is described by Darcy's law.

For a two-phase medium with homogeneous, isotropic solid and constant fluid density, this law is given in the form:

$$q_i = -k_{ij}\kappa_r \frac{\partial}{\partial x_j} (P_w - \rho_w g_j x_j) \quad (3.5)$$

where q_i is the specific flow vector, P_w is pore pressure, k is the tensor of absolute permeability of the medium, κ_r is the relative permeability which is a function of fluid degree of saturation S_w , ρ_w is the fluid density, g_i is i -th component of the gravity vector g . The air pressure is assumed to be constant and equal to zero.

When the soil is partially saturated (i.e. three-phase medium), the Darcy's law becomes:

$$q_i^w = -k_{ij}^w \kappa_r^w \frac{\partial}{\partial x_j} (P_w - \rho_w g_k x_k) \quad (3.6)$$

$$q_i^g = -k_{ij}^w \frac{\mu_w}{\mu_g} \kappa_r^g \frac{\partial}{\partial x_j} (P_g - \rho_g g_k x_k) \quad (3.7)$$

where k_{ij} is saturated mobility coefficient, μ is dynamic viscosity and κ_r are the relative permeabilities; the latter are related to degree of saturation S_w and this relation may be expressed by empirical laws, for example, of the van Genuchten form (van Genuchten 1980):

$$\kappa_r^w = S_e^b \left[1 - (1 - S_e^{1/a})^a \right]^2 \quad (3.8)$$

$$\kappa_r^g = (1 - S_e)^c \left[1 - S_e^{1/a} \right]^{2a} \quad (3.9)$$

In those laws, a , b and c are constant parameters and S_e is the effective saturation, that is defined as:

$$S_e = \frac{S_w - S_r^w}{1 - S_r^w} \quad (3.10)$$

where S_r^w is residual wetting fluid saturation.

3.1.2. BALANCE LAWS

For small deformations, the single fluid mass balance may be expressed as

$$\frac{\partial \zeta}{\partial t} = -q_{i,i} + q_v \quad (3.11)$$

where q_v is the volumetric fluid source in [1/sec], and ζ is the variation of fluid content or variation of fluid volume per unit volume of porous material due to diffusive fluid mass transport, as introduced by Biot (1956).

When there are two fluids, water and air, the balance fluid relation (3.11) becomes:

$$\frac{\partial \zeta_w}{\partial t} = -\frac{\partial q_i^w}{\partial x_i} + q_v^w \quad (3.12)$$

$$\frac{\partial \zeta_g}{\partial t} = -\frac{\partial q_i^g}{\partial x_i} + q_v^g \quad (3.13)$$

The balance of momentum has the form:

$$\frac{\partial \sigma_{ij}}{\partial x_j} + \rho g_i = \rho \frac{\partial \dot{u}_i}{\partial t} \quad (3.14)$$

where ρ is the bulk density, and \dot{u}_i is the velocity of the material point.

For a two-phase soil $\rho = (1-n)\rho_s + nS_w\rho_w$ and for a three-phase one $\rho = (1-n)\rho_s + n(S_w\rho_w + S_g\rho_g)$; ρ_s , ρ_w and ρ_g are the densities of the solid and fluid phases, respectively. Note that $(1-n)\rho_s$ corresponds to the dry density of the matrix, ρ_d . The two fluids completely fill the pore space, and we have $S_w + S_g = 1$.

If the acceleration $\partial \dot{u}_i / \partial t$ is zero the equation (3.14) provides static equilibrium of the medium, and so it reduces to:

$$\sigma_{ij,i} + \rho g_i = 0 \quad (3.15)$$

3.1.3. EQUILIBRIUM EQUATION OF THE LIQUID PHASE

The variables that govern the fluid diffusion in a porous medium are the pressure, saturation and mechanical volumetric strains (ε). In particular, the constitutive equation for a single pore fluid, at full saturation is:

$$\frac{\partial P_w}{\partial t} = M \left[\frac{\partial \zeta_w}{\partial t} - \alpha \frac{\partial \varepsilon}{\partial t} \right] \quad (3.16)$$

where M is Biot modulus, α is Biot coefficient and ε is the volumetric strain. The Biot modulus is related to the drained bulk modulus of the porous medium, K , and the fluid bulk modulus, K_w , via n and α , as follows:

$$M = \frac{K_w}{n + (\alpha - n)(1 - \alpha) \frac{K_w}{K}} \quad (3.17)$$

If the compressibility of grains is neglected compared to that of the drained bulk material ($\alpha = 1$), we have:

$$M = \frac{K_w}{n} \quad (3.18)$$

For $S < 1$, the constitutive response of the pore fluid is described by:

a) the saturation equation:

$$\frac{\partial S}{\partial t} = \frac{1}{n} \left[\frac{\partial \zeta}{\partial t} - \alpha \frac{\partial \varepsilon}{\partial t} \right] \quad (3.19)$$

b) the relation between saturation and pore water pressure (retention curve): $P_w = h(S)$;

c) the relation between relative permeability and saturation.

In the interaction between the phases, if there is a single fluid phase it is assumed that the soil may be dry ($S = 0, P_w = 0$) or fully saturated ($S=1, P_w>0$).

For unsaturated soil, eq. (3.22) becomes:

$$S_w \frac{\partial P_w}{\partial t} = \frac{K_w}{n} \left[\frac{\partial \zeta_w}{\partial t} - n \frac{\partial S_w}{\partial t} - S_w \frac{\partial \varepsilon}{\partial t} \right] \quad (3.20)$$

$$S_g \frac{\partial P_g}{\partial t} = \frac{K_g}{n} \left[\frac{\partial \zeta_g}{\partial t} - n \frac{\partial S_g}{\partial t} - S_g \frac{\partial \varepsilon}{\partial t} \right] \quad (3.21)$$

where K_w and K_g are the fluid bulk moduli.

The relation between saturation and pressure is expressed by the retention curve, also known as Soil Water Characteristic Curve (SWCC). A large number of closed-form, empirical equations have been proposed to best fit laboratory data for SWCCs; the formulation implemented in FLAC, the software used in this thesis, is the following Van Genuchten form, here recalled:

$$P_c(S_w) = P_0 \left[S_e^{-1/a} - 1 \right]^{1-a} \quad (3.22)$$

where $P_0 = \frac{\rho_w g}{\alpha}$ is a parameter related to the air entry value and the matrix suction (Appendix A, §A.2) is

$$P_g - P_w = P_c(S_w) \quad (3.23)$$

3.2. SOIL CONSTITUTIVE LAW

Soils can rarely be described as ideally elastic or perfectly plastic. Elastoplastic models form yet the basis for solving most geotechnical engineering calculations. With the advent of powerful computers, the possibility of

performing analyses based on more realistic constitutive soil models has become widely available.

A hierarchical approach is often followed with enriching simple constitutive laws (Mohr-Coulomb) with additional equations aimed at representing other features of soil behaviour, for example, under cyclic conditions.

The aim of this paragraph is to describe those ingredients added to the selected basic soil model, Mohr-Coulomb law, for modelling some particular aspects of soil behaviour in the whole domain or in smaller zones of it.

3.2.1. SIMPLIFIED MODELS

3.2.1.1. *Hysteretic model*

The equivalent-linear method has been in use for many years to calculate wave propagation (time histories and response spectra) in soil and rock under seismic excitation. The method does not *directly* model any nonlinearity of soil because no hysteresis is described, but strain-dependent modulus and damping are roughly considering an equivalent deformation for the entire signal (as in Shake, QUAD4, etc.).

Nowadays the use of hysteretic model is widespread to reproduce the correct physics of soil response under cyclic loading.

A further motivation to use a hysteretic damping model is to overcome the need for additional damping to avoid numerical spurious oscillation in continuous approaches.

Nonlinear stress/strain response implies stiffness modulus degradation. Considering an ideal soil, in which the stress depends only on strain (not on the number of cycles or time), an incremental constitutive relation can be derived from the degradation curve, described by $\bar{\tau}/\gamma = M_S$, where $\bar{\tau}$ is the normalized (on initial stiffness G_0) shear stress, γ is the shear strain and M_S is the normalized secant modulus. That means:

$$\bar{\tau} = M_S \gamma \quad (3.24)$$

Once defined the normalized secant modulus, the normalized tangent modulus may be written as:

$$M_t = \frac{d\bar{\tau}}{d\gamma} = M_s + \gamma \frac{M_s}{d\gamma} \quad (3.25)$$

The incremental shear modulus in a nonlinear simulation is then given by $G_0 \cdot M_t$, where G_0 is the small-strain shear modulus of the material.

Note that the Masing rule (1926) is used when applying the formulation presented in (3.25). For the first loading cycle, both stress and strain axes are scaled by one-half compared to those for subsequent cycles.

Many hysteresis models are developed by noting that the S-shaped curve of modulus versus logarithm of cyclic strain can be represented by sigmoidal curves.

The sigmoidal curves are monotonic within the defined range of strains and have the appropriate asymptotic behaviour, this makes the functions well-suited for the purpose of representing modulus degradation curves. In this model formulation, the secant modulus, M_s , can be expressed as:

$$M_s = y_o + \frac{a}{1 + \exp\left(-\frac{(\log_{10} \gamma - x_o)}{b}\right)} \quad (3.26)$$

where a , b , x_o and y_o are parameters regulating the curvature and position of the $G/G_0 - \gamma$ curve, to calibrate on experimental data.

3.2.1.2. *Dynamic Pore Pressure Generation: Finn and Byrne Models (1991)*

Seismic loads can induce significant volumetric strains in unsaturated soils due to the high compressibility of the pore air. If a soil is saturated, such loading can induce pore pressure rise and effective stress reduction.

Martin et al. (1975) proposed the following incremental shear-volume coupling equation for sand under simple shear loading:

$$\Delta \varepsilon_{vd} = C_1(\gamma - C_2 \varepsilon_{vd}) + \frac{C_3 \varepsilon_{vd}^2}{\gamma + C_4 \varepsilon_{vd}} \quad (3.27)$$

where:

- $\Delta\varepsilon_{vd}$ is the increment of volumetric strain in percent per each cycle of shear strain;
- ε_{vd} is the accumulated volumetric strain from previous cycles in percent;
- γ is the amplitude of shear strain in percent for the cycle in question;
- C_1, C_2, C_3, C_4 are model parameters depending on the relative density.

Byrne (1991) proposed a modified and simpler volume change model with two calibration parameters. The governing equation was expressed as:

$$\frac{\Delta\varepsilon_{vd}}{\gamma} = C_1 \exp\left(-C_2 \frac{\varepsilon_{vd}}{\gamma}\right) \quad (3.28)$$

where C_1 and C_2 are model parameters. The author suggests to express C_2 as function of C_1 , according to $C_2 = 0.4/C_1$, so in eq. (3.28) only one parameter is required. Byrne (1991) has noted that C_1 can be derived from relative densities, D_r , as follows:

$$C_1 = 7600(D_r)^{-2.5} \quad (3.29)$$

Furthermore, using an empirical relation between D_r and the normalized standard penetration test values, $(N_1)_{60}$:

$$D_r = 15[(N_1)_{60}]^{1/2} \quad (3.30)$$

then,

$$C_1 = 8.7[(N_1)_{60}]^{-1.25} \quad (3.31)$$

Having computed the engineering shear strain (see FLAC User's Manual – Section 3: Dynamic Analysis), we insert it into (3.28) and obtain $\Delta\varepsilon_{vd}$. It is then possible to update ε_{vd} , as follows, and save it for use in (3.28).

$$\varepsilon_{vd} = \varepsilon_{vd} + \Delta\varepsilon_{vd} \quad (3.32)$$

We also save one-third of $\Delta\varepsilon_{vd}$ and revise the direct strain increments input to the model at the next cycle:

$$\Delta\varepsilon_{11} = \Delta\varepsilon_{11} + \frac{\Delta\varepsilon_{vd}}{3} \quad (3.33)$$

$$\Delta\epsilon_{22} = \Delta\epsilon_{22} + \frac{\Delta\epsilon_{vd}}{3} \quad (3.34)$$

$$\Delta\epsilon_{33} = \Delta\epsilon_{33} + \frac{\Delta\epsilon_{vd}}{3} \quad (3.35)$$

One effect that has been shown to be very important is the effect of rotation of principal axes: volume decrease may occur even though the magnitude of deviatoric strain (or stress) is kept constant. Such rotations of axes occur frequently in earthquake situations.

3.3. BOUNDARY CONDITIONS (B.C.)

Different boundary conditions should be applied during the various stages of analysis.

Here, details will be provided on the boundary conditions typically adopted under static and dynamic loading conditions for simulating earth dam response.

3.3.1. B.C. FOR THE DAM STATIC ANALYSIS

Either stress or displacement may be applied at the boundary of a solid body. Displacements are specified in terms of prescribed velocities at given points (Eq. (3.14) is not invoked at those points). At a stress boundary, forces are derived as follows:

$$F_i = \sigma_{ij}^b n_j \Delta s \quad (3.36)$$

where n_i is the unit outward normal vector of the boundary segment, and Δs is the length of the boundary segment over which the stress σ_{ij}^b acts.

The applied conditions to numerical model boundaries in the static stage are:

- x and y displacements on the foundation boundaries;
- water flow on the foundation boundaries;
- pore pressure on the foundation boundaries and on the upstream slope boundaries;

As explained in detail in Chapter 4 (§4.3.6), on the upstream slope was initially assigned a hydraulic boundary condition called seepage condition. However, this boundary condition did not work well for the problem at hand. So the issue was overcome by imposing a hydraulic boundary condition suitable for a rapid drawdown, as will be explained in §4.3.6.

3.3.2. B.C. FOR THE DAM DYNAMIC ANALYSIS

Numerical methods relying on the discretization of a finite region of space require that appropriate conditions be enforced at the artificial numerical boundaries. In dynamic problems, fixed or elastic boundaries (used for static problems) cause the reflection of outward propagating waves back into the model (non-absorbent borders). The use of a larger model can minimize the problem, since material damping will absorb most of the energy in the waves reflected from distant boundaries, but this solution leads to larger computational times. The alternative is to use quiet (or absorbing) boundaries. Several formulations have been proposed.

Viscous frontiers, proposed by Lysmer & Kuhlemeyer (1969), are local borders that absorb only the volume waves (P and S) with plane wave front acting normally to the border. They provide an exact solution for the one-dimensional (vertical) propagation of volume waves in a linear elastic medium.

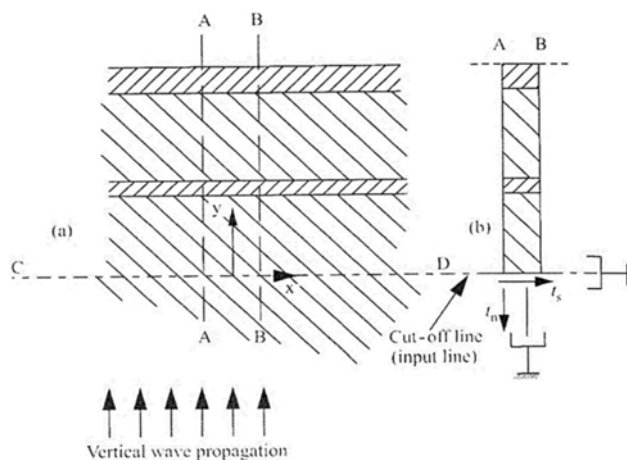


Figure 3-1. One-dimensional propagation of vertical waves: a) 2-D domain; b) 1-D scheme. (Zienkiewicz et al., 1980).

If a subsoil with horizontal stratification is hit by a plane wave front which propagates in the vertical direction, the problem geometry can be considered one-dimensional.

Then, assuming that the medium is linearly elastic, with a single-phase and neglecting volume forces, the equilibrium equation (3.14) becomes:

$$\frac{\partial \sigma_{ij}}{\partial x_j} - \rho \frac{\partial \dot{u}_i}{\partial t} = 0 \quad (3.37)$$

that in the reference system (x, y) of Figure 3-1a, may be expressed in the two equations:

$$\frac{\partial \sigma_{xy}}{\partial y} - \rho \ddot{u}_x = 0 \quad (3.38)$$

$$\frac{\partial \sigma_{yy}}{\partial y} - \rho \ddot{u}_y = 0 \quad (3.39)$$

The stress, σ_{xy} and σ_{yy} , may be expressed through the elastic relationships:

$$\sigma_{xy} = G \frac{\partial u_x}{\partial y} \quad (3.40)$$

$$\sigma_{yy} = \bar{K} \frac{\partial u_y}{\partial y} \quad (3.41)$$

where G and \bar{K} indicate respectively the shear stiffness and the oedometric modulus of soil.

The equations (3.38) and (3.39) then become:

$$\frac{\partial^2 u_x}{\partial y^2} - \frac{\rho}{G} \ddot{u}_x = 0 \quad (3.42)$$

$$\frac{\partial^2 u_y}{\partial y^2} - \frac{\rho}{\bar{K}} \ddot{u}_y = 0 \quad (3.43)$$

Equation (3.42) represents a shear wave that propagates with velocity $V_s = \sqrt{G/\rho}$.

It is the sum of an in-going shear wave, which travel in the positive direction along y (u_{xI}), and out-going shear wave, which travel in the negative direction (u_{xO}):

$$u_x = u_{xI}(y - V_S t) + u_{xO}(y + V_S t) \quad (3.44)$$

Equation (3.43) represents a P-wave travelling with velocity $V_p = \sqrt{K/\rho}$.

It is the combination of an incident wave u_{yI} and an out-going wave u_{yO} for which we have:

$$u_y = u_{yI}(y - V_P t) + u_{yO}(y + V_P t) \quad (3.45)$$

At the border CD the waves that propagate into the interior of the model must be cancelled while outgoing waves u_{xO} and u_{yO} should remain unchanged (radiative condition).

This condition can be reproduced by imposing that along the border CD tangential stress t_x and a normal stress t_y act according to the following relationships:

$$t_x = \sigma_{xy} = \frac{G}{V_S} \frac{\partial u_x}{\partial y} \quad (3.46)$$

$$t_y = \sigma_{yy} = \frac{\bar{K}}{V_P} \frac{\partial u_y}{\partial y} \quad (3.47)$$

Conditions (3.46) and (3.47) correspond to position two viscous dampers in the tangential and normal direction to the border (Figure 3-1b).

The expressed radiative condition can also be applied to bi- or tri-dimensional geometries placing the viscous dampers in each node of the border but, differently from the one-dimensional case, the radiative condition is not exact since it does not simulate the correct transmission of waves impinging obliquely at the border.

3.3.3. APPLICATION OF THE DYNAMIC INPUT

The dynamic input can be applied to a discretized model in one of the following ways:

- a) an acceleration history;
- b) a velocity history;
- c) a stress (or pressure) history;
- d) a force history.

Dynamic input can be applied either in the x- or y-directions corresponding to the xy-axes for the model, or in the normal and shear directions to the model boundary.

One restriction when applying velocity or acceleration input to model boundaries is that these boundary conditions cannot be applied along the same boundary as a quiet (viscous) boundary condition (compare Figure 3-2(a) to Figure 3-2(b)), because the effect of the quiet boundary would be nullified.

To apply the input motion at a quiet boundary, a stress boundary condition is used (i.e., a velocity record is transformed into a stress record and applied to a quiet boundary).

A velocity wave may be converted to a stress wave using the formula:

$$\sigma_{xy} = 2(\rho V_S)v_s \quad (3.48)$$

or

$$\sigma_{yy} = 2(\rho V_P)v_n \quad (3.49)$$

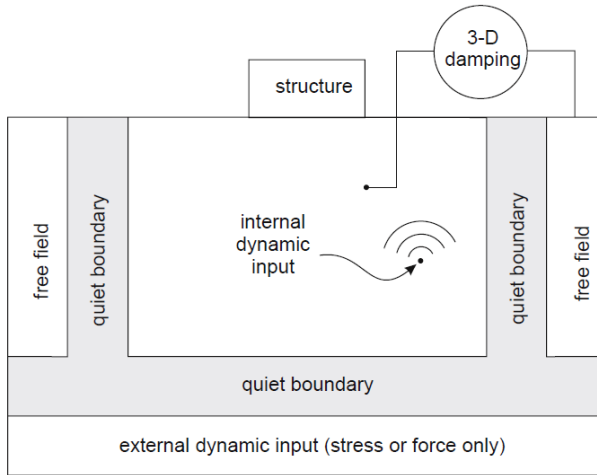
where:

- σ_{yy} is the applied normal stress;
- σ_{xy} is the applied shear stress;
- V_P is the velocity of P-wave propagation through medium;
- V_S is the velocity of S-wave propagation through medium;
- v_n is the input normal particle velocity;
- v_s is the input shear particle velocity.

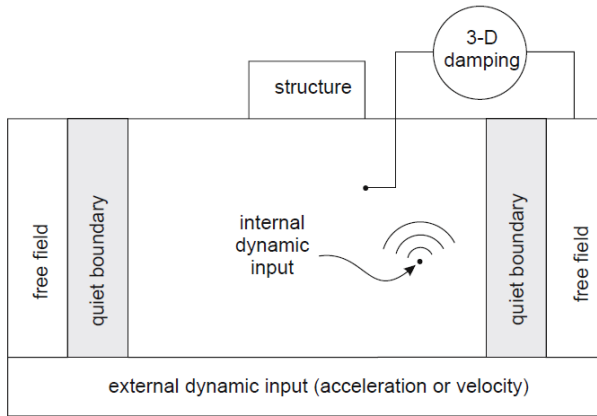
The input requires a factor of two in this relation because $\frac{1}{2}$ of the stress is absorbed by the viscous dashpots.

Mejia and Dawson (2006) showed the difference between the external dynamic input when a flexible or a rigid base is assumed in FLAC (Figure 3-2). According to the authors, a rigid base is only appropriate for cases with a large impedance contrast at the base of the model. While, a compliant base (Figure 3-3) is almost always the preferred option because downward propagating waves are absorbed, while for a rigid base these waves are reflected back into the model. Although the presence of these reflections is not always obvious in complex nonlinear FLAC analyses,

they can have a major impact on analysis results, especially when cyclic degradation or liquefaction soil models are employed.



(a) Flexible base



(a) Rigid base

Figure 3-2. Boundaries and dynamic input (ITASCA, 2005).

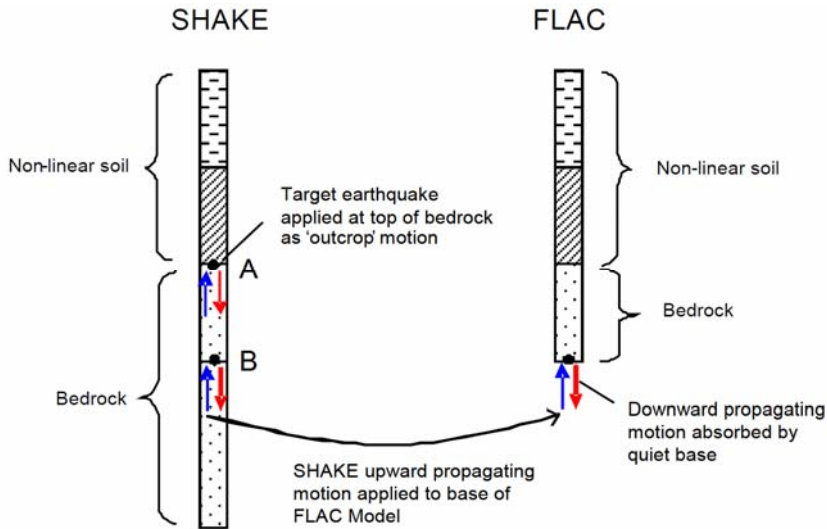


Figure 3-3. Compliant base deconvolution procedure (Mejia et al., 2006).

3.4. SLOPE STABILITY ANALYSIS IN A CONTINUUM APPROACH

For slopes, the factor of safety F_s is traditionally defined as the ratio of the actual soil shear strength to the minimum shear strength required to prevent failure (Bishop, 1955). In 1996 Duncan defined F_s as the factor by which the soil shear strength must be divided to bring the slope to the verge of failure. An obvious way of computing F_s with a finite element or finite difference program is simply to reduce the soil shear strength until collapse occurs. The resulting factor of safety is the ratio of the soil actual shear strength to the reduced shear strength at failure. This reduction technique was used as early as 1975 by Zienkiewicz et al. (1975), and has since been applied by Naylor (1982), Donald & Giam (1988), Matsui & San (1992), Ugai (1989), Ugai & Leshchinsky (1995) and others (Dawson et al., 1999).

The shear strength reduction technique has a number of advantages over the method of slices for slope stability analysis. Most importantly, the critical failure surface is found automatically. Nowadays, with the increasing computational velocity, the technique became a reasonable alternative to the method of slices, and is been used increasingly in engineering practice. A comparison between the different types of

procedures in terms of stability number will be provided at the end of this section.

The procedure to perform slope stability analysis with the strength reduction technique was described by Dawson et al. (1999).

Considering a homogeneous slope made of a linear elastic-perfectly plastic soil with a Mohr-Coulomb yield condition, to perform slope stability analysis with the shear strength reduction technique, simulations are run for a series of trial factors of safety $F_{S,trial}$ with c and ϕ adjusted according to the equations:

$$c_{trial} = \frac{1}{F_{S,trial}} c \quad (3.50)$$

$$\phi_{trial} = \arctg \left(\frac{1}{F_{S,trial}} \operatorname{tg} \phi \right) \quad (3.51)$$

The value of $F_{S,trial}$ at which collapse occurs, can be found more efficiently using bracketing and bisection.

First, upper and lower brackets are established. The initial lower bracket is any $F_{S,trial}$ for which a simulation converges (unbalanced force ratio is less than 10^{-3}). The initial upper bracket is any $F_{S,trial}$ for which the simulation does not converge. Next, a point midway between the upper and lower brackets is tested. If the simulation converges, the lower bracket is replaced by this new value. If the simulation does not converge, the upper bracket is replaced. The process is repeated until the difference between upper and lower brackets is less than a specified tolerance (10^{-3}).

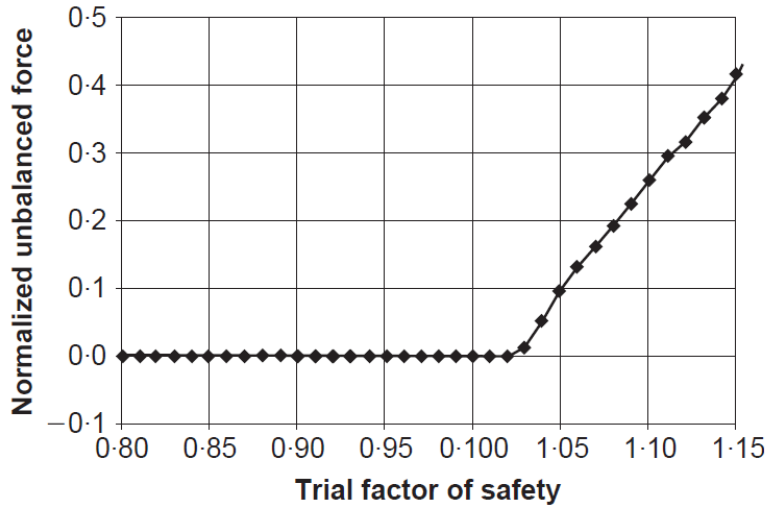


Figure 3-4. Unbalanced force as the trial factor of safety is increased (Dawson et al., 1999).

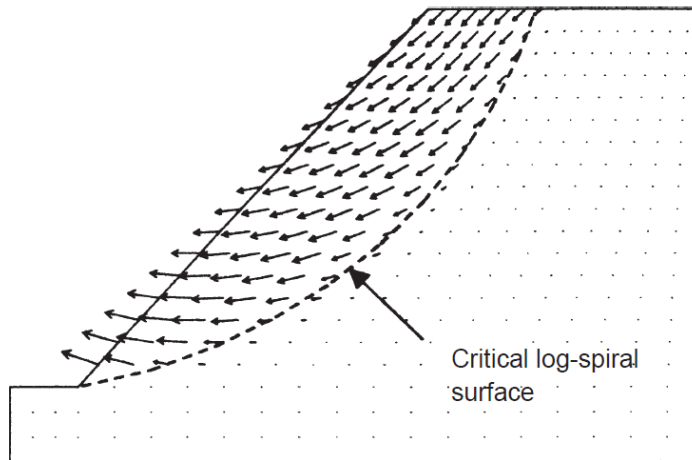


Figure 3-5. Velocity yield at collapse, along with critical log-spiral surface (Dawson et al., 1999).

Dawson et al. (1999) computed slope stability factors with the strength reduction technique and then compared them to an upper-bound limit analysis solution based on a log-spiral failure mechanism (Chen, 1975; Michalowski, 1995). The solutions of the limit analysis are presented in the form of dimensionless stability numbers N_s given by:

$$N_s = \frac{\gamma}{c} H_c \quad (3.52)$$

where H_c is the critical height for a slope with soil unit weight γ and cohesion c . Values of N_s are tabulated for various values of the slope angle β (from the horizontal), the friction angle ϕ and the pore pressure coefficient r_u . The pore pressure coefficient, introduced by Bishop (1954), specifies the pore pressure as a fraction of the overburden stress. The pore pressure u at a depth z below the ground surface is $u = r_u \cdot \gamma \cdot z$.

The analyses were performed for a wide range of slope angles, soil friction angles and pore pressure coefficients (r_u).

Strength-reduction safety factors were close to the limit analysis stability numbers when the numerical mesh was sufficiently refined (Figure 3-6). The similarity between the two solutions, obtained by entirely different methods, supports the widely held view that the log-spiral solution is an exact solution.

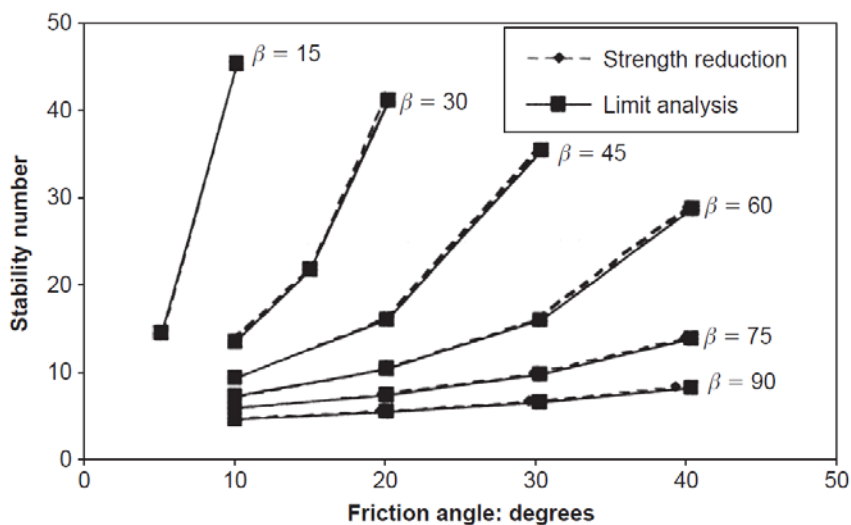


Figure 3-6. Strength-reduction and limit-analysis stability numbers for the $r_u = 0$ case. Fine mesh (Dawson et al., 1999).

4. The case study

In this Chapter the case study selected to study the rapid drawdown of earth dams is drawn in detail.

The geometric and mechanical features of the sample dam are firstly exposed; then, the procedure adopted for simulating the different analysis stages is described.

4.1. CAMPOLATTARO DAM

The Campolattaro dam is a zoned earth dam located in Southern Italy, near the town of Campolattaro (Benevento, Italy). The dam intercepts the Tammaro stream. It is located in an area (Central Appennines) characterized by very high seismicity (Figure 4-1).

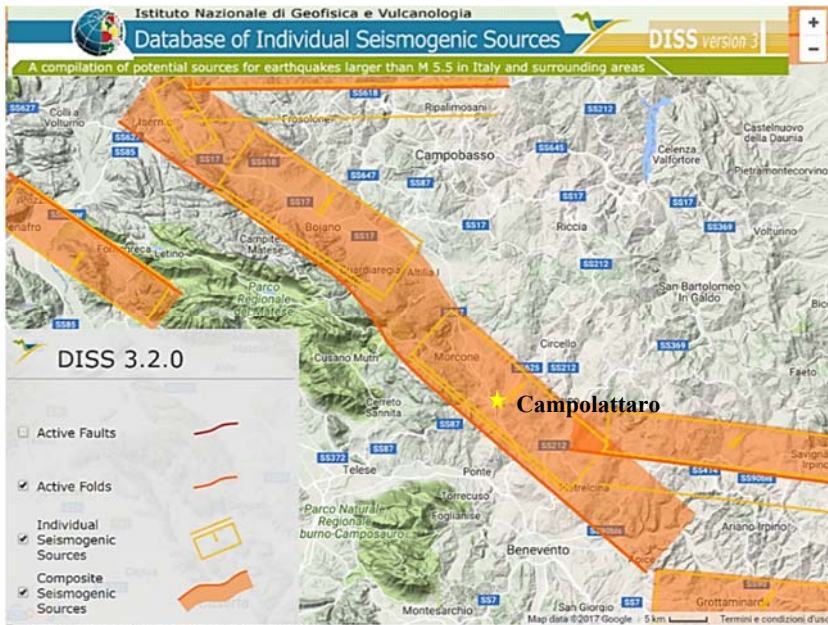


Figure 4-1. Location of Campolattaro in the INGV active faults map (DISS Working Group, 2015).

It is characterized by a maximum height equal to 60 m. The maximum water storage of the reservoir is of about 125 million m³, for a plan dimension of 256 km².

It was built between the 1980s and the 1990s using clayey silt of low plasticity for the core and coarser soils for the shells. The reference cross section, n. 10, is showed in Figure 4-2.

Two sub-vertical drains are interposed between the clayey core and the shells. During construction, the foundation soil mechanical properties were improved by acrylic resin injections, also reducing the soil permeability. Moreover, seepage flow underneath the embankment is prevented by two impervious concrete diaphragms, one under the cofferdam and another under the inspection tunnel of the dam.

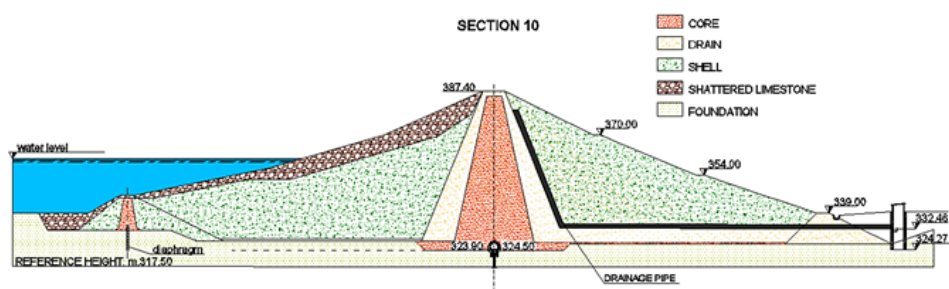


Figure 4-2. Cross section of the Campolattaro dam.

Drillings carried out from the crest of the dam in 2009 allowed to identify the foundation depth under the core; this is located at about 63.5 m from the top, so, for hydraulic watertightness, the core has been deepened about 3.5 m in the foundation plane.

In 1989 a first assessment of dam safety under seismic loading was performed (Progetto Speciale n. 29-20 per la Campania). According to DM 07/03/1981, the town of Campolattaro was included in the medium seismicity zone ($S=9$), with a seismic coefficient $C = (S-2)/100 = 0.07$. However, the designer considered a higher seismicity of the dam site since seismic coefficients of 0.1 and 0.05 in the horizontal and vertical direction were adopted, respectively.

The assessment was carried out by means of the pseudo-static approach, evaluating the dam stability by the limit equilibrium method (Bishop, 1955).

4.2. SOIL MATERIALS

The physical and mechanical characterization of the dam materials is based on the latest campaigns of surveys led in 2009 and 2016.

Investigations on shells and drains were carried out in 2009, while the data available for the core were integrated with the 2016 campaign. The geotechnical characterization for the original design allowed to compare, and sometimes to complete, the required information.

4.2.1. SHELLS

The shells are made of sandy gravel. The dry unit weight and permeability are the mean values derived from the report of the government assistant (official document of 12.02.1999). These parameters are equal to:

- $\gamma_d = 21.09 \text{ kN/m}^3$;
- $k = 1.68 \cdot 10^{-3} \text{ cm/s} = 1.68 \cdot 10^{-5} \text{ m/s}$.

The friction angle of the material, which in the laboratory tests performed in 1984 at the University of Naples "Federico II" was found in the range of $40^\circ - 45^\circ$, has been re-computed by adopting the results of the SPT tests carried out in sections 5, 10 and 13 during the 2009 campaign.

The Schmertmann abacus (1975) and the experimental correlation of Hatanaka and Uchida (1996) were used.

depth z [m]	Section			$N_{\text{SPT},\text{min}}$	γ_d [kN/m ³]	σ'_v [kPa]	Dr [-]	ϕ' [°]	Schmertmann			Hatanaka & Uchida		
	5 N_{spt}	10 N_{spt}	13 N_{spt}						C_n	N_{corr}	ϕ' [°]			
3	100	100	70	70	21.09	63.27	0.8	50	1.14	79.8	59.9			
6	52	100	100	52	21.09	126.54	0.75	48	0.92	47.8	50.9			
9.2	100	41	40	40	21.09	194.03	0.6	43	0.76	30.5	44.7			
12	100	100	140	100	21.09	253.08	0.8	47	0.66	66.2	56.4			
15.5	100	100	100	100	21.09	326.89	0.78	46	0.57	56.9	53.7			
18	26	100	100	26	21.09	379.62	0.3	-	0.52	13.5	36.4			
21	100	100	100	100	21.09	442.89	0.7	-	0.47	46.7	50.5			
23.8	47	66	51	47	21.09	501.94	0.4	-	0.43	20.1	40.0			

Table 4-1. SPT tests in shells and friction angle evaluation.

The values determined on site are higher and close to the one (40°- 45°) provided by laboratory tests carried out in 1984 during the design stage. Therefore the friction angle assumed in the analysis of this thesis is 43°.

The friction angle considered in the design of the dam was $\varphi' = 35^\circ$.

4.2.2. DRAINS

The drains consist of sand with gravel. The dry unit weight and permeability are the mean values derived from the report of the government assistant, considering the lack of recent experimental data. These parameters are equal to:

- $\gamma_d = 19.75 \text{ kN/m}^3$;
- $k = 5.27 \cdot 10^{-4} \text{ cm/s} = 5.27 \cdot 10^{-6} \text{ m/s}$.

No recent data are available for drains, so the parameters adopted in the design stage were considered ($c' = 0 \text{ kPa}$ and $\varphi' = 30^\circ$) for the new computations.

4.2.3. CORE

On the core of the dam extensive investigation has been carried out during design, construction and operation stages.

The results from the 2009 and 2016 survey campaigns are here used to characterize the mechanical behaviour of this soil.

- **2009**

The material is predominantly a clay silt with sand or silty clay with sand, whose physical and mechanical properties were determined by laboratory tests conducted on undisturbed samples taken in sections 5, 10 and 13. These are equal to:

- $\gamma_n = 20.63 \text{ kN/m}^3$;
- $\gamma_s = 26.67 \text{ kN/m}^3$;
- $\gamma_d = 17.38 \text{ kN/m}^3$;
- $\gamma_{\text{sat}} = 20.86 \text{ kN/m}^3$;
- $w = 18.87 \%$;

- $e = 0.54$;
- $n = 34.85 \%$;
- $S_r = 92.62 \%$.

The results of triaxial and shear tests are showed in the following figures.

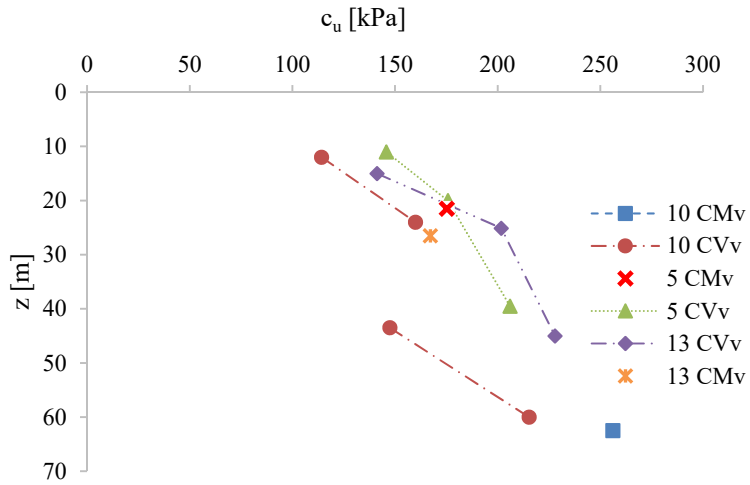


Figure 4-3. Triaxial UU test results, 2009.

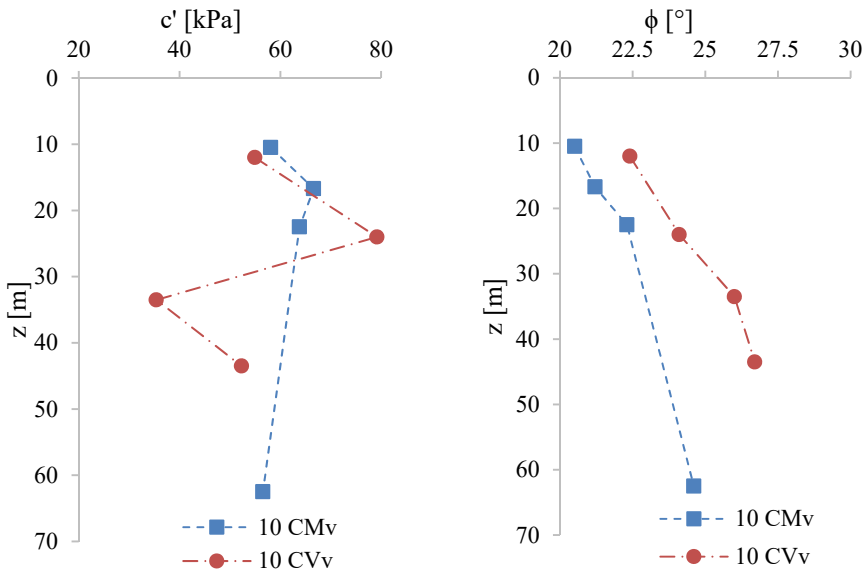


Figure 4-4. Shear test and triaxial CIU test results, 2009.

- 2016

One drilling survey (S1) was performed long the core axis and two undisturbed samples were collected between the depths of 26.5 m and 27.5 m. Table 4-2 summarized the test results.

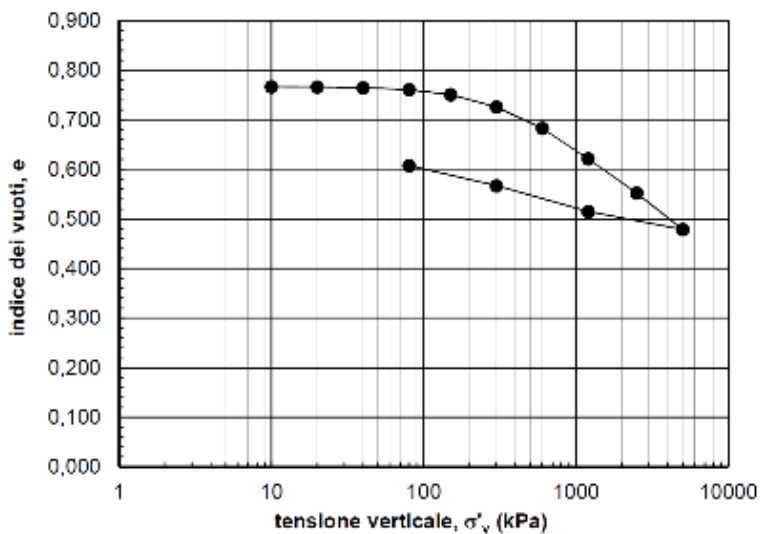


Figure 4-5. Oedometric test result on sample S1-C1, 2016.

Parameter	S1-C1	S1-C2
γ [kN/m ³]	19.97	20.71
γ_s [kN/m ³]	26.30	26.31
γ_d [kN/m ³]	16.62	17.68
γ_{sat} [kN/m ³]	20.30	20.96
w [%]	25.44	17.18
e [-]	0.58	0.49
n [%]	36.81	32.76
S _r [%]	92.87	94.44
w _L [-]	0.609	0.473
w _p [-]	0.223	0.194
I _p [-]	0.386	0.279
I _A [-]	0.857	0.797
c _u [kPa]	182	-
c' [kPa]	23	-
ϕ' [°]	23.5-24	-

Table 4-2. Test results on samples S1-C1 and S1-C2.

A Down-Hole test was also performed (Figure 4-6) along the central axis of the core.

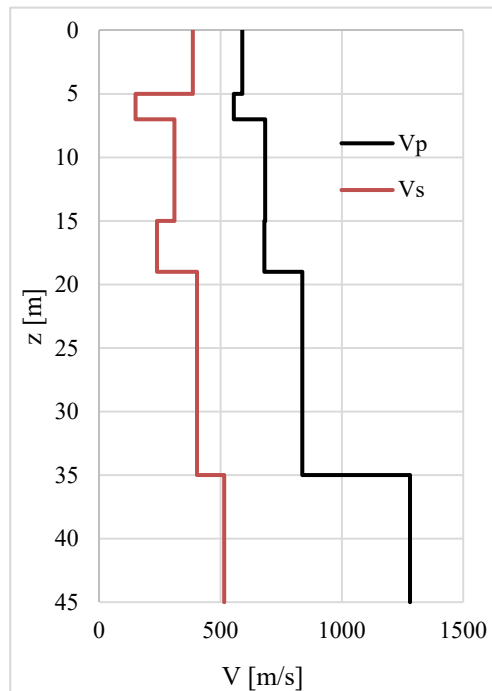


Figure 4-6. Down-Hole results on core (2016).

The V_s profile shows an increasing trend with depth, except for a couple of zones (5-7 m and 15-19 m) due to some inhomogeneity of the core material. In the first 5 m, due to the presence of shell material used as core protection, the V_s is higher.

The values assumed for the core and the cofferdam are:

- $\gamma_d = 17.38 \text{ kN/m}^3$;
- $n = 35 \%$;
- $k = 1.49 \cdot 10^{-11} \text{ m/s}$;
- $c' = 50 \text{ kPa}$
- $c_u = 100 \text{ kPa}$
- $\varphi' = 23^\circ$

4.2.4. FOUNDATION

The foundation soil consists of a silty, clayey-sandstone formation dating back to the Miocene Age. A layer of alluvial deposits, removed during the construction stages, covers the marl formation.

The recent survey campaigns (2009 and 2016) allowed the dam subsoil to be reconstructed. During the drilling of 2016 it was possible to perform a visual analysis of the foundation soils. The drilling has shown:

- a few meters of landfill;
- a yellow sandy silt up to -10 m from g.l.;
- a blue-gray clay layer, thick about 10 m;
- a gray-blue marl clay formation which represents the rigid bedrock.

The results from 2009 and 2016 survey campaigns are used to understand the mechanical behaviour of the material.

- **2009**

The material is predominantly composed of slightly sandy clay silt, whose physical and mechanical properties were determined by laboratory tests conducted on undisturbed samples taken in sections 5, 10 and 13. The following average results were obtained:

- $\gamma_n = 20.53 \text{ kN/m}^3$;
- $\gamma_s = 26.62 \text{ kN/m}^3$;
- $\gamma_d = 17.21 \text{ kN/m}^3$;
- $\gamma_{\text{sat}} = 20.74 \text{ kN/m}^3$;
- $w = 19.30 \%$;
- $e = 0.55$;
- $n = 35.35 \%$;
- $S_r = 93.94 \%$;
- $c' = 130 \text{ kPa}$;
- $\phi' = 22^\circ$;
- $c_u = 200 \text{ kPa}$.

- **2016**

One drilling survey (S2) was performed and four undisturbed samples were collected between the depth of 21 m and 23.7 m.

The soil analysed is a clayey silt of medium to high plasticity.

Table 4-3 summarizes the test result.

Parameter	S2-C1	S2-C2	S2-C3	S2-C4
γ [kN/m ³]	-	-	22.05	22.41
γ_s [kN/m ³]	26.57	26.78	26.69	26.93
γ_d [kN/m ³]	-	-	19.62	19.82
γ_{sat} [kN/m ³]	-	-	22.26	22.47
w [%]	-	-	14.16	13.04
e [-]	-	-	0.36	0.36
n [%]	-	-	26.5	26.37
S _r [%]	-	-	93.78	100
w _L [-]	0.427	0.553	0.539	0.534
w _p [-]	0.173	0.215	0.181	0.208
I _p [-]	0.326	0.339	0.358	0.326
I _A [-]	0.795	0.968	0.896	0.959

Table 4-3. Test results on samples S2-C1, S2-C2, S2-C3 and S2-C4.

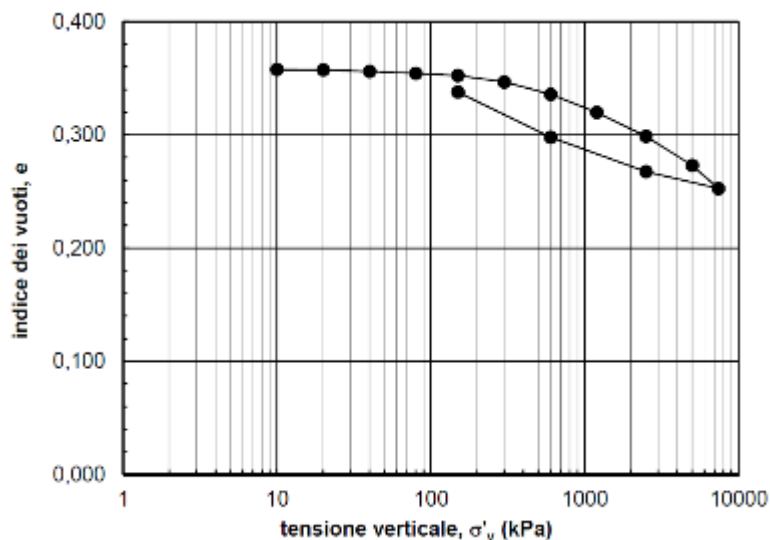


Figure 4-7. Oedometric test result on sample S2-C4 (2016).

The values assumed for the foundation are:

- $\gamma_d = 17.21 \text{ kN/m}^3$;
- $n = 30 \%$;
- $k^1 = 10^{-9} \text{ m/s}$;
- $c' = 130 \text{ kPa}$
- $c_u = 200 \text{ kPa}$
- $\phi' = 22^\circ$

The V_s values estimated by Down-Hole test vary from 300 m/s to 1200 m/s. The rigid rock layer (bedrock) is at the depth of 24 m from the ground level.

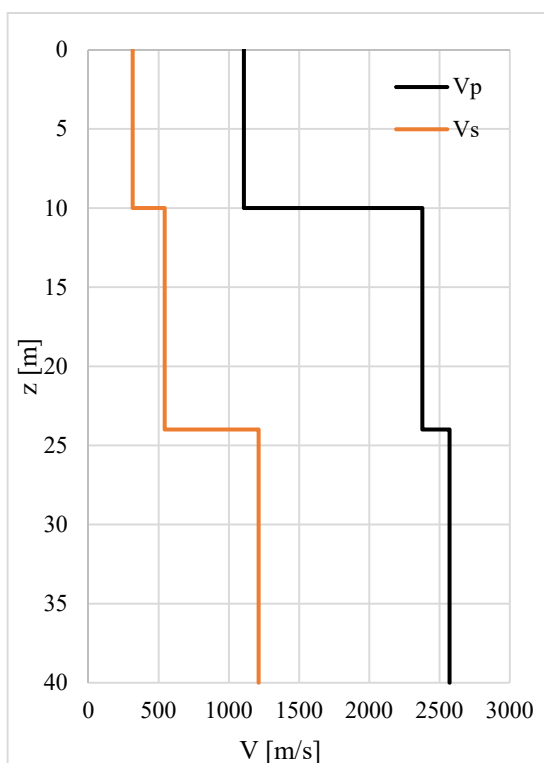


Figure 4-8. Down-Hole results on foundation soil (2016).

The shear velocity of the first 30 m ($V_{s,30}$), according to the current Italian technical regulation (§3.2.2, DM 14.01.2008), is 481 m/s that corresponds to a subsoil category of type B.

¹ Permeability value used in the original design.

4.2.5. MAIN PARAMETERS FOR THE DIFFERENT DAM ZONES

Parameter	γ_d [kN/m ³]	n	c' [kPa]	ϕ' [°]	c _u [kPa]	k [m/s]
Core	17.38	0.35	50	23	100	$1.49 \cdot 10^{-11}$
Shells	21.09	0.5	0	43	0	$1.68 \cdot 10^{-5}$
Drains	19.75	0.5	0	30	0	$5.27 \cdot 10^{-6}$
Foundation	17.21	0.30	130	22	200	10^{-9}

Table 4-4. Synthesis of the soil parameters derived from the in situ investigation.

4.3. NUMERICAL MODELLING

4.3.1. GEOMETRY

The Campolattaro dam has been analysed by a two-dimensional model. The complexity of the geometry (as the case of Camastra or Menta dam), the variability of the foundation level along the longitudinal axis, or the shape of the valley (see El Infiernillo dam) did not required the use of a 3D model.

For the Campolattaro dam the foundation level at the base of the embankment is almost horizontal, with the exception of the extreme sections closer to the abutments. In addition, the considerable abutment-abutment length L (about 700 m) makes the stiffening effects exerted by the abutments negligible. According to Gazetas (1987) who compared the results of 2D vs 3D dynamic analyses of dams in narrow canyon valleys, Campolattaro falls in the case of wide-trapezoidal canyon with a geometric ratio L/H larger than 6. This means that its dynamic response in terms of fundamental period is not affected by the shape of the valley (Figure 4-9).

The geometry of the overall analysis domain must be defined and quantified. Simplifications and approximations may be necessary during this process.

When constructing the finite difference grid, the following items should be considered:

- the geometry of the model should reproduce the real one as accurately as possible;

- in many cases, geometric discontinuities suggest a natural form of subdivision of the model in small regions called zones;
- mesh generation is also influenced by the type of boundary conditions and applied loads.

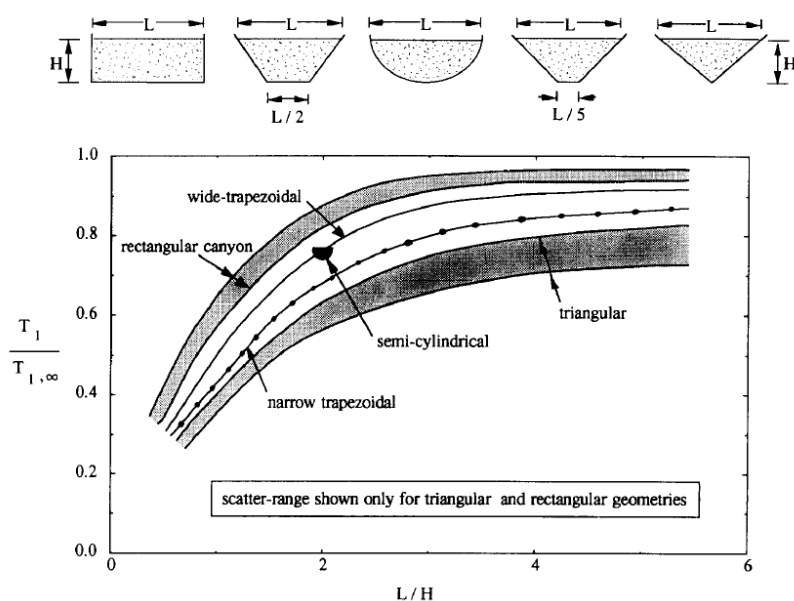


Figure 4-9. Effect of canyon geometry on the fundamental natural period of earth dams (Gazetas and Dakoulas, 1992).

In combination with the above factors, the size and the number of zones depend largely on material behaviour. For linear material behaviour, the procedure is relatively straightforward and only the zones where unknowns vary rapidly need a refined mesh of smaller elements. For nonlinear material behaviour the mesh generation must take into account the boundary conditions, the material properties and, in some cases, the geometry, which may all vary throughout the solution process. In all cases a mesh of regular shaped elements will give the best results. Elements with widely distorted geometries or long thin elements should be avoided (Potts and Zdravkovik, 1999).

For the case at hand, the geometry model was generated assuming the following simplifications:

- the foundation plane was considered horizontal without deeping the core within the foundation;

- the upstream shell was considered made of only one material, identified as shell in Figure 4-2.

The discretized model consists of 3678 elements. The model includes the dam body (width base 338 m, width crest 9 m and height of about 59 m) and its foundation, represented as a rectangular domain of about 1 km and 170 m in the horizontal and vertical direction, respectively (Figure 4-10).

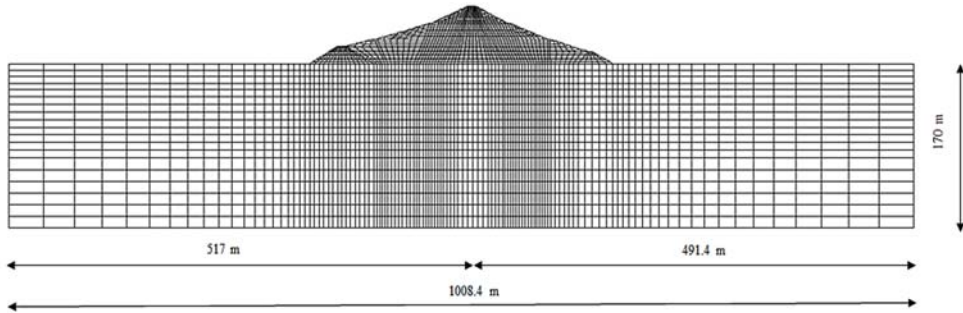


Figure 4-10. 2D grid model.

The mesh adopted for the foundation should prevent numerical distortion of the propagating wave during the dynamic analysis. Both the frequency content of the input wave and the wave-speed characteristics of the soil may affect the numerical accuracy in wave transmission simulation. Kuhlemeyer and Lysmer (1973) show that, for an accurate representation of wave transmission through a model, the element size, Δl , must be smaller than approximately one-tenth to one-eighth of the wavelength associated with the highest frequency component of the input wave:

$$\Delta l \leq \left(\frac{1}{10} \div \frac{1}{8} \right) \lambda_{\min} \quad (4.1)$$

where λ_{\min} is the wavelength associated to the highest frequency component of the input motion and stiffness property of soil media ($\lambda_{\min} = V_s / f_{\max}$).

For dynamic input with a high f_{\max} ($\gg 10$ Hz), the Kuhlemeyer and Lysmer requirement may necessitate a very fine spatial mesh and a corresponding small timestep. The consequence is that accurate analyses may be prohibitively time- and memory-consuming. In such cases, it may be possible to adjust the input by recognizing that most of the energy for the input history is contained in lower-frequency components. By filtering the

history and removing high frequency components, a coarser mesh may be used without significantly affecting the results.

4.3.2. INTERACTION BETWEEN THE PHASES

As far as the interaction between the soil phases in the various zones of the dam is concerned, during construction, reservoir filling, operation and seismic stages, the fine-grained materials (core and filters) were modelled by a two-phase coupled formulation (§3.1), while the coarser materials of the shells were treated by a decoupled approach assuming a completely drained behaviour due to their higher permeability.

During drawdown stages, instead, a three-phase coupled formulation (§3.1) was implemented for the dam soils, with exception of the dam foundation. The soil water retention characteristics were defined through the Van Genuchten (1980) model (§3.1.3, eq. 3.22).

Table 4-5 provides the values adopted for the Van Genuchten soil-water characteristic curve (Figure 4-11) and relative permeability law for the dam soil materials (§3.1.1, eqs. 3.8 and 3.9).

Parameter	a [-]	b [-]	c [-]	P_0 [Pa]	S_r [-]
Core	0.145	0.5	0.5	$6.45 \cdot 10^4$	0
Shells	0.904	0.5	0.5	$1.24 \cdot 10^4$	0.306
Drains	0.507	0.5	0.5	$5.83 \cdot 10^3$	0.436

Table 4-5. Parameters adopted for the hysteretic model of dam and foundation materials.

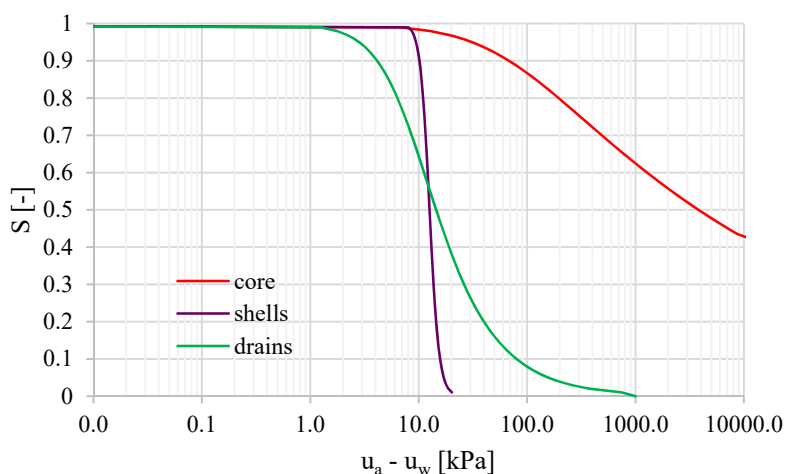


Figure 4-11. SWCCs for dam materials.

4.3.3. CONSTITUTIVE MODELS

In the following paragraph, details on the constitutive laws adopted for each zone of the model will be provided. A hierarchical procedure was adopted. By starting from simple constitutive laws (the Mohr-Coulomb criterion), new ingredients were added for modelling some particular aspects of soil behaviour in the whole domain or in smaller zones of it.

For all material of the dam embankment, the plasticity and failure behaviour were regulated by the Mohr-Coulomb criterion.

The elastic response at small strains (G_0) was related to the confining pressure (p') by the following relation:

$$G_0 = A + B \cdot \frac{p'}{p'_{ref}} + C \cdot \left(\frac{p'}{p'_{ref}} \right)^2 \quad (4.2)$$

where p' represents the mean effective stress, p_r is a reference pressure (1 kPa), A , B and C are parameters calibrated on literature or experimental results.

For the shells and filters of Campolattaro dam, measurements carried out in the shells of the Camastra dam using the SASW technique (Pagano et al., 2008) were used (Figure 4-12), due to similarity in geometrical, age and soil features of the two dams.

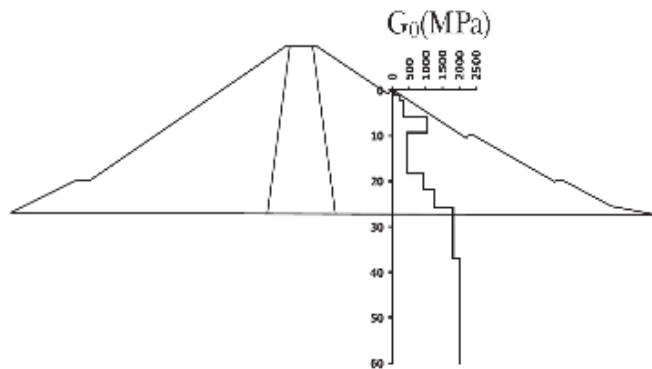


Figure 4-12. Shear modulus (G_0) at small strains vs depth. Measurements refer to the shells of the Camastra dam using the SASW technique (Pagano et al., 2008).

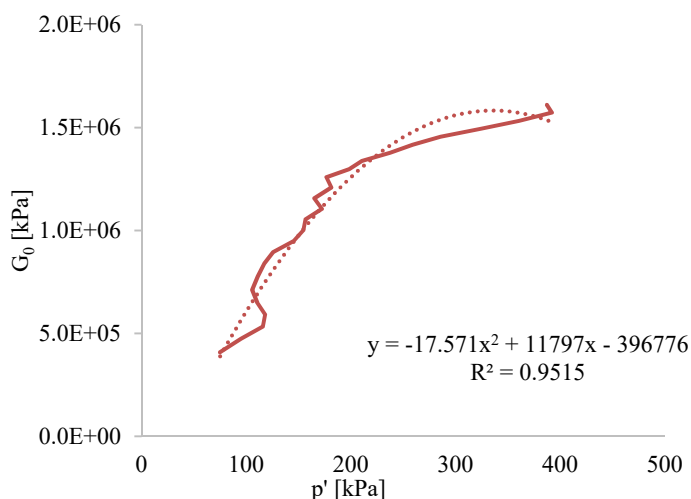


Figure 4-13. Shells elastic stiffness relation.

By interpolating the SASW measurements with the relation (4.2) (Figure 4-13), the following parameters were thus obtained:

Soil	A [kPa]	B [kPa]	C [kPa]	ν [-]
Shell	-396776	11797	-17.57	0.3

Table 4-6. Shell parameters for elastic stiffness relation.

To compute the initial Young modulus, a Poisson ratio $\nu=0.3$ was adopted.

For the core of Campolattaro dam, the parameters A, B, C were calibrated on the base of the Down-Hole (DH) test results (Figure 4-6) carried out in 2016.

Figure 4-14 shows that an almost linear relation between shear stiffness and mean effective stress p' can be obtained, so the parameters of Equation (4.2) for the core and the cofferdam are:

Soil	A [kPa]	B [kPa]	C [kPa]	ν [-]
Core	-187054	2693.1	0	0.3

Table 4-7. Core parameters for elastic stiffness relation.

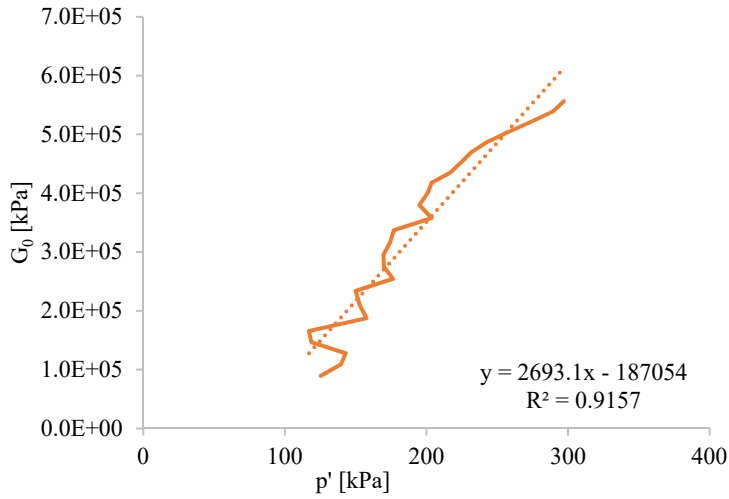


Figure 4-14. Core and cofferdam elastic stiffness relation.

For the foundation, a stratified configuration with depth was assumed according to the V_s values measured (shown in Figure 4-8) and reported in Table 4-8.

z [m]	V_s [m/s]	G_0 [MPa]	ν [-]
0-10	316	196	0.3
10-24	540	580	0.3
24-170	1200	2528	0.3

Table 4-8. Foundation stiffness.

The hysteretic behaviour of the soil has been represented by sigmoidal functions already implemented in FLAC (Eq. 3.26, §3.2.1.1). This function illustrates the stiffness and damping variation with increasing the shear strain level.

For the shell material, as previously done by Dello Russo (2015), the hysteretic parameters were obtained by fitting the $G/G_0-\gamma$ curve provided in Costanzo et al. (2011) for the coarse grained materials of Melito dam (Lirer, 2008).

For the filters, the shear modulus reduction curves have been referred to the data published in the literature (Seed et al., 1986).

For the core and the foundation, the sigmoidal functions were calibrated on the results obtained from resonant column and cyclic shear tests (2016 surveys campaign) (Figure 4-15).

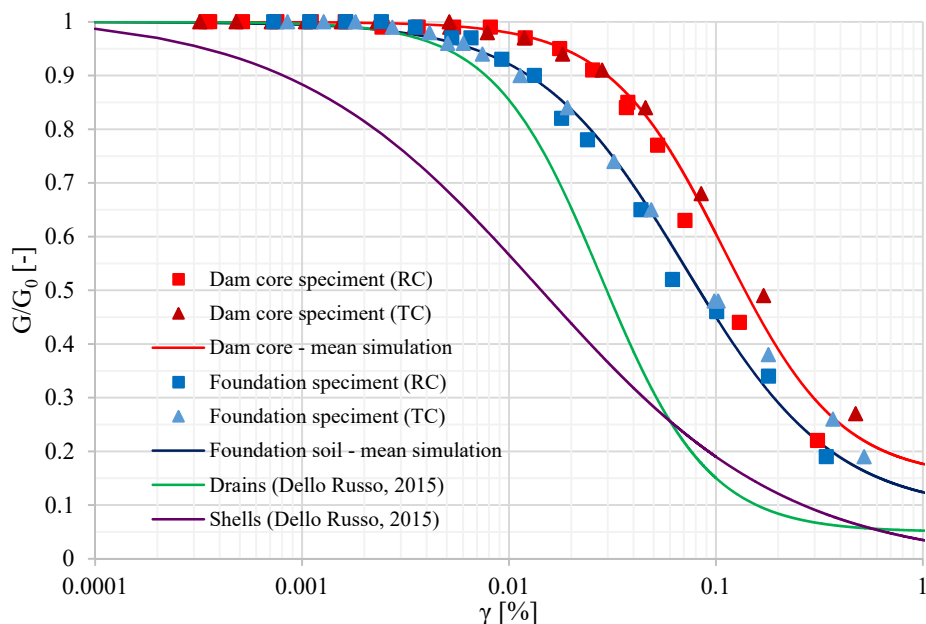


Figure 4-15. G/G_0 - γ curves for grained materials.

Table 4-9 provides the values of the hysteretic model for all dam soil materials.

Parameter	a	b	x_0	y_0
Core	0.85	-0.28	-0.96	0.15
Shells	1.025	-0.6	-1.85	0.01
Drains	0.95	-0.26	-1.555	0.05
Foundation	0.912	-0.36	-1.15	0.088

Table 4-9. Parameters adopted for the hysteretic model of dam and foundation materials.

The distortional-volumetric coupling, which can be generated in the dam soil under strong earthquakes, has been described by the Finn-Byrne model (§3.2.1.2). The Byrne formulation (eq. 3.28) has been used for the dam core and for the shells. In situ SPT test results carried out in 2009 were used to calibrate the model parameters C_1 and C_2 . For the core the volumetric threshold (shear strain) was evaluated from the resonant column test results; for the shells was imposed higher, as indicated in literature (Table 4-10).

Parameter	C ₁	C ₂	γ_v [%]
Core	0.135	2.96	0.02
Shells	0.086	4.625	0.01

Table 4-10. Parameters adopted for the Finn-Byrne model.

4.3.4. STATIC STAGES: CONSTRUCTION, FIRST RESERVOIR FILLING AND OPERATION

The construction of the dam embankment has been simulated in accordance with the real loading history.

Original design documents report that the construction of the dam began in 1986 and ended in 1992; Figure 4-16 shows the reference construction law documented in an old publication of “Cassa per il Mezzogiorno” (Diga di Campolattaro – Ente appaltante: Agenzia per la promozione dello Sviluppo del Mezzogiorno).

Five stages of construction can be identified as detailed in Table 4-11.

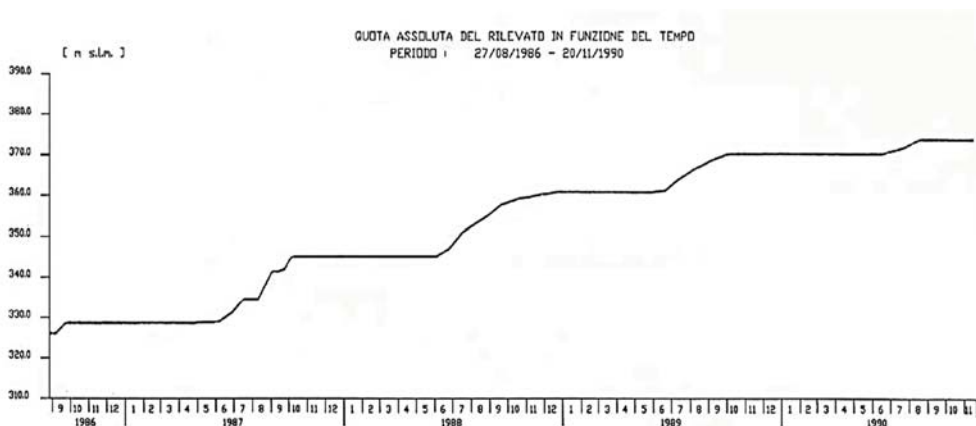


Figure 4-16. Height (a.s.l.) of the embankment from 1986 to 1990.

In 1990, the dam height was 45 m. To complete the construction, other two stages (7 m each) in 1991 and 1992 were supposed in this thesis since no information was available on such an issue.

Seven construction phases, thus, were considered in the construction analysis, each followed by a consolidation phase.

Stage	Year	Phase	Δh [m]	Time [months]
1	1986	Construction	3	2
		Consolidation	-	7
2	1987	Construction	15	5
		Consolidation	-	7
3	1988	Construction	15	5
		Consolidation	-	7
4	1989	Construction	10	5
		Consolidation	-	7
5	1990	Construction	5	3
		Consolidation	-	9

Table 4-11. Embankment height increasing per year.

Unfortunately, no monitoring data during the construction stage were available, so it was not possible to perform a back analysis to compare measured and predicted dam response.

Before starting the construction phase of the dam, a geostatic stress field was generated in the foundation with the gravity load procedure, implemented in FLAC.

The dam construction consists in the activation of one row of elements for each step of construction for a total number of 7 horizontal layers with thickness ranging from 4 to 15 meters.

Any layer activation was realized by the following steps (M1):

- 1) application of the well-known procedure called “dense liquid method” for which the behaviour of the material is assimilated to that of a liquid having its own weight but no stiffness. This latter is later restored at the activation of the following soil layer. In this way, the analysis reproduces the stress and strain induced in a real dam (Mattar and Naylor, 1988). At this stage, average values of the soil stiffness for each layer are adopted by “gravity loading procedure”;
- 2) introduction of material stiffness dependency on the mean effective stress p' .
- 3) Regeneration of the stresses acting on the embankment and foundation, according to the new stiffness and strength distribution.

The weight of the layer has been applied in a very short time.

Before moving to the next step, a phase of consolidation has been carried out.

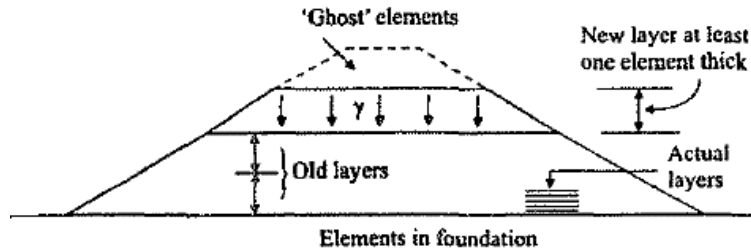


Figure 4-17. Element modelling of fill construction (Potts and Zdravkovik, 1999).

In order to save computational time, a second construction procedure (M2), consisting in the application of a uniform distributed load equal to the layer weight, has been developed. Steps 2) and 3) are still valid.

Figure 4-18 shows a comparison between the settlements predicted for the central section of the dam core using the M1 and the M2 procedures.

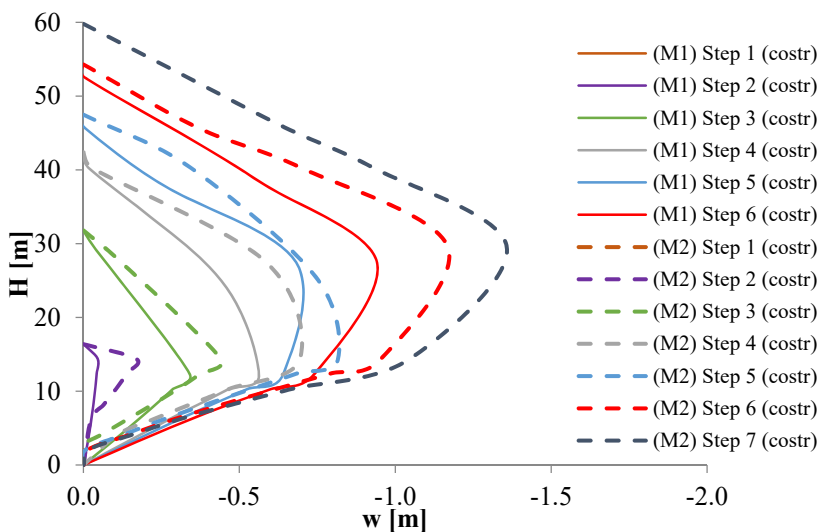


Figure 4-18. Comparison between the settlements predicted along the core axis using M1 and M2 procedures.

To improve the shape of settlements vs dam height, the total number of horizontal layers activated for each step of construction was increased from 7 to 11 layers (M3), and the core permeability was set equal to the higher value found in the design reports ($1.49 \cdot 10^{-9}$ m/s), thus saving computational time.

Finally, in the last model (M4), the dam core was not deepened into the foundation.

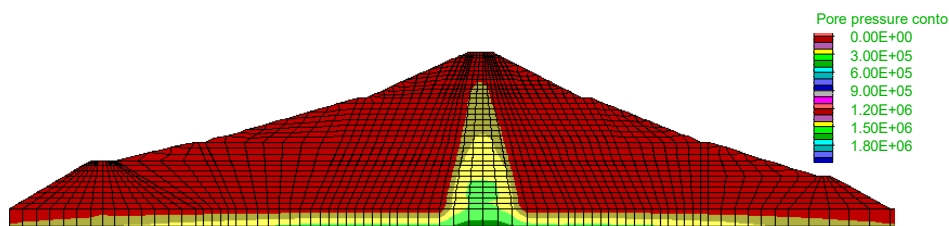


Figure 4-19. Pore pressure (pp) contours at the end of the construction (M4).

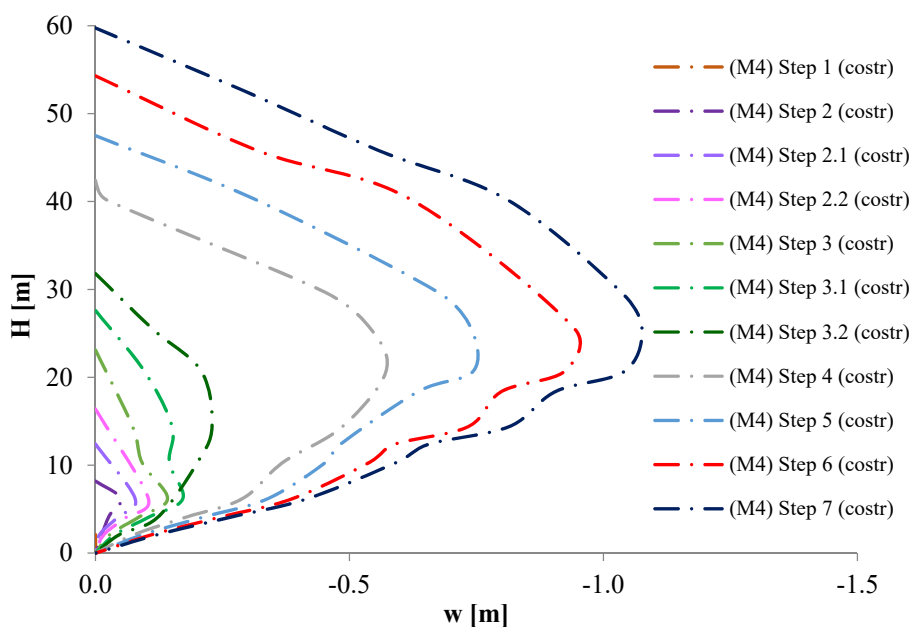


Figure 4-20. Settlements predicted for the core axis (M4).

Predictions provided by the final M4 model are shown in Figure 4-19 in terms of pore pressures induced in the core by the construction and in Figure 4-20 as settlements along the dam core axis.

The impounding stage has been hypothesized to occur in about 4 months (0.5 m/day) after the end of the construction.

The simulation of the reservoir impounding has been done by simultaneously:

- 1) applying a water pressure on the upstream side of the dam assuming a hydrostatic distribution regulated by the current level of the reservoir;
- 2) initializing the pore pressure (hydrostatic pressure) in the nodes of the wet boundary;
- 3) applying the stress ($\sigma_n = \gamma_w h$) along the upstream side of the shell to have (together with the hydraulic condition) zero effective stresses on the wet boundary of the dam.

4.3.5. DYNAMIC STAGE

The dynamic analysis has been made by means of the same mathematical and numerical modelling tool used for the simulation of the static phases.

The initial state of the dynamic analysis in terms of stresses, pore pressures and soil model internal variables comes from the static analysis. In such a context, dynamic analyses have continuity with the static analysis, thanks to a unified approach where time is a variable of the problem such as it occurs in reality.

The input motion for the dynamic analysis has been derived from the procedure explained in Chapter 2:

- 1) Definition of the return period for each limit state, considering a nominal life (V_N) of 50 years

	OLS $P_{V_R} = 81 \%$	DLS $P_{V_R} = 63 \%$	LLS $P_{V_R} = 10 \%$	CLS $P_{V_R} = 5 \%$
T_R [years]	45	75	710	1460

Table 4-12. Return period for the selected reference life.

- 2) Estimation of PGAs for selected return periods at the reference site (§2.3.3.1), that for an existing earth dam at the specific site are:

Limit State	P_{V_R} [%]	λ [years ⁻¹]	T_R [years]	a_{max} [g]
OLS	81	0.02222	45	0.0797
DLS	63	0.01333	75	0.1037
LLS	10	0.00141	710	0.3264
CLS	5	0.00068	1460	0.4360

Table 4-13. Expected PGAs at the dam site.

3) Disaggregation of seismic hazard for the reference site (M,R)

Limit State	P_{V_R} [%]	M	R [km]
OLS	81	4.5-5	0-10
DLS	63	4.5-5.5	0-10
LLS	10	5-7	0-10
CLS	5	5.5-7.5	0-10

Table 4-14. Magnitude-distance combination for the reference site.

4) Selection of a series of accelerograms (spectrum compatibility criterion) for each limit state. Since the purpose of the study concerns the rapid drawdown after a strong earthquake, the dynamic analyses were performed with input motion corresponding to the ultimate limit states.

In paragraph §2.3.4 the procedure followed for the selection of a series of accelerograms using a computer software was explained. The importance of the parameters related to the spectral compatibility was highlighted. For the case study, the fundamental period of the dam, calculated using eq. (2.12), was roughly estimated as:

$$T_1 = \frac{2.6 \cdot H}{V_s} = \frac{2.6 \cdot 60}{400} = 0.39 \text{ s}$$

where 400 m/s is the average shear velocity of the dam core. So the period range assumed was 0.1÷0.5 seconds.

For a zoned dam, however, the materials that constitute the dam body have different stiffnesses and therefore it is not easy to identify the value of V_s to be used in equation (2.12). So, using eq. (4.2) adopted in the FLAC model, it was possible to assess the average stiffness for each dam zone and, consequently, the corresponding average shear velocity (\bar{V}_s).

Table 4-15 shows the estimated average values of \bar{V}_s and their contribution (weighted according to the surface area, $V_{S,\text{weighted}}$) depending on the geometry of the dam zone considered.

Defining the percentage weighed according to the surface area as the ratio of the zone area (A_z) to the overall cross-section area (A_{CS}),

the evaluation of the average shear velocity for the dam is reported in Table 4-15.

ZONE	A_z [m ²]	$\frac{A_z}{A_{CS}}$	\bar{V}_s [m/s]	$V_{S,weighted}$ [m/s]
Upstream shell	4545.44	0.447	639.0	285.3
Downstream shell	3650.08	0.359	691.4	247.9
Upstream filter	417.17	0.041	719.1	29.5
Downstream filter	417.52	0.041	671.6	27.6
Core	1148.61	0.113	420.5	47.5
	Tot 10178.81 (A_{CS})		Average 628.3	Sum 637.7

Table 4-15. Average dam shear velocity evaluation.

By inserting the average shear velocity reported in Table 4-15 in eq. (2.13), the period of the dam is 0.248 s for the average value and 0.245 s for the weighted value.

These values are close to the fundamental period of the dam calculated numerically with FLAC using the transfer function between the signals at the dam top and base, considering input motions (only the horizontal component) of different intensities (PGAs), as shown in Table 4-16.

The more refined study on the fundamental period of the Campolattaro dam confirmed the chosen range (0.2T÷2.0T).

Strain level	a_g [g]	Fundamental Period, T [s]	Fundamental Frequency, f [Hz]
Very small strains	0.003	0.233	4.297
Small strains	0.03	0.256	3.906
Large strains	0.3	0.293	3.418

Table 4-16. Assessment of the fundamental period of the Campolattaro dam.

In the following the accelerograms selected for the Life Safety Limit State (LLS) and Collapse Limit State (CLS) are showed, respectively. In each set of accelerograms, the spectra with a scale

factor $F_s > 2$ (Eq. 2.11, §2.3.6) were automatically excluded, while when $F_s \leq 2$ the D_{rms} value (Eq. 2.12) was evaluated (only earthquake with $D_{rms} \leq 0.16$ were selected).

LLS									
ID	Earthquake	Date	M	Fault Mechanism	Epicentral distance [km]	PGA [g]	FS	Scaled PGA [g]	D_{rms}
822	Umbria Marche (aftershock)	03/10/1997	5.3	normal	5	0.156	2.01	0.314	0.058
982	Friuli (aftershock)	16/09/1977	5.4	thrust	9	0.191	1.65	0.314	0.067
4674	South Iceland	17/06/2000	6.5	strike slip	5	0.318	0.98	0.314	0.069
6332	South Iceland (aftershock)	21/06/2000	6.4	strike slip	6	0.529	0.59	0.314	0.071
822	Umbria Marche (aftershock)	03/10/1997	5.3	normal	5	0.187	1.67	0.314	0.077
169	Calabria	11/03/1978	5.2	normal	10	0.078	4.04	0.314	-
4674	South Iceland	17/06/2000	6.5	strike slip	5	0.338	0.93	0.314	0.129

Table 4-17. LLS earthquakes set.

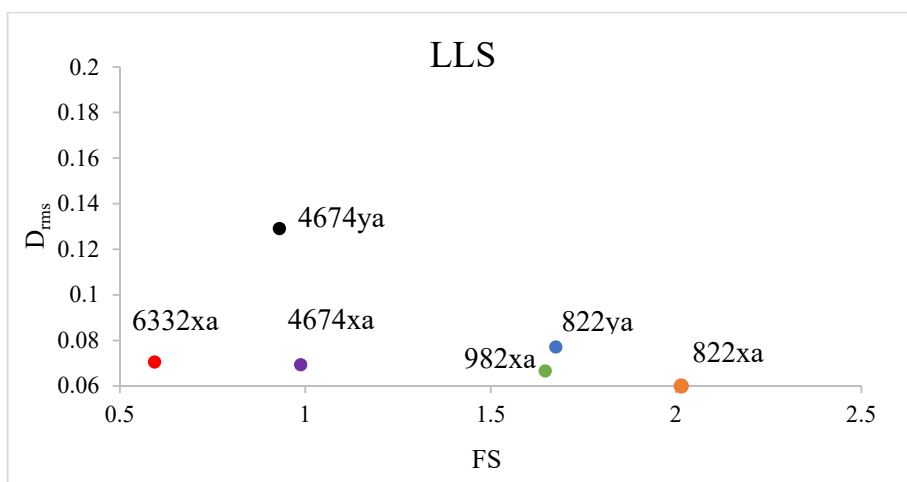
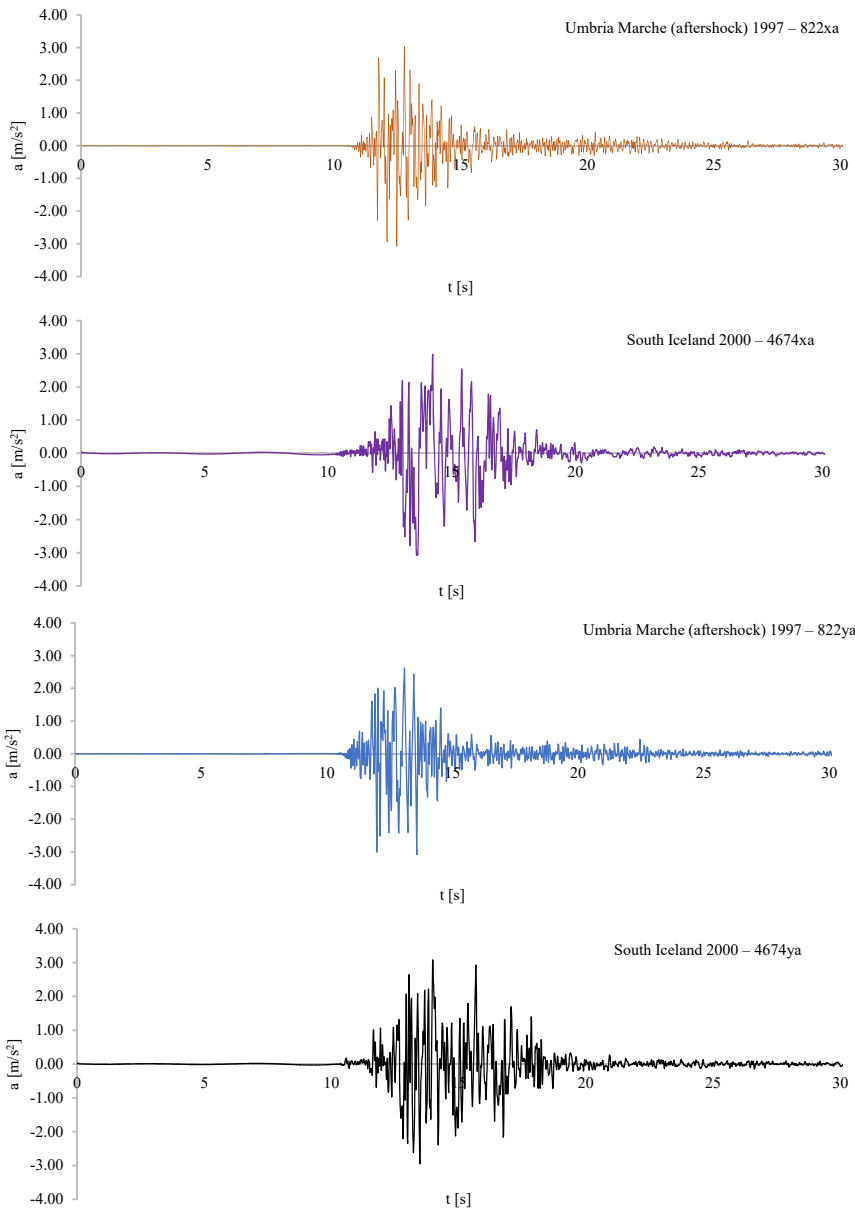


Figure 4-21. Selected Life Safety Limit State accelerograms: D_{rms} vs F_s .



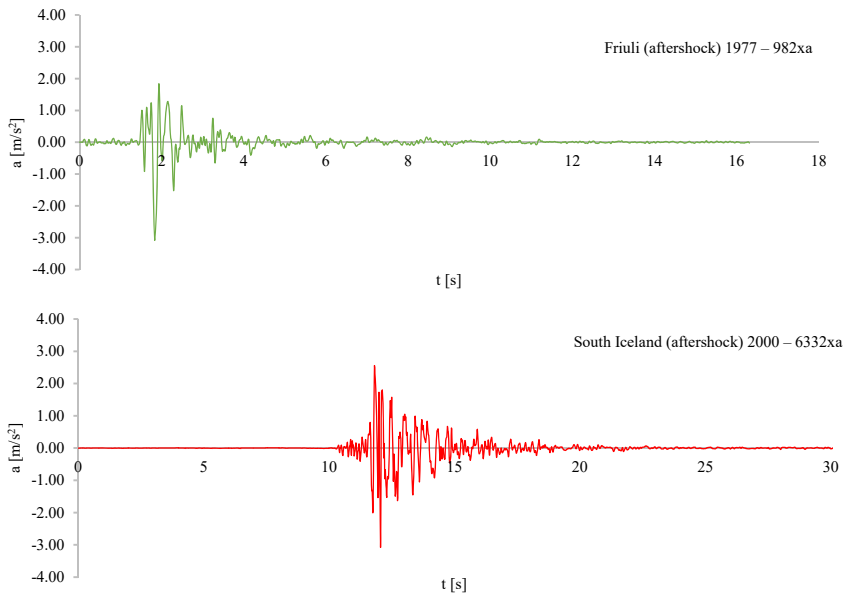
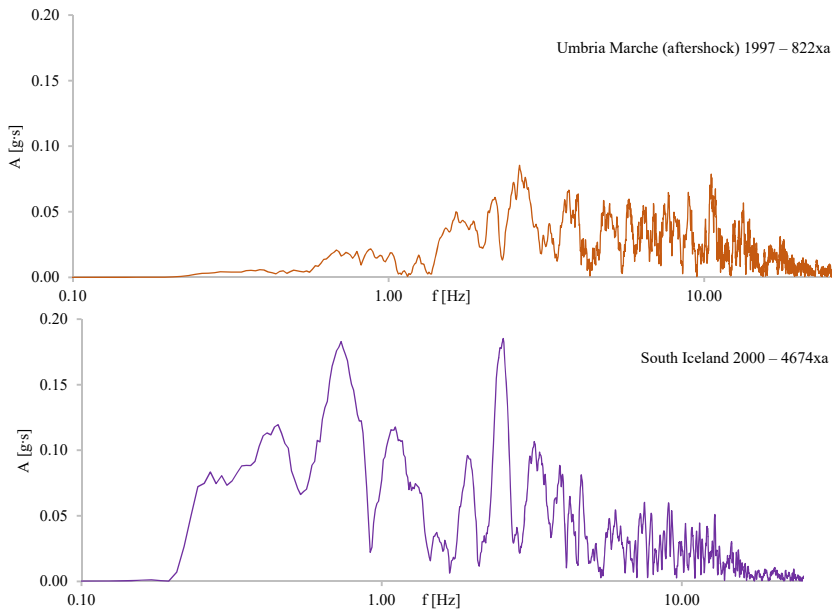


Figure 4-22. LLS: acceleration time histories.



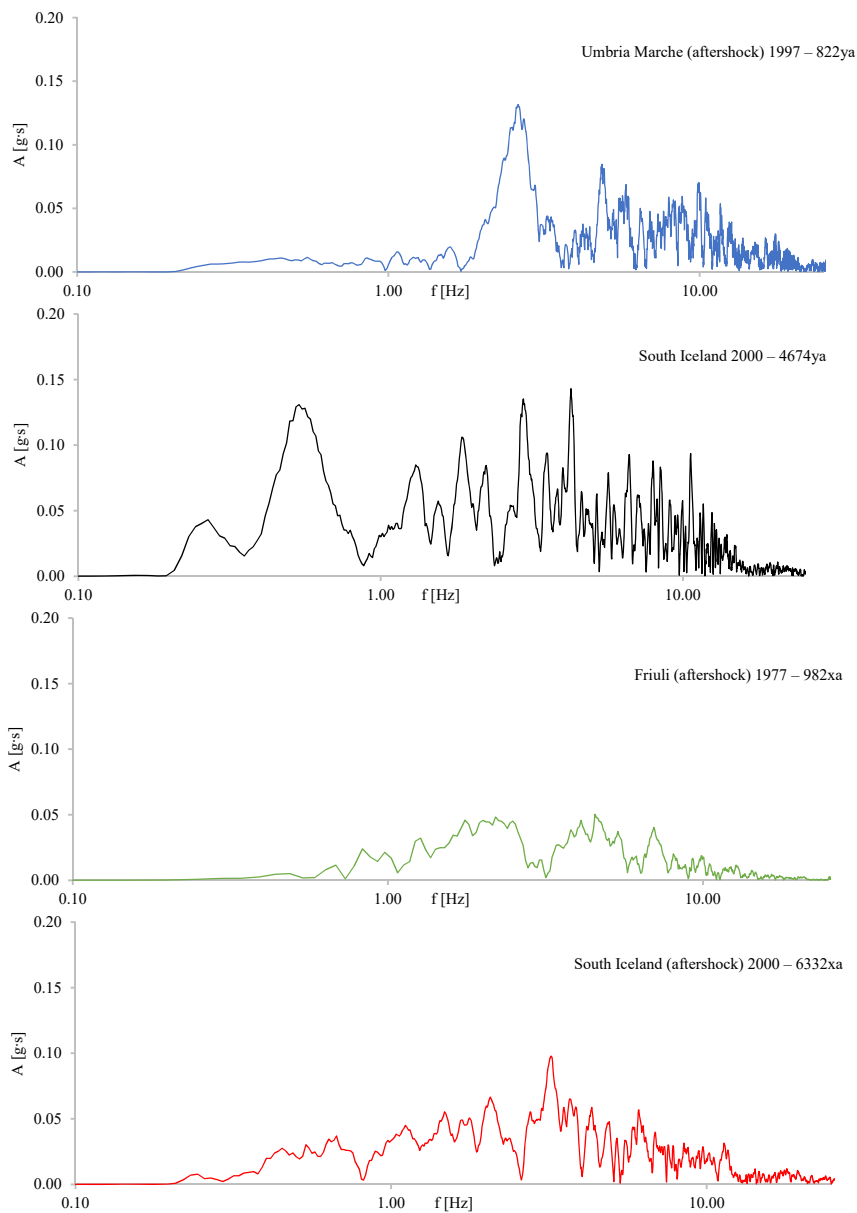


Figure 4-23. LLS: amplitude Fourier Spectra.

CLS									
ID	Earthquake	Date	M	Fault mechanism	Epicentral distance [km]	PGA [g]	FS	Scaled PGA [g]	D _{rms}
7142	Bingol	01/05/2003	6.3	strike slip	14	0.297	1.40	0.415	0.037
6341	South Iceland (aftershock)	21/06/2000	6.4	strike slip	20	0.051	8.08	0.415	-
6277	South Iceland	17/06/2000	6.5	strike slip	15	0.518	0.80	0.415	0.062
4674	South Iceland	17/06/2000	6.5	strike slip	5	0.318	1.31	0.415	0.067
6326	South Iceland (aftershock)	21/06/2000	6.4	strike slip	14	0.116	3.57	0.415	-
182	Tabas	16/09/1978	7.3	oblique	12	0.385	1.08	0.415	0.085
182	Tabas	16/09/1978	7.3	oblique	12	0.338	1.23	0.415	0.127

Table 4-18. CLS earthquakes set.

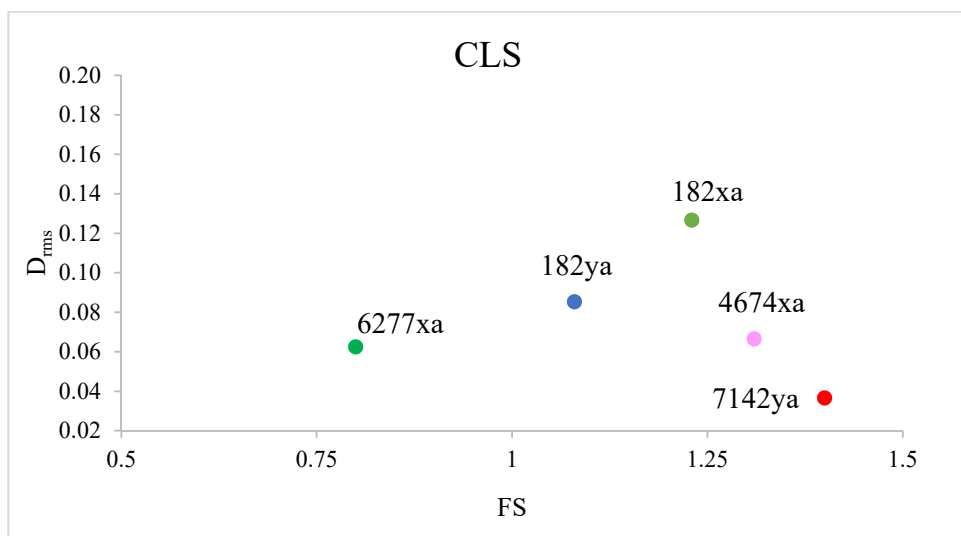
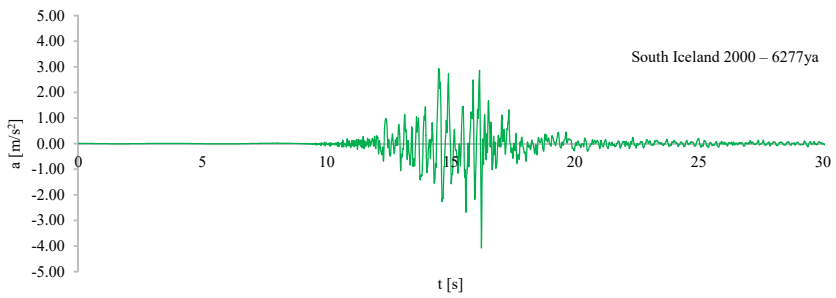
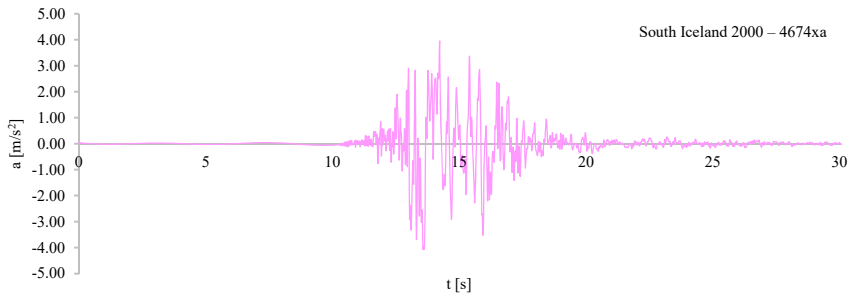
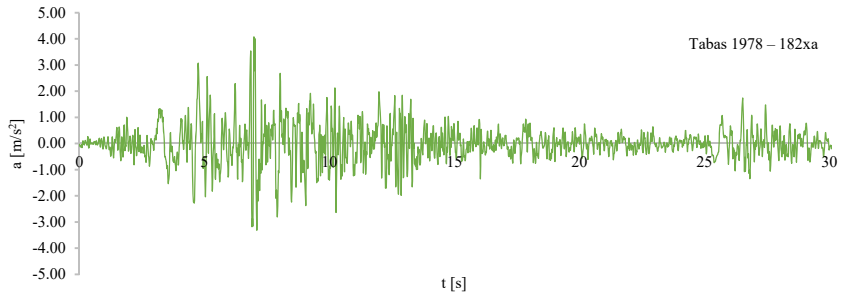
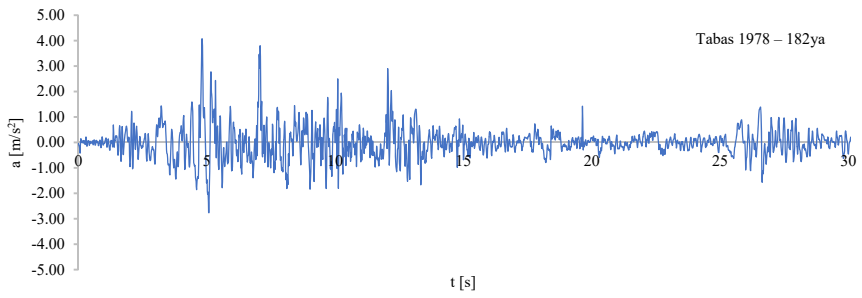


Figure 4-24. Selected Collapse Limit State accelerograms: D_{rms} vs F_s.



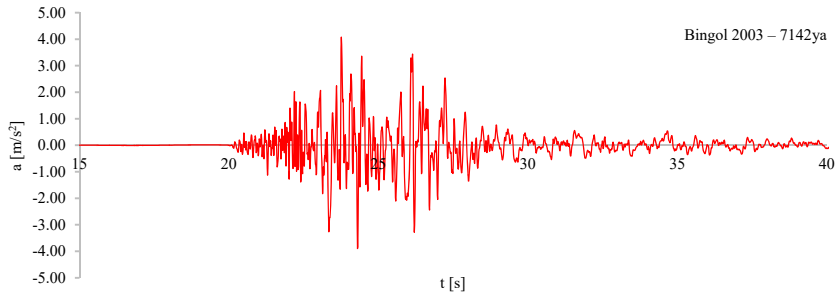
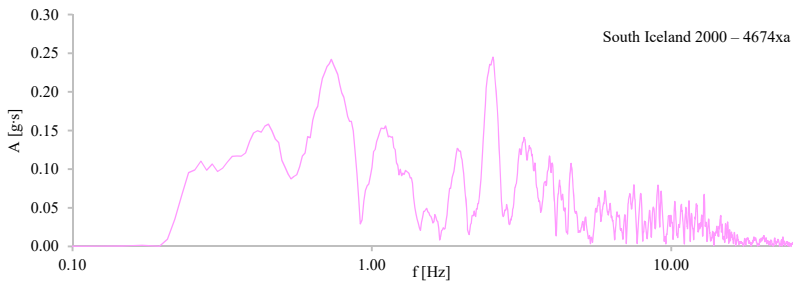
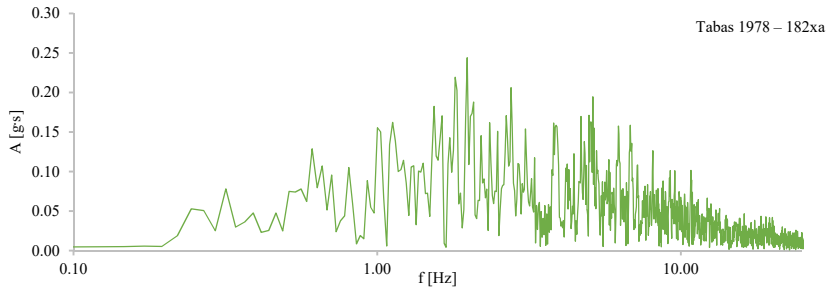
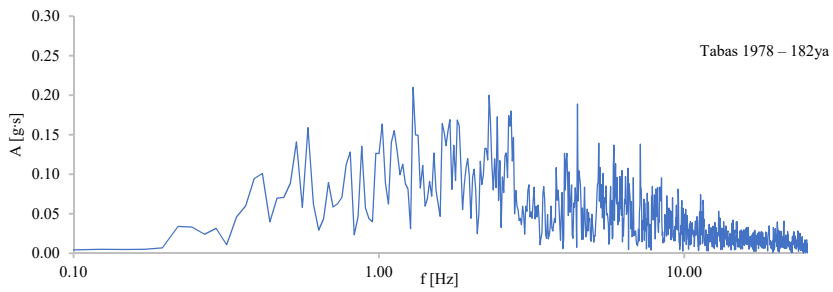


Figure 4-25. CLS: acceleration time histories.



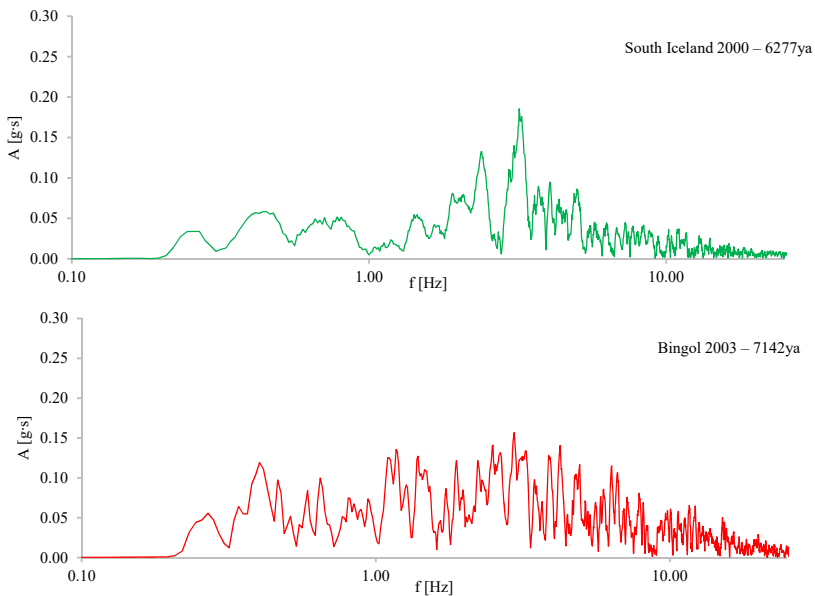


Figure 4-26. CLS: amplitude Fourier Spectra.

The natural input motions selected are outcrop motions. The appropriate input motion at the bottom boundary of the discretized 2D model were computed through a “deconvolution” analysis using the 1D wave propagation code, EERA (Bardet et al., 2000).

The deconvoluted input motion is applied at the base of the model, using the transformation into stress record due to the viscous boundaries assigned. Equation 3.48 was used, so $\sigma_{xy} = 4.08 \cdot 10^6 v_s$ since the input motion was assumed horizontal.

4.3.6. DRAWDOWN STAGE

The drawdown analysis has been made by a coupled transient seepage formulation, taking into account two immiscible fluids in porous media (3-phase approach). The formulation is suitable for problems encountered in reservoir simulation, in which a fluid displaces another and simultaneous flow of the two fluids takes place in the porous medium with no mass transfer between them.

The initial state of the drawdown analysis in terms of stresses, pore pressures and soil internal variables comes from the dynamic analysis.

Additional variables related to the partial saturation were assigned to soils in this stage. Literature soil water characteristic curves (Van Genuchten, 1980), selected in terms of saturated permeability, were assigned to dam soils (Figure 4-11).

The drawdown phases were simulated by lowering the water level from the maximum level to the complete emptying, following the procedure already described for the simulation of the impounding stage.

Five drawdown rates were assumed, considering a slow drawdown (0.5 m/day) that needs about four months to complete the lowering operations and a rapid drawdown (4-6 m/day) that needs only 10 days.

Figure 4-27 shows the water level changes over time for different drawdown rates. The reference time in this stage is set at the occurrence of the earthquake (day 0), so the lowering operations start a day after the seismic event (day 1). This assumption allows the partially saturated variables to be assigned to the model and it simulates a real interval of time that may elapse between the event and the beginning of the drawdown stage.

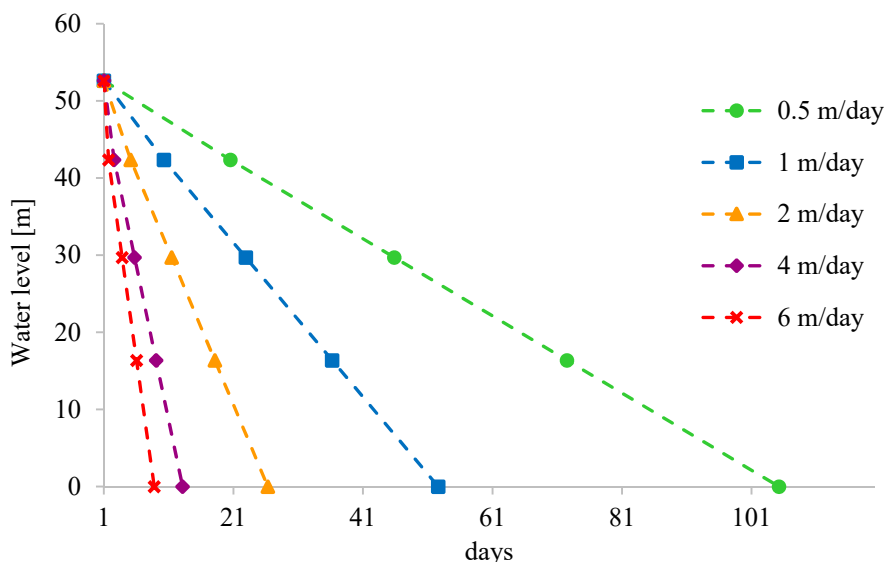


Figure 4-27. Water level changes during the drawdown.

The water lowering operations were carried out dividing the drawdown stage into several steps (different values of drawdown ratio, L/H), without

interrupting the time continuity because time is a variable of the problem. The final goal is to assess the overall stability of the dam using the strength reduction method, detailed in section §3.4.

On the upstream slope was initially assigned a hydraulic boundary condition, called seepage condition. In this way, along the selected slope the air (non-wetting fluid) pressure is zero ($P_{nw} = 0$, atmospheric pressure) and the boundary remains impermeable to the water as long as the water pressure, P_w , is less than the atmospheric pressure.

However, it was found that this boundary condition had not worked well for the problem at hand. When the water pressure on the upstream side was removed to simulate the reservoir lowering, on the same boundary the seepage condition is imposed, so the air pressure is set to zero, but on the same nodes the water pressure is zero too. This means that the soil suction is zero ($P_{nw} - P_w = 0$) and, due to the SWCC law, the degree of saturation for the shells is 100%. Over time the saturation degree should decrease because of the water flow, but the seepage condition does not allow it.

This problem was overcome by imposing a hydraulic boundary condition suitable for a rapid drawdown. The water level on the upstream shell of the dam is modelled as an applied water pressure, so when it is removed layer by layer (one row of elements), on the same element the water pressure is set to zero. Repeating the procedure on following elements, the pressure is released on the boundary where the drawdown is just completed. Over time, the saturation degree and the water pressure decrease.

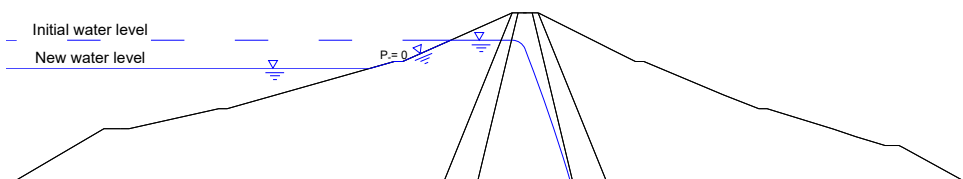


Figure 4-28. Upstream slope boundary condition applied during drawdown stages.

5. Results

In this section, the main results of the different stages of the dam lifetime will be provided.

In §5 and §5.2 the results of the static and seismic simulation are discussed. Later on in §5.3, the dam response to drawdown simulation will be detailed trying to highlight the effects on dam stability of the different initial conditions, drawdown rate and ratio.

The input motions causing higher permanent displacements in the dam embankment during the seismic stage were considered in order to perform the subsequent simulation of the reservoir drawdown.

A synopsis of the performed analyses is reported in Table 5-1.

Static Stage		Dynamic Stage		Drawdown Stage
Construction	Reservoir	Limit State	Earthquake	Rate [m/day]
✓	Full	×	×	0.5
				1
				2
				4
				6
✓	Full	LLS	Umbria Marche (aftershock) – 822xa	×
			Umbria Marche (aftershock) – 822ya	×
			Friuli (aftershock) – 982xa	×
			South Iceland (aftershock) – 6332xa	×
			South Iceland – 4674ya	×
			South Iceland – 4674xa	0.5
			South Iceland – 4674xa	1
			South Iceland – 4674xa	2
			South Iceland – 4674xa	4
			South Iceland – 4674xa	6
✓	Full	CLS	Bingol – 7142ya	×
			Tabas – 182xa	×
			Tabas – 182ya	×
			South Iceland – 6277xa	×
			South Iceland – 4674xa	0.5
			South Iceland – 4674xa	1
			South Iceland – 4674xa	2
			South Iceland – 4674xa	4
			South Iceland – 4674xa	6

Table 5-1. Performed 2-D analyses.

5.1. STATIC ANALYSES

In chapter 4 (§4.3.4) the procedure adopted for simulating the dam construction and the calibration of the model itself were explained.

Here some results, in term of stresses, displacements and pore pressures (pp), are presented.

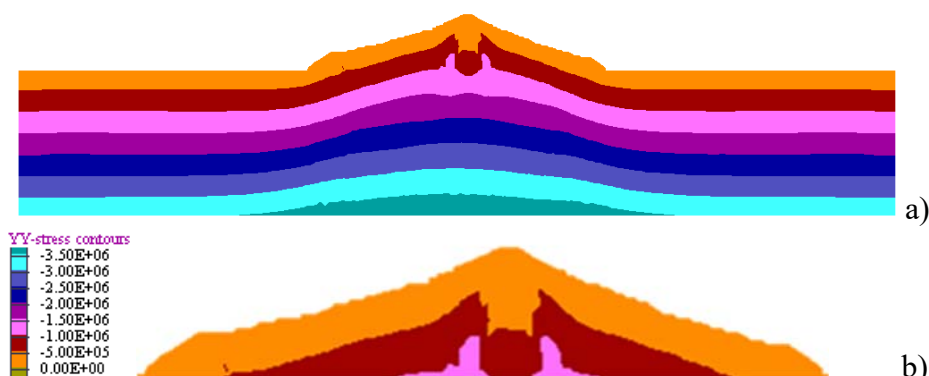


Figure 5-1. Contours of vertical total stress at the end of the dam construction: a) whole model; b) zoom on the dam cross-section.

The vertical total stress contours for a zoned earth dam (Figure 5-1) are affected by the stiffness contrast between core and shells that produces an inhomogeneous distribution of vertical stresses. The phenomenon, known as arch effect, leads to a stress reduction in the core and an increase in the stiffer shells.

As mentioned in Chapter 4 (§4.3.4), no monitoring data during the construction stage were available, so it was not possible to perform a back analysis to compare measured and predicted dam response during this stage. Figure 5-1 and Figure 5-2 show the predicted response.

Core settlements vs dam height, plotted in Figure 5-3, exhibit a distorted profile upwards in the first construction stages and distorted downwards later. This pattern is common to what observed for other zoned earth dams, such as Camastra dam (Fontanella et al., 2008), and is compatible with the analytical solution proposed by Pagano (1998) for predicting dam settlements assuming that soil stiffness varies linearly with the height.

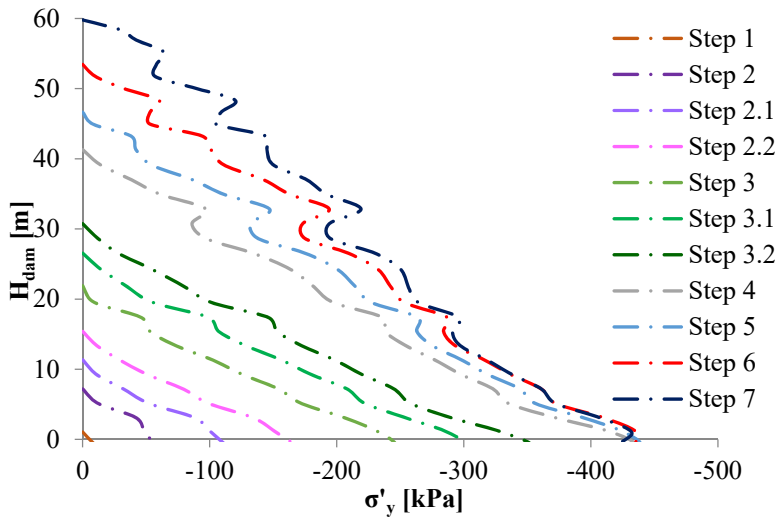


Figure 5-2. Vertical effective stresses computed during construction along the core axis.

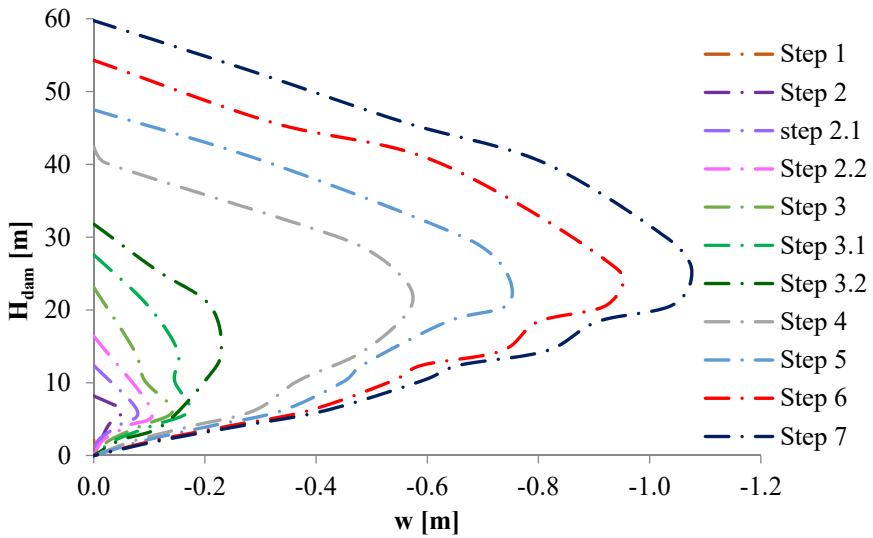


Figure 5-3. Settlement computed during construction along the core axis.

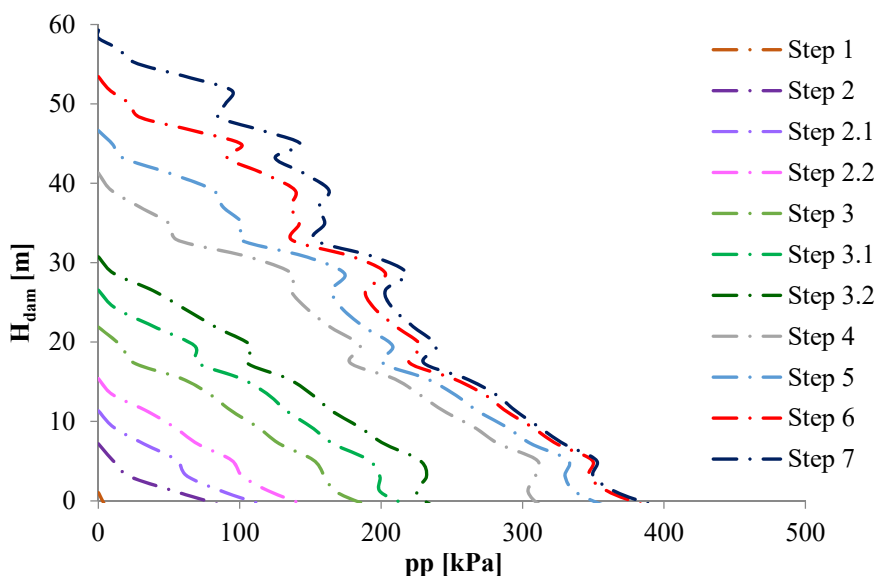


Figure 5-4. Pore pressure computed during construction along the core axis.

Significant increments of pore water pressure were calculated in the core throughout the entire construction process. The pore pressure values are higher along the core axis, placed at higher distance from the drainage boundaries (drains).

The pore pressure contours for the filling stages are showed in Figure 5-5.

The pore pressure increments due to the construction stage are visible (and almost unchanged) until the external water level has reached 25.48 m (Figure 5-5a and b).

After the maximum water level had been reached (52.62 m), a consolidation stage was simulated to reach the steady-state conditions. Due to the low permeability of the core, this stage lasted almost 32 years (Figure 5-6), a time compatible with the consolidation properties of the core and of the foundation clay.

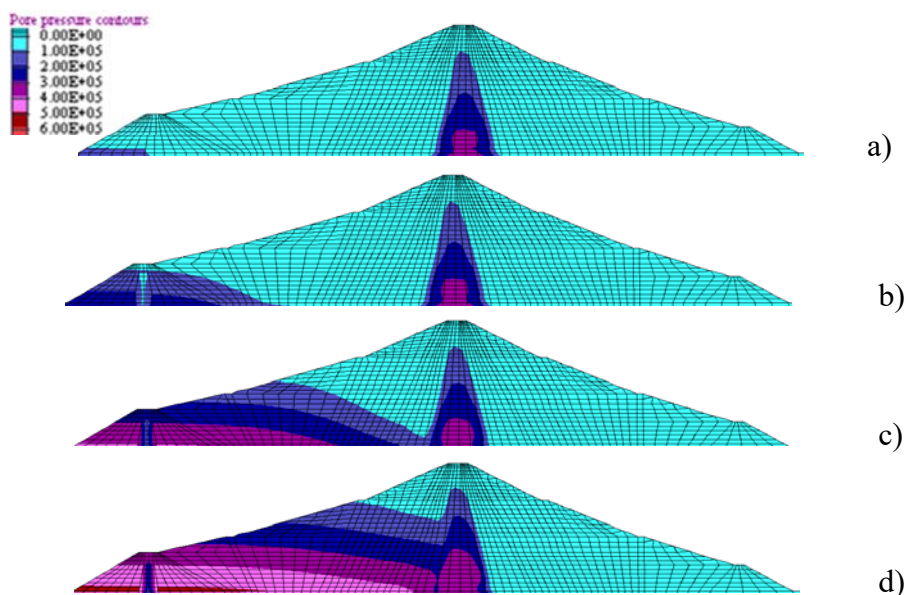


Figure 5-5. Pore pressure contours at different stages of the 1st filling of the reservoir: a) water level +12.37 m; b) water level +25.48 m; c) water level +42.36 m; d) water level +52.62 m.

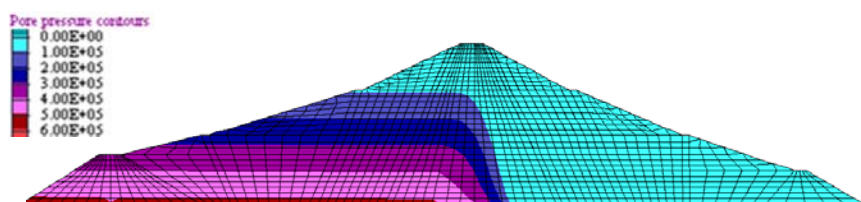


Figure 5-6. Steady state for maximum water level.

5.2. SEISMIC ANALYSES

All earthquakes corresponding to the two limit states (LLS and CLS) have been applied considering full reservoir and steady-state conditions reached after the impounding stage.

Figure 5-7 shows the amplification factor, along the core axis, for all the seismic inputs considered; $|a_{\max}|$ and $|a_{\max,b}|$ are the maximum absolute accelerations in the dam body and at the dam base, respectively.

The seismic signals are amplified moving from the bottom to the top of the dam body with different amplification factors. The inputs corresponding to

the Life-Safety Limit State induce an amplification in the range from 1.25 up to 2.7, the maximum value corresponding to the South Iceland aftershock (6332xa). The inputs adopted for to the CLS assessment induce an amplification in the range $1.5 \div 2.25$; the maximum value corresponding to the South Iceland earthquake (6277ya). For the CLS, as expected, the amplification is lower due to the higher strain level induced in the dam and the beneficial effect of damping.

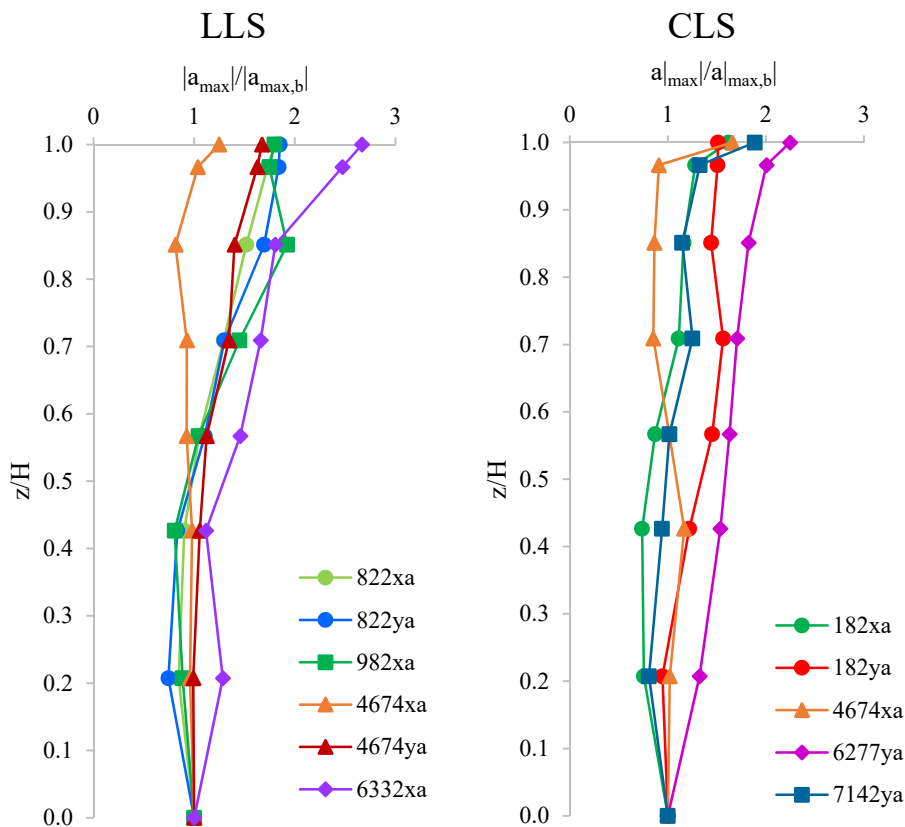


Figure 5-7. Profiles of $|a_{max}|/|a_{max,b}|$.

Results expressed in terms of maximum (downstream direction) and minimum (upstream direction) horizontal acceleration profiles for the two limit states (LLS and CLS) are presented in Figure 5-8, Figure 5-9 and Figure 5-10. The acceleration profiles are computed in the middle section of the whole analysis domain.

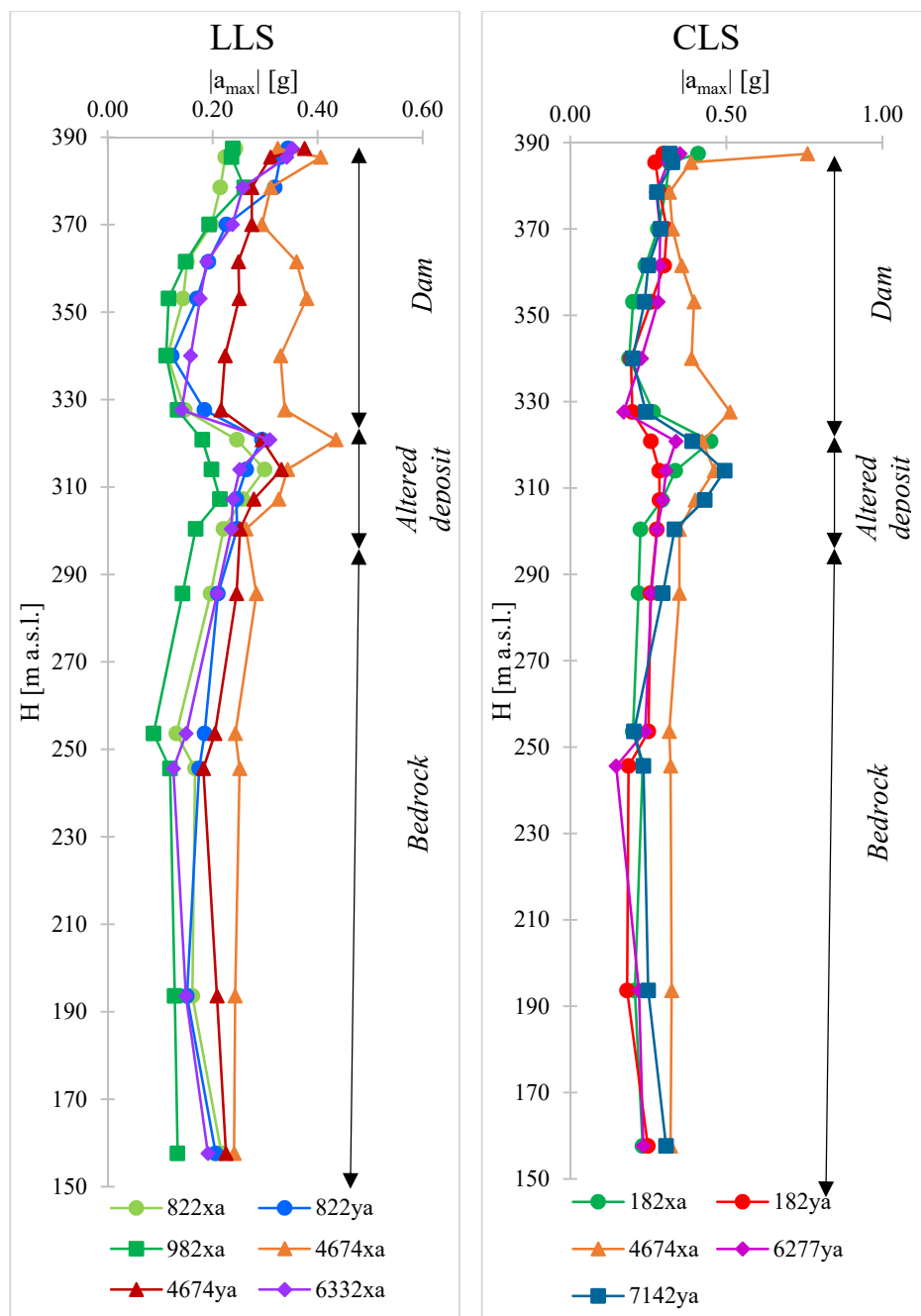


Figure 5-8. Absolute acceleration profiles in the central section of the model.

Due to the deconvolution of the outcrop input motions (§4.3.5), at the base of the model boundary (156.7 m a.s.l.) the signals have different maxima.

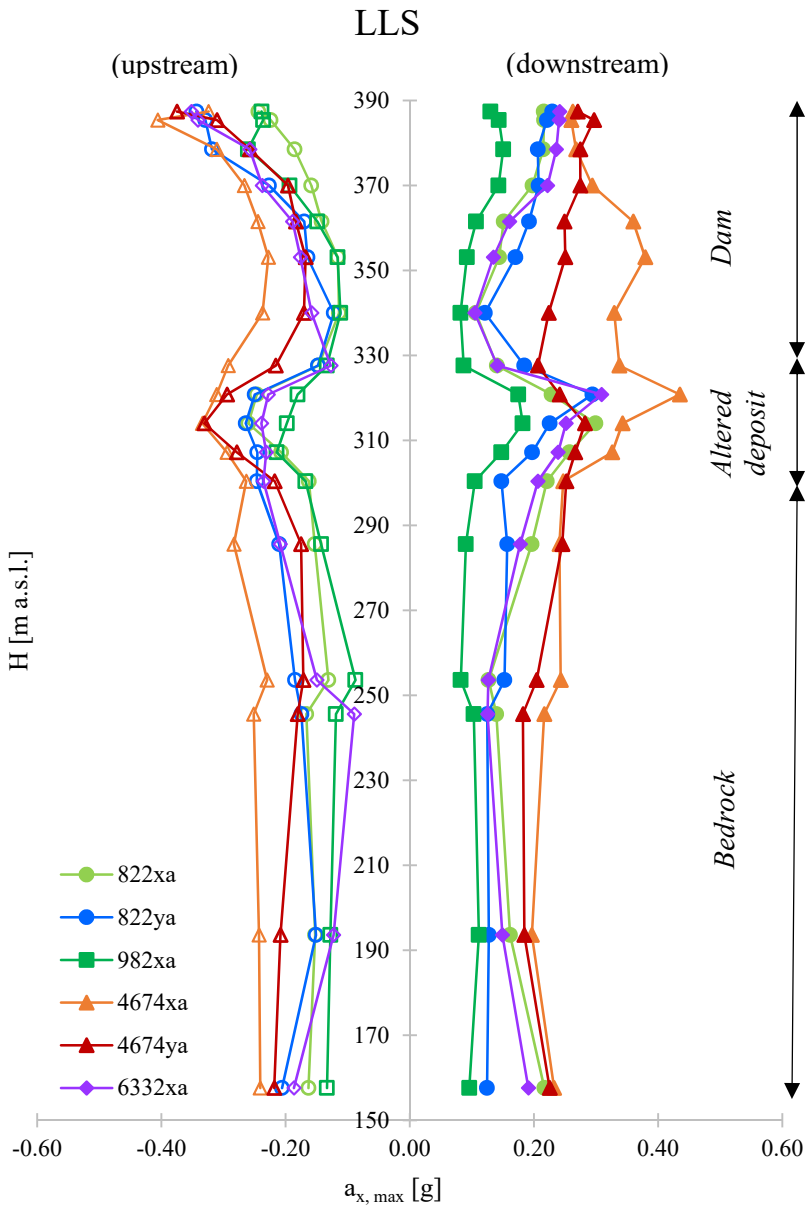


Figure 5-9. Minimum and maximum acceleration profiles (LLS) in the central section of the model.

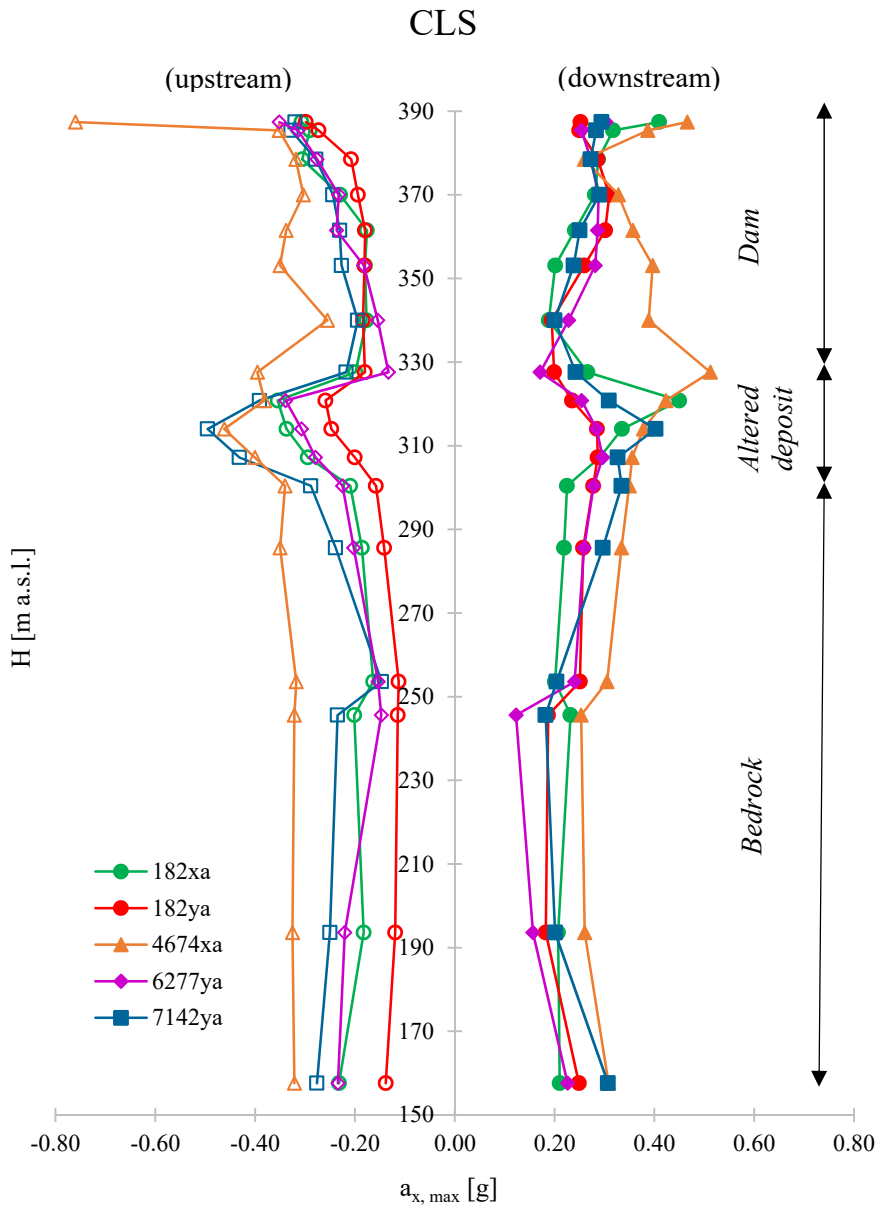


Figure 5-10. Minimum and maximum acceleration profiles (CLS) in the central section of the model.

From Figure 5-8 to Figure 5-10, the profiles show almost unaltered seismic wave propagation in the bedrock. Then, the altered deposit of much lower velocity ($V_s = 316$ m/s) modifies the propagation pattern and site

amplification starts appearing with maximum effects at the dam base for the signal 4674xa for both LLS and CLS case.

In the lower part of the dam embankment, the maximum (positive in the downstream direction) and the minimum (negative in the upstream direction) of acceleration are deamplified. This behaviour is less pronounced for the South Iceland earthquake (4674xa). This signal induces higher acceleration on the crest of the dam. This probably occurs due to the dominant frequency of the signal (Figures 4-25 and 4-28) which is very close to the fundamental frequency of the dam (Table 4.10).

Figure 5-11 and Figure 5-12 show, for each LLS input motion, the acceleration time histories calculated at the dam base and dam crest. As expected, the seismic signal propagating from the base to the top of the dam is amplified. Moreover, at the dam crest the motion is not null also after the end of the applied input signal, due to free oscillations of the structure.

From Figure 5-11 to Figure 5-18 the horizontal and vertical displacement time histories (black line) are also reported. The displacements consist of an elastic and a plastic part. The elastic displacement disappears when the earthquake ends, the plastic displacement, instead, increases with the duration of the accelerometric signal. For the LLS, the South Iceland earthquake provides horizontal residual displacements that are negative (upstream direction) and equal to 25 cm and 7 cm for the signal 4674xa and 4674ya, respectively. As the vertical residual displacements regard, the South Iceland earthquake provides the larger settlements at the dam crest, equal to 9 cm and 1 cm for the signal 4674xa and 4674ya, respectively.

For the CLS set of input motions, the dam response, in terms of acceleration and displacement, is similar to the LLS one. However, the displacement magnitude is greater, due to the higher severity of the input motions.

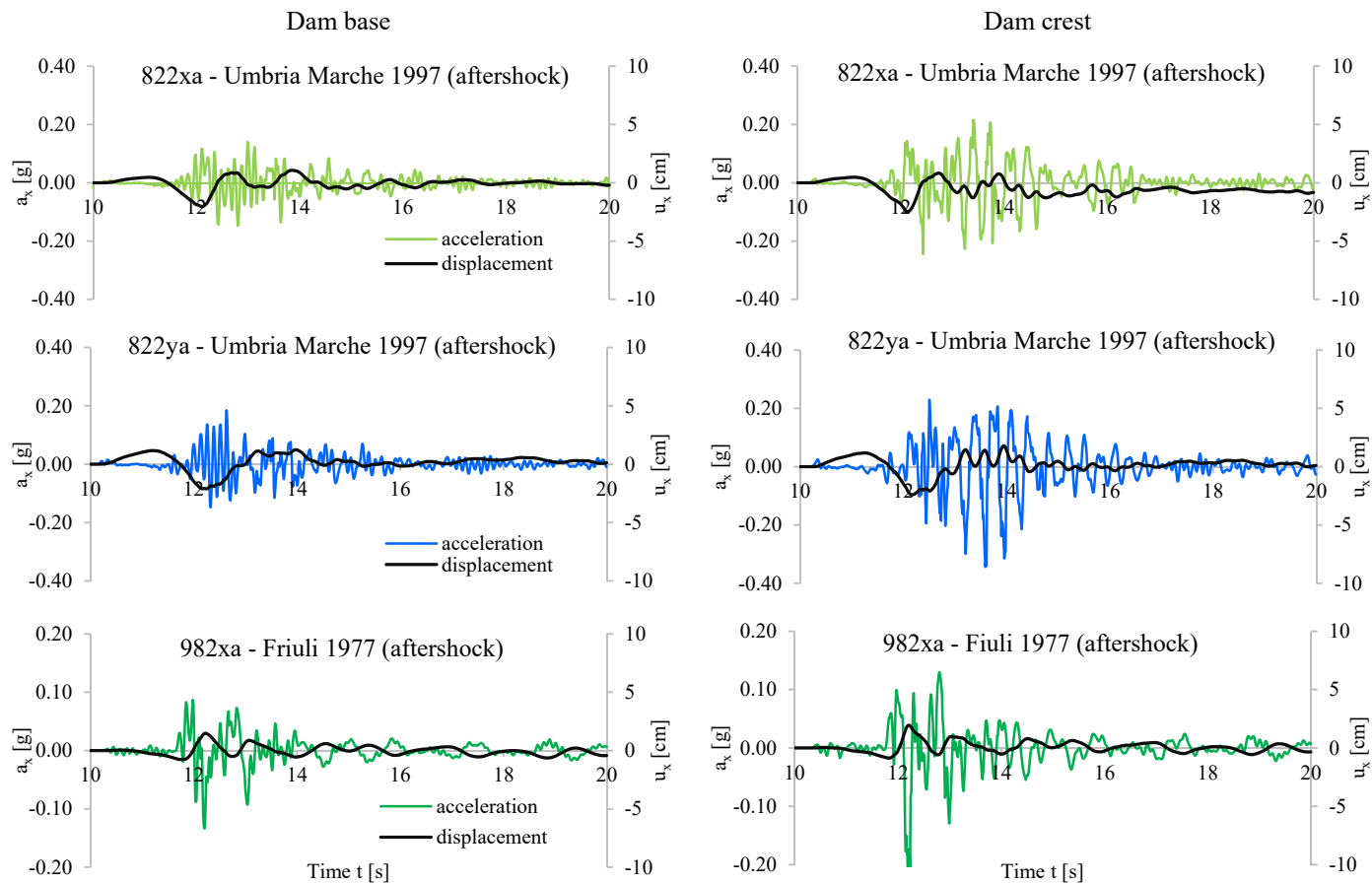


Figure 5-11. Horizontal acceleration and displacement time histories at dam base and dam crest for LLS (full reservoir condition).

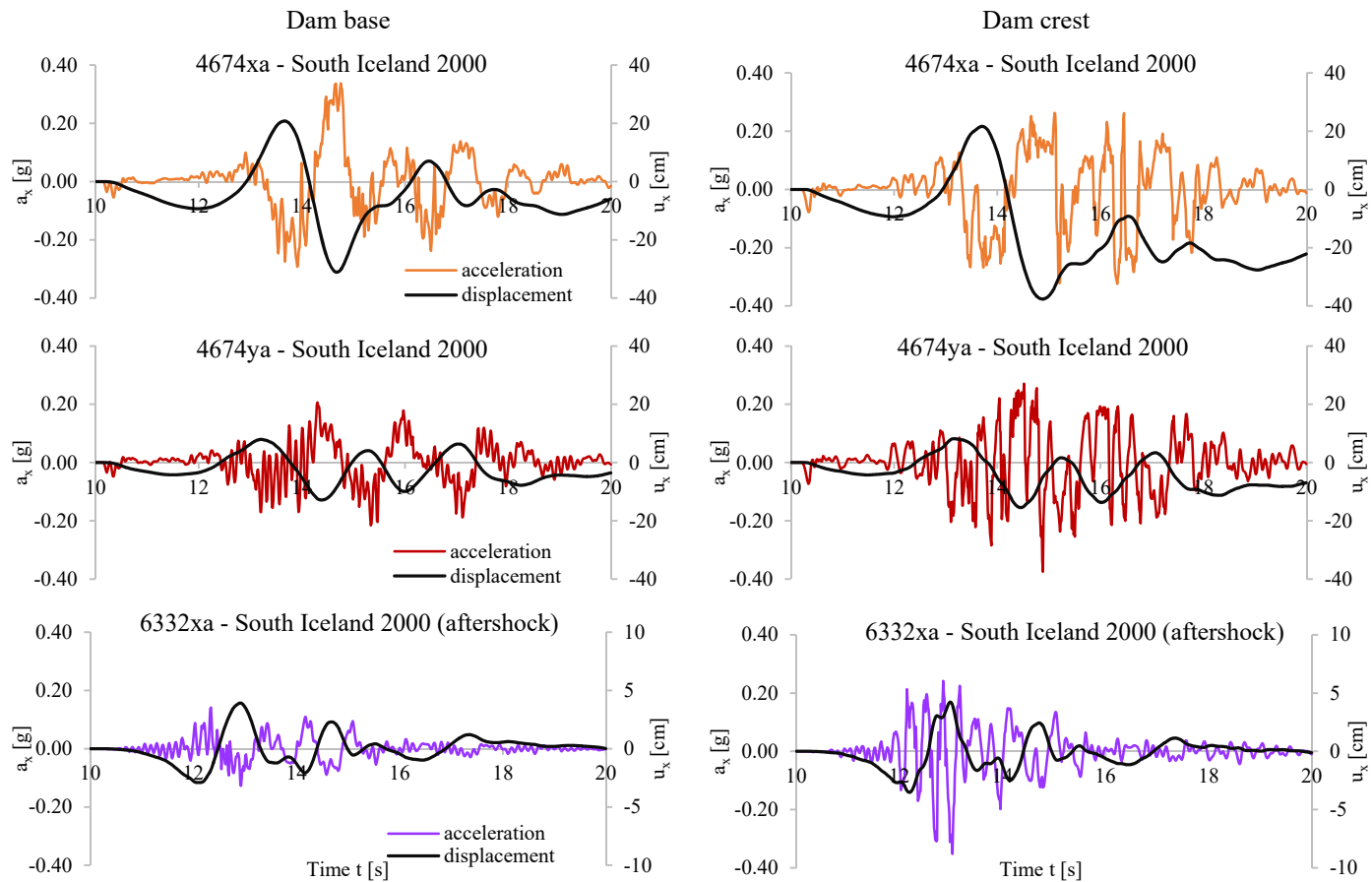


Figure 5-12. Horizontal acceleration and displacement time histories at dam base and dam crest for LLS (full reservoir condition).

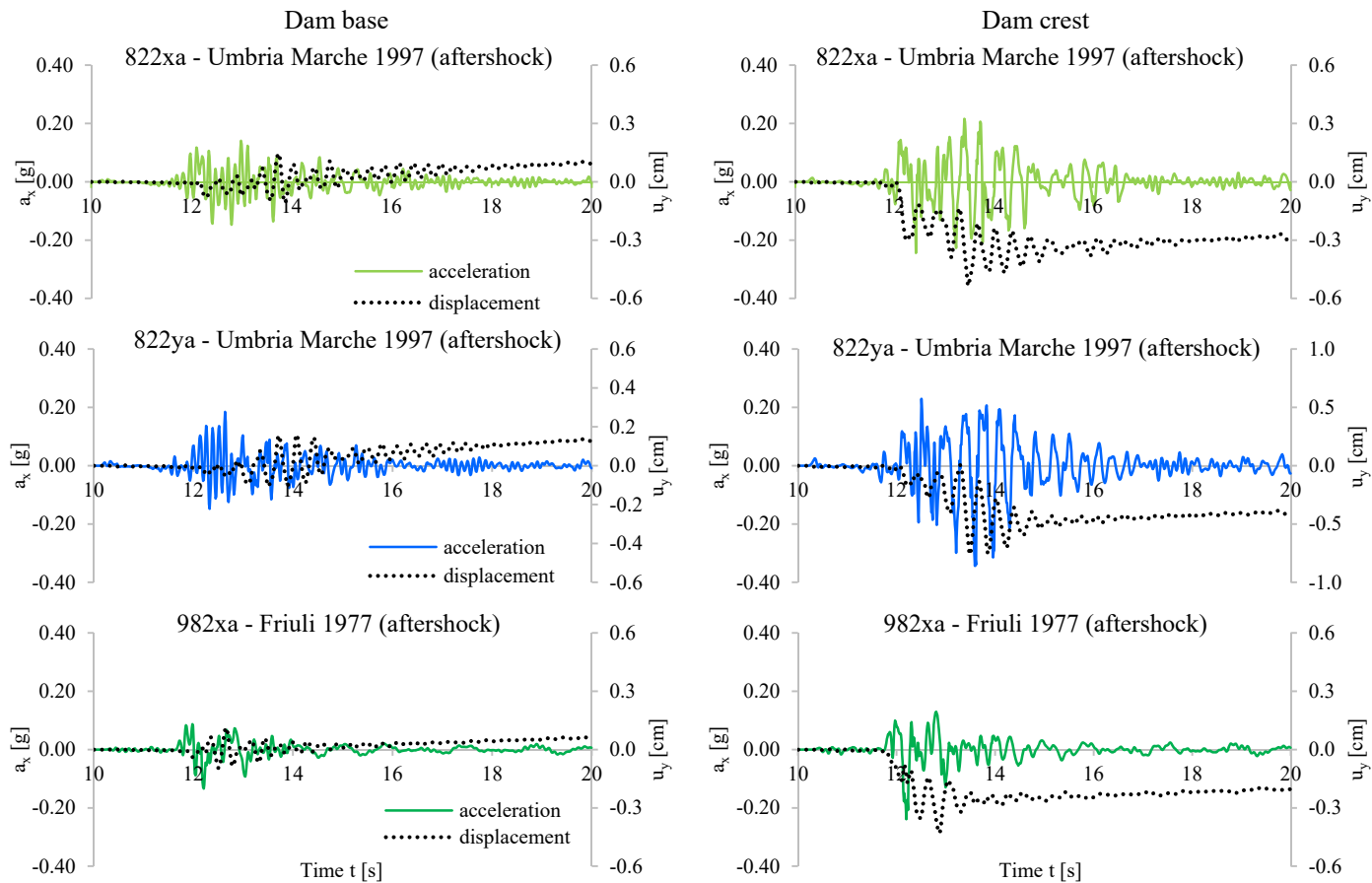


Figure 5-13. Horizontal acceleration and vertical displacement time histories at dam base and dam crest for LLS (full reservoir condition).

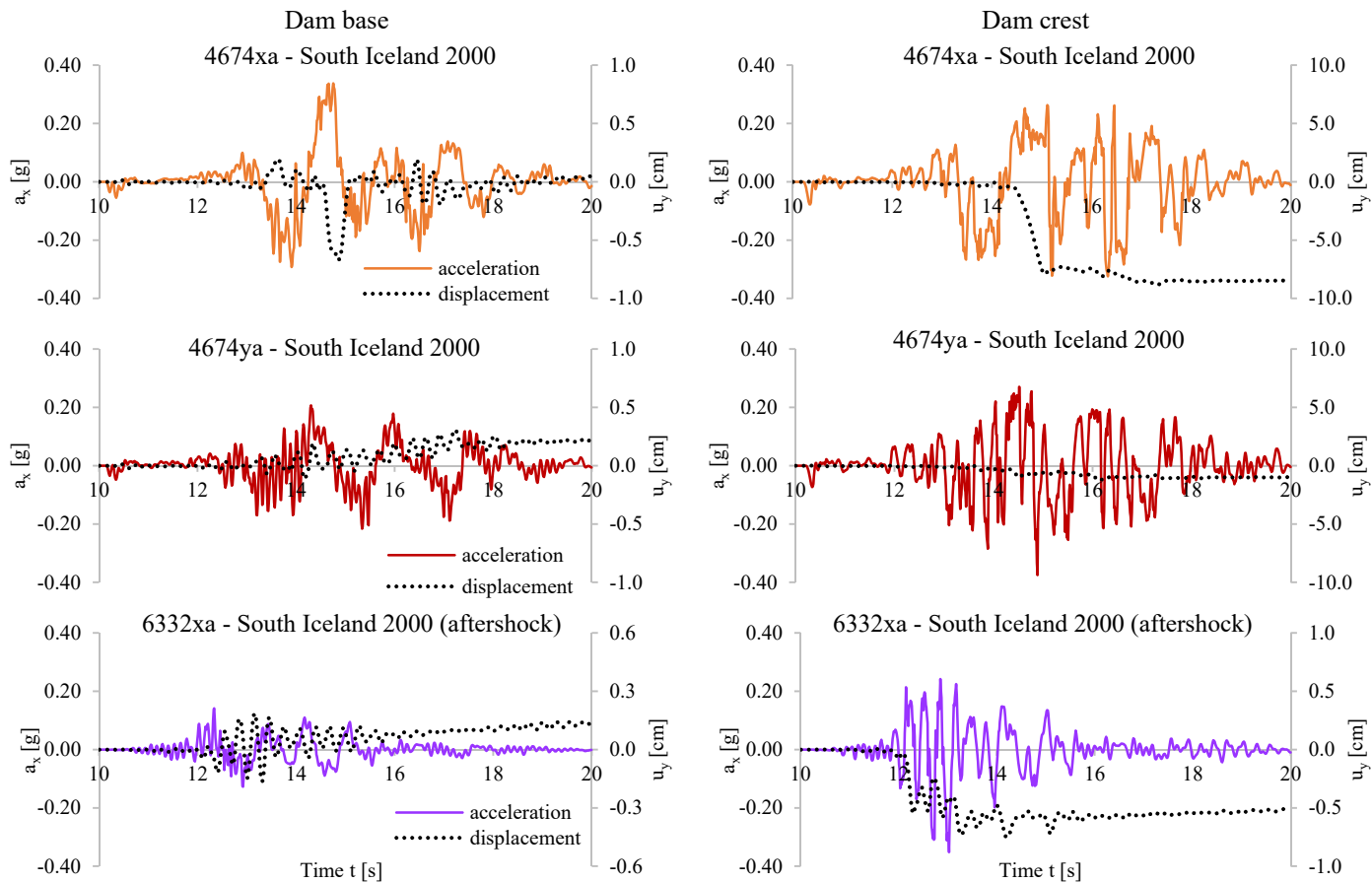


Figure 5-14. Horizontal acceleration and vertical displacement time histories at dam base and dam crest for LLS (full reservoir condition).

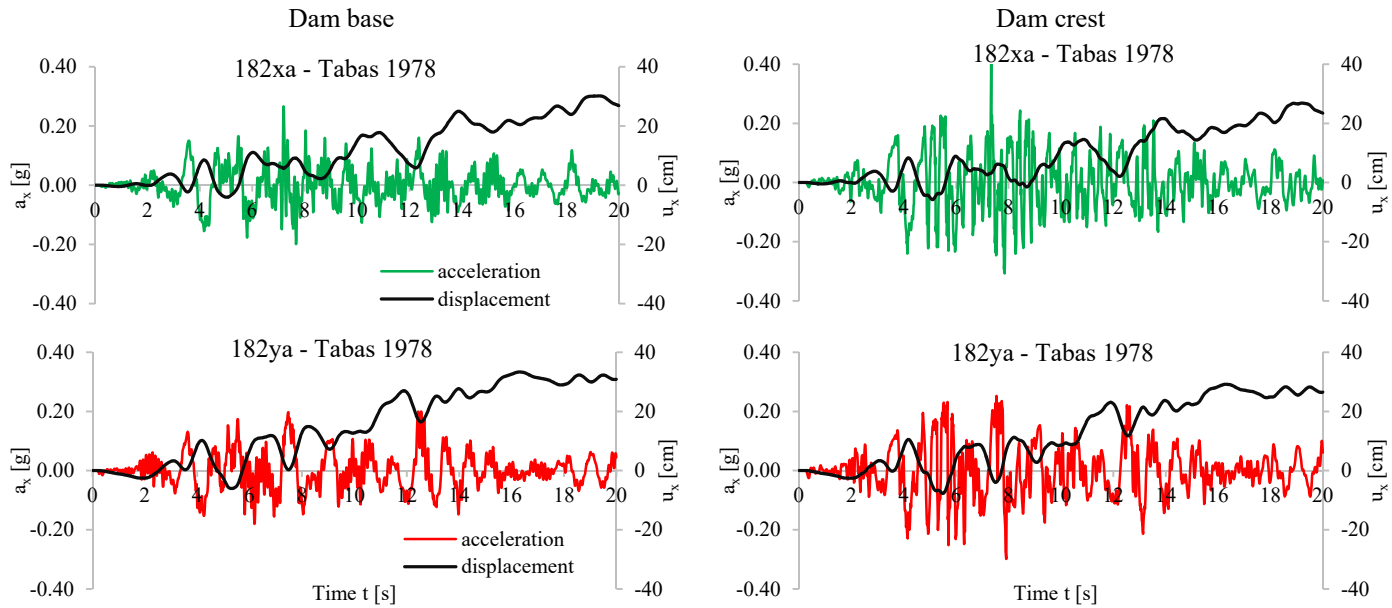


Figure 5-15. Horizontal acceleration and displacement time histories at dam base and dam crest for CLS (full reservoir condition).

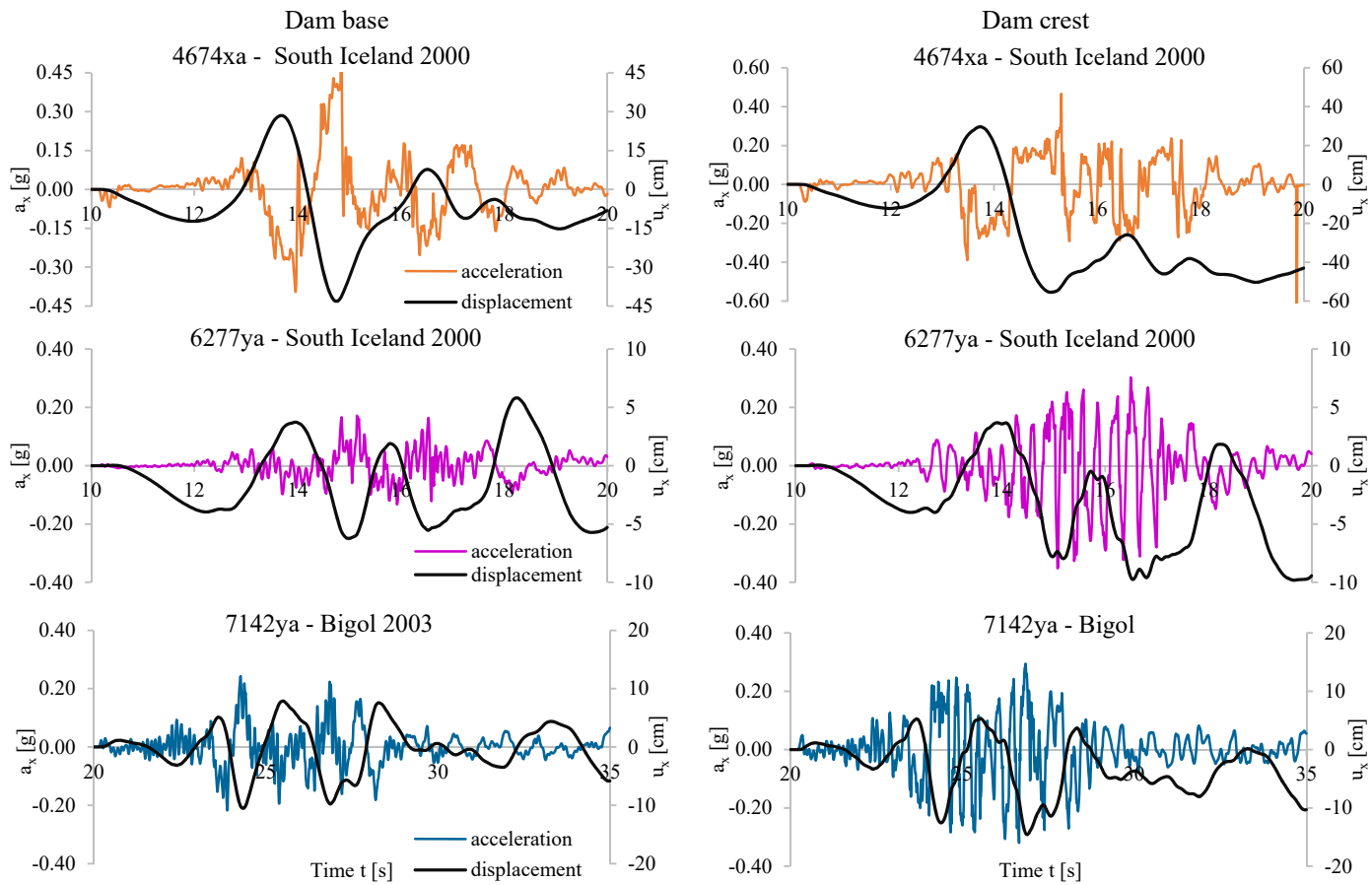


Figure 5-16. Horizontal acceleration and displacement time histories at dam base and dam crest for CLS (full reservoir condition).

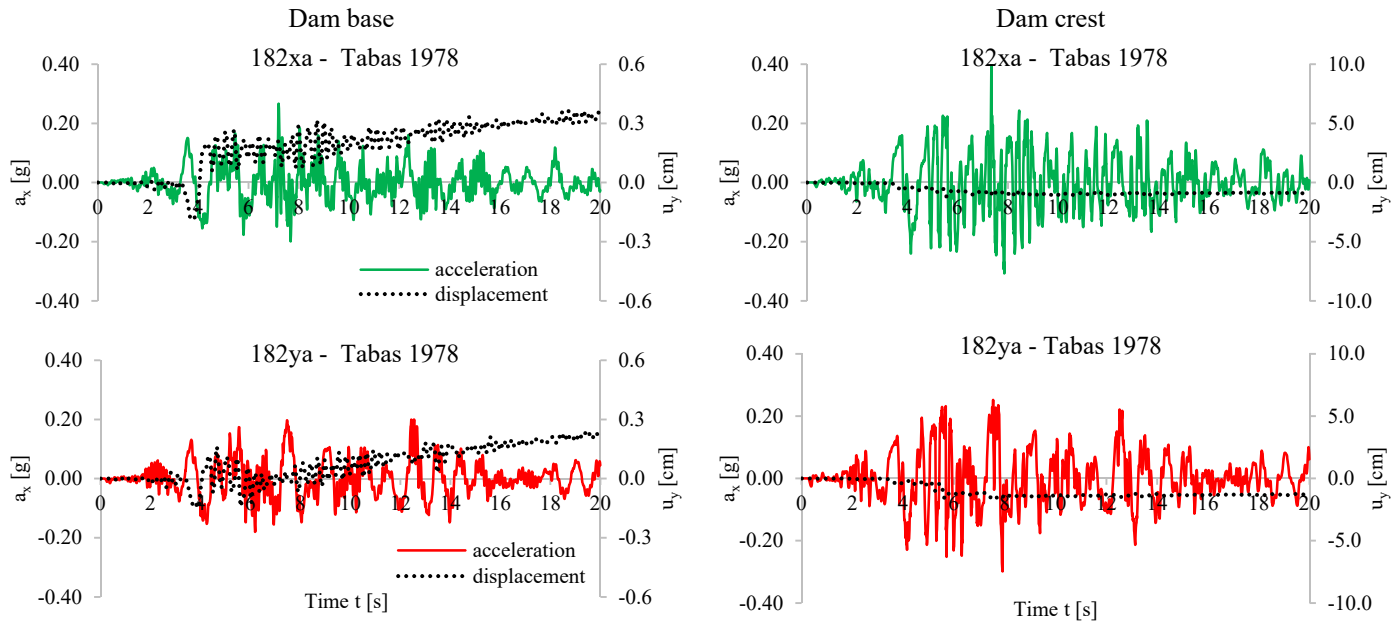


Figure 5-17. Horizontal acceleration and vertical displacement time histories at dam base and dam crest for CLS (full reservoir condition).

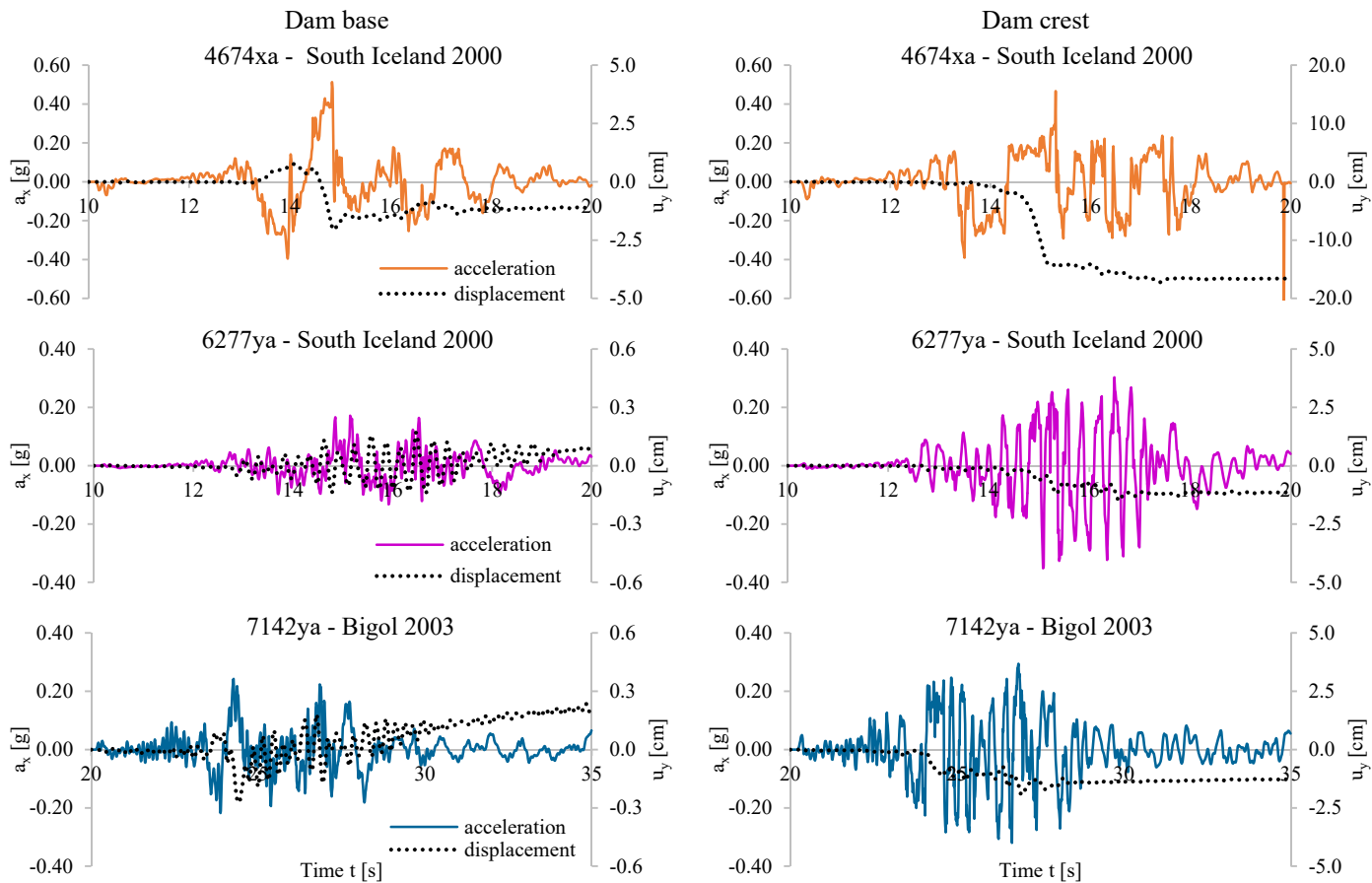


Figure 5-18. Horizontal acceleration and vertical displacement time histories at dam base and dam crest for CLS (full reservoir condition).

The permanent crest displacements in the horizontal direction are mostly negative (upstream direction), as better shown in Figure 5-19.

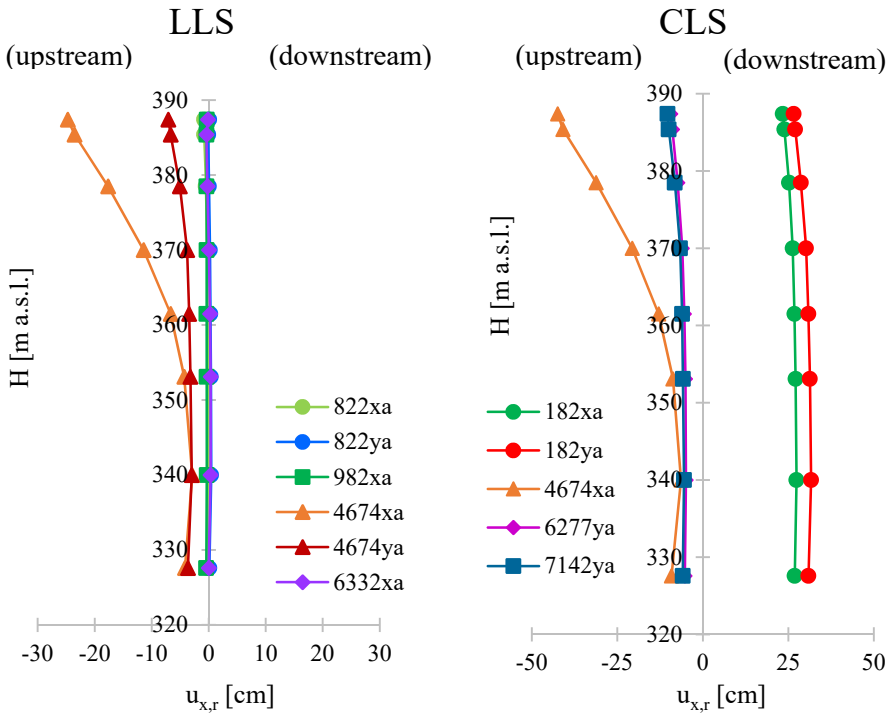


Figure 5-19. Horizontal residual displacement along the dam core axis.

The contours of residual horizontal displacement are provided, as an example, for the LLS South Iceland earthquake (4674xa). Figure 5-20a shows a yielding zone on the upstream shell, where the horizontal maximum displacements are located. Figure 5-20b shows permanent settlements, mostly concentrated on the upstream shell and close to the dam crest. These trends are found for most of the applied input motions both for the LLS and the CLS assessment of dam response.

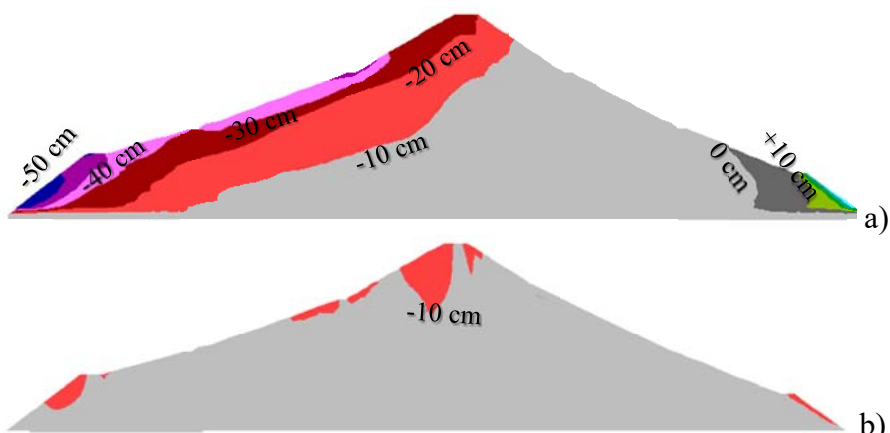


Figure 5-20. LLS: Residual displacement after the South Iceland earthquake (4674xa): a) horizontal displacements; b) vertical displacements.

Table 5-2 and Table 5-3 report a comparison between the main parameters of the adopted input motions and of the dam response expressed in terms of acceleration and displacements. In particular, the tables contain:

- the design acceleration at the dam site ($a_{g,NTC}$);
- the input acceleration at the model base after the deconvolution (a_{modelb});
- the maximum acceleration at the dam base ($a_{max,b}$) at the core axis;
- the maximum acceleration at the dam crest ($a_{max,crest}$) at the core axis;
- the horizontal and vertical residual displacements evaluated at the dam crest ($u_{x,r}$ and $u_{y,r}$).

LLS						
Earthquake	$a_{g,NTC}$ [g]	a_{modelb} [g]	$a_{max,b}$ [g]	$a_{max,crest}$ [g]	$u_{x,r}$ [cm]	$u_{y,r}$ [cm]
822xa	0.314	0.217	0.147	0.244	-0.81	-0.27
822ya	0.314	0.206	0.184	0.344	0.09	-0.39
982xa	0.314	0.133	0.133	0.239	-0.34	-0.19
4674xa	0.314	0.241	0.338	0.324	-24.73	-8.65
4674ya	0.314	0.225	0.216	0.375	-7.08	-1.01
6332xa	0.314	0.191	0.141	0.352	-0.12	-0.52

Table 5-2. LLS: comparison between the main parameters of the accelerometric signals and dam permanent displacements.

Earthquake	CLS					
	$a_{g,NTC}$ [g]	a_{modelb} [g]	$a_{max,b}$ [g]	$a_{max,crest}$ [g]	$u_{x,r}$ [cm]	$u_{y,r}$ [cm]
182xa	0.415	0.232	0.266	0.410	23.40	-0.83
182ya	0.415	0.249	0.199	0.298	26.56	-1.31
4674xa	0.415	0.321	0.512	0.760	-42.42	-15.1
6277ya	0.415	0.234	0.171	0.352	-9.41	-1.51
7142ya	0.415	0.307	0.242	0.320	-10.30	-1.28

Table 5-3. CLS: comparison between the main parameters of the accelerometric signals and dam permanent displacements.

Since for the dam core the Finn and Byrne (1991) model has been added to the Mohr-Coulomb constitutive law (§4.3.3), it was possible to compute the pore water pressures accumulated during the cyclic loading. Figure 5-21 shows the pore pressure contours due to the South Iceland earthquake (4674xa – LLS) simulation, which represents the most severe signal also in terms of seismic induced excess pore water pressures. The pore pressure distribution acting before the earthquake is provided in Figure 5-6.

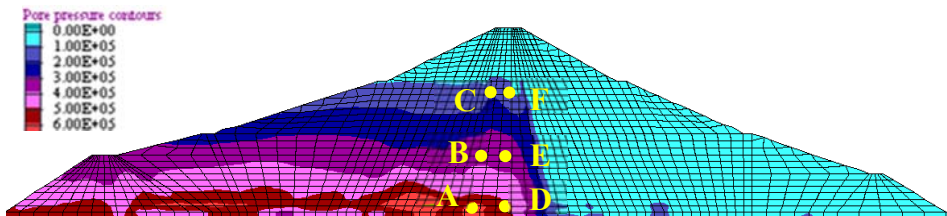


Figure 5-21. LLS: Pore pressure contours at the end of the dynamic stage considering the 4674xa input signal.

For the sake of clarity, time histories of the excess pore water pressures are presented in Figure 5-22 for some points of the core. Higher excess pore water pressures have been found at the core base (points A and D). With increasing elevation, the excess pore water pressures decrease; higher values were found in the center of the core with respect to the upstream side (points A, B and C).

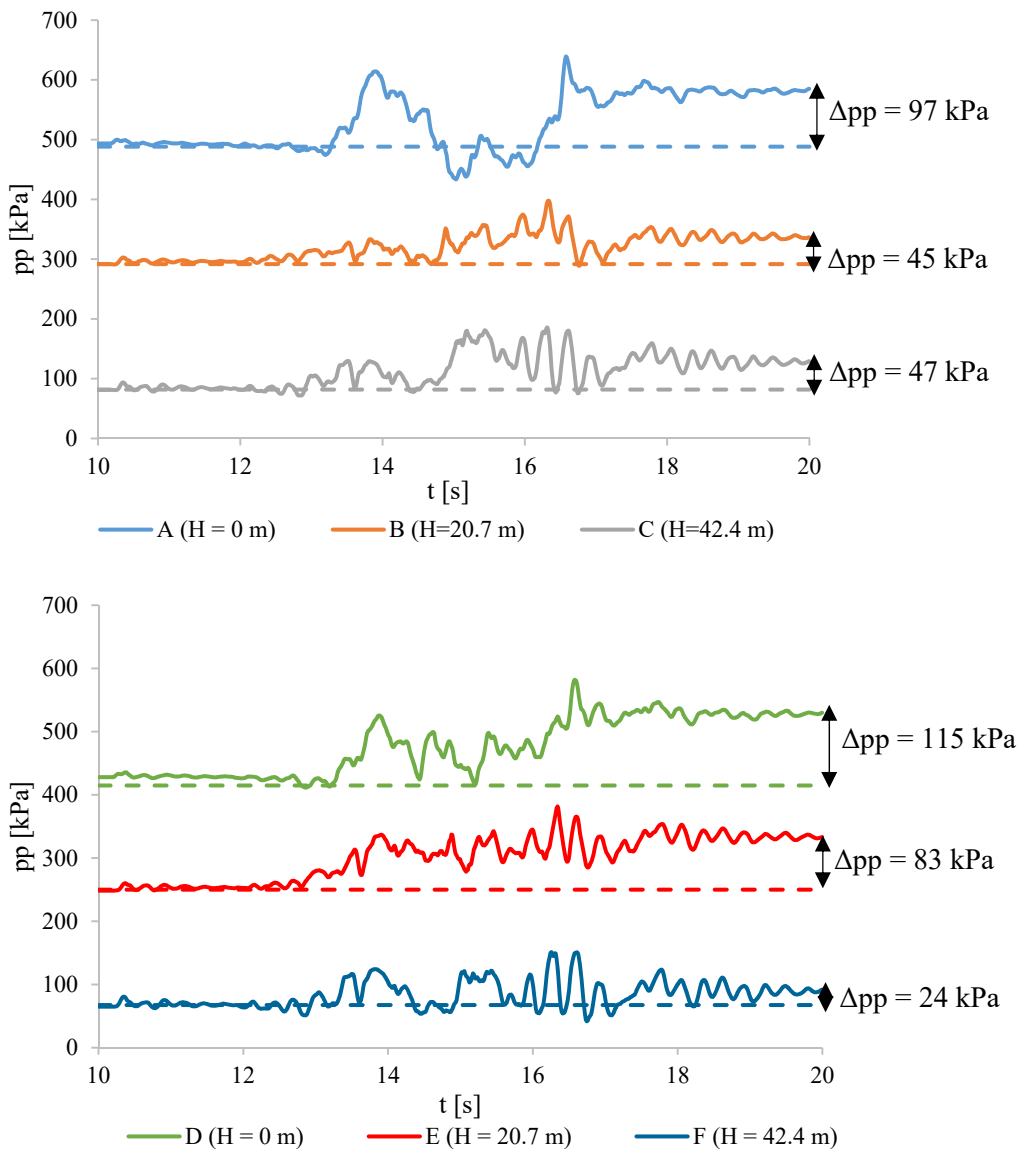


Figure 5-22. LLS: Pore pressure histories in some points of the core (South Iceland earthquake - 4674xa).

5.3. DRAWDOWN ANALYSES

This section illustrates the response of the dam to the drawdown of the reservoir considering different:

- initial conditions;
- drawdown rates;
- drawdown ratios.

The performed seismic analyses evidenced the South Iceland earthquake as the most severe seismic input for both limit states (LLS and CLS). Thus, the drawdown analysis has been performed after the dynamic analysis performed with the above mentioned accelerogram, scaled to 0.32g and 0.43g for the LLS and the CLS, respectively.

As anticipated in §4.3.6 (Figure 4-27) five drawdown rates were considered to carry out the water level lowering. So five drawdown analyses were performed.

In order to appreciate the different stress states arising in the dam before starting the drawdown and later on, effective stress paths (ESP) and total stress paths (TSP) for the reference points #3 and #5 (shown in Figure 5-23) are presented, considering the overall loading history imposed to the dam.

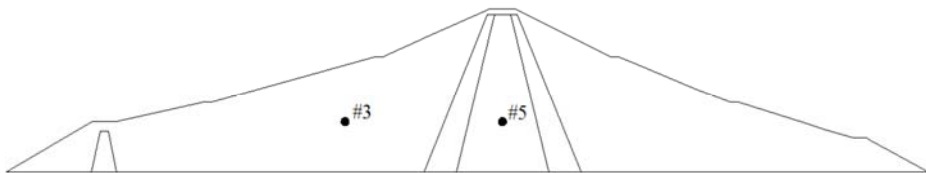


Figure 5-23. Reference points where the stress paths were plotted.

The effective stress path of point 3 (in the upstream shell) shows an increase of the mean effective (p') and deviator stress (q) during the construction stages due to the increase of the major principal stress (σ_1), and then a reverse path due to the first filling operations. Subsequently, due to the earthquake (LLS), there is a clear change in the drawdown initial stress state. The stress paths caused by the drawdown are strongly linked to the pore pressure dissipation over time (i.e. drawdown rates), as it will be better explained in the ensuing.

The TSP of point 3 is superimposed to the ESP for the construction stage, because completely drained behaviour for the shell material ($p = p'$) was assumed in the simulation. Then, in the first reservoir filling the mean stress (p) keeps increasing while the deviatoric stress remains almost constant.

Finally, after the earthquake, the stress paths caused by the drawdown show a sudden reverse. When the drawdown is slow (0.5 m/day), the stress path for the last stages is parallel to that of the reservoir filling. It may be related to the same filling/drawdown velocity, i.e. 0.5 m/day.

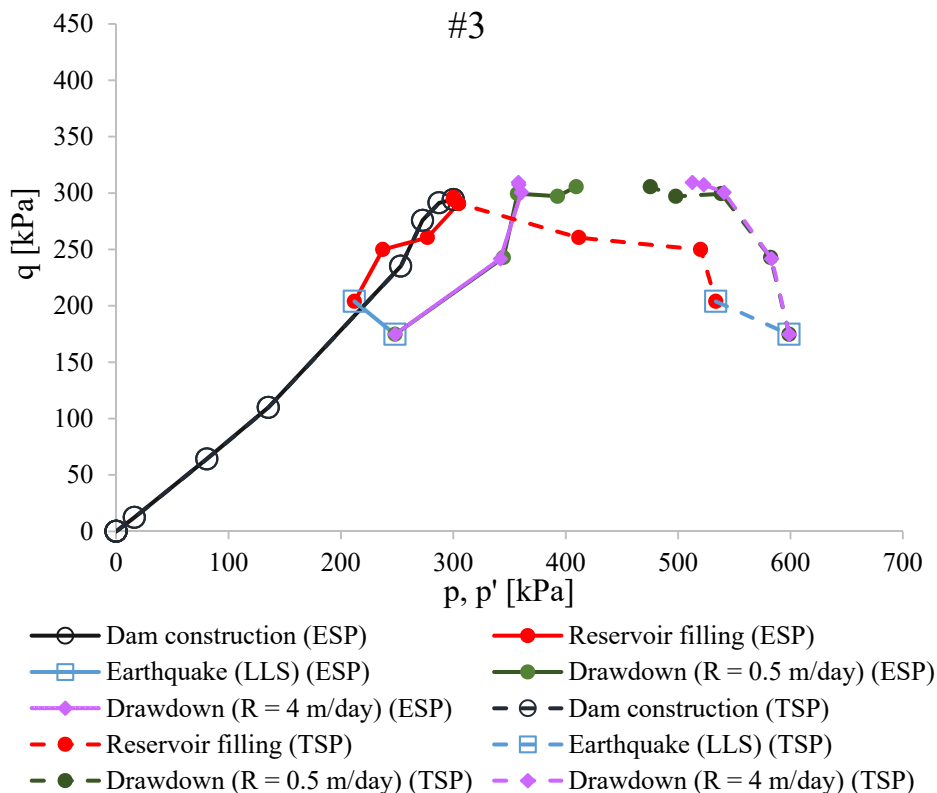


Figure 5-24. Stress path at point #3.

The effective stress path at point 5 (core axis) shows a similar path of point #3 during the construction stages. Then, q decreases and p' increases when the reservoir is filled. This depends on the increase of the minor principal stress (σ_3) while the major stress experiences a little change, until the steady-state condition is reached. Simultaneously p' increases because the excess water pressure developed during the construction stage is dissipating.

The drawdown operations make the effective stress path to move to the right or left, depending on whether the drawdown is slow or fast, respectively.

The total stress path of point 5 is only translated horizontally from the effective stress path by a value equal to the core pore water pressure.

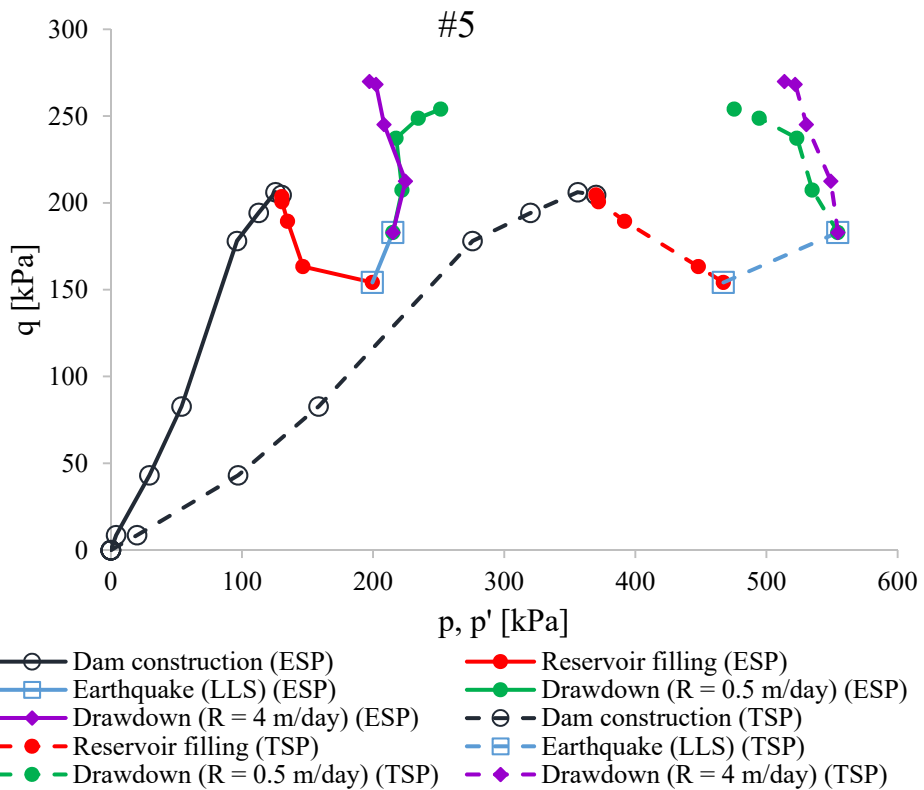


Figure 5-25. Stress path at point #5.

To appreciate the influence of the initial stress state on dam stability during the drawdown, the factor of safety (FOS) was evaluated with the procedure illustrated in §3.4. In particular, for a fixed drawdown rate (0.5 m/day), this factor was determined considering different ratios up to $L/H = 1$. The drawdown analyses will be performed both with and without the seismic stage simulation (LLS and CLS).

Some results in terms of factor of safety are presented below; the dashed line represents the variation of the FOS with the drawdown ratio L/H for the drawdown analysis, without the simulation of the seismic stage. The FOS represents the slope stability soon after the imposed drawdown in terms of L/H (i.e., no steady-state conditions have been reached in the embankment).

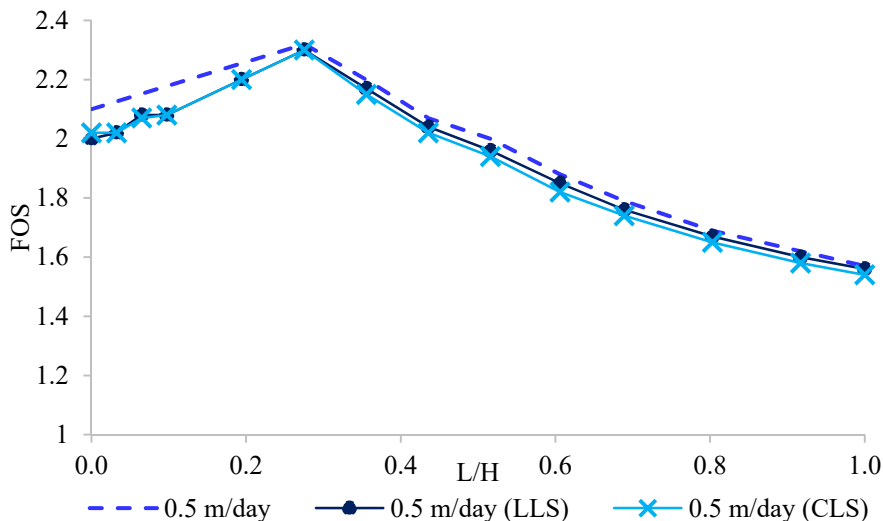


Figure 5-26. Effect of the initial state: 0.5 m/day.

From Figure 5-26 it emerges that higher FOS values are always found if the drawdown is carried out without simulating the earthquake. Conversely, the occurrence of an earthquake (LLS or CLS) could reduce the FOS computed in the upstream shell during the drawdown, especially for $L/H < 0.3$. In short, two transient phenomena are superimposed in the dam embankment: one due to the earthquake and another due to the drawdown, which starts soon after (1 day after).

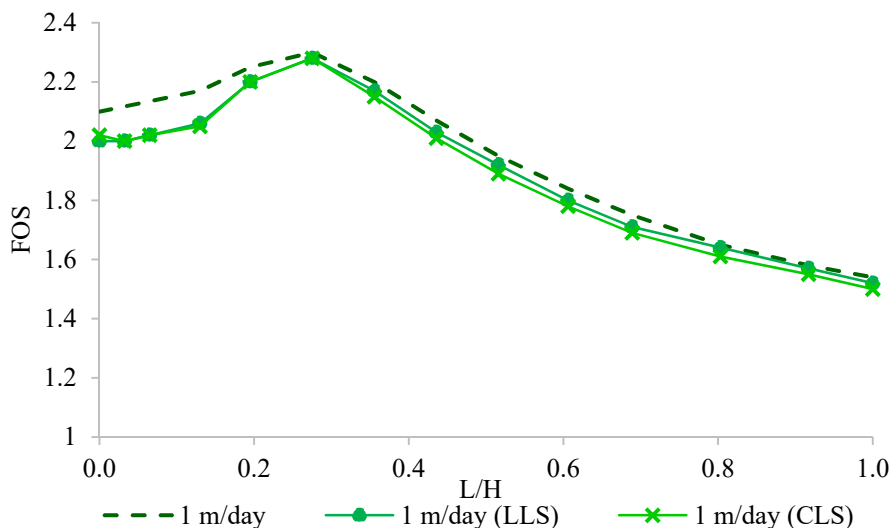


Figure 5-27. Effect of the initial state: 1 m/day.

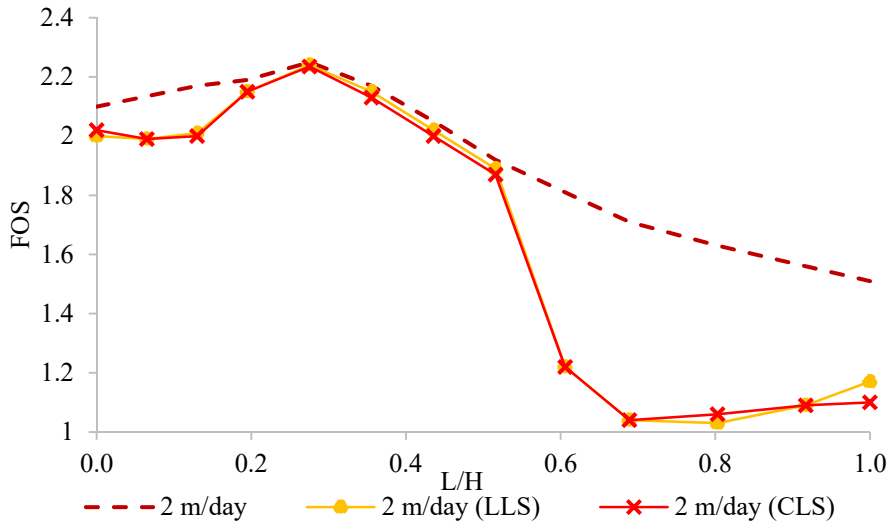


Figure 5-28. Effect of the initial state: 2 m/day.

The response observed in Figure 5-26, is also affected by the drawdown rate, as it can be observed in figures from Figure 5-27 to Figure 5-29, corresponding to the drawdown rate of 1 m/day up to 4 m/day, respectively.

It could be stated that more rapid is the drawdown simulated after the earthquake stage, lower is the dam stability up to $L/H < 0.3$.

For $L/H > 0.3 \div 0.5$, the effect of an increase of drawdown rate (Figure 5-28; Figure 5-29) on dam stability is more important than the past loading history suffered by the dam.

It is worth point out that in the drawdown analyses dam stability is evaluated at the end of the emptying operations for every L/H . This means that non-steady state conditions have been reached in the embankment. For this reason, in the above figures we do not observe the expected increase in FOS after the drawdown. This will occur if steady-state conditions are expected to occur.

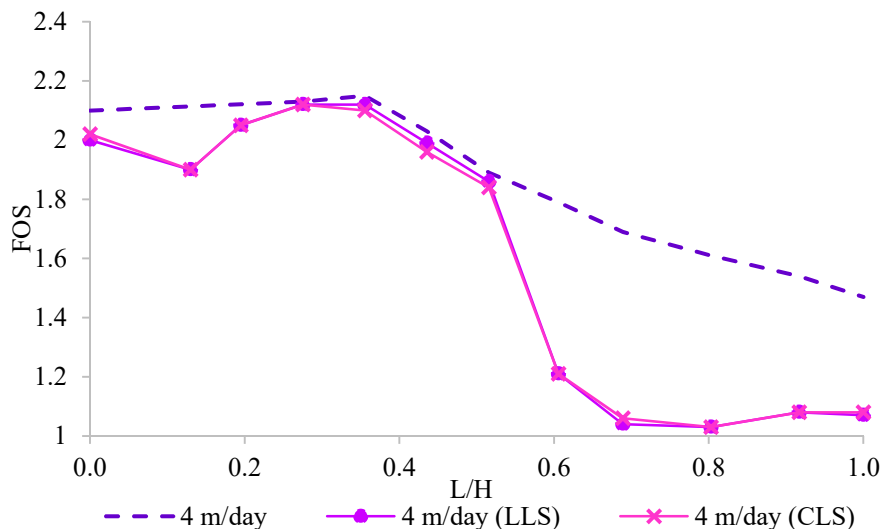


Figure 5-29. Effect of the initial state: 4 m/day.

As previously observed, drawdown rate is a crucial variable for dam stability.

A close correlation between the pore pressure changes due to a rapid drawdown, permeability and drawdown rates exists. After a suddenly water level lowering, the nodes placed on the boundary denote a sudden decrease of pore pressure. Conversely, if the nodes are far enough from the boundary they may not be affected by the change of the external loads caused by the drawdown. So a seepage from this latter zone to the former one starts developing.

Considering a slow drawdown rate (0.5 m/day), the pore pressure decrease in the upstream shell occurs until the reservoir water level is above the cofferdam of the Campolattaro dam. After that, the low permeability of the cofferdam obstructs the free draining of the water in the upstream zone. In Figure 5-30 pore pressure evolution for a drawdown rate of 0.5 m/day are shown for the whole cross section of the dam.

Figure 5-31 shows the water head changes for points #3, #4 and #5 from the steady state condition reached after the first reservoir filling (day 0), at the end of the seismic event and during a slow drawdown (more than 100 days).

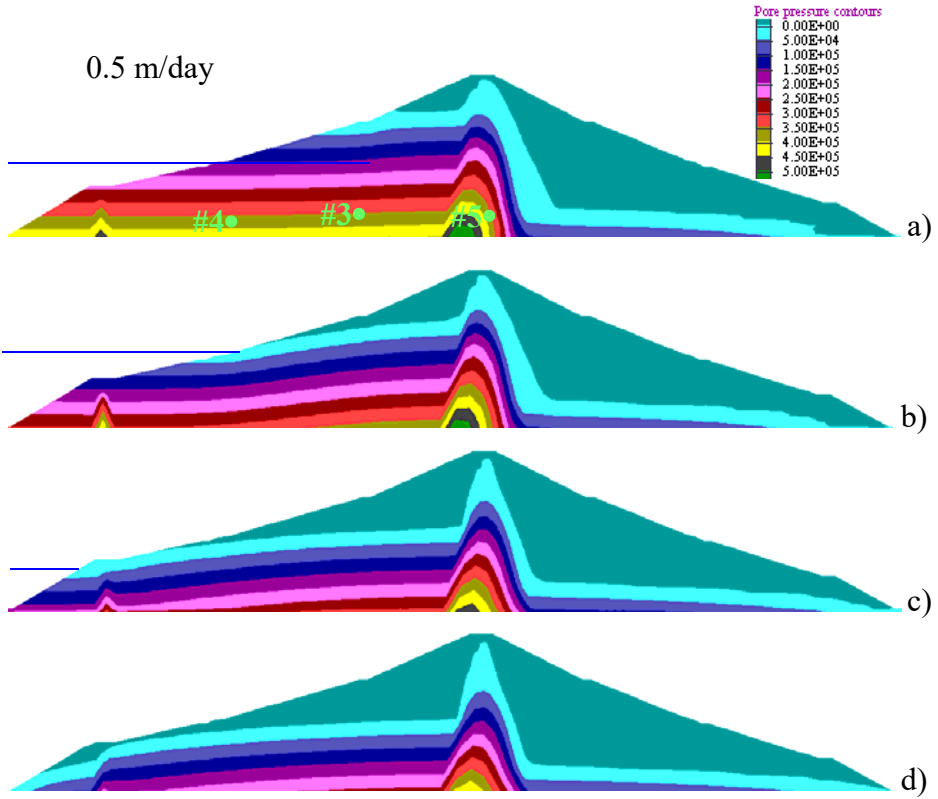


Figure 5-30. Pore pressure contours during a slow drawdown (0.5 m/day) from top to bottom: a) $L/H = 0.2$; b) $L/H = 0.4$; c) $L/H = 0.7$; d) $L/H = 1$.

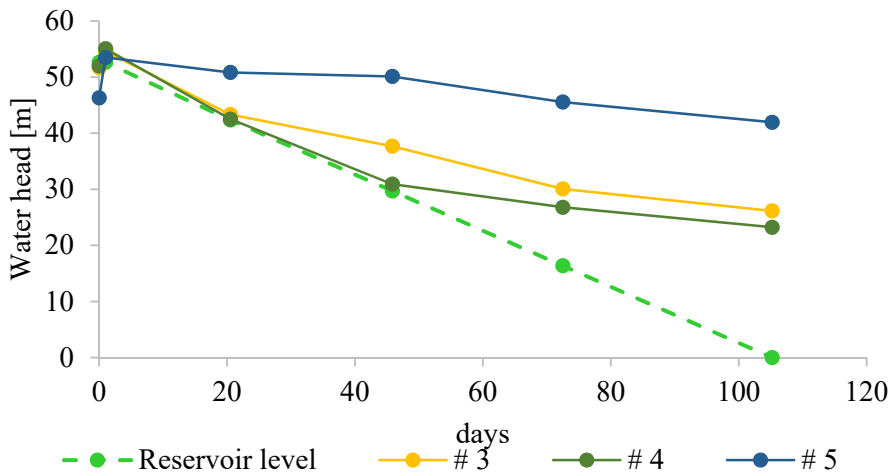


Figure 5-31. Water head changes during a slow drawdown (0.5 m/day).

When a rapid drawdown (4 m/day) is considered, the pore pressure changes in the upstream shell are not so evident as in the previous case (Figure 5-32). This occurs because the change in external water level does not allow the drainage of the upstream shell, even if the latter is made of a highly permeable soil.

This statement is further supported by Figure 5-33 where the water head changes in points #3 and #4 are plotted.

The water head in point #3 is affected by the lowering of the water level above the point itself. When the external water level has reached the dam mid height ($L/H \approx 0.5$), the pore pressure change no longer occurs, if steady state conditions are not reached ($t > 14$ days).

Instead, point #4, located closer to the upstream boundary, follows the change of the reservoir level.

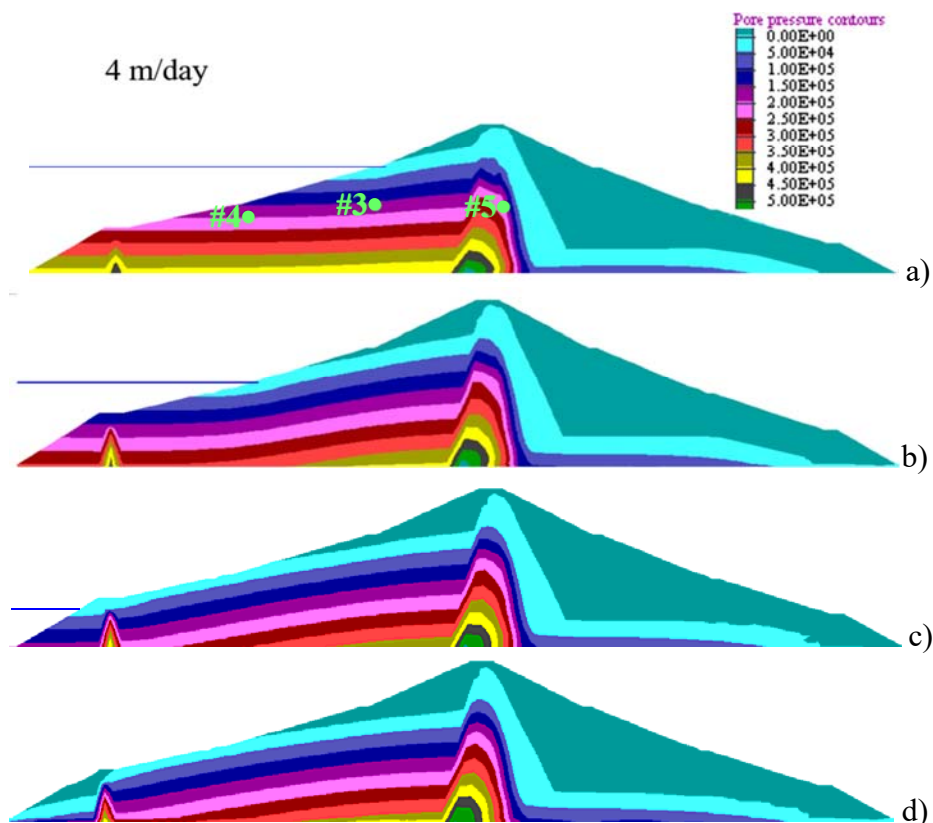


Figure 5-32. Pore pressure contours during a rapid drawdown (4 m/day) from top to bottom: a) $L/H = 0.2$; b) $L/H = 0.4$; c) $L/H = 0.7$; d) $L/H = 1$.

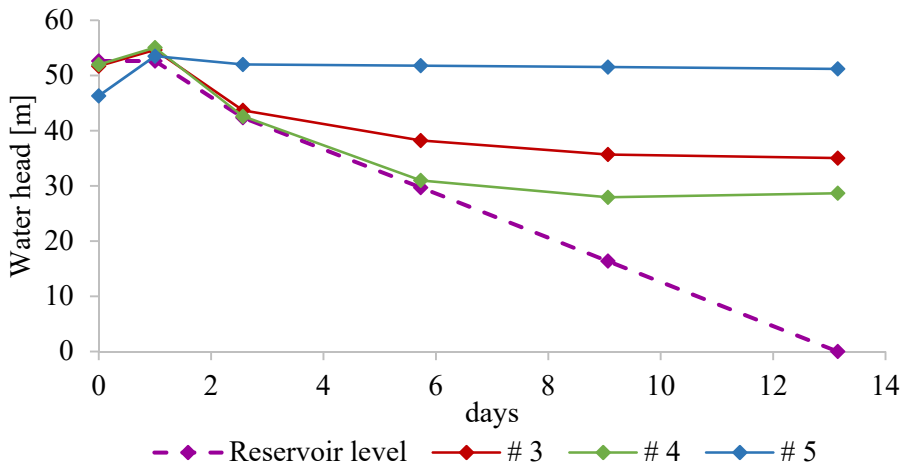


Figure 5-33. Water head changes during a rapid drawdown (4 m/day).

The point placed in the core (#5) is not influenced by the fast drawdown. This means that when the dam experiences a rapid drawdown, the core does not notice what is happening on its boundary and still retains the seismic-induced pore water pressures.

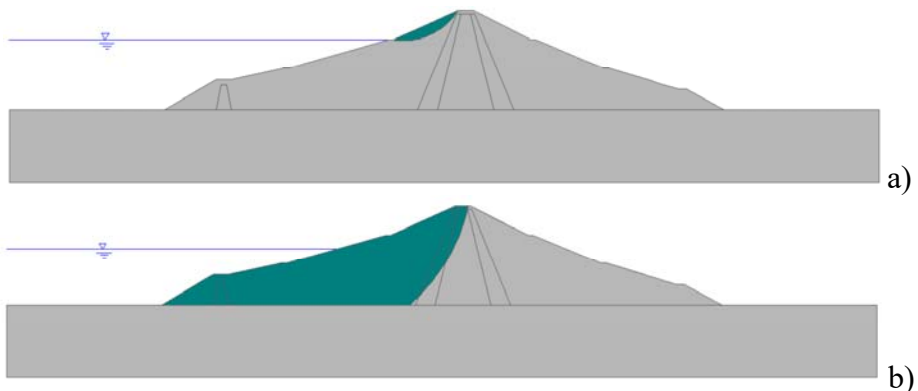


Figure 5-34. Sliding surface: a) $L/H = 0.2$; b) $L/H = 0.4$.

Figure 5-35 highlights the FOS evolution for different drawdown rates and initial conditions. When the drawdown is performed without simulating the seismic phase, an increase of the factor of safety is observed in the first stages of the drawdown, associated with a deepening of the sliding surface (Figure 5-34). Furthermore, the FOS is higher as slower the drawdown rate is: soils are becoming more and more unsaturated and this causes an increase of the shear resistance of the soil (see Appendix A §A.5).

If the drawdown is modelled after a strong earthquake, it can be observed that, in the first stages of drawdown, the FOS firstly decreases (with this reduction more pronounced for higher drawdown rates) and then increases up to reach the dashed curves corresponding to the drawdown simulated without the seismic stage. The decrease in slope stability observed for water lowering soon after the earthquake may be due to the seismic-induced pore water pressure and stress redistribution. After that, with $L/H > 0.3$ (figures Figure 5-28 and Figure 5-29) the effects of the initial conditions on the FOS become less important (dashed and continuous lines superimposed). For very high drawdown rates (2 or 4 m/day) the FOS abruptly drops to 1 when $L/H = 0.5$ (Figures Figure 5-28 and Figure 5-29), i.e. when the reservoir has been emptied for almost half of the dam height.

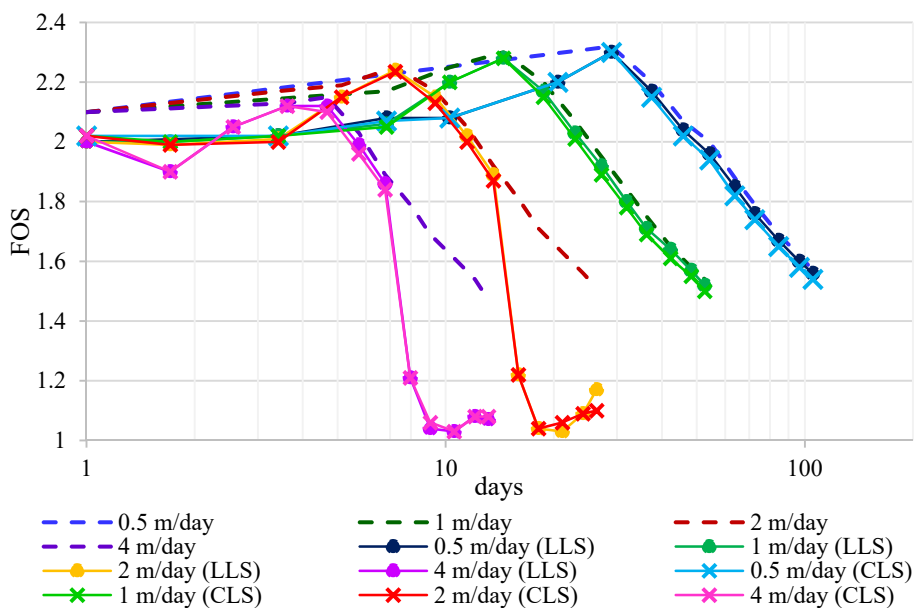


Figure 5-35. Dam FOS over time.

The reason why the earth embankment becomes unstable is that, in consequence of having discharged the water load, soil strength is decreased remarkably by the decrease of total normal stresses and of the insufficient decrease of the pore pressure that should be accompanied with that of the former. Akai (1957), to explain the mechanism of this type of failure, drew Mohr circles in a soil element near the upstream slope, from which the position of stress circle and the strength just after drawdown and in the following period are cleared, referring to Table 5-4.

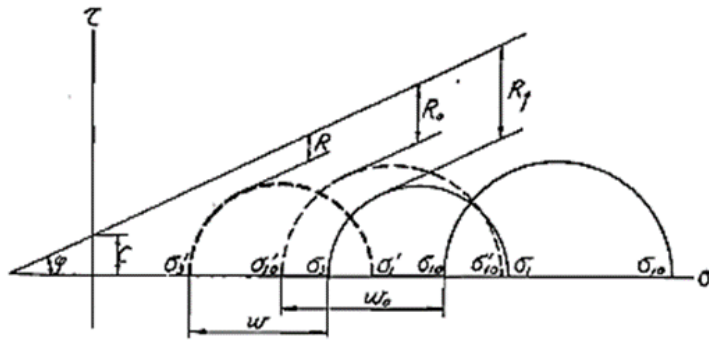


Figure 5-36. Mohr stress circles and residual strengths in the embankment before and after drawdown (Akai, 1957).

	Before drawdown	Just after drawdown	After lapse
Total stresses	σ_{10}, σ_{30}	σ_1, σ_3	σ_1, σ_3
Pore pressure	w_0	w	$w \rightarrow 0$
Effective stresses	$\sigma_{10}', \sigma_{30}'$	σ_1', σ_3'	$\sigma_1' \rightarrow \sigma_1, \sigma_3' \rightarrow \sigma_3$
Strength	R_0	$R (< R_0)$	$R \rightarrow R_f$

Table 5-4. Relation between stresses, pore pressure and residual strength in an earth embankment before and after drawdown (Akai, 1957).

As mentioned before, in this study the dam stability is evaluated at the end of the emptying operations for every L/H, so the beneficial influence of the time lapse on the final strength cannot be appreciated, as reported by Akai (1957).

The Mohr-Coulomb failure envelope is presented in Figure 5-37 for the upstream shell (without the cofferdam). The represented stress couples correspond to the point on the Mohr's circle which is closest to the shear failure surface ($c' = 0$ kPa and $\phi' = 43^\circ$). In the τ - σ' plot, the stresses are represented considering the soil suction influence as reported in eq. 3.4 (§3.1) in accordance with stress formulation by Bishop (1960).

Comparing the initial failure envelope of the upstream shell with the plots corresponding to a 4 m/day drawdown (Figure 5-38), it can be noticed that initially there are small stress changes and the most vulnerable part of the upstream shell is close to the boundary (Figure 5-38a, $\sigma'_n < 10$ kPa).

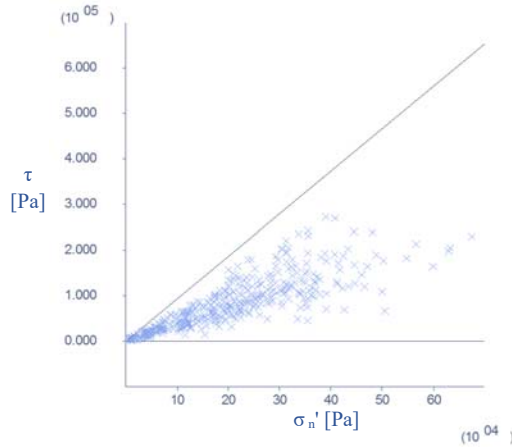


Figure 5-37. Failure surface plot, shear stress vs normal stress: stress state before the drawdown.

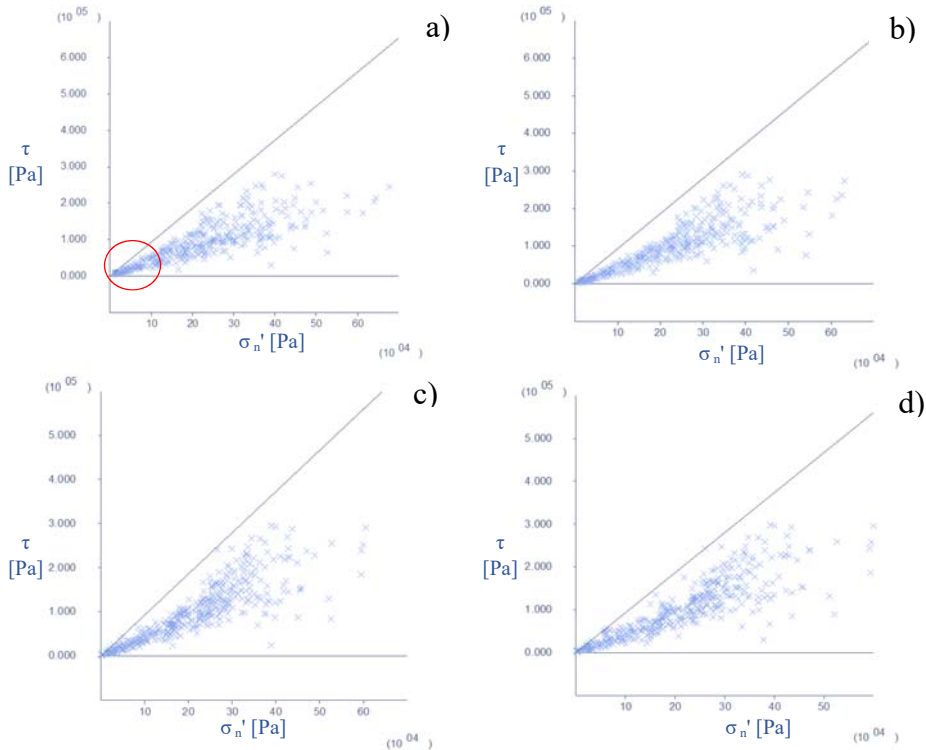


Figure 5-38. Failure surface plot, shear stress vs normal stress ($R=4$ m/day): a) $L/H = 0.2$; b) $L/H = 0.4$; c) $L/H = 0.7$; d) $L/H = 1$.

Then, in the upper mid height of the dam the seepage starts, the pore pressures decrease (as shown in Figure 5-41 and Figure 5-42) and there is an increase in strength. When $L/H \geq 0.4$, the total stresses decrease due to the reservoir load removal, but the soil is still completely saturated (positive

pore pressure, as plotted in Figure 5-43 and Figure 5-44). Therefore, there is a resulting reduction in the effective stress state on the upstream boundary and some points move close to the failure envelope (Figure 5-38c – d). The total stress, effective stress and pore pressure changes play their role in the overall stability of the dam; there is an initial increase of the factor of safety ($L/H < 0.4$) and then a descending branch ($L/H > 0.4$) as shown in Figure 5-29.

Figure 5-39 shows the Mohr-Coulomb failure envelope during the 0.5 m/day drawdown. When the drawdown rate is slow (0.5 m/day), the beneficial effect of the time lapse on the stress state, showed in Figure 5-36, was observed soon after the drawdown. Indeed, the progressive pore pressure decrease balances the total stress reduction, keeping the upstream shell under the failure envelope.

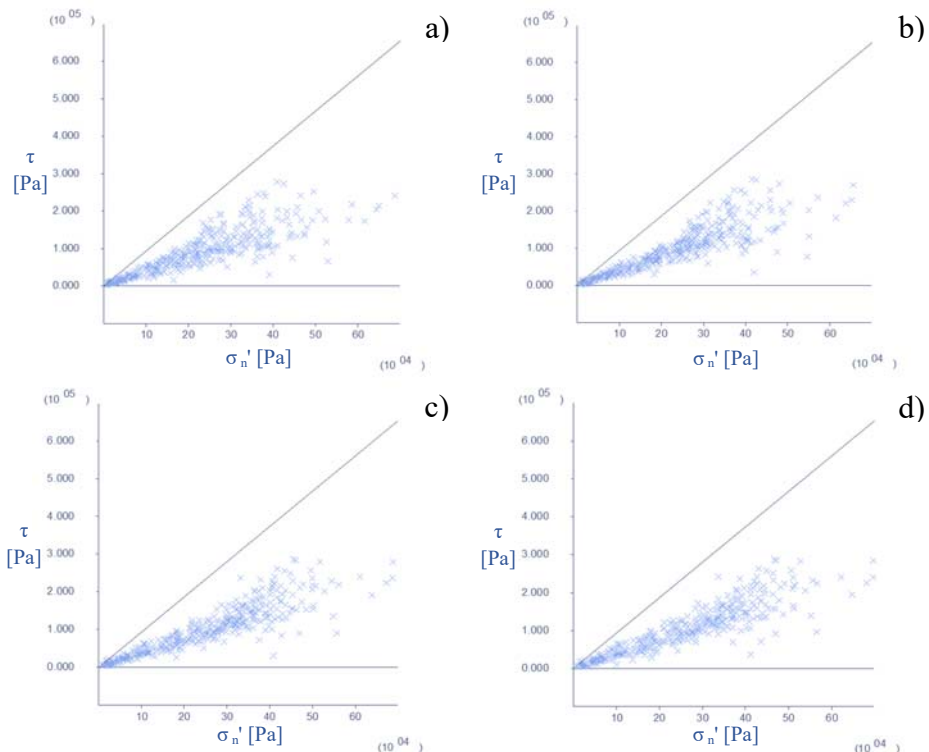


Figure 5-39. Failure surface plot, shear stress vs normal stress ($R=0.5$ m/day): a) $L/H = 0.2$; b) $L/H = 0.4$; c) $L/H = 0.7$; d) $L/H = 1$.

The pore pressure evolution for such drawdown analyses is plotted in Figure 5-45 - Figure 5-48. The pore pressures show negative values in a

superficial zone of the upstream shell whose thickness increases with the amount of L/H . In this zone an increase in shear strength is obtained due to negative pore water pressure generation and soil suction contribution. So a critical zone may be envisaged within the upstream shell between the saturated and unsaturated portion. Furthermore, this interface may also be located between different materials, which have different shear strength. In terms of the overall stability of the dam, this response promotes a deeper failure surface, thus generating an increase of the safety factor with respect to the other cases previously considered.

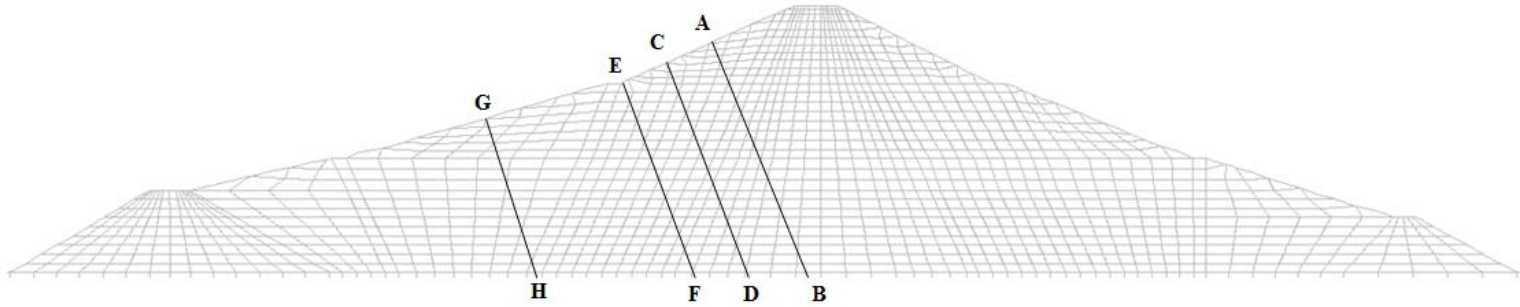


Figure 5-40. Reference lines.

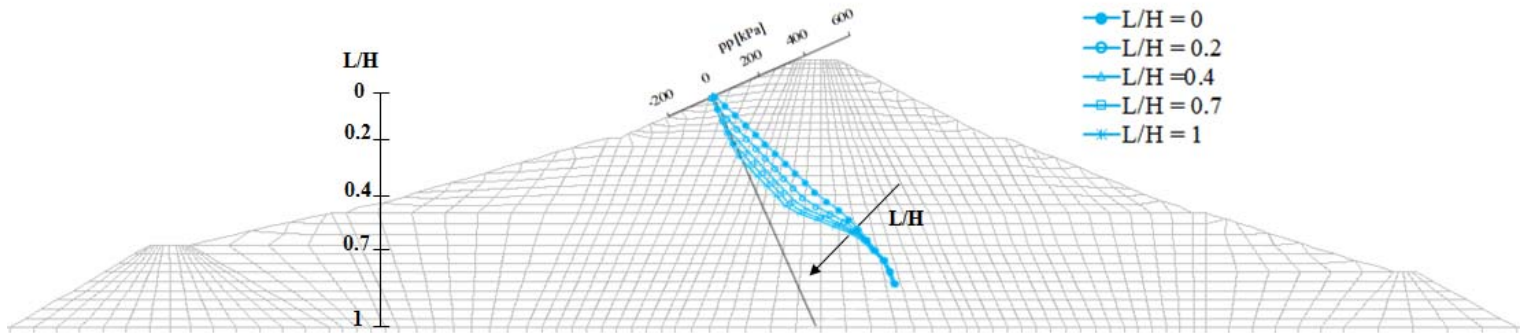


Figure 5-41. Pore pressure vs depth for $R = 4$ m/day (line AB).

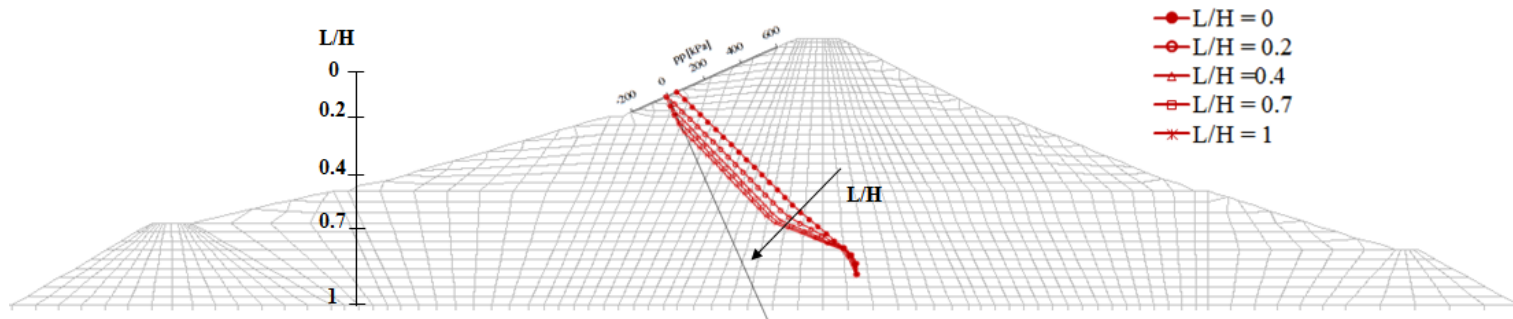


Figure 5-42. Pore pressure vs depth for $R = 4$ m/day (line CD).

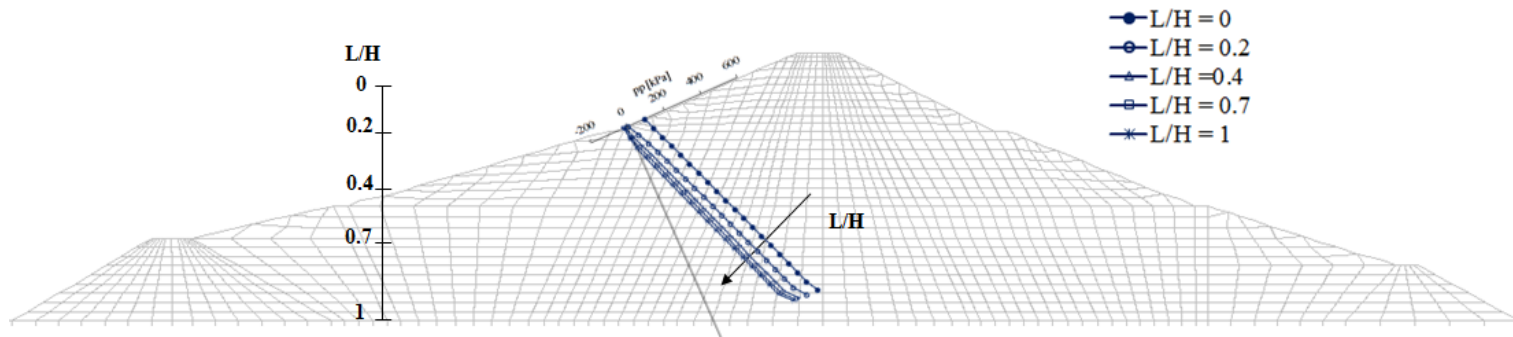


Figure 5-43. Pore pressure vs depth for $R = 4$ m/day (line EF).

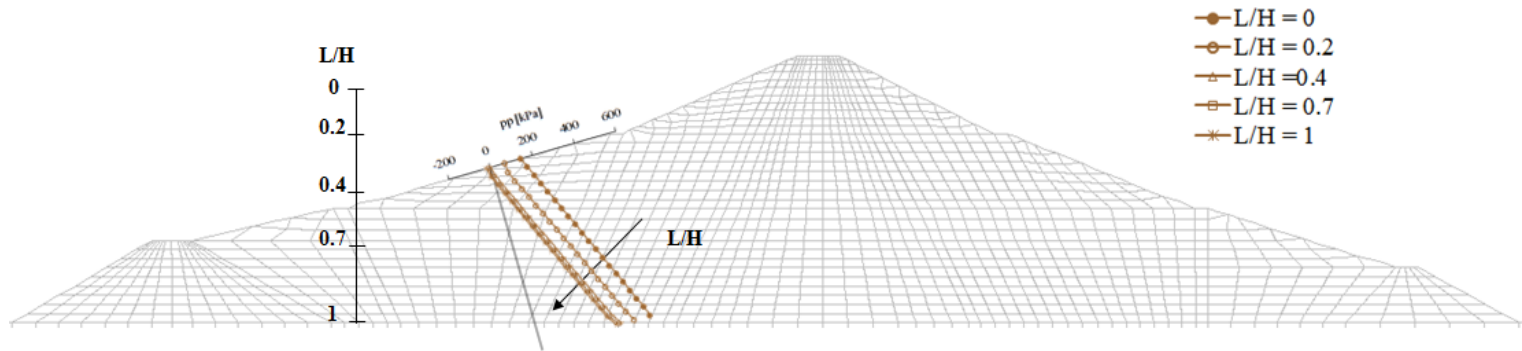


Figure 5-44. Pore pressure vs depth for $R = 4$ m/day (line GH).

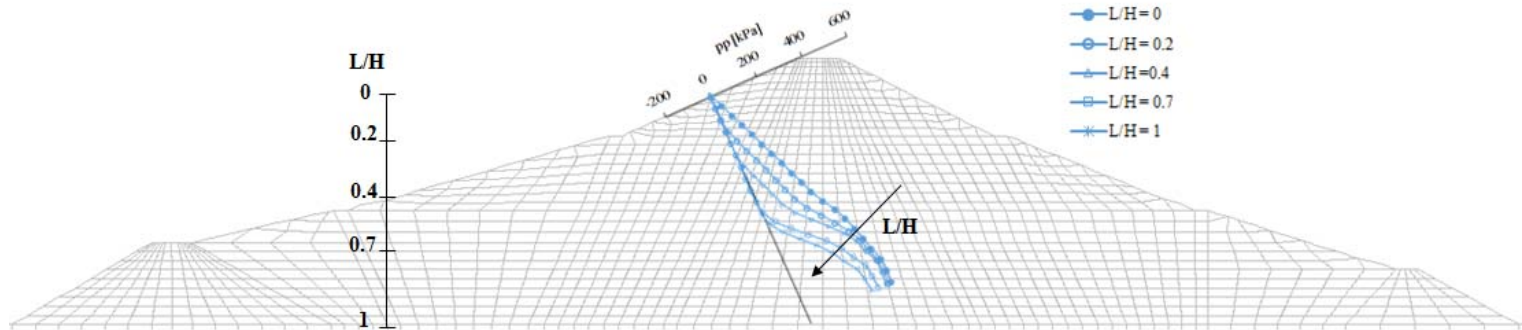


Figure 5-45. Pore pressure vs depth for $R = 0.5$ m/day (line AB).

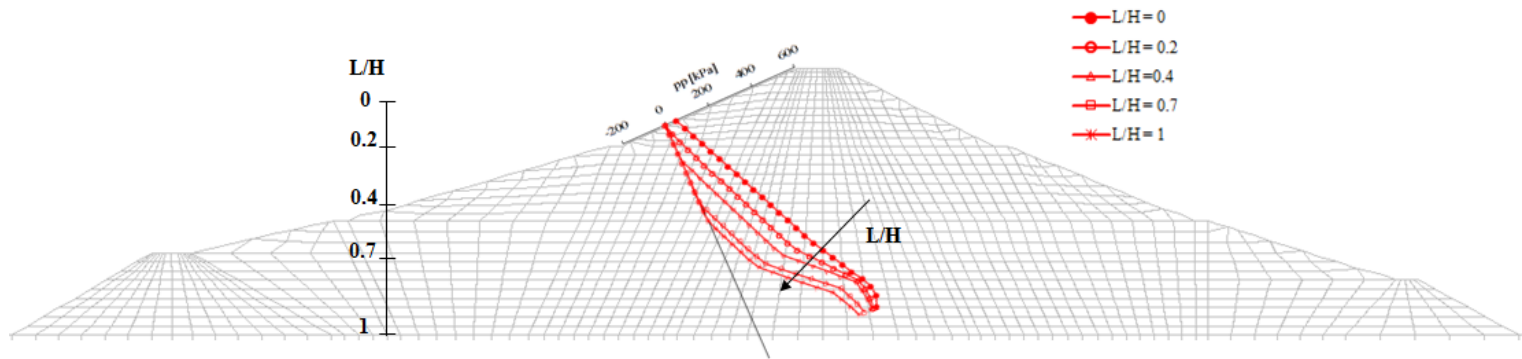


Figure 5-46. Pore pressure vs depth for $R = 0.5$ m/day (line CD).

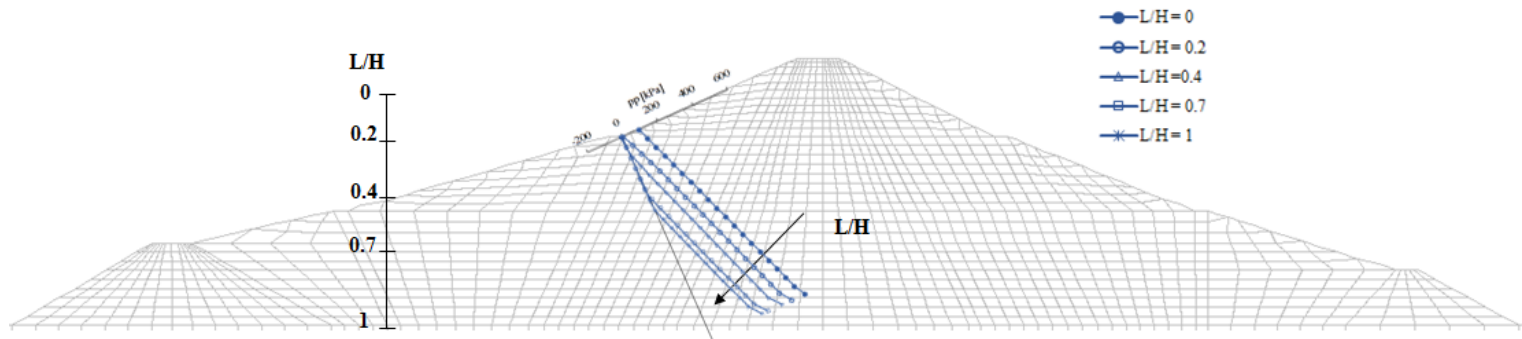


Figure 5-47. Pore pressure vs depth for $R = 0.5$ m/day (line EF).

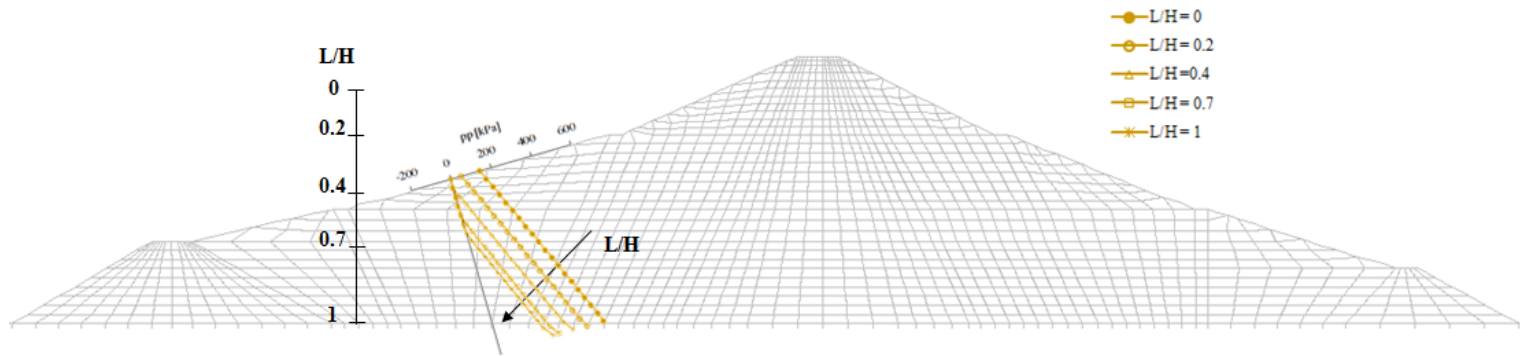


Figure 5-48. Pore pressure vs depth for $R = 0.5$ m/day (line GH).

Since the drainage conditions on slope stability during the drawdown depends on the hydraulic conductivity of the upstream shell, the variation of the FOS with the dimensionless drawdown rate (R/k) has been plotted in Figure 5-49. It can be observed that as the drawdown progresses and reaches $L/H > 0.7 \div 1$ (complete emptying), slope instability occurs for $R/k > 0.65$. For low drawdown ratio ($L/H = 0.2 \div 0.4$) the FOS is less affected by the ratio R/k .

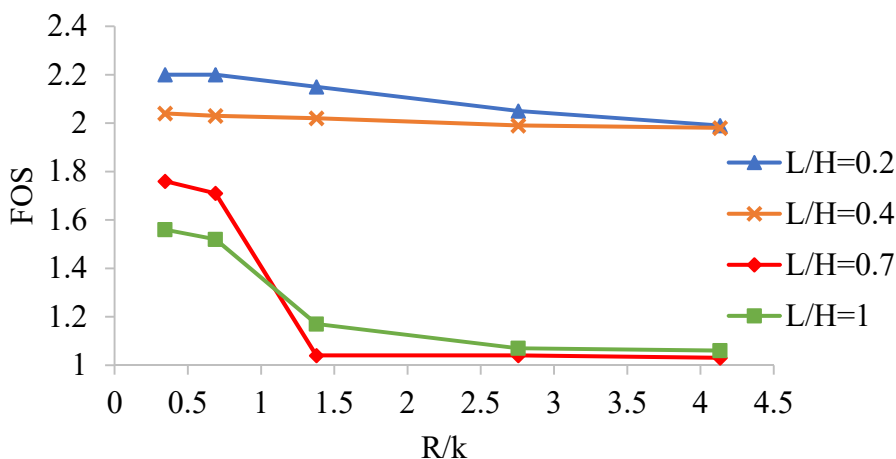


Figure 5-49. FOS vs dimensionless drawdown rate, R/k .

In order to evaluate the relationship between dam displacements and the dimensionless drawdown rate R/k , vertical displacements at the crest and toe of the upstream shell have been represented in Figure 5-50, for different drawdown ratio. It may be observed that the displacements are larger for higher drawdown rates R/k and drawdown ratios L/H .

The displacement pattern seems to be highly indicative of the sliding surface mobilized in the upstream shell. The dam crest moves downward in the reservoir direction. At the same time, for compatibility, the dam toe is forced to have an upward motion (positive displacement).

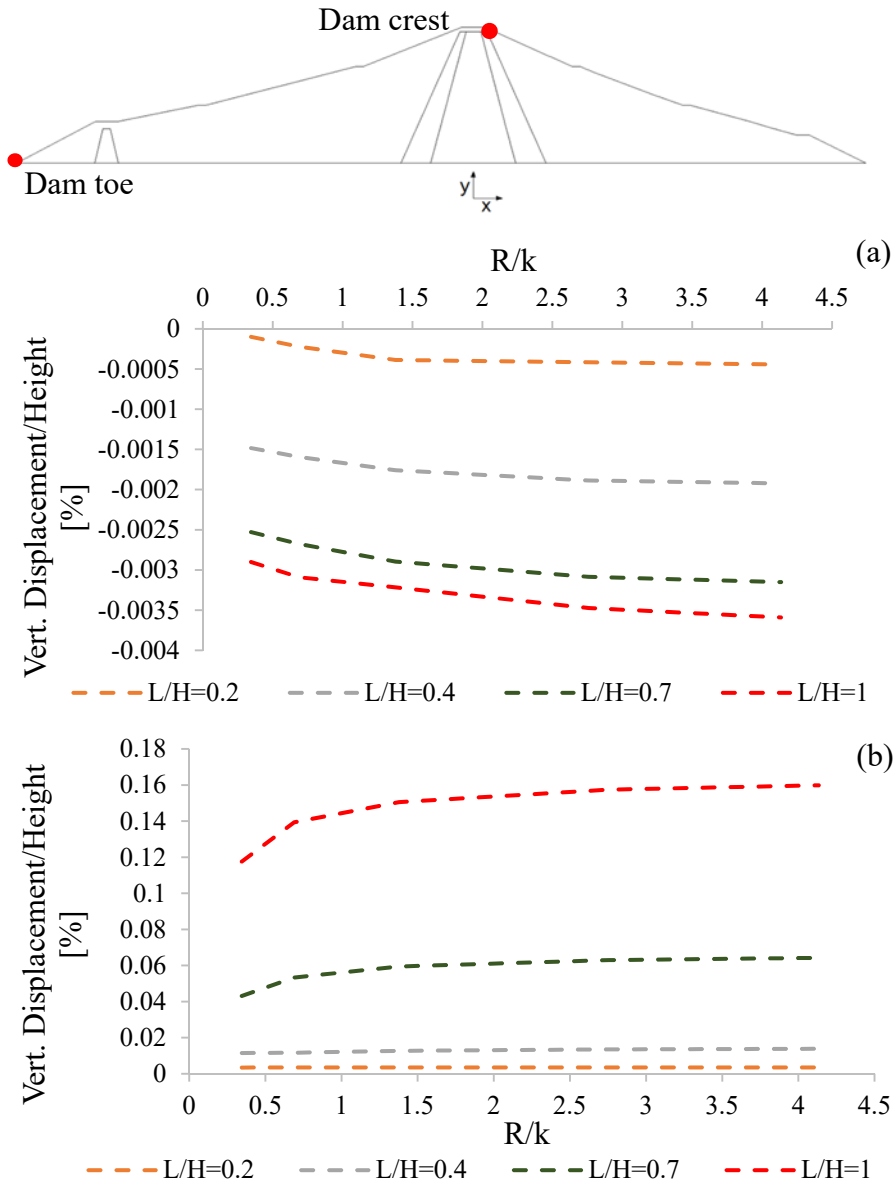


Figure 5-50. Displacement versus drawdown ratio for different drawdown rate R : (a) dam crest; (b) dam toe.

6. Final remarks

The research activity carried out during the PhD period focused on the numerical modelling of earth dams. In particular, dam response to a drawdown of the reservoir after a strong earthquake was investigated, accounting for different operating conditions. The interest on such a topic comes from the fact that in Italy and worldwide there are many large dams, most of which earth dams, placed very close to active faults and hence subjected to high seismic hazard. In such conditions, the structure may be asked to face the earthquake first and the emergency rapid drawdown later. Individually, each stage may be critical from the viewpoint of dam stability; if the two stages occur simultaneously or consequentially the effects on the dam embankment may be dangerous.

Worth mentioning are the last earthquakes occurred in central Italy (L'Aquila, 2009; Amatrice and Norcia, 2016) where the authorities in charge of the dam safety acted completely unprepared to face the emergency, due to the lack of pre-arranged predictive/interpretative tools. Especially for the latest events (Amatrice and Norcia, 2016) the negative effects of a rapid drawdown carried out after a strong earthquake arose greater interest than in the past. The seismic activity near the Campotosto Lake (central Italy), made of Sella Pedicate, Rio Fucino and Poggio Cancelli dams, caused huge apprehension in the local authorities and population, worried about dam safety after a so long and severe seismic sequence (2016-2017). Dam managers, on the other hand, were wondering whether lowering the reservoir or not.

This issue is not easy to deal with because the behaviour of an earth dam is strongly affected by its past loading history. There may be the influence of the construction phases on the seismic response of the dam (Sica, 2008), as well as the influence of the seismic stage on the response of the dam to a drawdown operation, as highlighted in this research work.

In addition to the past loading history suffered by the dam soils, other factors may have an appreciable influence on the response of the dam during the drawdown stage, such as the drawdown ratio (L/H) and rate (R), which mean how much and how quick the lowering of the reservoir is.

To solve the overall boundary value problem, encompassing several stages of the dam lifetime (construction, first filling, operation, seismic stage, drawdown), a continuum approach was adopted. In such a context, the seismic and the drawdown analyses have continuity with the former ones (construction, first filling and operation), thanks to a unified approach where time is a variable of the problem like it occurs in reality. A coupled transient seepage formulation combined to a rather simple elasto-plastic constitutive soil model (Mohr-Coulomb) - enriched in a hierarchical manner with additional features and equations in order to improve the description of soil behaviour under different loading conditions - allowed deformation and consolidation phenomena of the embankment to be simulated.

As the set of constitutive equations of the soil is concerned, under cycling loading the hysteretic behaviour of the soil was described by adding sigmoidal functions describing soil stiffness and damping variation with the mobilized shear strain, whose parameters have properly been calibrated on the results of laboratory tests ad hoc carried out on the sample dam (Campolattaro Dam). The excess pore water pressure generation in the finer soils of the embankment was accounted for by implementing the Byrne and Finn model (1991) calibrated on the results of Standard Penetration Tests, recently performed in the dam core.

The drawdown simulation has been made yet by a coupled transient seepage formulation, but taking into account the partial saturation of the soil (3-phase approach), i.e. implementing the field equations of two immiscible fluids through porous media.

As the seismic response of the selected dam is concerned, the performed analyses showed that for most of the applied horizontal inputs (whose acceleration spectra are compatible with the code requirements) the acceleration profiles versus depth show an almost unaltered seismic wave propagation in the stiffer foundation soils (bedrock). When the altered shallow deposit ($V_s = 316$ m/s) is encountered, site amplification occurs. Higher values of acceleration and displacement were computed at the dam crest due to a combination of factors, such as the embankment geometry and material stiffness inhomogeneity. Since several input motions were adopted, it was possible to assess dam safety against the two limit states of LLS and CLS, in accordance with the performance based philosophy.

The drawdown analyses were carried out after the simulation of the seismic stage, considering different drawdown ratios (L/H) and rates (R). However, to appreciate the role of different initial conditions acting in the soils of the embankment and its foundation, the drawdown analyses were also performed without including the seismic stage in the simulation process. The stress paths at some reference points of the embankment highlighted the role of the earthquake stage in changing the stress state of the soil, thus providing different initial conditions for the subsequent drawdown stage.

Dam safety after the drawdown was ascertained in terms of global factor of safety (FOS) against slope stability. The latter, evaluated with the strength reduction method by Dawson et al. (1999), was determined considering different amount of water lowering, starting from the ratio $L/H=0$ up to $L/H = 1$ (full emptying of the reservoir). From the performed stability analyses it emerged that higher FOS values are found if the drawdown is carried out without simulating the earthquake. Conversely, the occurrence of an earthquake (whichever its severity, LLS or CLS) could reduce the safety of the upstream shell during the drawdown, especially at the beginning of the lowering operations, i.e. for $L/H < 0.3$.

In short, if the drawdown is carried out after a strong earthquake, dam stability may further decrease due to the seismic-induced stress changes experienced by the dam embankment.

Dam response during a drawdown is obviously affected also by the drawdown rate, i.e. the rapidity of the reservoir lowering. As expected, the slower the drawdown rate, the safer towards slope stability (higher FOS values) is the dam: soils become more and more unsaturated and this causes an increase of its shear resistance. Conversely, the faster the drawdown, the smaller is the FOS and the less important become the effects of the initial conditions on the slope stability. For very high drawdown rates (2 or 4 m/day) the FOS abruptly drops to 1 even for $L/H = 0.5$, i.e. when the reservoir has been emptied for almost half the dam height.

It follows that a sudden change in the external water level, without allowing the time for the drainage, may involve unsafer conditions, also in a highly permeable soil like the upstream shell of a zoned earth dam, as the case at hand. In this condition, two transient phenomena are superimposed in the

dam embankment: re-distribution of the pore pressure changes due to the earthquake and stress changes caused by the drawdown.

It is worth pointing out that in the performed drawdown analyses, dam stability has been evaluated at the end of the emptying operations for every ratio L/H considered. This means that steady-state conditions have not been reached in the embankment, and the expected increase in FOS after the drawdown has not been observed yet in the analysis time.

The various factors that influence the stability of an existing earth dam during the drawdown operations should always be considered (past loading history with occurred earthquakes, drawdown rate and ratio).

For the selected case study, a limit drawdown rate to carry out a safe total emptying of the reservoir ($L/H=1$) is definitely 1 m/day. Alternatively, a combination of different drawdown ratios and rates can be selected. Initially, even a very rapid drawdown ($R \approx 4\text{m/day}$) can be applied until $L/H \leq 0.4$; then to avoid slope instability the complete emptying can be achieved with a very slow drawdown rate ($R \leq 0.5$ m/day).

As further developments of the performed research, an extensive parametric study may be performed considering dams different from the selected one, from the viewpoint of typology and properties of the construction materials. The role of soil permeability, for example, should be better investigated, considering that in most existing dams the upstream shell could have modified its hydraulic properties due to silting.

A further improvement of the work can consist in implementing a more advanced constitutive model able to better represent soil behaviour under unsaturated conditions by accounting for soil skeleton deformation under cycles of wetting and drying due to change in reservoir level.

APPENDIX

UNSATURATED SOIL MECHANICS²

A.1. INTRODUCTION

The general field of soil mechanics can be subdivided into the portion dealing with saturated soils and the portion dealing with unsaturated soils. The differentiation between saturated soils and unsaturated soils becomes necessary due to basic differences in the material nature and engineering response. An unsaturated soil has more than two phases, and the pore-water pressure is negative relative to pore-air pressure. Any soil near the ground surface, present in an environment where the water table is below the ground surface, will be subjected to negative pore-water pressures and possible reduction in degree of saturation.

An unsaturated soil is commonly defined as having three phases: (1) solids, (2) water, and (3) air. It is, however, more correct to recognize the existence of a fourth phase, namely, the air-water interface or the contractile skin (Fredlund and Morgenstern, 1977).

The ground surface climate is an important factor that controls the depth to the groundwater table and therefore the thickness of the unsaturated soil zone (Figure A-1). The zone between the ground surface and the water table is referred to as the unsaturated soil zone. This is somewhat of a misnomer since the capillary fringe immediately above the water table is essentially saturated. A more correct term for the entire zone above the water table is the “*vadose zone*” (Bouwer, 1978). However, the entire zone subjected to negative pore-water pressures has become widely referred to as the unsaturated soil zone in geotechnical engineering.

The unsaturated soil zone forms a transition between the water in the atmosphere and the groundwater (i.e., positive pore-water pressure zone).

² From “*Unsaturated Soil Mechanics in Engineering Practice*” by Fredlund D.G., Rahardjo H. and Fredlund M. D., 2012 Ed. John Wiley & Sons, Inc.

The pore-water pressures in the unsaturated soil zone can range from zero at the water table to a maximum tension on the order of 1,000,000 kPa under dry soil conditions (Croney et al., 1958). The degree of saturation of the soil can range from 100% to zero. The changes in soil suction result in distinct zones of saturation. Soils in situ start at saturation at the water table and tend to become unsaturated toward the ground surface.

Soils near the ground surface are often referred to as problematic soils, but it is the handling of highly negative pore-water pressures that tends to present the most serious problem for geotechnical engineers. Common problematic soils are expansive soils, collapsible soils, and residual soils.

Any of the above soils, as well as other soil types, can also be compacted, once again giving rise to a material with negative pore-water pressures.

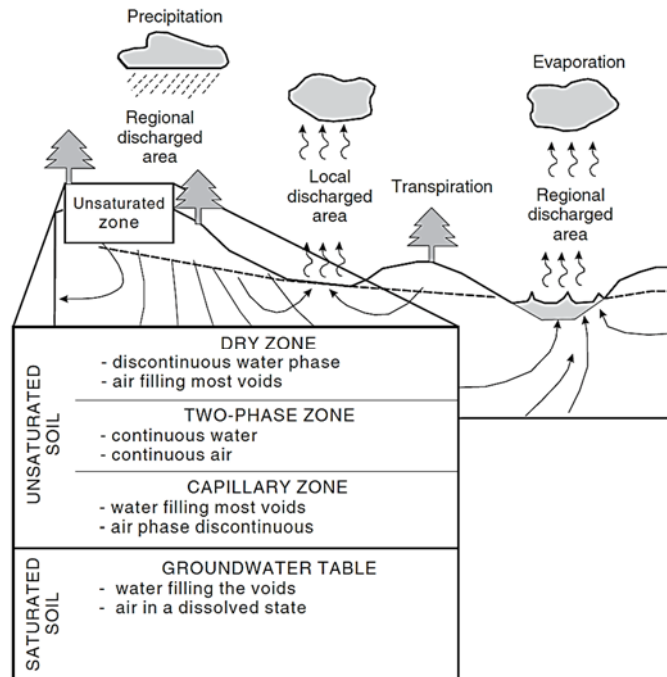


Figure A-1. Subdivisions of unsaturated soil zone (vadose zone) on local and regional basis (Fredlund et al., 2012).

The presence of even the smallest amount of free air renders a soil unsaturated. Even a small amount of air, likely occurring as occluded air bubbles, renders the pore fluid compressible. It is possible for a soil to

remain essentially saturated while the pore-water pressure becomes negative relative to the air phase.

The zone immediately above the water table is referred to as the *capillary zone* and is characterized as being essentially saturated while having negative pore-water pressures. Soil in the capillary zone is generally embraced within the context of an unsaturated soil. It is the negative pore-water pressure relative to the internal or external air pressure that qualifies the soil as an unsaturated soil.

Generally it is a larger amount of air (i.e., about 15% air by volume) that makes the air phase continuous throughout the soil. The principles and concepts required to describe the behaviour of an unsaturated soil become necessary as the pore-air and pore-water pressures begin to become significantly different. Terzaghi (1943) clearly described the important role of the air-water interface in understanding unsaturated soil behaviour.

The mechanical behaviour of a soil (i.e., the volume change, distortion, and shear strength) needs to be described in terms of fundamental state variables. The state of stress consists of a combination of stress state variables, that for unsaturated soils are saturation and porosity.

A.2. SOIL SUCTION

The state variable of greatest relevance to unsaturated soil mechanics is soil suction. Soil suction is the general term which may be used when referring to matric suction, osmotic suction, or total suction.

Soil suction can be quantified in terms of the relative humidity immediately adjacent to the water surface and is called “total suction.” There are two primary components to soil suction, namely, matric and osmotic suction.

It has been possible to formulate solutions for most geotechnical engineering problems through use of matric suction and osmotic suction, recognizing the sum of the two components as total suction.

Total, matric, and osmotic suctions can be defined as follows (Aitchison, 1964):

Matric or capillary component of free energy: Matric suction is the equivalent suction derived from the measurement of the partial pressure of the water vapor in equilibrium with the soil-water relative to the partial pressure of the water vapor in equilibrium with a solution identical in composition with the soil-water.

Osmotic (or solute) component of free energy: Osmotic suction is the equivalent suction derived from the measurement of the partial pressure of the water vapor in equilibrium with a solution identical in composition with the soil-water relative to the partial pressure of water vapor in equilibrium with free pure water.

Total suction or free energy of soil-water: Total suction is the equivalent suction derived from the measurement of the partial pressure of the water vapor in equilibrium with the soil-water relative to the partial pressure of water vapor in equilibrium with free pure water.

The mathematical relationship between the components of soil suction can be written as follows:

$$\psi = (u_a - u_w) + \pi \quad (\text{A.1})$$

where:

- $u_a - u_w$ = matric suction [kPa];
- u_a = pore-air pressure [kPa];
- u_w = pore-water pressure [kPa];
- π = osmotic suction [kPa].

Matric suction is commonly associated with the capillary phenomenon arising from the surface tension of water. Several experimental observations showed that the air-water interface (i.e., contractile skin) possesses a property called *surface tension*. This phenomenon results from intermolecular forces acting on molecules in the contractile skin. These forces are different from those that act on molecules in the interior of the water (Figure A-2).

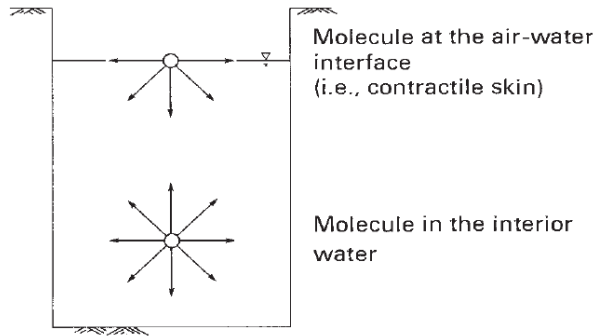


Figure A-2. Surface tension phenomenon at air-water interface: intermolecular forces acting on contractile skin (Fredlund et al., 2012).

A molecule in the interior of the water experiences equal forces in all directions, which means there is no unbalanced force. A water molecule within the contractile skin experiences an unbalanced force toward the interior of the water. A tensile pull is generated along the contractile skin in order for the contractile skin to be in equilibrium. The property of the contractile skin that allows it to exert a tensile pull is called its surface tension, T_s (units of mN/m). Surface tension is tangential to the contractile skin surface and its magnitude decreases slightly as temperature increases.

The capillary phenomenon is associated with the matric suction component of total suction. The height of water rise in a capillary tube and the radius of curvature of the air-water interface have direct implications to the water content–matric suction relationship in soils.

Force equilibrium of capillarity water in the vertical direction requires that:

$$2\pi r T_s \cos \alpha_1 = \pi r^2 h_c \rho_w g \quad (\text{A.2})$$

where:

- r = radius of the capillary tube;
- T_s = surface tension of water;
- α_1 = contact angle;
- h_c = capillary height;
- g = gravitational acceleration.

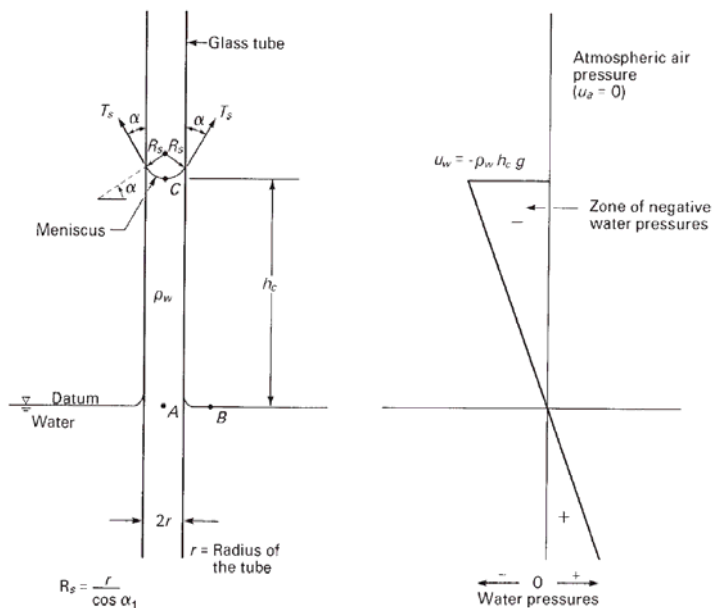


Figure A-3. Physical model of capillarity (Fredlund et al., 2012).

The maximum height of water in the capillary tube, h_c , depends on the radius of the tube:

$$h_c = \frac{2T_s \cos \alpha_1}{\rho_w g r} \quad (\text{A.3})$$

Points A, B, and C in the capillary system shown in Figure A-3 are in hydrostatic equilibrium. The water pressures at points A and B are atmospheric. Point C is located at a height h_c from the datum. The hydrostatic equilibrium among points C, B, and A requires that the hydraulic heads at all three points be equal. In other words, the hydraulic head at point C is also equal to zero. This means that the pressure head at point C is equal to the negative value of the elevation head at point C. The water pressure at point C can be calculated as:

$$u_w = -\rho_w g h_c \quad (\text{A.4})$$

The water pressures above point A in the capillary tube are negative, so the water in the capillary tube is said to be under tension. On the other hand, the water pressures below point A (i.e., water table) are positive due to hydrostatic pressure conditions. At point C, the air pressure is atmospheric

and the water pressure is negative. The matric suction ($u_a - u_w$) at point C can then be expressed as follows:

$$u_a - u_w = \rho_w g h_c \quad (\text{A.5})$$

Substituting Eq. (A.3) into Eq. (A.5) allows matric suction to be written in terms of surface tension:

$$u_a - u_w = \frac{2T_s}{R_s} \quad (\text{A.6})$$

Surface tension has the ability to support a column of water, h_c , in a capillary tube. The surface tension associated with the contractile skin places a reaction force on the wall of the capillary tube. The vertical component of this reaction force produces compressive stresses on the wall of the tube. In other words, the weight of the water column is transferred to the tube through the contractile skin. The contractile skin results in an increased compression on the soil structure in the capillary zone. As a result, the presence of matric suction in an unsaturated soil produces a volume decrease and an increase in the shear strength of the soil.

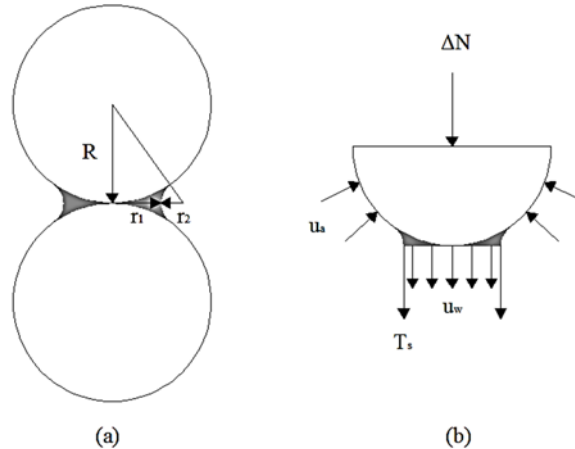


Figure A-4. Soil-water-air interaction: a) geometry of toroidal meniscus; b) forces equilibrium.

For a warped or saddle-shaped surface (i.e., three-dimensional membrane), the force equilibrium in the vertical direction can be extended using the Laplace equation:

$$u_a - u_w = T_s \left(\frac{1}{r_2} - \frac{1}{r_1} \right) \quad (\text{A.7})$$

Where r_1 and r_2 are radii of curvature of a warped membrane in two orthogonal principal planes (Figure A-4a).

Due to the geometry of two unsaturated contacts particle system, it follows that:

$$r_2 = \frac{r_1^2}{2(R - r_1)} \quad (\text{A.8})$$

Rearranging Eq. (A.7) gives:

$$u_a - u_w = \frac{T_s}{R} \left(\frac{2 - 3(r_1/R)}{(r_1/R)^2} \right) \quad (\text{A.9})$$

The pressure acting on the membrane closes in on the two soil particles, increasing the contact forces, ΔN ,

$$\Delta N = (u_a - u_w) \pi \cdot r_1^2 + T_s \cdot 2 \cdot \pi \cdot r_1 \quad (\text{A.10})$$

Substituting Eq. (A.3) into Eq. (A.5) it gives

$$\Delta N = T_s \cdot \pi \cdot R \cdot \left(2 - \frac{r_1}{R} \right) \quad (\text{A.11})$$

Such relation indicates that the increase of normal stress produced by the suction tends asymptotically to a finite value when the suction tends to infinity (i.e. $r_1 \rightarrow 0$)

$$\Delta N = 2 \cdot T_s \cdot \pi \cdot R \quad (\text{A.12})$$

A.3. SOIL WATER CHARACTERISTIC CURVE

The Soil Water Characteristic Curve (SWCC) provides a conceptual understanding between the mass (and/or volume) of water in a soil and the energy state of the water phase (matric suction). The amount of water in the soil can be defined using more than one variable. Variables used to define the amount of water in the soil are

- (i) gravimetric water content, $w = m_w/m_s$;
- (ii) volumetric water content, $\theta = V_w/V = V_w/(V_s+V_v) = n_w$;
- (iii) degree of saturation, $S_r = V_w/V_v$;
- (iv) volume of water, V_w , referenced to the original volume of the specimen, V_0 (i.e., V_w/V_0).

Where

- m_w = mass of water;
- m_s = mass of soil solids;
- V_w = volume of water;
- V_v = volume of voids;
- V_s = volume of solids;
- V = total volume.

Water storage is always measured as the slope of the volumetric water content versus soil suction relationship. Most permeability functions assume that it is the change in degree of saturation that initiates the calculation of a significant decrease in the coefficient of permeability. Figure A-5 shows a typical SWCC with its three distinct zones of desaturation.

The reliability of estimated unsaturated soil property functions is quite closely related to the accuracy with which the SWCC is defined.

The key transition points on the SWCC are the air-entry value and the residual value for suction and water content. These transition points are defined on the degree of saturation versus soil suction plot and subdivide the SWCC into the “boundary effect” zone (saturated soil mechanics principles are still valid), the “transition” zone (theories of unsaturated soil mechanics need to be applied), and the “residual” zone. The same three zones of desaturation can be defined for the drying (or desorption) branch and the wetting (or adsorption) branch.

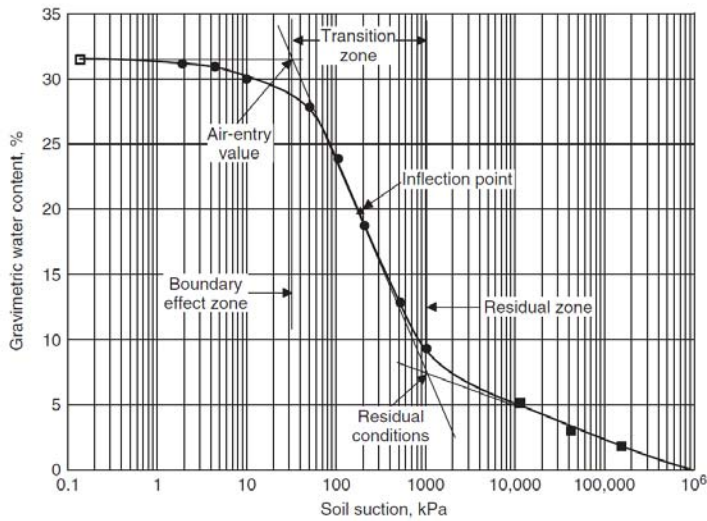


Figure A-5. Typical desorption SWCC showing distinct zones of desaturation (Fredlund et al., 2012).

A large number of closed-form, empirical equations have been proposed to best fit laboratory data for SWCCs. There are many equations in research literature, both two-parameter and three-parameter SWCC equations. Each SWCC equation is written in terms of gravimetric water content (w) with the realization that the equations can also be written in terms of volumetric water content (θ) or degree of saturation (S). Some equations are written in terms of dimensionless water content Θ_d , and others are written in terms of normalized water content Θ_n . The saturated gravimetric water content is designated as w_s (θ_s , saturated volumetric water content), and the gravimetric residual water content is designated as w_r (θ_r , residual volumetric water content).

Each of the SWCC equations has one variable that bears a relationship to the air-entry value of the soil and a second variable that is related to the rate at which the soil desaturates. A third variable is used for some equations and it allows the low-suction range near the air-entry value to have a shape that is independent of the shape of the SWCC in the high-suction range near residual conditions.

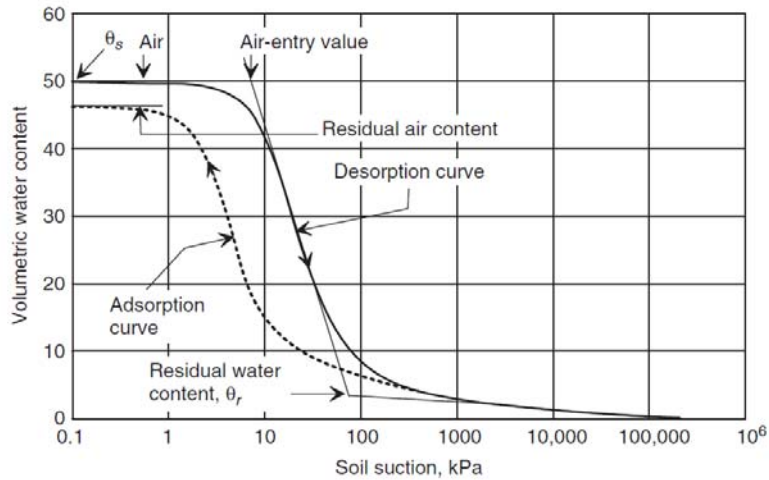


Figure A-6. Typical SWCC curve for silt soil (Fredlund et al., 2012).

Figure A-6 shows a typical SWCC for a silt soil along with identification of some of its main characteristics. The air-entry value of the soil is the matric suction where air starts to displace water in the largest pores in the soil. The residual water content is the water content where a larger suction change is required to remove additional water from the soil. In other words, there is a change in the rate at which water can be extracted from the soil (on a logarithm scale).

These definitions are quite vague and empirical construction procedures have been proposed for the quantification of air entry value and residual conditions.

The empirical procedure for defining residual water content and residual soil suction is shown in Figure A-6 (Fredlund, 1997; Vanapalli et al., 1998). A tangent line is drawn through the inflection point of the SWCC. The SWCC relationship in the high-suction range is approximated using another line that extends through zero water content and 10^6 kPa. The residual water content θ_r is approximated as the ordinate of the point at which the two lines intersect (Figure A-6).

The main curve shown in Figure A-6 is a desorption curve. The adsorption curve differs from the desorption curve as a result of hysteresis related to wetting and drying. The end point of the adsorption curve may differ from the starting point of the desorption curve because of air entrapment in the

soil. The drying and wetting SWCCs have similar forms (i.e., are essentially congruent).

Typical SWCCs (i.e., desorption curves) for soils ranging from sands to clays are shown in Figure A-7. The saturated water content and the air-entry value (or bubbling pressure), $(u_a - u_w)_b$, generally increase with the plasticity of the soil.

Other factors such as stress history and secondary soil structure also affect the shape of the SWCCs.

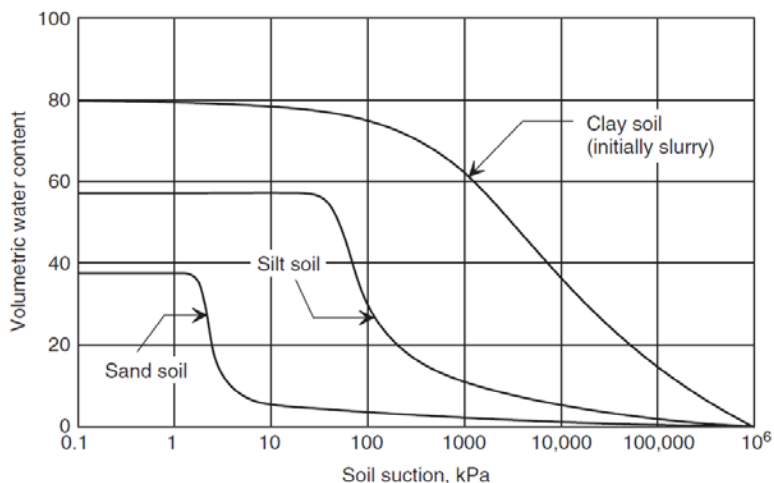


Figure A-7. Comparative desorption SWCCs for sand, silt, and clay soils (Fredlund et al., 2012).

Equations proposed by Brooks and Corey (1964), Van Genuchten (1980) and Fredlund and Xing (1994) are the most used.

The power law proposed by Brooks and Corey (1964) represents desaturation of the soil when the soil suction is greater than the air-entry value:

$$\theta_w = \begin{cases} \theta_s & (u_a - u_w) < (u_a - u_w)_b \\ \theta_r + (\theta_s - \theta_r) \left(\frac{u_a - u_w}{(u_a - u_w)_b} \right)^{-\lambda} & (u_a - u_w) \geq (u_a - u_w)_b \end{cases} \quad (\text{A.13})$$

where λ (0.2÷5) is pore-size distribution index. Equation (A.13) suggest that there is a sharp discontinuity in the soil suction versus water content

near the air-entry value for the soil. Although some coarse-grained sands may have a rapid change in water content at low soil suctions, most medium- and fine-textured soils show a gradual curvature in the air-entry region of the SWCC.

Van Genuchten (1980) proposed the use of a continuous function between soil suction and normalized water content:

$$\Theta = \frac{(\theta - \theta_r)}{(\theta_s - \theta_r)} = \left[\frac{1}{1 + (\alpha(u_a - u_w))^n} \right]^m \quad (\text{A.14})$$

where α is a parameter related to the inverse of air entry value [L^2/F], n is related to rate of water extraction from soil once air-entry value has been exceeded, m is primarily related to residual water content conditions.

Equation (A.14) provides additional flexibility to the SWCC. In an attempt to obtain a closed-form expression for hydraulic conductivity, van Genuchten (1980) fixed the relationship between the m and n parameters:

$$m = 1 - \frac{1}{n} \quad (\text{A.15})$$

The Fredlund and Xing (1994) equation overcomes the problem which occurs at high-soil-suction values beyond residual conditions (the results become asymptotic to a horizontal line as soil suction goes to infinity) applying a correction factor that directs the SWCC equation to a soil suction of 10^6 kPa at zero water content. The Fredlund and Xing (1994) equation is written as follows:

$$\theta = C(u_a - u_w)\theta_s \left[\frac{1}{\ln \left(e + \left(\frac{(u_a - u_w)^n}{a} \right) \right)} \right]^m \quad (\text{A.16})$$

where e is irrational constant equal to 2.71828, used when taking the natural logarithm and C is a correction factor directing the SWCC to 10^6 kPa at zero water content,

$$C(u_a - u_w) = \left[\frac{\ln \left(1 + \frac{u_a - u_w}{(u_a - u_w)_r} \right)}{\ln \left(1 + \frac{10^6}{(u_a - u_w)_r} \right)} \right] \quad (\text{A.17})$$

A.4. PERMEABILITY FOR UNSATURATED SOILS

The intrinsic permeability of a soil, K , represents the characteristics of the porous medium and is independent of the fluid properties. The porous medium, in turn, is a function of the volume-mass properties of the soil. In geotechnical engineering, the coefficient of permeability k_w is used to embrace the overall effect of variables related to the porous medium and the pore fluid.

The coefficient of permeability in a saturated soil is a function of the void ratio (Lambe and Whitman, 1979). However, it is generally assumed to be a constant when analysing most steady-state and transient flow problems in saturated soils.

The coefficient of permeability in an unsaturated soil is significantly affected by combined changes in void ratio and degree of saturation (or water content) of the soil. Water flows through the pore space filled with water; therefore, the percentage of the voids filled with water is an important factor. As a soil begins to desaturate, air first replaces some of the water in the large pores. The onset of desaturation causes water to flow through the smaller pores. The pathway through the smaller pores leads to increased tortuosity and consequently much slower flow. An increase in matric suction in the soil leads to a further decrease in the pore volume occupied by water. The air-water interface is drawn closer and closer to the soil particles. As a result, the coefficient of permeability with respect to the water phase decreases rapidly as the space available for water flow is reduced.

The coefficient of permeability with respect to the water phase, k_w , can be predicted using three approaches (Mualem, 1986):

- Empirical approach. Permeability is estimated by saturated permeability (k_s) and other parameters determined from experimental seepage tests.
- Macroscopic approach. A water laminar flow is supposed, so a power law is used ($k_w = k_s \cdot S_e^\delta$, where δ is an empirical constant for the permeability function related to the pore-size distribution index λ).
- Statistical approach. The soil is considered a network of capillary tubes with different diameters and connected to each other, the flow can occur only through canals occupied by water.

Several relations have been proposed:

Brooks and Corey (1964)

$$k_w(u_a - u_w) = \begin{cases} k_s & (u_a - u_w) < (u_a - u_w)_b \\ k_s \left(\frac{(u_a - u_w)_b}{u_a - u_w} \right)^\eta & (u_a - u_w) \geq (u_a - u_w)_b \end{cases} \quad (\text{A.18})$$

Where $\eta = 2 + 3\lambda$.

Gardner (1958)

$$k_w(u_a - u_w) = \frac{k_s}{1 + a \left\{ (u_a - u_w) / (\rho_w g) \right\}^n} \quad (\text{A.19})$$

Where a and n are constant.

Van Genuchten (1980)

$$k_w(u_a - u_w) = k_s \left(\frac{1 - (\alpha(u_a - u_w))^{n-2} [1 + (\alpha(u_a - u_w))^n]^m}{[1 + (\alpha(u_a - u_w))^n]^{2n}} \right) \quad (\text{A.20})$$

A.5. SHEAR STRENGTH OF UNSATURATED SOILS

In the case of an unsaturated soil the stress state can be described in terms of the net normal stresses ($\sigma - u_a$) and the matric suction ($u_a - u_w$).

Theories of shear strength for an unsaturated soil have been proposed as extensions to the concepts and mathematical equations that have been used for shear strength theories for saturated soils. The Mohr-Coulomb failure criterion was extended to embrace unsaturated soils by Fredlund et al. (1978). The extended shear strength equation for an unsaturated soil can be written as follows:

$$\tau = c' + (\sigma_n - u_a) \tan \phi' + (u_a - u_w) f_1 \quad (\text{A.21})$$

where:

τ = shear strength;

c' = effective cohesion intercept;

σ_n = total normal stress on the failure plane at failure;

ϕ' = effective angle of internal friction;

f_1 = soil property function defining the relationship between shear strength and soil suction, the derivative of which [i.e., $df_1/d(u_a - u_w)$] gives the instantaneous rate of change in shear strength with respect to soil suction (Fredlund, 2005).

The form of Eq.(A.21) allows the shear strength envelope with respect to matric suction to be either linear or curved, depending upon the experimental test results. Shear strength envelopes that are measured over a wide range of matric suction values tend to show a curved shape.

Under low-suction conditions (i.e., less than the air-entry value of the soil), the derivative of f_1 tends to a value equal to the tangent of the effective angle of internal friction of the saturated soil (i.e., $\tan \phi'$). The shear strength envelope starts to become curved as the air-entry value for the

soil is exceeded. There generally appears to be a gradual curvature in the shear strength envelope up to residual suction conditions. At high suction conditions (i.e., greater than residual soil suction), the derivative of f_1 has been shown to tend toward zero for several soils with varying silt and clay

contents (Nishimura and Fredlund, 2001). Sandy soils have shown that the slope may even become negative at suctions greater than the residual value (Donald, 1956; Gan and Fredlund, 1996).

A linear form of the general shear strength equation (i.e., Eq. (A.21)) was published by Fredlund et al. (1978). Some of the earlier unsaturated soil shear strength data sets (e.g., Bishop et al., 1960) show a close fit to the linear shear strength equation (Fredlund and Rahardjo, 1993a). The linear form (i.e., $f_1 = \tan \phi_b$) is convenient to use for illustrating the effect of matric suction on shear strength.

So the linear form of Eq. (A.21) is:

$$\tau_{ff} = c' + (\sigma_f - u_a)_f \tan \phi' + (u_a - u_w)_f \tan \phi^b \quad (\text{A.22})$$

where:

c' = intercept of the “extended” Mohr-Coulomb failure envelope on the shear stress axis where the net normal stress and the matric suction at failure are equal to zero, also referred to as “effective cohesion”;

$(\sigma_f - u_a)_f$ = net normal stress state on the failure plane at failure;

u_{af} = pore-air pressure on the failure plane at failure;

ϕ = angle of internal friction associated with the net normal stress state variable, $(\sigma_f - u_a)_f$;

$(u_a - u_w)_f$ = matric suction on the failure plane at failure;

ϕ_b = angle indicating the rate of increase in shear strength with respect to a change in matric suction, $(u_a - u_w)_f$.

A comparison of Eq.(A.22) and the shear strength for saturated soils (i.e., $\tau_{ff} = c' + (\sigma_f - u_w)_f \tan \phi'$) reveals that the shear strength equation for an unsaturated soil takes the form of an extension of the shear strength equation for a saturated soil. Two stress state variables are used to describe the shear strength of an unsaturated soil while only one stress state variable [i.e., effective normal stress $(\sigma_f - u_w)_f$] is required for a saturated soil.

The proposed shear strength equation for an unsaturated soil exhibits a smooth transition to the shear strength equation for a saturated soil. The pore-water pressure u_w approaches the pore-air pressure u_a as the soil

approaches saturation and the matric suction $u_a - u_w$ goes to zero. As the matric suction component vanishes, Eq. (A.22) reverts to the equation for a saturated soil.

The failure envelope for unsaturated soils is obtained by plotting a series of Mohr circles corresponding to failure conditions in a three-dimensional manner, as illustrated in Figure A-8. The three-dimensional plot has the shear stress τ as the ordinate and the two stress state variables $\sigma - u_a$ and $u_a - u_w$ as abscissas. The frontal plane represents saturated soil conditions where matric suction is zero. The $\sigma - u_a$ axis reverts to the $\sigma - u_w$ axis on the frontal plane since the pore-air pressure becomes equal to the pore-water pressure at saturation.

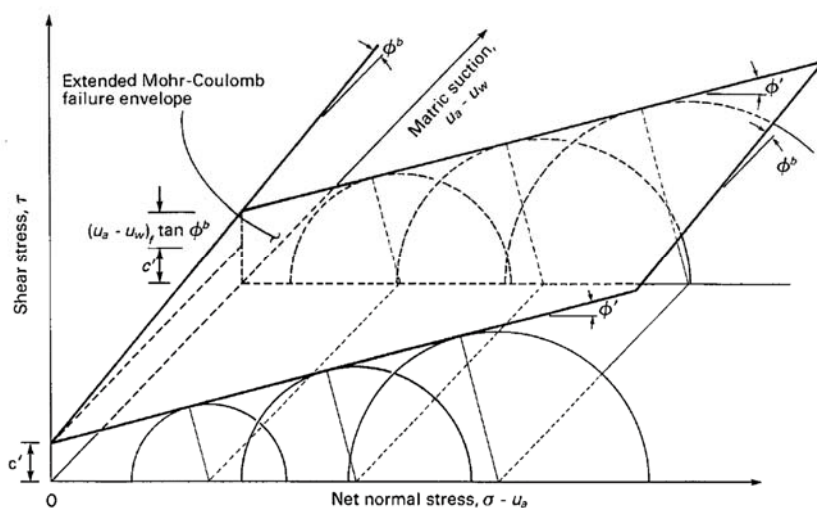


Figure A-8. Extended Mohr-Coulomb failure envelope for unsaturated soils (Fredlund et al., 2012).

The location of the Mohr circle plot in the third dimension is a function of the matric suction.

Figure A-8 shows a planar failure envelope that intersects the shear stress axis, giving a cohesion intercept c' .

The envelope has slope angles of ϕ' and ϕ_b with respect to $\sigma - u_a$ and $u_a - u_w$ axes, respectively. Both angles are assumed to be constants. The cohesion intercept c' and the slope angles ϕ' and ϕ_b are the strength parameters used to relate shear strength to the stress state variables. The shear strength parameters represent many factors which have influenced

the results of the shear strength test. Some of these factors are density, void ratio, degree of saturation, mineral composition, stress history, and strain rate. In other words, these factors have been combined and are expressed mathematically in terms of the shear strength parameters.

The mechanical behaviour of an unsaturated soil is affected differently by changes in net normal stress than by changes in matric suction (Jennings and Burland, 1962). The increase in shear strength due to an increase in net normal stress is characterized by the friction angle ϕ' . The increase in shear strength caused by an increase in matric suction is characterized by the angle ϕ_b when assuming linear failure conditions. The value of ϕ_b appears to be consistently equal to or less than ϕ' .

The failure envelope intersects the shear stress versus matric suction plane along a line of intercepts. The line of intercepts represents the increase in strength as matric suction increases. The shear strength increase with respect to an increase in matric suction is defined by the angle ϕ_b . A linear form for the line of intercepts can be written as follows:

$$c = c' + (u_a - u_w)_f \tan \phi_b \quad (\text{A.23})$$

where:

c = intercept of the extended Mohr-Coulomb failure envelope with the shear stress axis at a specific matric suction $(u_a - u_w)_f$. At zero net normal stress, the intercept can be referred to as the “total cohesion intercept.”

The extended Mohr-Coulomb failure envelope can be presented as a horizontal projection onto the shear strength τ versus $\sigma - u_a$ plane. The horizontal projection can be shown for various matric suction values $(u_a - u_w)_f$. The horizontal projection of the failure envelope onto the τ versus $\sigma - u_a$ plane results in the series of contours shown in Figure A-9. The lines have cohesion intercepts that depend upon the magnitude of the corresponding matric suctions.

The cohesion intercept reverts to the effective cohesion c' when matric suction goes to zero. All lines of equal suction have the same slope angle ϕ' as long as the failure plane is planar. The equation for each of the contour lines can be written as:

$$\tau_{ff} = c + (\sigma_f - u_a)_f \tan \phi' \quad (\text{A.24})$$

where c = total cohesion intercept.

Substituting Eq. (A.23) into Eq. (A.24) yields the equation for the extended Mohr-Coulomb failure envelope. Equation (A.22) is the same as Eq. (A.24) and Figure A-9 is a two-dimensional representation of the extended Mohr-Coulomb failure envelope. The failure envelope projections illustrate the increase in shear strength as matric suction is increased at a specific net normal stress. Equation (A.24) is a convenient form of the shear strength equation to use when performing simple analytical studies involving unsaturated soils.

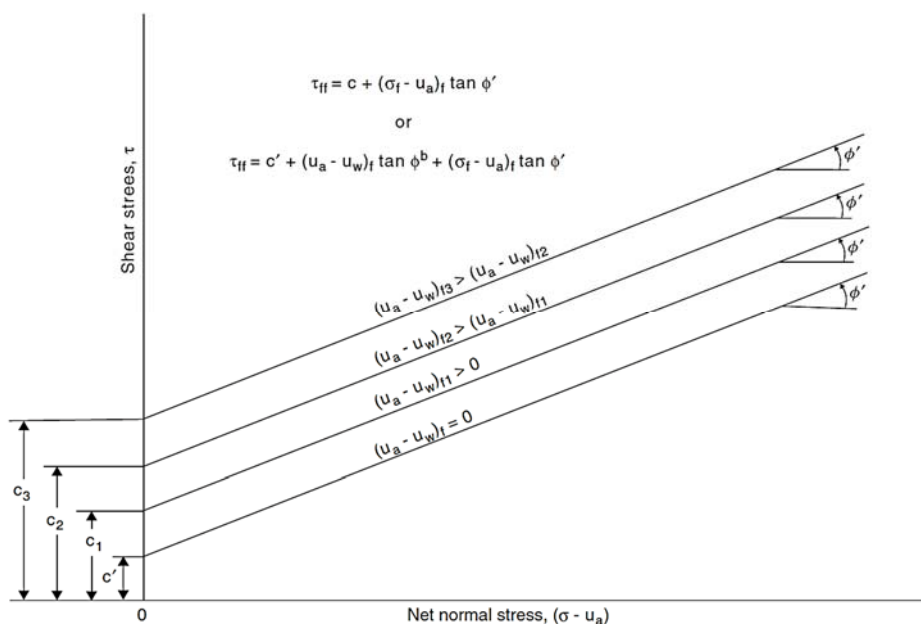


Figure A-9. Horizontal projection of failure envelope onto τ versus $\sigma - u_a$ plane viewed parallel to matric suction $u_a - u_w$ axis as contour lines of failure envelope on $\sigma - u_a$ plane (Fredlund et al., 2012).

References

- Abdel-Ghaffar, A. M. and Elgamal, A.W. M., 1987a. *Elasto-plastic seismic response of 3D earth dams: application*. Journal of Geotechnical Engineering 113(11), 1309-1325.
- Abdel-Ghaffar, A. M. and Elgamal, A.W. M., 1987b. *Elasto-plastic seismic response of 3D earth dams: theory*. Journal of Geotechnical Engineering 113(11), 1293-1308.
- Abouseeda H. and Dakoulas P., 1998. *Non-linear dynamic earth dam-foundation interaction using a BE-FE method*. Earthquake Eng Struct Dyn; 27:917-36.
- Achilleas G. Papadimitriou, George D. Bouckovalas, Konstantinos I. Andrianopoulos, 2013. *Methodology for estimating seismic coefficient for performance-based design of earth dams and tall embankments*. Soil Dynamics and Earthquake Engineering 56 57-73.
- Agenzia per la promozione dello Sviluppo del Mezzogiorno, 1989. *Progetto speciale n. 29-20 per la Campania – Relazione generale*.
- Akai K., Ohnishi Y., Murakami T. and Horita M., 1979. *Coupled stress flow analysis in saturated/unsaturated medium by finite element method*. Proc. Third Int. Conf. Num. Meth. Geomech. 1: 241-249, Aachen Akaike.
- Albano M., 2013. *Numerical modeling of the seismic performance of bituminous faced rockfill dams*. PhD Thesis, Università degli studi di Cassino e del Lazio Meridionale.
- Albano M., Modoni G., Croce P. and Russo G., 2015. *Assessment of the seismic performance of a bituminous faced rockfill dam*. Soil Dynamics and Earthquake Engineering 75 (2015) 183–198.
- Aliberti D., Cascone E. and Biondi G., 2016. *Seismic performance of the San Pietro dam*. Geotechnical Engineering in Multidisciplinary Research: from Microscale to Regional Scale CNRIG2016; Procedia Engineering 158 (2016) 362 – 367.
- Alonso E. E., Gens A. and Josa A. 1990. *A constitutive model for partially saturated soil*. Géotechnique 40 No. 3, 405-430.
- Alonso E. E. and Romero E., 2003. *Collapse behaviour of sand*. Proceedings of the 2nd Asian Conference on Unsaturated Soils. Osaka. 325-334.
- Alonso E. and Pinyol N., 2009. *Slope stability under rapid drawdown conditions*. Universitat Politècnica de Catalunya, Barcelona.
- Alonso, E.E., Pinyol, N.M., *Numerical analysis of rapid drawdown: Applications in real cases*. Water Science and Engineering (2016), <http://dx.doi.org/10.1016/j.wse.2016.11.003>.
- Algrmissen S.T., Perkins D.M., Thenhaus P.C., Hanson S.L., Bender B.L., 1982. Probabilistic estimates of maximum acceleration and velocity in rock in the contiguous United States. U.S. Geological Survey. Open-File report 82-1033, Washington, DC.
- Ambraseys N., 1960. *The seismic stability of earth dams*. In: Proceedings of the second world conference on earthquake engineering, vol. 2, Tokyo, Japan; p. 1345-63.

- Ambraseys N. and Menu J.M., 1988. *Earthquake-induced ground displacements*. Earthquake Eng Struct Dyn; 16:985-1006.
- Ambraseys N. and Sarma S.K., 1967. *The response of earth dams to strong earthquakes*. Geotechnique; 17(3):181-213.
- Ambraseys N., Smit P., Berardi R., Rinaldis D., Cotton F. and Berge C., 2000). *Dissemination of European strong-motion data*. European Commission DGXII for Science, Research and Development, Brussels, Belgium.
- Anderson J.G., Trifunac M.D., 1978. Uniform risk functionals for characterization strong earthquake ground motion. Bulletin of the Seismological Society of America; 68:205–18.
- Amorosi A. and Elia G, 2008. *Analisi dinamica accoppiata della diga Marana Capacciotti*. Rivista Italiana di geotecnica 4.
- Aubry D., Benzenati I. and Modaressi A., 1991. *A coupled static/dynamic strain and pore pressure analysis for embankment dams*. Dam. En.g 1991;11(1):53-94.
- Aubry D., Benzenati I. and Modaressi A., 1993. *Numerical predictions for Model n. 1, 2, and 7*. In: Arulanandan, Scott, editors. Verification of numerical procedures for the analysis of soil liquefaction problems. Rotterdam: Balkema; 1993. p. 45–66. p. 315–22 and p. 817–22.
- Aubry D., Chouvet D., Modaressi H. and Modaressi A., 1985. *GEFDYN 5: Logiciel d'analyse du comportement statique et dynamique des sols par e'le'ments finis avec prise en compte du couplage sol-eau-air*. Rapport scientifique, Ecole Centrale Paris.
- Aubry D. and Modaressi A., 1996. *GEFDYN, Manuel Scientifique*. Ecole Centrale Paris.
- Ausilio E., Costanzo A., Silvestri F. and Tropeano G., 2008. *Prediction of seismic slope displacements by dynamic stick-slip analyses*. Seismic Engineering International Conference (MERCEA'08), Reggio Calabria and Messina, Italy.
- Ausilio E., Silvestri F. and Tropeano G., 2007. *Simplified relationships for estimating seismic slope stability*. ECSMGE – ETC12 Workshop: “Geotechnical aspects of EC8”, Madrid, Spain.
- Ausilio E., Silvestri F., Troncone A. and Tropeano G., 2007. *Seismic displacement analysis of homogeneous slopes: a review of existing simplified methods with reference to Italian seismicity*. In: Earth geotechnical engineering, Fourth ICEGE, Thessaloniki, Greece; 1614 p.
- Bardet J. P., Ichii K. and Lin C. H., 2000. *EERA: A Computer program for Equivalent-linear Earthquake site Response Analysis of Layered soil deposits*. Department of Civil Engineering, University of Southern California.
- Berilgen M.M., 2007. *Investigation of stability of slopes under drawdown conditions*. Computers and Geotechnics 34 (2007) 81–91.
- Bilotta E., Pagano L. and Sica S., 2008. *Asincronismo del moto sismico di dighe in terra*. Italian Geotechnical Journal; 4(08):54-77. (in Italian).

- Bilotta E., Pagano L. and Sica S., 2010. *Effect of ground-motion asynchronism on the equivalent acceleration of earth dams*. Soil Dynamic and Earthquake Engineering 30(2010)561-579.
- Biondi G., Cascone E. and Rampello S., 2011. *Valutazione del comportamento dei pendii in condizioni sismiche*. Rivista Italiana di Geotecnica, pp 11-34.
- Biot M.A., 1941. *General theory of three-dimensional consolidation*. J. Appl. Phys., 12, pp. 155-164.
- Biot M.A., 1956b. *Theory of Propagation of Elastic Waves in a Fluid-Saturated Porous Solid: II Higher Frequency Range*. Journal of the Acoustical Society of America, 28, pp. 179-191.
- Biot M.A., 1957. *The elastic coefficients of the theory of consolidation*. Journal of Applied Mechanics, Trans. ASME, 24, 594-601.
- Biot M.A., 1962. *Mechanics of deformation and acoustic propagation in porous media*. Journal of Applied Physics (33): 1482-1498.
- Bishop A.W., 1954. *Use of pore-pressure coefficients in practice*. Geotechnique vol 4, no 4, pp 148-152.
- Bommer J., Acevedo A., 2004. *The use of real earthquake accelerograms as input to dynamic analysis*. Journal of Earthquake Engineering, 8(Special Issue 1), 43-91.
- Bommer J., Acevedo A., Douglas J., 2003. *The selection and scaling of real earthquake accelerograms for use in seismic design and assessment*. Proceedings of the international conference on seismic bridge design and retrofit. American Concrete Institute.
- Bozzoni F., Chiarolla S. and Lai C. G., 2015. *Valutazione della risposta sismica di dighe in terra della Regione Campania mediante approcci semplificati*. Progettazione Sismica – Vol. 6, N. 1, Anno 2015 (in Italian).
- Bray J.D. and Travasarou T., 2007. *Simplified procedure for estimating earthquake-induced deviatoric slope displacements*. Journal of Geotechnical and Geoenvironmental Engineering ASCE 133(4) (2007) 381-392.
- Calabresi G., Rampello S., Sciatti A. and Amorosi A., 2000. *Diga sulla Marana Capacciotti: Verifica delle condizioni di stabilità e analisi del comportamento in condizioni sismiche*. Res. Rep. Dip. di Ingegneria Strutturale e Geotecnica, Università di Roma La Sapienza.
- Calabresi G., Rampello S., Callisto L., and Cascone E., 2004. *Diga S. Pietro sul fiume Osento: Verifica delle condizioni di stabilità e analisi del comportamento in condizioni sismiche*. Research Rep., Univ. Di Roma La Sapienza, Rome.
- Casagrande A., 1937. *Seepage through dams*. Contributions to soil mechanics, 1925-1940. Boston Society of Civil Engineers.
- Cascone E. and Rampello S., 2003. *Decoupled seismic analysis of an earth dam*. Soil Dynam Earthq Eng; 23:349-65.

- Costanzo A., Sica S. and Silvestri F., 2011. *Verifica della sicurezza in condizioni sismiche della diga sul fiume Melito (CZ)*. Rivista italiana di geotecnica (in Italian).
- Chan A. H. C., 1995. *User manual for DIANA-SWANDYNE II*. School of Engineering, Univ. of Birmingham, Birmingham, UK.
- Chopra A.K., 1967. *Earthquake response of earth dams*. ASCE Journal of Soil Mechanics and Foundations Division; 93(SM2):65-81.
- Cornell C.A., 1968. *Engineering seismic risk analysis*. Bulletin of the Seismological Society of America; 58:1583–606.
- Crespellani T., Madiari C. and Vannucchi G., 1998. *Earthquake destructiveness potential factor and slope stability*. Geotechnique 48(3) (1998) 411-419.
- Dakoulas P. and Gazetas G., 1985. *A class of inhomogeneous shear models for seismic response of dams and embankments*. Soil Dyn Earthquake Eng; 4 (4):166-82.
- Dello Russo A., 2014. *Seismic response of soil embankments in Near-source conditions*. Ph.D. Thesis, University of Naples “Federico II”.
- Dello Russo A., Sica S. and Simonelli A. L., 2013. *Effetti della propagazione sismica near-source su grandi rilevati in terra: analisi parametriche*. Incontro Annuale dei Ricercatori di geotecnica, 16-18 settembre 2013 – Perugia, Italia.
- Dello Russo A., Sica S. and Simonelli A. L., 2014. *Propagazione sismica Near-Source: effetti su grandi rilevati in terra*. XXV Convegno Nazionale di Geotecnica, 4-6 giugno 2014 - Baveno (VB), Italia.
- Dello Russo A., Sica S. and Simonelli A.L., 2015. *Seismic propagation in near-source conditions: effects on large embankments*. XVI European Conference Soil Mechanics Geotechnical Engineering, 13-17 September 2015 – Edinburgh, Scotland.
- Derosa R., Bozzoni F. and Lai C.G., 2015. *Valutazione della risposta sismica di dighe in terra mediante approcci semplificati: applicazione a casi di studio in Sicilia*. ANIDIS 2015 (in Italian).
- Desai C.S. and Sherman W.C., 1971. *Unconfined transient seepage in sloping banks*. Jnl. of the Soil Mech. and Found. Div. ASCE, N° SM2: 357-373.
- Desai C.S., 1972. *Seepage analysis of earth banks under drawdown*. Jnl. of the Soil Mech. and Found. Div., ASCE, N° SM11: 1143-1162.
- Desai C.S., 1977. *Drawdown analysis of slopes by numerical method*. Jnl. of the Soil Mech. and Found. Div., ASCE, N° GT7: 667-676.
- DISS Working Group, 2015. *Database of Individual Seismogenic Sources (DISS), Version 3.2.0: A compilation of potential sources for earthquakes larger than M 5.5 in Italy and surrounding areas*. <http://diss.rm.ingv.it/diss/>, Istituto Nazionale di Geofisica e Vulcanologia; DOI:10.6092/INGV.IT-DISS3.2.0.
- Dowson E.M., Roth W.H. and Drescher A., 1999. *Slope stability analysis by strength reduction*. Géotechnique, 49(6), 835-840 (1999).

- Elgamal A. W., Abdel-Ghaffar A. M. and Prevost J. H., 1985. *Elastoplastic Earthquake Shear Response of One-Dimensional Earth Dam Models*. Earthquake Engineering & Structural Dynamics 13(5), 617-633.
- Elgamal A. W., Abdel-Ghaffar A. M. and Prevost J. H., 1987. *2D Elastoplastic Seismic Shear Response of Earth Dams: Theory*. Journal of Engineering Mechanics 113(5), 689-701.
- Elgamal A. W., Abdel-Ghaffar A. M. and Prevost J. H., 1987. *2D Elastoplastic Seismic Shear Response of Earth Dams: Applications*. Journal of Engineering Mechanics 113(5), 702-719.
- Elgamal A., W., Parra E., Yang Z. and Adalier K., 2002. *Numerical analysis of embankment foundation liquefaction countermeasures*. J. Earth. Engng., 6, 4, pp. 447-471.
- Elgamal A., Yang Z. and Parra E., 2002. *Computational modelling of cyclic mobility and post-liquefaction site response*. Soil Dynamics and Earthquake Engineering; 22(4):259-271.
- Elgamal A.M., Scott R.F., Succarieh M.F. and Yan L., 1990. *La Villita Dam response during earthquakes including permanent deformation*. J Geotech Eng ASCE;116(10):1443-62.
- Elgamal A.W., 1992. *Three-dimensional seismic analysis of La Villita Dam*. Journal of Geotechnical Engineering 118, No.12, 1937-1958.
- Elgamal A.W. and Gunturi R.V., 1993. *Dynamic behaviour and seismic response of El Infiernillo Dam*. Earthquake Engineering and Structural Dynamics 22:665-84.
- Elia G., 2004. *Analisi FEM di problemi al contorno in condizioni statiche e dinamiche con un modello costitutivo avanzato*. Ph. D. Thesis, Technical University of Bari, Italy.
- Elia G., Amorosi A., Chan A.H.C. and Kavvadas M. J., 2011. *Numerical Prediction of the Dynamic Behavior of Two Earth Dams in Italy Using a Fully Coupled Nonlinear Approach*. International Journal of Geomechanics, December 2011:504-518.
- EN 1998-1, 2003. *Eurocode No.8: design of structures for earthquake resistance of structures*. CEN European Committee for Standardisation.
- EN 1998-5. *Eurocode 8: Design of structures for earthquake resistance - Part 5: foundations, retaining structures and geotechnical aspects*. Bruxelles, Belgium: CEN European Committee for Standardization.
- Eurocode 8, 2003. *Design of structures for earthquake resistance. Part 1: general rules, seismic actions and rules for buildings*. Draft January 2003.
- Finn W.D.L., Lee K.W. and Martin G.R., 1977. *An effective stress model for liquefaction*. Proc. ASCE, Journal of Geotechnical Engineering Division, Vol. 103, N. GT6.
- Finn W.D.L. and Bathia S.K., 1981. *Prediction of Seismic Porewater pressures*. Proc. in the Tenth Int. Conf. on Soil Mechanics and Foundation Engineering, Vol. 3, A.A. Balkema, Rotterdam, pp. 201-206.

- Finn W.D.L. and Ledbetter R.H., 1991. *Evaluation of liquefaction effects and remediation strategies by deformation analysis*. Proc. Int. Conf. on Geotechnical Eng. for Coastal Development, GEOCOAST 91, pp. 1-20.
- Finn L.W.D, Yogendrakumar M, Yoshida N and Yoshida H., 1986. *TARA-3: a program to compute the response of 2-D embankments and soil-structure systems to seismic loadings*. Canada: Department of Civil Engineering, University of British Columbia.
- Finn L., Ventura C.E. and Schuster N.D. 1995. *Ground motions during the 1994 Northridge earthquake*. Canadian Journal of Civil Engineering, Vol 22, 300-315.
- Finn L.W.D., Ledbetter R.H. and Marcusson W.F., 1997. *North American practise for evaluating the seismic safety of embankment dams*. In: Ishihara K. editor. Earthquake Geotechnical Engineering. Rotterdam: Balkema; p. 1227-52.
- Finn L.W.D., 2000. *State-of-the-art of geotechnical earthquake engineering practice*. Soil Dyn Earthquake Eng 2000; 20:1-15.
- Fontanella E.M., 2008. *Analisi a ritroso del comportamento meccanico di una diga in terra zonata in fase costruttiva e di esercizio*. Rivista Italiana di Geotecnica (RIG) 4/2008, 11-24 (in Italian).
- Fontanella E.M. and Pagano L., 2008. *Approcci semplificati per l'interpretazione delle misure delle dighe in terra*. Rivista Italiana di Geotecnica 3/2008 pp.95-108 (in Italian).
- Fredlund D.G., Rahardjo H. and Fredlund M. D., 2012. *Unsaturated Soil Mechanics in Engineering Practice*. Ed. John Wiley & Sons, Inc.
- Galadini F., Meletti C. and Rebez A., 2000. *Le ricerche del GNDT nel campo della pericolosità sismica (1996–1999)*. CNR-Gruppo Nazionale per la Difesa dai Terremoti (CNR-GNDT), Rome, 397.
- Gazetas G., 1982. *Shear vibration of vertically inhomogeneous earth dams*. Int J Numer Anal Methods Geomech 1982;6:219-41.
- Gazetas G., 1987. *Seismic response of earth dams: some recent developments*. Soil Dyn Earthquake Eng; 6(1):3-47.
- Gazetas G., Dakoulas P., 1992. *Seismic analysis and design of rockfill dams: state-of-the-art*. Soil Dyn Earthquake Eng;11: 27-61.
- Gens A., 1982. *Stress-strain and strength of a low plasticity clay*. Ph.D. Thesis Imperial College, London.
- Gruppo di lavoro MPS, 2004. *Redazione della mappa di pericolosità sismica prevista dall'Ordinanza PCM 3274 del 20 marzo 2003*. Rapporto conclusivo per il dipartimento di Protezione Civile, INGV, Milano – Roma, aprile 2004, 65 pp. + 5 appendici, Internet web site: <http://zonesismiche.mi.ingv.it/elaborazioni/>.
- Guan G. S., Rahardjo H. and Choon L. E., 2010. *Shear strength equations for unsaturated soil under drying and wetting*. Journal of Geotechnical and Geoenvironmental Engineering, ASCE, 136(4), 594-606.

- Gupta I.D., 2002. The state of the art in seismic hazard analysis. ISET Journal of Earthquake Technology 2002; 39(4):331–46.
- Harder L-F, Bray J.D., Volpe R.L. and Rodda K., 1998. *Performance of earth dams during the Loma Prieta Earthquake*. USGS Professional: 1552 (D).
- Hardin B.O. and Drnevich V.P., 1972. *Shear modulus and damping in soils: design equations and curves*. J Soil Mech Found Division, ASCE; 98(SM7):667-92.
- Icold, 1980. *Deterioration of dams and reservoirs. Examples and their analysis*. ICOLD, Paris. Balkema, Rotterdam.
- Icold, 2001. *Design features of dams to resist seismic ground motion*. Bulletin 120.
- Icold, 2010. *Selecting seismic parameters for large dams: guidelines*. Bulletin; 72.
- Icold, 2012. *Dam safety and Earthquakes*. Position paper of International Commission on Large Dams, chaired by Dr. Martin Wieland.
- Idriss I.M. and Sun J.I., 1992. *SHAKE91- a computer program for conducting equivalent linear seismic response analysis of horizontally layered soil deposits*. User's Guide. Center for Geotechnical Modeling, Civil Engineering Department, U.C. Davis.
- Iervolino I. and Cornell C.A., 2005. *Record Selection for nonlinear seismic analysis of structures*. Earthquake Spectra, 21(3), 685-713.
- Iervolino I. and Cornell C.A., 2008. *Probability of occurrence of velocity pulses in near-source ground motions*. Bulletin of the Seismological Society of America; 98(5):2262-2277.
- Iervolino I., Giorgio M., Galasso C. and Manfredi G., 2008. *Prediction relationships for a vector valued ground motion intensity measure accounting for cumulative damage potential*. 14th World Conference on Earthquake Engineering, Beijing, China, October 12-17.
- Iervolino I., Galasso C., Manfredi G. and Giorgio M., 2009. *Analisi di pericolosità sismica vettoriale per parametri di picco e integrali del moto sismico*. ANIDIS, Bologna (in Italian).
- Iervolino I., Manfredi G. and Cosenza E., 2006. *Ground-motion Duration Effects on Non-Linear Structural Response*. Earthquake Engineering and Structural Dynamics 35, 21-38.
- Iervolino I., Galasso C., Cosenza E., 2009. *REXEL: computer aided record selection for code-based seismic structural analysis*. Bulletin of Earthquake Engineering, 8:339-362. DOI 10.1007/s10518-009-9146-1.
- Ishibashi I. and Zhang X., 1993. *Unified dynamic shear moduli and damping ratios of sand and clay*. Soils and Foundations; 33(1):182-91.
- Itasca Consulting Group Inc., 2005. *FLAC - Fast Lagrangian Analysis of Continua. Version 5.0, User's Manual*.
- Itasca Consulting Group Inc., 2011. *FLAC - Fast Lagrangian Analysis of Continua. Version 7.0, User's Manual*.

- Jommi C., 2000. *Remarks on the constitutive modelling of unsaturated soils*. Experimental evidence and theoretical approaches in unsaturated soils, Balkema, Rotterdam, 139-153.
- Kramer S.L., 1996. *Geotechnical earthquake engineering*. New Jersey: Prentice-Hall Inc.
- Kramer S.L. and Smith M.W., 1997. *Modified Newmark model for seismic displacements of compliant slopes*. J Geotech Geoenviron Eng ; 123(7):635-44.
- Krinitzsky E.L., 1995. *Deterministic versus probabilistic seismic hazard analysis for critical structures*. International Journal of Engineering Geology 1995; 40: 1–7.
- Krinitzsky E.L., 1998. The hazard in using probabilistic seismic hazard analysis for critical structures. In: Geotechnical earthquake engineering and soil. III ASCE geotechnical special publication, vol. 75(1). Dakoulas, Yougain, Holtz, editors.
- Kuhlemeyer R.L. and Lysmer J., 1973. *Finite Element Method accuracy for wave propagation problems*. Journal of Soil Mechanics & Foundations Division, ASCE, 99 (SM5), pp. 421-427.
- Kwok A. O. L. et al., 2007. *Use of exact solutions of wave propagation problems to guide implementation of nonlinear seismic ground response analysis procedures*. J. Geotech. Geoenviron. Eng., 133(11), 1385–1398.
- Lambe T.W. and Whitman R.V., 1969. *Soil Mechanics*. Ed. John Wiley & Sons, New York.
- Lane P.A. and Griffiths D.V., 2000. *Assessment of stability of slopes under drawdown conditions*. Jnl. Geotech. and Geoenv. Engng. 126(5): 443-450.
- Lysmer J. and R. L. Kuhlemeyer, 1969. *Finite dynamic model for infinite media*. J. Eng. Mech. Div. ASCE, 95 (EM4), 859-877.
- Madiai C., 2009. *Correlazioni tra parametri del moto sismico e spostamenti attesi del blocco di Newmark*. Rivista Italiana di Geotecnica (2009) 23-43.
- Malhotra K.P., 2006. *Seismic risk and design loads*. Earthquake Spectra 2006; 22(1): 115–28.
- Martin G. R., Finn W. D. L. and Seed H. B., 1975. *Fundamentals of Liquefaction under Cyclic Loading*, J. Geotech., Div. ASCE, 101(GT5), 423-438 (1975).
- Mejia L.H. and Dawson E.M., 2006. *Earthquake deconvolution for FLAC*. 4th International FLAC Symposium on Numerical Modeling in Geomechanics – 2006 – Hart & Varona (eds.) Paper: 04-10.
- Meletti C., Montaldo V., 2007. *Stime di pericolosità sismica per diverse probabilità di superamento in 50 anni: valori di ag*. Progetto DPC-INGV S1, Deliverable D2, <http://esse1.mi.ingv.it/d2.html> (in Italian).
- Ministero dei Lavori Pubblici (M.LL.PP.), D. M. 24/03/82. *Norme tecniche per la progettazione e la costruzione delle dighe di sbarramento*. Supplemento alla Gazzetta Ufficiale 04/08/82, n. 212 (in Italian).
- Ministero dei Lavori Pubblici (M.LL.PP.), D.M. 14/01/2008. *Norme Tecniche per le costruzioni*. (in Italian).

- Ministero Delle Infrastrutture e Dei Trasporti (MIT), DECRETO 26 giugno 2014. *Norme tecniche per la progettazione e la costruzione degli sbarramenti di ritenuta (dighe e traverse)*. GU n.156 del 08/07/2014 (in Italian).
- Morgenstern, 1963. *Stability charts for earth slopes during rapid drawdown*. Géotechnique 13(1):121-131.
- Neumann S.P., 1973. *Saturated-unsaturated seepage by finite elements*. Jnl. Hydraul. Div., ASCE, 99, HY12: 2233-2250.
- Newlin C.W. and Rossier S.C., 1967. *Embankment drainage after instantaneous drawdown*. Soil Mechanics and Foundations Division. Journal vol 93, no SM6, pp 79-95.
- Newmark N.M., 1965. *Effect of earthquakes on dams and embankments*. Géotechnique;15(2):139-60.
- Pagano L., 1998. *Interpretation of mechanical behaviour of earth dams by numerical analysis*. Proc. Workshop in Naples on Prediction and Performance in Geotechnical Engineering, Naples, pp. 89-150.
- Pagano L., 1998. *Steady state and transient unconfined seepage analysis for earthfill dams*. In: Proceedings of VIII ABAQUS Users' Conference. Milano; pp. 577-585.
- Pagano L., Desideri A. and Vinale F., 1998. *Interpreting the settlement profiles of earth dams*. J Geotechn Geoenviron Eng, ASCE; 124(10): 923-32.
- Pagano L., Mancuso C. and Sica S., 2008. *Prove in sito sulla diga del Camastra: tecniche sperimentali e risultati*. Italian Geotechnical Journal; 3 (08):11-28. (in Italian).
- Pagano L., Desideri A. and Sica S., 2004. *Rappresentazione delle misure realizzate su dighe in terra*. XXII Convegno Nazionale di Geotecnica, Palermo, pp.569-577 (in Italian).
- Pagano L., Sica S. and Desideri A., 2006. *Representativeness of measurements in the interpretation of earth dam behavior*. Canadian Geotech J 2006; 43(1):87-99.
- Pagano L., Sica S. and Fenelli G.B., 2003. *Interpreting the Camastra Dam behaviour in 40 years of operation*. In: Proceedings of the third international symposium on deformation characteristics of geomaterials ISLyon03; p. 1389-94.
- Papadimitriou A.G., Bouckovalas G.D. and Andrianopoulos K.I., 2014. *Methodology for estimating seismic coefficients for performance-based design of earth dams and tall embankments*. Soil Dynam Earthq Eng, 2014; 56: 57-73.
- Papadimitriou A.G., Andrianopoulos K.I., Bouckovalas G.D. and Anastasopoulos K., 2010. *Improved methodology for the estimation of seismic coefficients for the pseudo-static stability analysis of earth dams*. In: Proceedings, 5th international conference on recent advances in geotechnical earthquake engineering and soil, dynamics; p. 24-9.
- Pastor M., Zienkiewicz O.C. and Chan A.H.C., 1990. *Generalized plasticity and the modelling of soil behaviour*. International Journal for Numerical and Analytical Methods in Geomechanics; 14:151-190.
- Pelecanos L., 2013. *Seismic response and analysis of earth dams*. PhD Thesis. Imperial College of Science, Technology & Medicine, London.

- Pelecinos L., Kontoe S. and Zdravković L., 2015. *A case study on the seismic performance of earth dams*. Géotechnique 65, No. 11, 923–935.
- Potts D. M. and Zdravković L., 1999. *Finite element analysis in geotechnical engineering. Theory*. Thomas Telford Limited.
- Potts D. M. and Zdravković L., 2001. *Finite element analysis in geotechnical engineering. Application*. Thomas Telford Limited.
- Prato C.A. and Delmastro E., 1987. *1-D seismic analysis of embankment dams*. J. Geotech Eng ASCE; 113(8):904-9.
- Rampello S. and Silvestri F., 1993. *The stress-strain behaviour of natural and reconstituted samples of two overconsolidated clays*. In Geotechnical Engineering of Hard Soils-Soft Rocks, Anagnostopoulos et al. (eds), Balkema, Rotterdam.
- Rampello S., Callisto L. and Fagnoli P., 2006. *Valutazione del coefficiente sismico equivalente*. Rapporto scientifico Linea 6.3 ‘Stabilità dei pendii’, Consorzio ReLuis (in Italian).
- Rampello S., Callisto L., 2008. *Stabilità dei pendii in condizioni sismiche*. In Opere Geotecniche in Condizioni Sismiche. XII Ciclo di Conferenze di Meccanica e Ingegneria delle Rocce, 2008, pp. 241-271.
- Rampello S., Callisto L. and Fagnoli P., 2008. *Evaluation of seismic coefficients for slope stability analysis using a displacement-based approach*. Panel Paper. In: Seismic Engineering International Conference commemorating the 1908 Messina and Reggio Calabria Earthquake (MERCEA), in press
- Rampello S., Callisto L. and Fagnoli P., 2009. *Two-dimensional seismic response analysis to evaluate permanent slope displacements*. In: Kokusho A, Tsukamoto A, Yoshimine A, editors. Performance-based design in earthquake geotechnical engineering. London: Taylor and Francis Group; p. 929-36.
- Rampello S., Cascone E. and Grosso N., 2009. *Evaluation of the seismic response of a homogeneous earth dam*. Soil Dynamics and Earthquake Engineering 29 782-798.
- Rathje E.M. and Antonakos G., 2011. *A unified model for predicting earthquake-induced sliding displacements of rigid and flexible slopes*. Eng Geol; 122:51-60.
- Reinius E., 1954. *The stability of the slopes of earth dams*. Géotechnique 5: 181-189.
- Resendiz D., Romo M.P. and Moreno E., 1982. *El Infiernillo and La Villita Dams: seismic behaviour*. Journal of Geotechnical Engineering Division ASCE; 108(GT1): 109-31.
- Reiter L., 1990. *Earthquake hazard analysis—issues and insights*. New York: Columbia University Press.
- Romeo R., Prestininzi A., 2000. *Probabilistic versus deterministic seismic hazard analysis: an integrated approach for siting problems*. Soil Dynamics and Earthquake Engineering 2000;20:75–84.
- Sarma S.K., 1973. *Stability analysis of embankments and slopes*. Géotechnique, 23, n.3, pp. 423-433.

- Sarma S.K., 1975. *Seismic stability of earth dams and embankments*. Geotechnique; 25(4):743-61.
- Saygili, G., Rathje, E.M., 2008. *Empirical predictive models for earthquake-induced sliding displacements of slopes*. Journal of Geotechnical and Geoenvironmental Engineering ASCE 134(6) (2008) 790-803.
- Seed H.B., 1979. *Considerations in the earthquake-resistant design of earth and rockfill dams*. Geotechnique; 29(3):215-63.
- Seed H.B. and Booker J.R., 1977. *Stabilization of potentially liquefiable sand deposits using gravel drains*. Journal of the Geotechnical Engineering Division, ASCE; 103(7):755-68.
- Seed H.B., Lee K.L., Idriss I.M. and Makdisi R., 1973. *Analysis of the slides in the San Fernando dams during the earthquake of Feb. 9 1971*. Report No. EERC 73-2, Earthquake Engineering Research Center, University of California, Berkeley, p. 150.
- Seed H.B., Lee K.L. and Idriss I.M., 1969. *Analysis of Sheffield Dam failure*. J. Soil Mech. Found. Div. ASCE, 95, SM6, pp. 1453-1490.
- Seed H.B., Makdisi F.I. and DeAlba P. 1978. *The performance of earthfill dams during earthquakes*. Journal of the Geotechnical Engineering Division, ASCE, Volume 104, No. GT7, pp. 967-994.
- Seed H.B. and Martin G.R., 1966. *The seismic coefficient in earth dam design*. Journal of Soil Mechanics Foundations Division ASCE; 92(SM3):105-34.
- Seed H.B., Murauka J., Lysmer J. and Idriss I.M., 1976. *Relationships between maximum acceleration, maximum velocity, distance from source and local site conditions for moderately strong earthquakes*. Bull. Seism. Soc. Of America, 66, 4, pp. 1323-134.
- Seed H.B., Seed R.B., Lai S.S. and Khamenchpour B., 1985. *Seismic design of concrete faced rockfill dams*. In: Concrete face rockfill dams-design, construction and performance. ASCE; 1985. p. 459-78.
- Seed H. B., Tokimatsu K., Harder L. F. and Chung R. M., 1985. *Influence of SPT Procedures in Soil Liquefaction Resistance Evaluations*. Journal of Geotechnical Engineering, ASCE, Vol. 111, No. 12, pp. 1425 – 1445.
- Seed H.B., Wong R.T., Idriss I.M. and Tokimatsu K., 1986. *Moduli and damping factors for dynamic analyses of cohesionless soils*. Journal of Geotechnical and Geoenvironmental Engineering ASCE; 112(11):1016-32.
- Sheng D., Fredlund D. G. and Gens A., 2008a. *A new modelling approach for unsaturated soils using independent stress variables*. Canadian Geotechnical Journal, 45, 511-534.
- Sheng D., Gens A., Fredlund, D. G. and Sloan S. W., 2008b. *Unsaturated soils: From constitutive modelling to numerical algorithms*. Computers and Geotechnics, 35, 810-824.
- Sheng D., Sloan, S. W. and Gens A., 2004. *A constitutive model for unsaturated soils: thermomechanical and computational aspects*. Computational Mechanics, 33, 453-465.

- Sica S., 2001. *Analisi del comportamento dinamico di dighe in terra*. Ph.D Thesis, Consorzio delle Università di Napoli e Roma (in Italian).
- Sica S., Santucci de Magistris F., Vinale F., 2002. *Seismic behaviour of geotechnical structures*. Annals of geophysics, vol. 45, n. 6, December 2002.
- Sica S., 2003. *Dynamic analysis of earth dams*. Constitutive modelling and analysis of boundary value problems in geotechnical engineering. A workshop in Napoli, 22-24 April 2003, Hevelius Edizioni.
- Sica S., Pagano L., Modaressi A., 2008. *Influence of past loading history on the seismic response of earth dams*. Computers and Geotechnics, 35 (1), pp. 61-85.
- Sica S. and Pagano L., 2009. *Performance-based analyses of earth dams: procedures and applications to a sample case*. Soils Found; 49(6):921-39.
- Sica S., Pagano L. and Modaressi A., 2008. *Influence of past loading history on the seismic response of earth dams*. Computers and Geotechnics; 35:61-85.
- Sica S., Pagano L. and Vinale F., 2008. *Interpretazione dei segnali sismici registrati sulla diga di Camastra*. (in Italian) Geotechnical Journal; 4(08):97-111.
- Silvestri S., d'Onofrio A., 2014. *Risposta sismica e stabilità dei centri abitati e infrastrutture*. XXV CNG – AGI – ROMA – ISBN 978-88-97517-03-0, 5-60 (in Italian).
- Skempton A.W., 1954. *The pore pressure coefficients A and B*. Géotechnique 4(4), 143-147.
- Spallarossa D., Barani S., 2007. *Disaggregazione della pericolosità sismica in termini di M-R-ε*. Progetto DPC-INGV S1, Deliverable D14, <http://esse1.mi.ingv.it/d14.html> (in Italian).
- Swaigood J. R., 1998. *Seismically-induced deformation of embankment dams*. In proceedings of sixth national conference on earthquake engineering. Seattle, Washington, U. S. A. May 31 - June 4 1998.
- Swaigood J.R. and Au-Yeung Y., 1991. *Behavior of dams during the 1990 Philippines earthquake*. Presented at the ASDSO 1991 annual conference, San Diego, 29 Sep- 2 Oct 1991.
- Swaigood J. R., P.E. and C.P.G., 2003. *Embankment dam deformations caused by earthquakes*. Consulting, Conifer, Colorado, U.S.A.
- Terzaghi K., 1943. *Theoretical Soil Mechanics*. John Wiley and Sons. New York.
- Terzaghi K. and Peck R.B. 1948. *Soil mechanics in engineering practice*. Wiley, New York.
- Terzaghi K., 1952. *Mechanisms of landslides. The geological survey of America*. Berkeley: Engineering Geology.
- Troncoso J.H., 1990. *Failure risks of abandoned tailing dams*. In: Proceedings of the international symposium on safety and rehabilitation of tailing dams, ICOLD, Paris, p. 82-89.

Troncoso J.H., Krause A.J. and Corser P.G., 1999. *Seismic design of lined face earth dams*. In: Proceedings of the second international conference on earthquake geotechnical engineering, Usbon; p. 703-9.

Urciuoli G., Pirone M. and Papa R., 2011. *Elementi di meccanica dei terreni parzialmente saturi*. Ed. Hevelius Edizioni (in Italian).

Viratjandr C. and Michalowski R. L., 2006. *Limit analysis of submerged slopes subjected to water drawdown*. Can. Geotech. J. 43: 802–814 (2006).

Wright S.G. and Duncan J.M., 1987. *An examination of slope stability computation procedures for sudden drawdown*. US Army Corps of Engineers, Washington DC.

Zienkiewicz O.C., Chan A.H.C., Pastor M., Schrefler B.A. and Shiomi T., 1999. *Computational Geomechanics* (with special reference to earthquake engineering). Wiley and Sons, Chichester.

Zienkiewicz O.C. and Shiomi T., 1984. *Dynamic behaviour of saturated porous media; the generalised Biot formulation and its numerical solution*. Int J Numer Anal Meth Geomech; 8:71-96.